The Dissertation Committee for Kyle J. Higdon Certifies that this is the approved version of the following dissertation:

Monte Carlo Sensitivity Analyses of DSMC Parameters for Ionizing Hypersonic Flows

Committee:

David B. Goldstein, Co-Supervisor

Philip L. Varghese, Co-Supervisor

Derek S. Liechty

Brett A. Cruden

Laxminarayan L. Raja

Monte Carlo Sensitivity Analyses of DSMC Parameters for Ionizing Hypersonic Flows

by

Kyle J. Higdon

Dissertation

Presented to the Faculty of the Graduate School of

The University of Texas at Austin

in Partial Fulfillment

of the Requirements

for the Degree of

Doctor of Philosophy

The University of Texas at Austin

August 2018

This dissertation is dedicated to my loving parents, Kevin and Camille, my brother, Wesley, and my sister, Holly.

Acknowledgements

The research presented in this dissertation was only made possible by the gracious support, guidance, and encouragement from my advisors, family, friends, and colleagues.

Special thanks are reserved for my advisors Prof. David Goldstein and Prof. Philip Varghese who were the driving force behind the bulk of this research. They were somehow able to mold me from a fresh undergraduate student into a doctoral candidate culminating in this dissertation. Our numerous conversations on the topics presented in this research were invaluable to its development. I would also like to thank them for allowing me to spend time on my personal running pursuits and coaching the Texas Running Club which allowed me to stay sane throughout these years. In addition, I wish to extend special thanks to my NASA Space Technology Research Fellowship collaborator Derek Liechty for his guidance on electronic excitation and charged particle modeling. I am grateful to NASA Ames researchers Brett Cruden and Aaron Brandis for their assistance and patience with my many questions on the EAST experiments and the NEQAIR code.

I must acknowledge the generous sources of funding that have supported me throughout my research. Thank you to the PECOS center and the Department of Energy for funding the first leg of this research through the PSAAP program. In addition, the computational resources provided by the Texas Advanced Computing Center have been invaluable for completing my simulations. Most of all, I would like to recognize the NASA Space Technology Research Fellowship (NSTRF) program for funding the majority of my research. This program has afforded me many opportunities above and beyond the research presented in this dissertation. The NSTRF allowed me to spend

summers at NASA Ames Research Center, NASA Langley Research Center, and NASA Johnson Space Center to collaborate with several researchers. The time spent working at the NASA labs and the friendships that I made with NASA employees and fellow interns will be invaluable to my career.

Finally, I could not have completed this dissertation without the love and support of my family members and friends. Foremost, my parents who took care of so much including alleviating my stress as I journeyed through graduate school. It is impossible to list the many ways in which they are behind the culmination of this research and the inspiration for my success. Another integral part of my support crew were my brother and sister who were always there for support and to go “rally catting” when need be. I would also like to express my thanks to my grandparents for teaching me the healing powers of running and telling me repeatedly that I needed to “put a period on it” and complete this dissertation. Last but not least, I would like to thank all my friends throughout these graduate years, especially Taylor Hall, Sarah Escobedo, Tim Haller, Saif Al-Shmaisani, and the many friends I made in the Texas Running Club.

Monte Carlo Sensitivity Analyses of DSMC Parameters for Ionizing Hypersonic Flows

Kyle J. Higdon, Ph.D.

The University of Texas at Austin, 2018

Co-Supervisors: David B. Goldstein and Philip L. Varghese

This work focuses on the development and sensitivity analyses of a direct simulation Monte Carlo (DSMC) code to understand the complex physical processes that occur during hypersonic entry into a rarefied atmosphere. Simulations are performed on 1-dimensional hypersonic shock scenarios that mimic the conditions of high altitude atmospheric entry to Earth and Saturn with the Computation of Hypersonic Ionizing Particles in Shocks (CHIPS) code. To model hypersonic entry problems accurately, the CHIPS code must resolve nonequilibrium flows and account for a number of complex gas dynamics processes at the molecular level. In this thesis, several high temperature models are added to the CHIPS code including charged particle models and electronic excitation. These models are refined using preliminary sensitivity analyses resulting in improved electronic excitation models and a new backward chemical reaction model.

The CHIPS simulations completed in this work reproduce rarefied hypersonic shock tube experiments performed in the Electric Arc Shock Tube (EAST) at NASA Ames Research Center. The CHIPS results are post-processed by the NEQAIR line-by-line radiative solver to compare directly to spectra measured experimentally in EAST. The DSMC techniques used to model hypersonic phenomena require numerous experimentally calibrated parameters. Many of these parameters are inferred from lower

temperature experiments, resulting in an unknown amount of uncertainty in the simulated results at the extreme conditions of hypersonic flow. A global Monte Carlo sensitivity analysis is performed by simultaneously varying the CHIPS input parameter values to understand the sensitivity of experimentally measured quantities simulated by the CHIPS and NEQAIR codes. The sensitivity of several of these output quantities is used to rank the input parameters, identifying the most important parameters for the simulation of the hypersonic scenario. It was concluded that experimentally measured radiation intensity is most sensitive to the following key processes: $N+e^- \rightleftharpoons N^+ + e^- + e^-$, $NO+N^+ \rightleftharpoons N+NO^+$, $N_2+N \rightleftharpoons N+N+N$, $N+O \rightleftharpoons NO^+ + e^-$, $N+N \rightleftharpoons N_2^+ + e^-$, and Z_{elec} for N, O, and N_2^+. In the future, this ranking can be used to identify which input parameters should be experimentally investigated, where model improvements could be beneficial, and aid in reducing the parameter space for DSMC calibrations to experimental data.

Table of Contents

List of Tables

List of Figures

CHAPTER 1

Introduction

1.1 MOTIVATION

Entry into a planetary atmosphere is a perilous journey where high temperatures produced by extreme Mach numbers result in complicated physics. During the initial phases of re-entry into Earth's atmosphere, for example, a vehicle passes through the low density upper atmosphere. Even in the rarefied regime, velocities are high enough that significant heat soaking occurs. In addition, spacecraft dynamics and radio communications remain critically affected by the surrounding flow. As a vehicle enters an atmosphere at hypersonic speeds, a bow shock wave develops that can produce temperatures much hotter than the, approximately 5,300 K, surface of the sun. At these temperatures, various physical processes become important including charged particle elastic collisions; rotational, vibrational, and electronic excitation; and neutral, ion, and electron chemical reactions. The understanding and prediction of these processes increases in complexity when considering that each entry scenario is unique. For example, a vehicle on a lunar return trajectory to Earth is expected to experience speeds of approximately 10 km/s into air [1] while a vehicle entering Saturn's atmosphere may encounter speeds of 28 km/s through a hydrogen-helium mixture [2]. The design of vehicles that can withstand these scenarios requires numerous experimental tests along with many numerical simulations. While experiments are useful for testing hypersonic entry conditions, they are costly and detailed flowfield properties are difficult to obtain. Predictive simulations are advantageous in that they can produce detailed results of various scenarios at relatively low cost, but many of these simulations have not been calibrated with experimental results and the uncertainty inherent in each simulation is

unknown. In addition, aspects of the physics are not well understood or modeled. This can lead to substantial uncertainty in the accuracy of predictive simulations with potentially dire consequences.

One such computational tool that is frequently applied to rarefied flight and entry scenarios is the direct simulation Monte Carlo (DSMC) method [3]. The DSMC method is a stochastic model of individual particles and their physics where each simulated 'particle' represents many real particles in the simulated domain. DSMC is generally applicable for rarefied flows where the Knudsen number is sufficiently large. In this regime, the continuum model breaks down and the Navier-Stokes equations begin to fail. DSMC is able to correctly model flow properties in large non-equilibrium regions via a probabilistic approach that uses rates or cross-sections from experiments or theory. The extreme conditions of hypersonic flows require various models for the high temperature physics present, necessitating a large number of input parameters. Often, these parameters are determined from low temperature experiments and extrapolated far outside of their calibrated temperature range. Although it is well known that these input parameters carry a certain degree of error, it is unclear how that error is propagated through a DSMC simulation. For this reason, a sensitivity analysis is required to determine which input parameters have the greatest effect on hypersonic results produced by DSMC simulations. By identifying which input parameters are the most important for a particular scenario, guidance is provided into determining where improved parameters are necessary. The parameters that are both important and contain a significant degree of uncertainty should become the subject of experimental or analytical efforts to reduce this uncertainty. In addition to obtaining a ranking of the hypersonic DSMC simulation's sensitivity to each input parameter, analysis of the most important parameters can indicate where improved physical models are required in the DSMC simulation. Finally,

this sensitivity analysis aids in reducing the parameter space for a DSMC calibration to experimental data.

1.2 OBJECTIVES

The objective of the current research is to study the sensitivity of experimentally measurable quantities to DSMC input parameters for ionizing hypersonic flows. In approaching this goal, a secondary objective is applying information obtained from preliminary sensitivity studies to develop improved DSMC models where necessary. DSMC simulations are performed with the Computation of Hypersonic Ionizing Particles in Shocks (CHIPS) code which primarily models a 1-dimensional unsteady shock wave [4]. Modeling hypersonic scenarios requires the addition of several models to the CHIPS code, including free electron movement, charged particle chemistry, and electronic excitation. Once these models are included in CHIPS, preliminary sensitivity analyses of various CHIPS output parameters are completed. These sensitivity studies are used to analyze the current CHIPS models and determine which physical processes have a significant effect on the results. This investigation indicates where new or improved models are required, and appropriate steps are taken to apply these models in the CHIPS code.

Once the CHIPS code includes these various models, the results are compared directly to experimental data. The CHIPS simulations completed in this research are meant to reproduce the conditions of NASA Electric Arc Shock Tube (EAST) experiments [1]. These experiments are limited to the measurement of radiative emissions due to the extreme speeds and temperatures produced during a hypersonic shock tube test. While the addition of advanced physics to the CHIPS code reproduces most of the required hypersonic physics, radiative processes are not yet simulated, and a post-

processing step is required. To compare with the EAST experimental data, the results of the CHIPS simulations are passed to the NASA Nonequilibrium Air Radiation program (NEQAIR) to produce emission spectra [5]. Once radiative quantities can be predicted by the CHIPS/NEQAIR codes, the results are directly compared with EAST experimental data. These comparisons are used to suggest final model and parameter improvements. After satisfactory agreement with the experimental results, a global Monte Carlo sensitivity analysis is performed which studies the sensitivity of macroparameters, such as radiative emission, to various DSMC input parameters. A ranking of the most important input parameters for each quantity of interest is compiled to inform future parameter calibrations or experimental investigations.

1.3 Literature Review

The following literature review summarizes relevant advancements in the major subject areas of this research. Recent advancements in the DSMC method are covered here, where the focus is on identifying studies completed on simulation approaches that will be investigated in this thesis. In addition, prior attempts at modeling radiation with the DSMC method are reviewed. This is followed by discussing several notable DSMC sensitivity analyses along with relevant hypersonic sensitivity analyses performed using other methods. Finally, an overview of the EAST experimental setup and data obtained from recent campaigns are described.

1.3.1 Direct Simulation Monte Carlo

The Computation of Hypersonic Ionizing Particles in Shocks (CHIPS) code evolving from this research is built from the DSMC codebase developed by Strand [6]. While many of the routines created by Strand have been rewritten or modified, the underlying structure of the CHIPS code has been substantially influenced by his

preceding work. Strand's DSMC code was created largely following the standard models employed in Bird's published algorithm and 1994 book which is widely cited as the standard for the DSMC method [3]. One particularly novel trait of Stand's implementation of DSMC, later incorporated in the CHIPS program, is its ability to simulate an unsteady shock wave. In previous publications, 1-dimensional unsteady shocks were simulated using DSMC by Goldstein et al. [7][8] and with a DSMC/Euler hybrid solver by Roveda et al. [9] More recently, the same unsteady shock method was applied by Zhu [10] who adapted Strand's approach. The merits of this technique and contrasts with other methods of modeling shock waves will be discussed in Chapter 2. Since the previously developed models for elastic collisions, rotational and vibrational relaxation, and neutral particle chemistry were reviewed in Strand's thesis [6], a brief summary of these models is covered in Chapter 2, but a full literature review is not included here. In the remaining DSMC literature review, a discussion of the models added to the CHIPS code, beyond the work of Strand, is provided.

A primary addition to the CHIPS code is the modeling of charged particles, necessitated by the weakly ionized plasma that is formed during hypersonic entry. The modeling of charged particles in DSMC presents many challenges, the most notable of which is the simulation of free electrons due to their high speed and collision frequency. A simplistic approach for modeling free electron movement was proposed by Bird, where the free electrons are tethered to an ion and forced to move with the ion [11]. This method neglects the possibility of charge separation by assuming quasi-neutrality, requiring a separate ambipolar diffusion calculation [12]. A second method for handling free electrons was proposed by Boyd where free electrons are moved with the average ion velocity [13]. More recently, an investigation of various DSMC charged particle models has been performed by Farbar and Boyd [14].

With the inclusion of charged particles, various particle interactions may be introduced that require special consideration. Elastic collision parameters must be defined for each particle pair. For collisions involving two charged particles, the standard DSMC models have difficulty reproducing the correct collision cross-section as these collisions follow a Coulombic force law. While generally incorrect, many past DSMC simulations of charged particle physics followed the recommendation of Bird, choosing arbitrary electron collision parameters and assuming that collisions involving ions were identical to neutral particle collisions [15]. This allowed for the existing elastic collision parameters for neutral-neutral collisions to be copied to neutral-ion and ion-ion collisions. In addition, Bird assumed that electron-electron collisions were unimportant, allowing them to be omitted from a DSMC calculation. This neglect of electron-electron collisions has been adopted for nearly all DSMC studies. Ozawa improved the simulation of electron collisions by providing collision-specific parameters for several electron-neutral particle interactions [16]. An attempt to model the Coulombic potential for charged-charged collisions in DSMC was completed by Gallis where a correction is applied to the velocity of a particle during the DSMC simulation of particle movement [17]. Recently, a comprehensive calibration of elastic collision parameters was completed by Swaminathan-Gopalan and Stephani that determined accurate collision-specific parameters for an ionized air mixture [18]. Parameter fits were computed by minimizing the error when comparing with standard collision integrals, thereby providing the best fit simulation of both viscosity and diffusion over a wide temperature range. Resonance in the neutral-electron collisions was accounted for with a piecewise parameter fit over the temperature range of interest. Ion-ion, ion-electron, and electron-electron collisions were represented by a second order polynomial fit dependent on the free electron number

density and whether the collision is attractive or repulsive. Reference [18] represents the most comprehensive study of charged elastic collision parameters to date.

In addition to the inclusion of charged particles, high temperature hypersonic DSMC simulations must address the modeling of electronic excitation. In previous studies, Bird [19], Carlson and Hassan [20], and Burt and Josyula [21] modeled electronic excitation by assuming that each particle contains a distribution of electronic levels. Since sparsely populated levels may have a significant impact on measured radiative results, this approach has the advantage of predicting weak radiative emission by circumventing the statistical scatter inherent to DSMC's particle nature. On the other hand, the use of a cell-based temperature to calculate the excited state distribution ignores the influence of collision energy on whether excitation occurs. Gallis and Harvey [22], and Ozawa [23] modeled electronic transitions directly by treating each excitation as a reaction with a specified cross-section determined from experiment. While this approach is advantageous for nonequilibrium simulations, a large number of experimental or ab-initio excitation rates would be required for a highly excited flow and currently available rates come with a substantial degree of uncertainty. In addition, each particle is assigned a single electronic level, requiring many particles to reproduce excited populations within the DSMC statistical scatter. Another electronic excitation model was proposed by Liechty and Lewis where each simulated particle is also assigned a single excited level, but excitation events are selected from the Boltzmann distribution depending on the total collision energy [24]. This approach follows a similar procedure typically used in DSMC for other internal modes by applying the Borgnakke-Larsen method [25]. It should be noted that this method does not consider the current excited state of the colliding particles and fails to distinguish between allowed and forbidden transitions.

The calculation of an electronic relaxation time, or electronic collision number, is a topic that must be addressed separately. In the previous literature, a wide range of electronic collision numbers have been suggested, following several different approaches. The variety of collision number solutions is mainly a result of the diverse scenarios where electronic excitation modeling has been applied. Bird proposed a constant collision number for neutral air species that is both state-independent and temperature independent [19]. In addition, Bird suggests that the collision number for neutral impact collisions is a factor of ten larger than for electron-neutral and ion-neutral collisions. Carson and Hassan performed a more rigorous estimate of the constant collision numbers from Landau and Teller theory but noted that the lack of experimental data could affect the determination of accurate collision numbers [20]. As an alternative, a state- and temperature-specific collision number was developed by Burt and Josyula which relies on excitation rates determined from the cell temperature [21]. Due to the reliance on the cell temperature, this method may incorrectly calculate the collision number, especially in strong nonequilibrium regions.

1.3.2 Radiation Modeling with DSMC

As previously mentioned, many hypersonic shock experiments rely on the measurement of radiative quantities due to the high temperatures experienced. Unfortunately, prediction of radiative emission with DSMC is challenging as it typically depends on the charged particle models, and their deficiencies, covered in the preceding section. There have been several attempts at directly modeling bound-bound transitions in DSMC. Bird [19] and Carlson and Hassan [20] modeled emission from fractions of grouped levels by applying a decay time for each tabulated transition. Similarly, Burt and Josyula directly modeled spontaneous emission by calculating the time to emission from

the Einstein coefficient for each transition [21]. While this approach models spontaneous emission by incorporating the electronically excited states of the DSMC simulation, confidence in the results relies on the ability to model the excited state distributions accurately and without significant statistical scatter.

An alternative method for obtaining radiative emission predictions from a DSMC simulation depends on post-processing or coupling DSMC with a radiative solver and is a common strategy in computational fluid dynamics simulations. Following this approach, Boyd and Phillips reproduced the Bow-Shock Ultra-Violet-2 hypersonic flight experiment by passing DSMC results to the nonequilibrium radiation code, NEQAIR [26]. Number densities and temperatures were post-processed by the NEQAIR code, assuming that a quasi-steady-state prevails. However, in Boyd and Phillips' DSMC simulation, electronic excitation was not directly modeled. The NEQAIR code was again used by Sohn, et al., but in a coupled model with DSMC [27]. Here, a DSMC simulation of the Stardust experiment was iteratively linked to NEQAIR by relying on the quasi-steady-state model to determine the excited state population. This population was passed back to the DSMC simulation where an escape factor was calculated based on coupling with the photon Monte Carlo method, adapted for DSMC by Ozawa, et al. [28] In this method, the radiative transfer equation is solved by tracing photon packets simulated from emission events and their absorption by the particles in the DSMC domain.

1.3.3 Sensitivity Analysis of DSMC Simulations

While the DSMC method has been used for quite some time, few sensitivity studies have been performed to analyze effect of input parameters on the simulated results. Existing sensitivity analyses typically have been restricted to the study of a single parameter. Although this approach is useful for understanding and interpreting the

underlying physics connected to variations of a single parameter, it neglects the coupling of parameters in determining some quantity of interest. More importantly, the method of varying a single input parameter may lead to wasted effort investigating a parameter that has a negligible effect on some quantity of interest when compared to other, more important input parameters.

In order to study the sensitivity of some quantity of interest to many input parameters simultaneously, a global sensitivity analysis is required. A previous sensitivity study of this nature was performed by Burt for a Mach 15.6 hypersonic compression corner DSMC simulation [29]. In this study, the sensitivity of the simulation results are analyzed for 14 input parameters, 6 aleatoric and 8 epistemic, but reactions rates are not considered due to the low enthalpy of the simulated flow. For epistemic uncertainties, Burt's sensitivity analysis is completed with a combination of Latin hypercube and importance sampling which only simulates the nominal, minimum, and maximum input parameter values and assumes a monotonic dependence in the simulated results. To date, the only other global sensitivity analysis of DSMC parameters was performed by Strand and Goldstein [30][31]. Since the assumption of monotonic simulated results is not necessarily valid, a global Monte Carlo method is used by Strand and Goldstein for the sensitivity analysis so that complex relationships between the parameters and the quantity of interest may be identified. Although informative for low Earth orbit entry, the work by Strand and Goldstein was outside of the more difficult hypersonic regimes encountered during atmospheric entry where high temperature physics such as electronic excitation, weakly ionized plasma, and radiation all play a role.

1.3.4 Brief Summary of EAST Experiments

The main objective of the current thesis is the completion of a global sensitivity analysis of experimentally measurable quantities to DSMC input parameters. As the focus of this research is on ionizing, hypersonic flows, reliable experiments must be selected from which a hypersonic scenario can be formed and act as the nominal simulated case for the sensitivity study. Due to the difficulty in creating reproducible, ionizing, hypersonic flows, especially without relying on an actual entering body, high-fidelity experimental data are rare. Fortunately, the experimental data produced in the NASA Electric Arc Shock Tube (EAST) are a prime candidate with a long history of successful experimental campaigns and will be used as the source of experimental results in this thesis [1][32][33]. The EAST data has an additional advantage over any other candidate as it has been the subject of a previous sensitivity study performed by Miki, et al. [34] In the following review, the EAST experimental setup will be discussed, and hypersonic scenarios will be chosen for DSMC modeling.

The EAST facility located at NASA Ames Research Center is able to reproduce the conditions of various re-entry scenarios with a high-enthalpy shock tube setup [32][33]. Figure 1.1 shows the main components of the EAST shock tube. The driver section initiates a shock through an electric arc discharge of a high voltage electrode into the driver gas, typically hydrogen or helium, which heats it rapidly. The driver gas is separated from the driven tube by a diaphragm that ruptures once a certain pressure is reached. This creates the shock that travels down the driven tube. An optional buffer section, that can be removed from the test setup, contains a buffer gas that prevents radiative heating of the driven section by the driver gas and improves test time by buffering the interface between the driver and test gas. Once the shock is created, it enters the 10.16 cm diameter driven section which is filled with a test gas composed of an

appropriate mixture composition to match the entry conditions of interest. When preparing the test gas, the driven section is pumped down to high vacuum and filled with the test gas until matching the entry scenario's pressure. Within the driven tube, the shock passes a windowed test section where various measurements are completed. Test times are typically on the order of a few microseconds which is enough to capture nonequilibrium shock radiation, decay to equilibrium, and the appearance of the contact surface between the driver and driven gases. Once the shock reaches the end of the driven section, it is dumped into a dump tank.

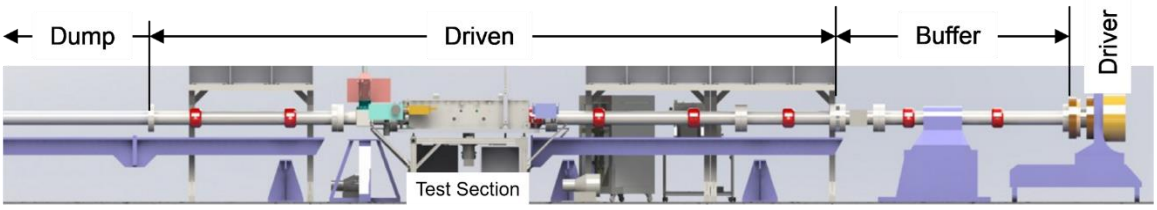

Figure 1.1 Visualization of the NASA Electric Arc Shock Tube experimental setup [2].

As the shock travels through the driven tube and test section, several measurements are taken. The shock tube is outfitted with multiple gauges spaced axially along the driven section and more frequently in the test section. These gauges are set to detect discontinuity in the pressure, emission, or electrical conductivity from which an x-t diagram can be formed, determining the shock velocity. In the test section, a slot window has been outfitted for imaging the shock. Spectrometers simultaneously capture the shock at four different azimuthal angles and at the same axial location. The spectrometers are attached to charge-coupled devices (CCDs) which are triggered by the incoming shock wave and are electronically shuttered to obtain a snapshot. The four spectrometers are

selected to measure the Vacuum Ultraviolet (VUV) ~120-200 nm, Ultraviolet/Visible (UV/Vis) ~200-500 nm, Visible/Near Infrared (Vis/NIR) ~500-900 nm, and Near Infrared (IR) ~900-1600 nm spectral ranges. A high vacuum box contains the optical path from the window to the camera to avoid absorption by oxygen and window materials are chosen to prevent interference at the measurement wavelengths.

Each one of the spectrometers has been calibrated and convolution functions are defined allowing for comparisons to spectral results. A detailed description of the calibrations and convolutions is provided by Cruden [33]. Radiance calibration is completed with an integrating sphere or a Deuterium arc source and the devices are translated to obtain a full field calibration. Spectral convolutions must be defined due to each spectrometer's instrument lineshape, which is determined by the spread function of the spectrometer optics as radiation passes through the spectrometer slit. Calibration with a spectral calibration lamp yields the instrument resolution functional fit. The VUV and UV/Vis cameras are fit with the square root of a Voigt function and the Vis/NIR camera uses a linearly weighted average of Gauss and Lorentzian functions. The IR camera employs a Gaussian fit for the instrument lineshape. Spatial calibration is completed with a ruled image and a spatial resolution function is determined from the combination of the optical resolution, CCD array resolution, and shock wave motion. The combination of these three effects are accounted for by their convolution, resulting in a broadened profile. The optical resolution estimated through ray-tracing is defined by a triangular function up to 900 nm and a trapezoidal function otherwise. The CCD camera function that accounts for the resolution limits is given by a square wave. Finally, the shock motion is typically approximated as a square pulse.

Recent experiments in the EAST facility have been completed over a wide range of shock velocities, pressures, and gas compositions. The results of many of these

experiments have been analyzed by Brandis and Cruden for re-entry into Earth's atmosphere from Low Earth Orbit, Lunar, and Mars return [1]. In this publication, benchmark cases were selected that demonstrated desirable experimental characteristics including test time, convergence to equilibrium, reliable spectral measurements, and proximity to the line of best fit through all the EAST results. As such, the benchmark cases identified by Brandis and Cruden will be focus of the Earth entry simulations performed in this thesis. The data collected in these experiments are available in the form of 3-dimensional spectral radiance measured as a function of position and wavelength. From these measurements, spatially resolved radiance integrated over some spectrum and spectrally resolved radiance integrated over some domain can be extracted. Since it is much more difficult to ensure that the domain of integration for the spectrally resolved radiance is consistent between the simulation and experiment, the focus of this dissertation will be on the modeling and sensitivity analysis of the spatially resolved radiance. In addition to Earth entry scenarios, the current research addresses the simulation of Saturn entry scenarios. These experiments were performed by Cruden and Bogdanoff in the EAST facility [2].

1.4 Dissertation Overview

The general structure of this dissertation is as follows. In Chapters 2 and 3, detailed descriptions of the DSMC models implemented in the CHIPS code are covered. This includes a quick review of the existing models followed by the specifics of the updated code structure, capabilities, and the addition of new physics. The CHIPS code is then used to simulate an 11-species ionizing, hypersonic shock scenario with and without electronic excitation in Chapter 4. These two nominal cases are studied in preliminary sensitivity analyses in Chapter 5 and input parameters are ranked based on the sensitivity

of several quantities of interest. In Chapter 6, the focus is on obtaining radiance measurements from the CHIPS code by post-processing with the NEQAIR radiative code. This method is studied with Saturn entry simulations that are directly compared with EAST experimental results. Further study of the sensitivity analysis and radiation results identifies several model improvements, the first of which is developed in Chapter 7. This chapter identifies deficiencies in the chemistry model currently used in the CHIPS code and presents a new model for handling backward reactions. Additional issues are addressed in Chapter 8, and final improvements are completed in the CHIPS code. A nominal simulation is chosen and CHIPS/NEQAIR results are compared with EAST experiments for a lunar return scenario. In Chapter 9, a final sensitivity study is performed on the lunar return scenario where radiative quantities of interest are investigated. Chapter 10 wraps up the thesis with conclusions and future work.

CHAPTER 2

CHIPS Baseline Methodology

2.1 OVERVIEW

The DSMC simulations performed in this research utilize the Computation of Hypersonic Ionizing Particles in Shocks (CHIPS) codebase developed at The University of Texas at Austin. The framework for the CHIPS code was created by Strand [6] as a baseline proof-of-concept for the sensitivity analysis and calibration of a 1-dimensional moving shockwave. Since the sensitivity analysis and calibration studies require multiple simulations with varying parameters, CHIPS is written as a subroutine that can be called by the appropriate program. In addition, CHIPS supports a range of individual DSMC simulation options including 1-dimensional unsteady shock simulations and 0-dimensional relaxations. As CHIPS is a particle simulation, movement and interactions between particles occur within each cell of the computational grid. These interactions include elastic, rotational, vibrational, electronic, and chemical exchanges between particles. CHIPS is able to simulate monatomic and diatomic molecules including neutral particles, ions, and electrons. Since many CHIPS simulations require more particles than a single processor can handle in a reasonable time, the code is MPI parallelized with separate methods utilized for 0-dimensional relaxations and 1-dimensional shocks to optimize the computational efficiency.

Higdon, K. J., Goldstein, D. B., and Varghese, P. L., "Sensitivity Analysis of Direct Simulation Monte Carlo Parameters for Ionizing Hypersonic Flows," *Journal of Thermophysics and Heat Transfer*, Vol. 32, No. 1, 2018, pp. 90-102.

Higdon, K. J., Goldstein, D. B., and Varghese, P. L., "Sensitivity Analysis of DSMC Parameters for an 11-Species Air Hypersonic Flow," *30th International Symposium on Rarefied Gas Dynamics*, AIP Conf. Proc. 1786, Victoria, B. C., July 2016.

D. B. Goldstein and P. L. Varghese supervised these projects and provided technical insight.

It should be noted that the models used in CHIPS are not intended to be state of the art. As the focus of the current research is on the computationally expensive sensitivity analysis of DSMC input parameters, state of the art models are only included or developed when necessary and the standard DSMC models are used otherwise. Many of the models used in CHIPS were chosen for their relative simplicity and computational efficiency. In fact, there are sophisticated models available in the literature for several physical processes simulated by the CHIPS code that may produce more accurate results. The current chapter focuses on restating the baseline models implemented in the first iteration of the CHIPS code, completed by Strand. The goal of Strand's efforts was to perform preliminary sensitivity analyses and calibration studies of hypersonic DSMC simulations. To reduce the complexity of the DSMC simulations, lower speed hypersonic shocks of ~8 km/s were studied using a 5-species air (N_2, N, O_2, O, NO) mixture which eliminated the need for high temperature air models. The following discussion will not be an in-depth review of the original computational models and structures included by Strand, but rather a brief summary of the methods selected for the CHIPS code. Improvements and additions to the baseline CHIPS code are discussed in the following chapter.

2.2 CHIPS SIMULATIONS

2.2.1 0-Dimensional Relaxation

The CHIPS codebase supports two main types of simulations, the first of which is a 0-dimensional (0D) relaxation. A 0D relaxation is useful to test basic physical processes and compare to analytical results. In a 0D relaxation, a single collision cell is assigned a set of particles representing an initial condition that determines a specified number density, species fractions, temperatures, etc. Typically, this initial condition is some non-

equilibrium state where one or more of the temperatures is assigned a different value from the others. The simulation is 0-dimensional in the sense that particles are not allowed to move in space. Although, the particles are allowed their own kinetic and internal energies. Particles can be selected for collisions where energy and momentum are exchanged between the colliding particles, and chemistry can occur. Over time, these collisions move the initial condition towards some equilibrium state. Samples of the particle, species, and bulk fluid properties are recorded at time intervals to describe the evolution of the gas towards equilibrium. To reduce the statistical scatter of the results, CHIPS has the capability to run multiple 0D simulations in parallel and ensemble average the results.

2.2.2 1-Dimensional Shock

While a 0D relaxation is useful for testing physics models, the premier capability of the CHIPS code is the simulation of a 1-dimensional (1D) shock. The CHIPS code performs a 1D simulation of an unsteady hypersonic shock in a form similar to a shock tube, following the method developed for DSMC by Strand and Goldstein [6][30][31]. Although an unsteady simulation presents its own set of challenges, modeling an unsteady shock has advantages over the simulation of steady shocks. In order to model a steady shock, the freestream and post shock conditions must be known *a priori*. Requiring that the post shock conditions be known severely limits the capability of the simulation to model real world hypervelocity scenarios. Knowledge of the post shock conditions is not possible in many real gas applications, especially in non-adiabatic conditions involving post shock radiation. In addition, the shock tends to wander a bit in a nominally steady shock simulation due to random walks in space. To mitigate this effect, artificial stabilization is applied to hold the shock steady. Other shock simulations

model a 2-dimensional (2D) blunt body to create a steady shock [35]. In this case, post shock conditions are not required, and the output parameters sampled from the stagnation line of the resulting bow shock mimic the simulation of a shock tube result. A significant amount of computational time is wasted modeling a 2D body when the only desired result is a stagnation line measurement. Another feature of a blunt body simulation is the shock standoff distance. When compared to shock tube measurements, the proximity of the wall to the shock may influence results of the post shock parameters. This restricts the amount of data that can be compared with experimental shock tube results.

In contrast, an unsteady shock can move freely through the domain and the freestream parameters are the only inputs required to develop the shock wave. Figure 2.1 presents a 5-step (a-e) description of this method. (a) Initially, a finite 1D domain is specified that is separated into a uniform grid of cells that must be larger than the distance the wave will travel during the simulation. At the left end of the domain, an inflow is initialized with some temperature and velocity. At every timestep, freestream particles are created by sampling from the Maxwellian velocity distribution. These particles propagate through the domain and at the right end of the domain they specularly reflect back into the freestream. (b) As in a shock tube, a shock develops from this wall and propagates upstream with some shock velocity. The shock is allowed to stabilize and move away from the wall. Once the shock has moved away from the wall, pressure sampling begins in two sampling regions that are a fraction of the domain size. The first region is located at the left end of the domain, near the freestream. The second sampling region is located near the wall but is offset from the right boundary so that localized wall effects do not pollute the pressure samples. After the pressure sampling has taken place over a fraction of the total timesteps, the pre- and post-shock pressures are known with a high degree of confidence. (c) Next, the shock speed is measured over a fraction of the

total time interval. Using Eqn. 2.1, the normalized pressure is calculated at every point in the domain where P is the current cell's pressure, P_1 is the pre-shock pressure, and P_2 is the post shock pressure.

$$P_{norm} = \frac{P - P_1}{P_2 - P_1} \qquad [2.1]$$

Since the normalized pressure has a certain amount of statistical noise, it is boxcar averaged to create a smooth profile. The shock position is then defined as the point where the normalized pressure is equal to 0.5. The pressure jump was chosen as the shock location's defining quantity because the pressure equilibrates faster than other post-shock quantities. (d) Once the shock is consistently defined by the pressure jump over a set number of timesteps, the shock speed is sampled at every timestep by comparing its current location to the shock location at the previous timestep. (e) Finally, sampling of the shock region is performed for the remainder of the simulation. The shock sample region is defined as a fraction of the simulation domain and moves with the shock wave. Macroscopic quantities such as number densities and temperatures (T_{tr}, T_{rot}, T_{vib}, T_e, T_{elec}) are periodically recorded and ensemble averaged over the remainder of the simulation. In this way, a quasi-steady representation of the moving shock wave is obtained. Care must be taken to ensure that the shock has fully developed. It is not uncommon to observe large fluctuations in the shock speed if it has not moved far enough away from the wall and fully developed.

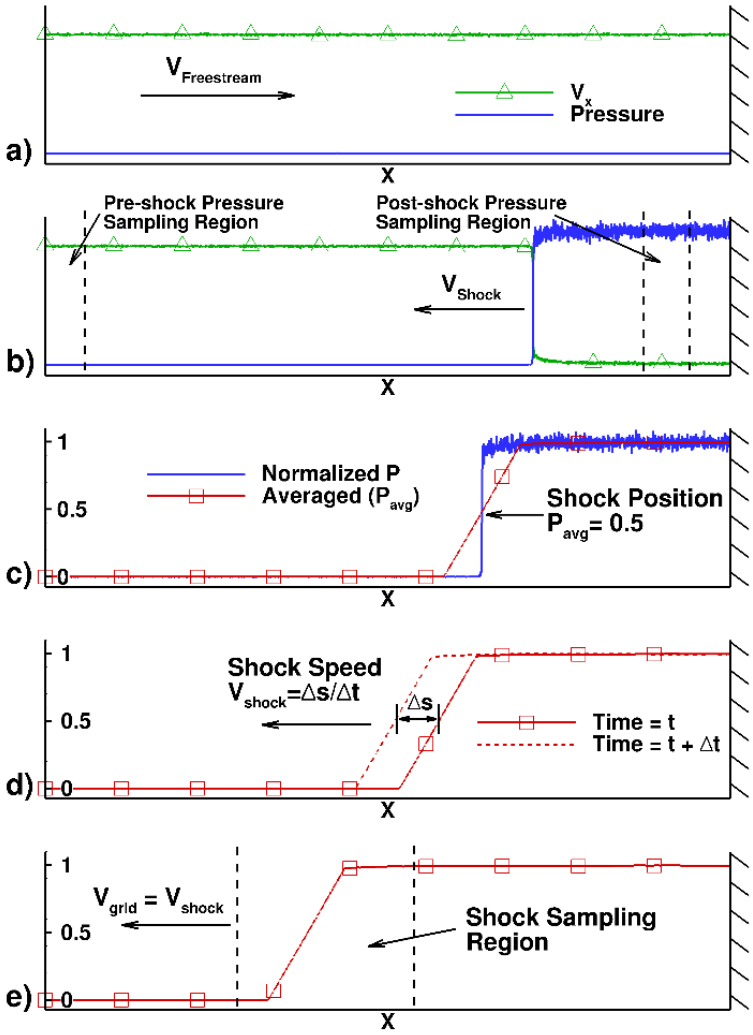

Figure 2.1 Schematic of the 1D unsteady shock wave development and various phases of the domain sampling.

The 1D shock simulation is MPI parallelized due to the domain size and the number of particles required to simulate an unsteady shock accurately. The number of simulated particles continues to grow as the shock moves further upstream and the particles entering from the freestream accumulate. For each shock simulation, the domain

is separated into regions normal to the flow and assigned to a processor. During every timestep, particles that cross processor boundaries must be reassigned. Also, occasional dynamic load balancing is applied across processors to share the workload efficiently. This is necessary since post-shock cells will have many more particles than the pre-shock cells.

2.3 CHIPS MODELS

2.3.1 Collision Model

Elastic collisions between particles are simulated using the variable hard-sphere (VHS) model which specifies the elastic collision cross-section based on the relative velocity of the colliding particles [15]. In this model, a reference cross-section is determined from a reference diameter, d_{ref}, and power-law temperature exponent, ω, that have been tabulated from experimental curve fits at some reference temperature, T_{ref}. The VHS model is only able to reproduce either the coefficient of viscosity or diffusion due to the assumption of isotropic scattering. To minimize this error, Boyd and Schwartzentruber suggest that VHS parameters for like-species collisions should be fit to experimental viscosity data while VHS parameters for unlike-species collisions should be calibrated with available diffusion data [36]. An alternative approach is to model neither viscosity or diffusion exactly and instead, choose VHS parameters that minimize the error in both coefficients as suggested by Swaminathan-Gopalan and Stephani [18]. Because Ref. [18] was published within the timeframe of this dissertation, it is not included in this research until Chapter 8. Instead, the VHS parameters adopted initially in this dissertation are taken from publications that follow the method described in Ref. [36].

When molecules collide inelastically, energy is transferred between the translational, rotational, and vibrational modes by employing the Borgnakke-Larsen model [25]. In this model, a fraction of the colliding particles are chosen to undergo an inelastic collision. The post-collision states are then selected from the appropriate equilibrium distribution based on the current collision energy. This process relaxes the gas mixture towards equilibrium, but still allows for significant non-equilibrium to be modeled.

The rotational energy is distributed to diatomic molecules assuming that the rotational modes are fully excited and can be modeled as a continuous distribution. Parker's model, Eqn. 2.2, is utilized in this dissertation to determine the rotational collision number, Z_{rot}^{Parker} [37]. In Eqn. 2.2, T_c is the cell temperature, Z_{rot}^{∞} is the collision number limit at high temperature, and T_{rot}^{*} is the characteristic temperature of the intermolecular potential.

$$Z_{rot}^{Parker} = \frac{Z_{rot}^{\infty}}{1 + \pi(1 + \pi/4)\left(\frac{T_{rot}^{*}}{T_c}\right) + \left(\frac{\pi^{\frac{3}{2}}}{2}\right)\left(\frac{T_{rot}^{*}}{T_c}\right)^{\frac{1}{2}}} \qquad [2.2]$$

The vibrational energy distribution is treated in a similar manner except that the vibrational modes are not fully excited. Instead, the simple harmonic oscillator model is used, and the vibrational energy is split into discrete vibrational levels. To determine the rate at which the vibrational energy is redistributed in a cell, the vibrational collision number, Z_{vib}^{MW}, of Millikan and White is calculated from Eqn. 2.3 using the cell temperature [38]. In this equation, ν is the collision frequency, τ_{MW} is the relaxation time, $\bar{c}$ is the average molecular speed, m_r is the reduced mass, and θ_{vib} is the characteristic

vibrational temperature. While Eqn. 2.3 is used here to calculate species-specific collision numbers, it must be noted that this equation was fit to experimental results for like-species collisions.

$$Z_{vib}^{MW} = \nu\tau_{MW} = \nu\left[\frac{exp\left(AT^{-\frac{1}{3}} + B\right)(101325)}{nk_BT_c}\right] \qquad [2.3]$$

$$A = 1.16 \times 10^{-3} m_r^{\frac{1}{2}} \theta_{vib}^{\frac{4}{3}} \qquad B = -1.74 \times 10^{-5} m_r^{\frac{3}{4}} \theta_{vib}^{\frac{4}{3}} - 18.42$$

2.3.2 Chemistry Model

Forward chemical reactions are assumed to follow the Arrhenius-type rate equation

$$k(T) = \Lambda T^{\eta} e^{-E_a/k_BT} \qquad [2.4]$$

where Λ and η are reaction-specific constants, E_a is the activation energy for the reaction, k_B is the Boltzmann constant, and T is the temperature of the gas. The Total Collisional Energy (TCE) model is used to convert Arrhenius-form reaction rates into reaction cross-sections, allowing molecules to undergo specific reaction types when the appropriate activation energy is obtained [3][15]. For each collision, the relative velocity and contributions from internal modes contribute to the total energy used in the TCE model. If the collision energy is less than the activation energy, the probability of a reaction occurring is identically zero. For a bimolecular reaction between species *i* and *j* that has a collision energy greater than the activation energy, the reaction probability for each collision, $k(T)$, is calculated as

$$\left(\frac{\sigma_R}{\sigma_T}\right)_k = \frac{\sqrt{\pi}\varepsilon\Lambda T_{ref}^{\eta}}{2\sigma_{ref}(k_B T_{ref})^{\eta-1+\omega}} \frac{\Gamma(\bar{\zeta}+\frac{5}{2}-\omega)}{\Gamma(\bar{\zeta}+\eta+\frac{3}{2})} \sqrt{\frac{m_r}{2k_B T_{ref}}} \frac{(E_c-E_a)^{\eta+\bar{\zeta}+\frac{1}{2}}}{E_c{}^{\bar{\zeta}+\frac{3}{2}-\omega}} \quad [2.5]$$

and for a termolecular reaction, the reaction probability is

$$\left(\frac{\sigma_R}{\sigma_T}\right)_k = \frac{\sqrt{\pi} n_T \varepsilon\Lambda T_{ref}^{\eta}}{2\sigma_{ref}} \frac{\Gamma(\frac{5}{2}-\omega)}{\Gamma(\eta+\frac{3}{2})} \sqrt{\frac{m_r}{2k_B T_{ref}}} \left(\frac{E_c}{k_B T_{ref}}\right)^{\eta-1+\omega} \quad [2.6]$$

where $\varepsilon = 1$ if $i \neq j$ or $\varepsilon = 2$ if $i = j$, $\bar{\zeta}$ is the average internal degrees of freedom between species *i* and *j*, m_r is the reduced mass of i and j, E_c is the total collision energy, n_T is the number density of the third body. Also, in Eqns. 2.5 and 2.6 σ_{ref}, T_{ref}, and ω are the VHS parameters for species i and j, and the Arrhenius reaction rate equation constants are Λ, η, and E_a. For each collision, the total cross-section is calculated. The total cross-section is found by

$$\sigma_T = \sigma_{VHS} + \sum_k \left(\frac{\sigma_R}{\sigma_T}\right)_k \sigma_{VHS} \quad [2.7]$$

where the first term is the VHS cross-section and the second term is the sum of the reaction cross-sections for all possible reactions between species *i* and *j*. In calculating the reaction probability, which appears in the second term of Eqn. 2.7, σ_T is usually assumed to be roughly equivalent to the VHS cross-section meaning that the reaction cross-section is small [3]. For high temperature simulations the reaction cross-section may become large enough that it is no longer small relative to the VHS cross-section.

Equation 2.7 allows for the correct reaction rate to be reproduced in DSMC for cases where the reaction cross-section is on the order of the VHS cross-section and is explained in detail by Strand and Goldstein [30].

CHAPTER 3

CHIPS Improvements

3.1 OVERVIEW

Although the baseline CHIPS codebase has the ability to model the appropriate physics for many hypersonic flows, there are still improvements that must be made to simulate the high temperature hypersonic shocks of interest and compare with experimental results. Previously, CHIPS only considered 5-species air (N_2, N, O_2, O, NO) for lower speed cases where charged particles are negligible [6]. In many hypersonic flow conditions, like lunar or Mars return, charged particles cannot be ignored since ionization and electronic excitation are important means of energy transport. Charged particle physics are also fundamental in experimental measurements of hypersonic flows since they are typically restricted to measurements of radiation transport due to the high temperature and velocity. For the hypersonic speeds experienced during Earth re-entry, a weakly ionized plasma is generated behind the shock wave that must be modeled. Unfortunately, including ionization is not easy and few DSMC codes consider this process. A major effort in this research is the enhancement of CHIPS capabilities and the addition of high temperature physics such as improved collision models and charged species interactions [4].

Higdon, K. J., Goldstein, D. B., and Varghese, P. L., "Sensitivity Analysis of Direct Simulation Monte Carlo Parameters for Ionizing Hypersonic Flows," *Journal of Thermophysics and Heat Transfer*, Vol. 32, No. 1, 2018, pp. 90-102.

Higdon, K. J., Goldstein, D. B., and Varghese, P. L., "Sensitivity Analysis of DSMC Parameters for an 11-Species Air Hypersonic Flow," *30th International Symposium on Rarefied Gas Dynamics*, AIP Conf. Proc. 1786, Victoria, B. C., July 2016.

D. B. Goldstein and P. L. Varghese supervised these projects and provided technical insight.

3.2 Codebase Enhancement

3.2.1 Code Restructure

Before improved physics can be added to CHIPS, an overhaul of the code structure is required. These changes are necessary to bringing the code closer to production quality designs such as DAC [39] or SPARTA [40] in the interest of future users. The original structure of the CHIPS code followed a rudimentary design where the entire program was housed in a single directory as shown in Fig. 3.1. The entire source code was contained in four files with multiple unrelated functions and subroutines contained in each file. In addition, the code was sparsely commented which, along with the subroutine grouping, made the code difficult to understand for a new user. While the original CHIPS code was intended to follow the Fortran 90-2003 style, much of the codebase retained the Fortran 77 approach through its adaptation of Bird's code [3].

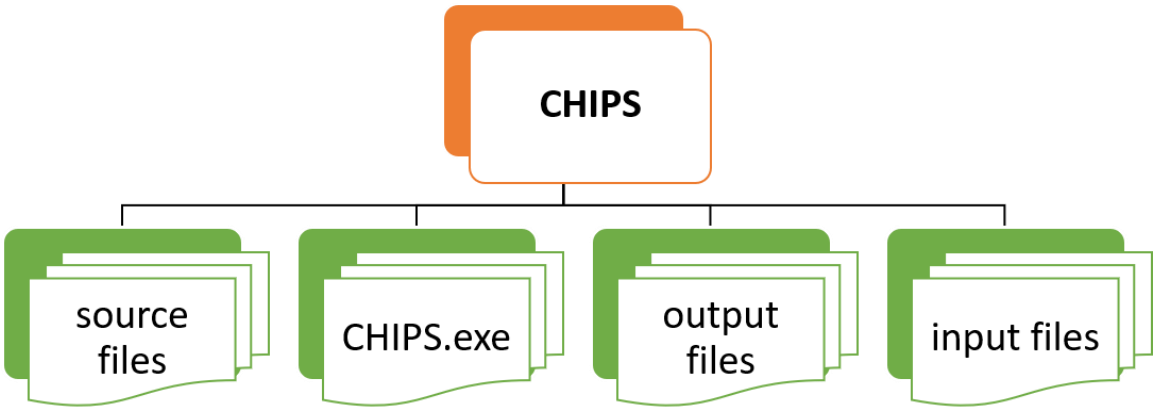

Figure 3.1 Schematic of the original CHIPS codebase layout.

To address these issues, a complete overhaul of the code structure is performed. Instead of a single directory that contains the entire codebase, the main directory is split up into four subdirectories mapped out in Fig. 3.2. The executable directory, *exec*,

contains the CHIPS executable, files that build the CHIPS program, and scripts to run the program on various systems. The *input* folder holds the CHIPS.inp file responsible for setting up the simulation environment along with the *species_data* and *chemistry_data* directories which store the species and chemistry input files required by the current simulation. Output files resulting from completed simulations are stored in the *output* directory. When required, the CHIPS code builds a *NEQAIR_input* directory within the *output* folder to house simulation results intended to be processed by the NEQAIR radiation code. Finally, the source file directory, *src*, contains the CHIPS source code and object files built from this source code.

To address the readability of the CHIPS code, descriptive comments were added when a subroutine was modified, and each subroutine was broken off into its own separate file to be rewritten as a module. By writing the subroutines as modules, information can be packaged and controlled in a uniform, centralized manner, minimizing the potential for error. Modules also allow for implicit interfaces and function overloading which reduces the confusion of redundant code. The modification of the subroutines into modules made it possible to eliminate most of the legacy Fortran 77 style approaches.

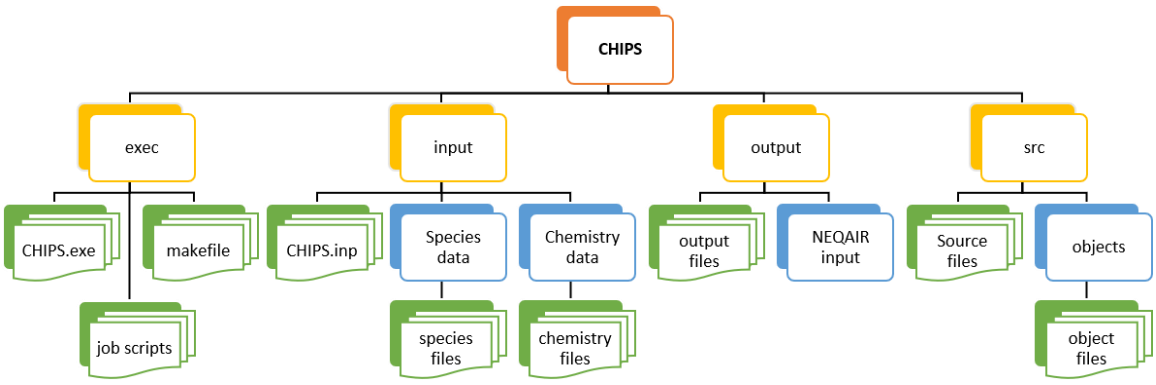

Figure 3.2 Schematic of the updated CHIPS layout.

3.2.2 Workflow Efficiency

As the complexity of the CHIPS codebase grows, the amount of effort required to document changes or effectively use the code increases. To prevent old versions from being lost and to record changes made to the code over time, a version control system was implemented using Git. Version control allows for changes to be committed to a repository along with a short text description of these changes and permits the possibility of rolling back the code if a bug has been introduced. Another advantage of version control is easy distribution of the codebase to new users and the ability to branch the code so that users can develop features to suit their needs. Edits made by multiple users are then streamlined so that they are effectively combined and implemented in the code while an administrator can ensure that the edits do not introduce bugs to the existing codebase. To improve the workflow even further, a new input parser was written for the CHIPS code in a way that is more malleable to in-file commenting or new input sections. The input parser enables a new user to quickly understand the meaning of each input variable and descriptive error checks guide the user towards acceptable values. This avoids unnecessary errors and wasted time performing simulations that would produce meaningless or unexpected results. In addition, the error checks avoid undescriptive program crashes that could require substantial time spent on debugging.

With the new code structure shown in Fig. 3.2, compilation of the CHIPS code becomes much more cumbersome. The original version of the CHIPS code contained only a few source files which allowed for easy command line compiling, but this is no longer reasonable since the CHIPS code has been split into over fifty different source files. To handle the compilation of CHIPS, a makefile was introduced in the *exec* folder that automates the compilation process. The makefile was also written to detect and handle multiple computing environments and provides various builds such as debugging

or production builds. In addition to the creation of a makefile, the CHIPS code was edited to allow simulations to be completed in serial. While a production level 1D shock must be run in parallel due to its computational cost, other simulation types can be run in serial, aiding in debugging and allowing for more intrusive code analysis tools to be used.

3.2.3 Computational Efficiency

While DSMC simulations of hypersonic shock waves are computationally expensive, the computational cost is orders of magnitude higher for the sensitivity analyses completed in this dissertation. Since the CHIPS code is run thousands of times for a sensitivity analysis, each minor improvement in its efficiency pays dividends in the overall cost. Major reductions in the CHIPS computational time were obtained through the application of various profiling tools. These tools were used to identify bottlenecks and inefficiencies in the CHIPS code that were remedied when possible. For example, a significant portion of each timestep was spent calculating the reaction probability for each chemical reaction. This computational cost was dramatically reduced by moving as many of the parameter calculations as possible to higher level loops or pre-calculating parameters at the beginning of the simulation.

The unsteady nature of the 1D moving shock wave simulated by CHIPS carries its own set of efficiency challenges. As time passes, particles are continuously added from the freestream. Nearly all of these particles will be present for the remainder of the simulation because particles accumulate behind the shock as it moves in the upstream direction. Since the shock is always moving upstream and into new collision cells, a cell that once contained a small number of fast freestream particles, generally traveling in the same direction becomes filled with highly collisional, slow moving particles as it is processed by the shock wave. While little can be done to reduce the computational cost of

the increased number of particles in the cell, besides load balancing the parallel processes, the computational efficiency of the unsteady shock simulation can be improved by addressing the number of collisions considered in a cell at each timestep. The number of collisions is determined from the no time counter (NTC) method developed by Bird [3] and updated by Nanbu [41]. The NTC method relies on a maximum collision cross-section, $(\sigma_T c_r)_{max,AB}$, determined for each species pair, A and B. This maximum collision cross-section is estimated at the beginning of the simulation and increased when a larger collision cross-section is observed in the cell. For an unsteady shock simulation, cells initially start out with a relatively low $(\sigma_T c_r)_{max,AB}$ which increases dramatically within the shock or, more generally, in nonequilibrium regions. As the shock moves further upstream after passing through a cell, the particles approach equilibrium, but $(\sigma_T c_r)_{max,AB}$ retains its large value. This leads to an unnecessarily large number of possible collisions considered in the post-shock region and results in a waste of computational time. Another difficulty arises in the initialization of $(\sigma_T c_r)_{max,AB}$ for each cell. If cells are initialized with too low of a $(\sigma_T c_r)_{max,AB}$ value, the correct shock structure is not modeled because multiple timesteps may be required to raise $(\sigma_T c_r)_{max,AB}$ to its appropriate value within the shock. This artificially increases the shock width by underestimating the number of collisions in the cells right before the shock, allowing for particles to more easily diffuse through this region.

As a solution, a specialized initialization and reduction method is applied to $(\sigma_T c_r)_{max,AB}$ within CHIPS. At the beginning of an unsteady shock simulation, the value of $(\sigma_T c_r)_{max,AB}$ is initialized in the typical DSMC manner. Once 5% of the total simulation time has passed and the value of $(\sigma_T c_r)_{max,AB}$ has grown organically within each cell, an inventory of the $(\sigma_T c_r)_{max,AB}$ values in every cell is taken for each species pair and the maximum value of $(\sigma_T c_r)_{max,AB}$ is determined. This maximum value is then

distributed to every cell in the simulation across all processors. Effectively, this reinitializes the value of $(\sigma_T c_r)_{max,AB}$ in every cell to be the maximum cross-section observed within the shock. The fraction, 5% of the total time, was chosen because it allows enough time for the beginning of a shock to be observed while avoiding interfering with the resultant fully developed shock and ensuring that shock sampling of output quantities occurs much later.

Once the reinitialization is complete, the following timesteps are subject to a reduction of $(\sigma_T c_r)_{max,AB}$ at each timestep. For each species pair in a timestep, the maximum collision cross-section observed during the current timestep, $(\sigma_T c_r)_{cell,AB}$, is determined. The value of $(\sigma_T c_r)_{max,AB}$ for the next time step is then adjusted by subtracting a percentage of the difference between the cell's maximum cross-section and the maximum cross-section observed during the current timestep, according to Eqn. 3.1.

$$\left\{(\sigma_T c_r)_{max,AB}\right\}_{t+1} = \left\{(\sigma_T c_r)_{max,AB}\right\}_t - R\left(\left\{(\sigma_T c_r)_{max,AB}\right\}_t - \left\{(\sigma_T c_r)_{cell,AB}\right\}_t\right) \quad [3.1]$$

The percentage value, R, used in CHIPS is set at 10%. This value has no physical significance but was selected to balance the rate of reduction while maintaining the integrity of the results. This approach solves the problem with exceedingly large maximum cross-sections in the post-shock region and results in significant speed-up of an unsteady shock simulation. A potential issue could arise if the values of $(\sigma_T c_r)_{max,AB}$ in the pre-shock region are reduced so much that this reintroduces the complication where the shock moves into new cells with too low of $(\sigma_T c_r)_{max,AB}$ values. Currently, this is avoided through both the MPI load balancing of cells and by restricting the reduction method to the post-shock region. As the shock moves upstream, processors grab new

cells and populate those cells with the particles passed from the previous owner of that cell. Since each processor holds its own copy of the cell data, the $(\sigma_T c_r)_{max,AB}$ values from the previous owner are not shared with the new processor. This essentially resets the values of $(\sigma_T c_r)_{max,AB}$ whenever a processor is delivered particles into a cell that has never been operated on in its memory and ensures that the maximum collision cross-section is large enough when the shock reaches that cell. While this may not be the most consistent method, it avoids the computational cost of sharing large arrays of $(\sigma_T c_r)_{max,AB}$ values between processors. Although resetting the $(\sigma_T c_r)_{max,AB}$ values can be a solution on its own, this is dependent on the number of available processors and can change from simulation to simulation.

A more reliable solution is to restrict the reduction method so that $(\sigma_T c_r)_{max,AB}$ is only allowed to reduce after the shock has passed the cell. The shock is tracked in this method by calculating the maximum translational temperature over all the cells and marking the cell that contains the maximum. If a cell is located further downstream than this marker, the $(\sigma_T c_r)_{max,AB}$ values are allowed to be reduced. Because the translational temperature tends to fluctuate between cells during a simulation, a problem can occur where the $(\sigma_T c_r)_{max,AB}$ values in the cells before the shock may still be reduced. This is especially true for low resolution simulations with few particles. To avoid this, the maximum translational temperature cell marker is shifted downstream by 1% of the domain. This ensures that the reduction scheme is applied only for cells in the post shock region. Since the translational temperature is already calculated in every cell for use in the various models and not many collisions occur in the pre-shock region, this approach is not detrimental to the code's efficiency. To further improve efficiency, this maximum translational temperature calculation is performed with the same frequency as load balancing. This avoids the computational cost of excessive communications between

processors. Alternative methods for handling the maximum collision cross-section can be investigated in the future.

3.3 MODEL IMPROVEMENTS

Although the baseline models for the CHIPS code were covered in the previous chapter, improvements have been made to these models when necessary throughout this research. These improvements should have significant application beyond the CHIPS code itself and should be considered for addition to similar hypersonic scenarios. The advancements completed take various forms, including the application of species-specific cases, higher accuracy parameters, model modifications, and the introduction of new methods. The improvements made to each separate section are detailed in the following discussion.

3.3.1 Collision Model Improvements

3.3.1a Elastic Collision Model

An update of the neutral particle (N_2, N, O_2, O, and NO) input parameters for the VHS model was compiled from a number of publications by Ozawa and summarized in Ref. [16]. These VHS values were selected to take advantage of their fit to high temperature data. Table 3.1 lists the VHS parameters used in the CHIPS code for 11-species air at a reference temperature, T_{ref}, of 1000 K. Since only like-species collision parameters were published, an arithmetic average is calculated to obtain collision specific values between particles listed in Table 3.1. As discussed in the previous chapter, the VHS model is only able to accurately reproduce either the coefficient of viscosity or diffusion. These VHS input parameters for like-species collisions are able to simulate the expected viscosity coefficient, but not the correct diffusion coefficient. In addition, it is

likely that employing an average for unlike-species collisions may not reproduce either of the coefficients correctly.

Table 3.1 11-species air heavy particle collision parameters.

Species	ω	d_{ref} [10^{-10} m]	Z_{rot}^{∞}	T_{rot}^{*} [K]	θ_{vib}
N_2	0.68	3.580	15.7	80.0	3371.0
N	0.65	3.107	–	–	–
O_2	0.68	3.370	14.4	90.0	2256.0
O	0.65	2.958	–	–	–
NO	0.65	3.410	5.0	117.0	2719.0
N_2^+	0.68	3.580	15.7	80.0	3371.0
N^+	0.65	3.107	–	–	–
O_2^+	0.68	3.370	14.4	90.0	2256.0
O^+	0.65	2.958	–	–	–
NO^+	0.65	3.410	5.0	117.0	2719.0

3.3.1b Inelastic Collision Models

In this iteration of the CHIPS code, the inelastic collision models covered in the previous chapter required updating to be in line with recent advancements. For a particular inelastic collision, the particle selection routine prohibiting double relaxation is followed [42]. In this method, chemical reactions are considered before testing for vibrational relaxation and, finally, rotational relaxation. If a particle undergoing an inelastic collision is accepted for any one of these procedures, the relaxation process ends, and the remaining energy is allocated to the translational energy. As discussed by Haas et al. [43], the collision number is related to the relaxation probability, P, obtained from continuum correlations through the involved degrees of freedom. A correction factor is also required for the rotational mode to map the DSMC relaxation time to the

experimental relaxation time utilized by Parker [36]. Using this correction, the rotational collision number is calculated for every collision pair as

$$Z_{rot} = \frac{15\pi Z_{rot}^{Parker}}{\xi_{tr}(\xi_{tr} + 2)} \quad [3.2]$$

where ξ_{tr} is the translational degrees of freedom of the colliding particles corresponding to the VHS model. The value of Z_{rot}^{Parker} is determined using the translational temperature as the cell temperature and from the parameters provided in Ref. [36], listed in Table 3.1 for each species. The probability of energy transfer to the rotational mode of a species for the selection routine prohibiting double relaxation is then calculated as

$$P_{rot} = \frac{\xi_{tr} + \xi_{rot}}{\xi_{tr} Z_{rot}} \quad [3.3]$$

The vibrational relaxation rate is calculated in a similar manner to rotational relaxation. The Millikan and White vibrational collision number from Eqn. 2.3 is employed, along with a high temperature correction developed by Park [44]. For elastic collisions modeled with VHS, the Park correction becomes

$$Z_{vib}^{Park} = \frac{\pi d_{ref}^2}{\sigma_{vib}^{Park}} \left(\frac{T_c}{T_{ref}}\right)^{\frac{1}{2}-\omega} \left(\frac{T_c}{50{,}000}\right)^2 \quad [3.4]$$

where the values of σ_{vib}^{Park} are listed in Table 3.1 for each species. This correction is then added to the Millikan and White collision number to obtain the vibrational collision number, Z_{vib}, and the corresponding vibrational relaxation probability, P_{vib}, shown in

Eqn. 3.5. The probability is again adjusted according to the selection procedure prohibiting double relaxation with consideration that a simple harmonic oscillator is used to represent the vibrational energy distribution in CHIPS [36]. In both Eqn. 3.4 and 3.5, the collision temperature is assumed to be equivalent to the cell translational temperature.

$$P_{vib} = \frac{\xi_{tr} + \dfrac{2\theta_{vib}/T_c}{\exp\left(\dfrac{\theta_{vib}}{T}\right) - 1}}{\xi_{tr} Z_{vib}} = \frac{\xi_{tr} + \dfrac{2\theta_{vib}/T_c}{\exp\left(\dfrac{\theta_{vib}}{T}\right) - 1}}{\xi_{tr}\left(Z_{vib}^{MW} + Z_{vib}^{Park}\right)} \qquad [3.5]$$

3.3.1c Chemistry Model

The current version of the CHIPS code relies on the TCE model to simulate both forward and backward reactions. After the completion of a preliminary sensitivity analysis, improvements were developed for the chemistry model and these advancements are detailed in Chapter 7. Until then, the Arrhenius rates listed in Table 3.2 are used in Eqn. 2.5 or 2.6 to calculate the probability of a neutral particle reaction. These rates are identical to the reaction rates used in the preceding 5-species air simulations performed by Strand [6]. Once a chemical reaction is selected to occur, the total energy of the reactants must be redistributed to the products. This process has been updated to correctly allocate energy to the appropriate internal and translational modes, following the recommendations in Appendix C of Boyd and Schwartzentruber [36]. The portion of the total collision energy available to each mode is now dependent on the current mode's degrees of freedom and the sum of the degrees of freedom from modes that have not yet been allocated.

3.3.2d Macroscopic Definitions

Particles in the CHIPS code retain their individual kinetic and internal energies, but in order to understand the gas properties, macroscopic quantities must be defined. For a single species, the separate temperatures and pressure are easily defined from the ensembled energy in each mode, considering the chosen model for each mode. The overall temperature of the species in CHIPS is defined by a weighted average of each mode's temperature where the weight factor is the degrees of freedom of that mode. These definitions are conveniently provided in Appendix D of Boyd and Schwartzentruber [36]. The calculation of the bulk gas mixture's macroscopic quantities is not as straight-forward. There are two main approaches to determining a gas mixture's macroscopic quantities: from the ensembled energy in a mode over all species or from the ensembled, individually calculated macroscopic quantities for each species. The first approach requires that each particle's energy is weighted by the species' degrees of freedom for that mode. The degrees of freedom are well defined for the translational and rotational modes. For the cell translational temperature, the calculation becomes

$$T_{tr} = \frac{1}{3k_B \sum_s N_s}\left\{\sum_s \left[m_s\left(\sum u_p^2 + \sum v_p^2 + \sum w_p^2\right)\right] - \frac{\left[\sum_s\left(m_s \sum u_p\right)\right]^2 + \left[\sum_s\left(m_s \sum v_p\right)\right]^2 + \left[\sum_s\left(m_s \sum w_p\right)\right]^2}{\sum_s m_s N_s}\right\} \quad [3.6]$$

where N_s is the number of particles in the cell of that species and u, v, and w are the velocity components of each particle of that species [35]. Summations of s are over each species in the mixture and summations of p are over the particles of that species. This method becomes difficult, for example, when the vibrational mode is modeled by a simple harmonic oscillator because the degrees of freedom are dependent on temperature.

In this case, the second approach is more appropriate since a degrees of freedom weighting is not needed to calculate a species vibrational temperature. The mixture's macroscopic vibrational temperature is instead calculated by some weighted average of each species' vibrational temperature. In the CHIPS code, the mixture vibrational temperature is calculated from a mass fraction weighting, following the work of Boyd and Schwartzentruber. For the translational temperature, this method results in the calculation

$$T_{tr_s} = \frac{m_s}{3k_B}\left\{\frac{\left[\sum\left(u_p^2 + v_p^2 + w_p^2\right)\right]_s}{N_s} - \left[\left(\frac{\left(\sum u_p\right)_s}{N_s}\right)^2 + \left(\frac{\left(\sum v_p\right)_s}{N_s}\right)^2 + \left(\frac{\left(\sum w_p\right)_s}{N_s}\right)^2\right]\right\} \quad [3.7]$$

$$T_{tr} = \frac{\sum_s \rho_s T_{tr_s}}{\rho} \quad [3.8]$$

where ρ_s is the species density and ρ is the mixture density. While in equilibrium, each method for calculating the translational temperature gives the same result, but in nonequilibrium this is not the case. For example, the first method typically results in a higher peak translational temperature within the highly nonequilibrium shock layer simulated by CHIPS. Although no conclusion about which method is more correct has been made, the CHIPS code represents mixture macroscopic quantities with the second method, following the equations listed in Boyd and Schwartzentruber [36]. This selection preserves the consistency between each macroscopic calculation by calculating them all in the same manner.

Table 3.2 Neutral particle dissociation, recombination, and exchange reaction rates.

#	Reaction	Forward Rate Coefficients			Backward Rate Coefficients		
		Λ [m^3/s]	η	E_a [10^{-19} J]	Λ [m^3/s]	η	E_a [10^{-19} J]
1	$N_2 + N_2 \rightleftharpoons N + N + N_2$	7.968×10^{-13}	−0.5	15.61	6.518×10^{-47}	0.27	0.0
2	$N_2 + N \rightleftharpoons N + N + N$	6.900×10^{-8}	−1.5	15.61	4.817×10^{-46}	0.27	0.0
3	$N_2 + O_2 \rightleftharpoons N + N + O_2$	3.187×10^{-13}	−0.5	15.61	6.518×10^{-47}	0.27	0.0
4	$N_2 + O \rightleftharpoons N + N + O$	3.187×10^{-13}	−0.5	15.61	6.518×10^{-47}	0.27	0.0
5	$N_2 + NO \rightleftharpoons N + N + NO$	3.187×10^{-13}	−0.5	15.61	6.518×10^{-47}	0.27	0.0
6	$O_2 + N_2 \rightleftharpoons O + O + N_2$	1.198×10^{-11}	−1.0	8.197	1.800×10^{-47}	0.27	0.0
7	$O_2 + N \rightleftharpoons O + O + N$	5.993×10^{-12}	−1.0	8.197	1.800×10^{-47}	0.27	0.0
8	$O_2 + O_2 \rightleftharpoons O + O + O_2$	5.393×10^{-11}	−1.0	8.197	1.800×10^{-47}	0.27	0.0
9	$O_2 + O \rightleftharpoons O + O + O$	1.498×10^{-10}	−1.0	8.197	1.800×10^{-47}	0.27	0.0
10	$O_2 + NO \rightleftharpoons O + O + NO$	5.993×10^{-12}	−1.0	8.197	1.800×10^{-47}	0.27	0.0
11	$NO + N_2 \rightleftharpoons N + O + N_2$	6.590×10^{-10}	−1.5	10.43	2.098×10^{-46}	0.27	0.0
12	$NO + N \rightleftharpoons N + N + O$	1.318×10^{-8}	−1.5	10.43	2.098×10^{-46}	0.27	0.0
13	$NO + O_2 \rightleftharpoons N + O + O_2$	6.590×10^{-8}	−1.5	10.43	2.098×10^{-46}	0.27	0.0
14	$NO + O \rightleftharpoons N + O + O$	1.318×10^{-8}	−1.5	10.43	2.098×10^{-46}	0.27	0.0
15	$NO + NO \rightleftharpoons N + O + NO$	1.318×10^{-8}	−1.5	10.43	2.098×10^{-46}	0.27	0.0
16	$N_2 + O \rightleftharpoons NO + N$	1.120×10^{-16}	0.0	5.175	2.490×10^{-17}	0.0	0.0
17	$O_2 + N \rightleftharpoons NO + O$	1.598×10^{-18}	0.5	0.4968	5.279×10^{-21}	1.0	2.719

3.4 CHARGED PARTICLES

The simulation of a high temperature hypersonic shock requires the modeling of charged particles and their interactions. Accurate modeling of charged particles becomes even more important for comparisons to shock tube experiments that rely on radiative measurements. For high temperature air simulations, the number of species must be increased from a 5-species model to an 11-species model including N_2, N, O_2, O, NO, N_2^+, N^+, O_2^+, O^+, NO^+, and e^-. With the addition of charged species, a separate set of challenges for DSMC are introduced, including the modeling of free electrons, charged particle collisions, and ionization/charge exchange reactions.

3.4.1 Free Electron Model

Free electrons provide a unique test for DSMC simulations. Since their mass is at least four orders of magnitude smaller than an atom, they tend to have collision frequencies and speeds that are much larger than the bulk particle average. This poses a problem in resolving the movement and collisions of electrons, requiring computationally expensive infinitesimal timesteps or sub-stepping methods. Instead of explicitly modeling the movement of free electrons, CHIPS was modified to utilize the quasi-neutral ionization model previously applied to DSMC by Bird [11]. In this model, the free electrons generated by the ionization reactions are constrained to move with their respective ions. Since the electrons move with the ions, charge neutrality is enforced. Still, the electrons can undergo collisions and carry their own velocity and energy. As long as the Debye length is much less than the characteristic length, the weakly ionized plasma created by the electrons remains quasi-neutral [45]. The Debye length is given by

$$\lambda_D = \sqrt{\frac{\epsilon_0 k_B T_e}{n_e e^2}} \qquad [3.9]$$

where ϵ_0 is the permittivity of free space, k_B is the Boltzmann constant, T_e is the electron temperature, n_e is the electron number density, and e is the elementary charge. In this research, the degree of ionization is low and the maximum Debye length experienced is on the order of a micrometer, which means that it is smaller than all characteristic lengths and the quasi-neutral assumption is valid. Although moving the electrons with the ions allows for a simplification of the DSMC process, it neglects the acceleration of the ions due to electrostatic forces. In order to include the effect of ambipolar diffusion, the electric field should be estimated from the Langmuir-Tonks equation following the work

of Bird [11]. In an ionizing hypersonic shock simulation, ambipolar diffusion causes the ions to move upstream towards decreasing electron density. The effects of ambipolar diffusion have not yet been included in the current version of CHIPS. Nevertheless, the results of the sensitivity analysis are not expected to be significantly affected by the omission of ambipolar diffusion.

3.4.2 Charged Collisions

Models for neutral particle collisions were discussed in the previous section, but charged particle collisions require special attention to accurately simulate their behavior. For ion-neutral and ion-ion elastic collisions, the VHS model is applied even though collision cross-sections are expected to be different when comparing with neutral-neutral collisions. Because of the ion's charge, the collision cross-section may be larger. This is especially true for ion-ion collisions due to the long-range repelling force between particles of like charge. Since the VHS model is limited to two free parameters, the model cannot capture the Coulombic forces present in ion-ion interactions. For ion-neutral cases, calibrated parameters had not yet been created for the VHS model before the completion of the preliminary sensitivity analysis. Recently, calibrated parameters for ion-neutral and ion-ion collisions have been published in Ref. [18] and modeling these interactions will be addressed before the final sensitivity study. In both the ion-neutral and ion-ion cases, charged collision parameters in CHIPS are assumed to be identical to the neutral parameters (Table 3.1) which is a common assumption for DSMC simulations. This assumption is incorrect particularly for ion-ion interactions but is sufficient for now as these interactions are comparatively rare for the scenarios studied in this dissertation. Electron-heavy parameters were compiled from a number of publications by Ozawa and a listed in Table 3.3 [16]. Electron-electron collisions are not

modeled in CHIPS as their frequency is high, but the effect on the flow properties is likely low.

Table 3.3 Electron-heavy collision parameters.

Collision Pair	ω	d_{ref} [10^{-10} m]
e^-+N_2	0.40	1.596
e^-+N	0.69	2.585
e^-+O_2	0.41	1.262
e^-+O	0.45	1.493
e^-+NO	0.55	1.913
$e^-+N_2^+$	0.40	1.596
e^-+N^+	0.69	2.585
$e^-+O_2^+$	0.41	1.262
e^-+O^+	0.45	1.493
e^-+NO^+	0.55	1.913

At the high temperatures experienced through a hypersonic shock, the interaction between heavy particles and electrons becomes important. In a few special cases, the VHS model was modified to add resonance peaks to the calculation of the collision cross-section, σ_T. For N_2-e^- and NO-e^-, these resonance peaks can be important for modeling electron collisions at low electron temperatures and the appropriate equations are found in Ref. [16]. Collisions between electrons and molecules are frequent, causing an increase in the vibrational relaxation rate. At low electron temperatures, an electron can be temporarily captured in a resonant state by nitrogen molecules. For N_2-e^- collisions simulated in this research, Lee provided a more specific relationship for the vibrational relaxation time that models the electron impact vibrational relaxation of N_2 accounting for this phenomenon [46]. Instead of the cell translational temperature, Lee's model is

dependent on the electron temperature and electron number density in a cell. To apply the more accurate relaxation time published by Lee, the relaxation time is calculated from the cell electron temperature and electron number density and then multiplied by the collision frequency to obtain Z_{vib}. This vibrational collision number replaces the corresponding value in Eqn. 3.5.

3.4.3 Chemical Reactions

Chemical reactions involving charged particles utilize the TCE model which requires these reactions to be in Arrhenius form. The nominal Arrhenius reaction rates for charged particle reactions used in the preliminary sensitivity analyses are tabulated in Tables 3.4 and 3.5. When an ion participates as a third body in a dissociation or recombination reaction, the reaction rate is taken as its corresponding neutral particle reaction (Table 3.4). Table 3.5 lists the nominal reactions that include charged particles. These reaction rates originate from Park [47] and Bird [19], but are also used in hypersonic DSMC simulations performed by Ozawa [16]. Many of the 11-species air reactions are included in this dissertation, but not every possible reaction. A few reactions have been omitted because of their low rates, the small concentration of charged particles, or the lack of published values. For these same reasons, some of the backward reaction rates are not included. When listed, the backwards reaction rates were calculated from the equilibrium constant and fit to an Arrhenius form over a range of temperatures. However, it must be noted that, in several cases, the pairs of forward and backward reaction rates taken from Refs. [6] and [16] produce an equilibrium constant inconsistent with published values since the forward and backward rates were compiled from separate sources. In addition, modeling the backward reaction rate in Arrhenius form incorrectly represents the temperature dependence of the equilibrium constant resulting in errors in

both the backward rate and the equilibrium concentration. Following the preliminary sensitivity analysis, a method will be developed in Chapter 7 to calculate the backwards reaction rates directly from the equilibrium constant, resolving the aforementioned issues.

Electron impact ionization (reactions #39 and #40 in Table 3.4) is treated in a slightly different manner than the other ionization reactions. In the TCE method, these reactions are related to dissociation reactions, but there is a difference in how the energy is distributed to separating particles. Typically, in a dissociation reaction, the collision energy is redistributed to the colliding diatomic molecule and the third body, resulting in a new kinetic energy and internal energy for the two particles through VHS and Larsen-Borgnakke calculations. Then energy is assigned to the dissociated atoms by splitting the post-collision internal energy of the diatomic molecule between the resulting atoms via VHS and adding it to the post-collision kinetic energy. In this way, all three particles that result from the dissociation reaction have separate energy. In the case of the ionization reactions #39 and #40 in Table 3.4, the separating particle is no longer a diatomic molecule. There is now no way to distribute internal energy to the ionizing particle during its collision with the third body. While the addition of an electronic excitation model could alleviate this problem, it is still common to find dissociation products in the ground electronic state. This means that the resulting ion and electron must have the same velocity in the same direction because they only inherit the center of mass velocity of the post-collision atom. Besides being unlikely, this can cause a scenario in future timesteps where the brother ion and electron are chosen to collide with each other but have a zero relative velocity. To prevent this from happening, a check has been placed in the code which prohibits collisions between zero relative velocity particles. Even though this method is not physically correct, it has little effect on the flow results. Due to the high collision frequency of electrons, the null relative velocity state is temporary.

The chemical reaction model must also handle the assignment of free electrons following the method described in Section 3.4.1. When an ionization reaction creates a free electron, this electron is paired with its parent ion. The free electron points to the index of its parent ion and the parent ion points to the index of the free electron. In the case of a charge exchange reaction, the handling of the indices is straightforward. The species of the reacting ion is changed to the species of the product ion, but the indices are unchanged. However, when a free electron capture reaction takes place, two scenarios can occur. First, the parent ion could recapture its own free electron which only requires the indices to be reset. For the second case, the ion is capturing a free electron that has been paired with a different ion. This means that the remaining, unpaired ion and free electron must have their isolated indices paired to each other. In addition, the free electron is teleported to the ion's spatial location, enforcing quasi-neutrality. This movement of the free electron to the ion's location, physically representing a charge diffusion across a cell, does not influence the results.

Table 3.4 Charged particle dissociation and recombination reaction rates.

#	Reaction	Forward Rate Coefficients			Backward Rate Coefficients		
		Λ [m^3/s]	η	E_a [10^{-19} J]	Λ [m^3/s]	η	E_a [10^{-19} J]
18	$N_2 + N_2^+ \rightleftharpoons N + N + N_2^+$	7.968×10^{-13}	−0.5	15.61	6.518×10^{-47}	0.27	0.0
19	$N_2 + N^+ \rightleftharpoons N + N + N^+$	6.900×10^{-8}	−1.5	15.61	4.817×10^{-46}	0.27	0.0
20	$N_2 + O_2^+ \rightleftharpoons N + N + O_2^+$	3.187×10^{-13}	−0.5	15.61	6.518×10^{-47}	0.27	0.0
21	$N_2 + O^+ \rightleftharpoons N + N + O^+$	3.187×10^{-13}	−0.5	15.61	6.518×10^{-47}	0.27	0.0
22	$N_2 + NO^+ \rightleftharpoons N + N + NO^+$	3.187×10^{-13}	−0.5	15.61	6.518×10^{-47}	0.27	0.0
23	$O_2 + N_2^+ \rightleftharpoons O + O + N_2^+$	1.198×10^{-11}	−1.0	8.197	1.800×10^{-47}	0.27	0.0
24	$O_2 + N^+ \rightleftharpoons O + O + N^+$	5.993×10^{-12}	−1.0	8.197	1.800×10^{-47}	0.27	0.0
25	$O_2 + O_2^+ \rightleftharpoons O + O + O_2^+$	5.393×10^{-11}	−1.0	8.197	1.800×10^{-47}	0.27	0.0
26	$O_2 + O^+ \rightleftharpoons O + O + O^+$	1.498×10^{-10}	−1.0	8.197	1.800×10^{-47}	0.27	0.0
27	$O_2 + NO^+ \rightleftharpoons O + O + NO^+$	5.993×10^{-12}	−1.0	8.197	1.800×10^{-47}	0.27	0.0
28	$NO + N_2^+ \rightleftharpoons N + O + N_2^+$	6.590×10^{-10}	−1.5	10.43	2.098×10^{-46}	0.27	0.0
29	$NO + N^+ \rightleftharpoons N + O + N^+$	1.318×10^{-8}	−1.5	10.43	2.098×10^{-46}	0.27	0.0
30	$NO + O_2^+ \rightleftharpoons N + O + O_2^+$	6.590×10^{-8}	−1.5	10.43	2.098×10^{-46}	0.27	0.0
31	$NO + O^+ \rightleftharpoons N + O + O^+$	1.318×10^{-8}	−1.5	10.43	2.098×10^{-46}	0.27	0.0
32	$NO + NO^+ \rightleftharpoons N + O + NO^+$	1.318×10^{-8}	−1.5	10.43	2.098×10^{-46}	0.27	0.0

Table 3.5 Ionization, electron impact dissociation, and charge exchange reactions.

#	Reaction	Forward Rate Coefficients			Backward Rate Coefficients		
		Λ [m^3/s]	η	E_a [10^{-19} J]	Λ [m^3/s]	η	E_a [10^{-19} J]
33	$N + O \rightleftharpoons NO^+ + e^-$	8.800×10^{-18}	0.0	4.404	1.494×10^{-10}	−0.65	0.0
34	$N + N \rightleftharpoons N_2^+ + e^-$	3.387×10^{-17}	0.0	9.319	4.483×10^{-12}	−0.5	0.0
35	$O + O \rightleftharpoons O_2^+ + e^-$	1.826×10^{-17}	0.0	11.13	2.49×10^{-12}	−0.5	0.0
36	$N_2 + e^- \rightleftharpoons N + N + e^-$	3.187×10^{-13}	−0.5	15.61	–	–	–
37	$O_2 + e^- \rightleftharpoons O + O + e^-$	5.993×10^{-12}	−1.0	8.197	–	–	–
38	$NO + e^- \rightleftharpoons N + O + e^-$	1.318×10^{-8}	−1.5	10.43	–	–	–
39	$N + e^- \rightleftharpoons N^+ + e^- + e^-$	1.00×10^{-14}	0.0	23.28	–	–	–
40	$O + e^- \rightleftharpoons O^+ + e^- + e^-$	3.00×10^{-12}	0.0	21.88	–	–	–
41	$O + O_2^+ \rightleftharpoons O^+ + O_2$	1.890×10^{-16}	−0.52	2.590	1.890×10^{-16}	−0.52	0.0
42	$N^+ + N_2 \rightleftharpoons N + N_2^+$	1.670×10^{-17}	−0.18	1.670	2.370×10^{-18}	−0.52	0.0
43	$O + NO^+ \rightleftharpoons O^+ + NO$	4.580×10^{-17}	0.01	7.041	–	–	–
44	$O^+ + N_2 \rightleftharpoons O + N_2^+$	1.511×10^{-18}	0.36	3.148	1.770×10^{-17}	−0.21	0.0
45	$N + NO^+ \rightleftharpoons N^+ + NO$	1.840×10^{-15}	−0.02	8.430	1.840×10^{-15}	−0.02	0.0
46	$O_2 + NO^+ \rightleftharpoons O_2^+ + NO$	3.985×10^{-17}	0.41	4.501	3.985×10^{-17}	0.41	0.0
47	$N + O_2^+ \rightleftharpoons N^+ + O_2$	1.444×10^{-16}	0.14	3.948	–	–	–
48	$N_2 + O_2^+ \rightleftharpoons N_2^+ + O_2$	1.644×10^{-16}	0.0	5.619	–	–	–
49	$N + NO^+ \rightleftharpoons O + N_2^+$	2.830×10^{-17}	0.4	4.901	4.100×10^{-18}	0.4	0.0
50	$O^+ + NO \rightleftharpoons N^+ + O_2$	2.324×10^{-25}	1.9	2.112	–	–	–
51	$O + NO^+ \rightleftharpoons N^+ + O_2$	1.660×10^{-18}	0.5	10.66	–	–	–
52	$N + NO^+ \rightleftharpoons O^+ + N_2$	5.645×10^{-17}	−1.08	1.767	–	–	–
53	$O + NO^+ \rightleftharpoons O_2^+ + N$	1.195×10^{-17}	0.29	6.709	–	–	–

3.5 ELECTRONIC EXCITATION

3.5.1 Collision Model

Modeling electronic excitation is crucial for accurate simulations of ionization in a high temperature hypersonic shock. Electronic excitation allows particles to climb the electronic energy ladder and obtain enough energy for ionization reactions to occur. In the present research, the electronic excitation model laid out previously by Liechty [24], developed assuming VHS cross-sections, will be followed. In this method, each

simulated particle is assigned a single excited level and excitation events are modeled following a similar procedure to other internal modes. This model is selected for its ability to simulate a non-equilibrium electronic level distribution and its simplicity because predetermined excitation cross-sections for individual transitions are not required. Input parameters for the electronic energy and degeneracy of the simulated electronic levels are required for each species. Electronic level degeneracies and energy values are compiled from the NIST [48] database and are combined together using the groups listed in Ref. [49]. From these data, each simulated particle is initialized with a single electronic level sampled from the Boltzmann distribution at its initialization temperature. As particles collide and react, electronic energy transfer is modeled following Borgnakke-Larsen by performing an acceptance-rejection procedure from the equilibrium distribution at the collision energy [25]. The probability of exciting to a selected level is determined from Eqn. 3.10, derived from the Boltzmann distribution. This probability is found to be

$$P_{elec_i} = \frac{g_i\left(E_c - E_{elec_i}\right)^{3/2-\omega}}{f_{max}} \qquad [3.10]$$

where i is the currently selected level, g_i is the degeneracy, E_{elec_i} is the electronic energy, and E_c is the collision energy contribution from the translational mode and the pre-collision electronic energy of the particle being considered. The normalization value, f_{max}, is defined as

$$f_{max} = max\left\{\left[g_j\left(E_c - E_{elec_j}\right)^{\frac{3}{2}-\omega}\right]_{j=1,J_{allow}}\right\} \qquad [3.11]$$

where J_{allow} is the maximum level possible for the collision energy, E_c.

Unlike rotational and vibration relaxation models that utilize an experimentally measured relaxation time, there is no general experimental relaxation time available for electronic excitation. Due to the absence of a relaxation time in the current model, an electronic excitation event is considered for every collision. However, a null excitation can occur when a particle considered for electronic excitation selects its current state; this occurs frequently for the ground state of a low temperature gas. While the absence of a relaxation time can result in an overprediction of electronic excitation, Liechty found that most equilibrium electronic energy level transition rates were within the error of published rates [49]. Although the equilibrium transition rates are relatively accurate using the current model, Chapter 8 demonstrates that assuming an electronic excitation event occurs for every collision overpredicts the nonequilibrium relaxation rate. Checking for an electronic excitation at every collision brings complications both with the inelastic collision procedures and the computational efficiency of CHIPS. In the particle selection procedure prohibiting double relaxation, an inelastic collision is complete once a single internal energy relaxation has been performed. In addition, the total probability of the various relaxations must not be greater than one. This means that electronic excitation must be excluded from this procedure since an electronic excitation event is performed for every collision. Once particles are selected to collide in the CHIPS code, electronic excitations are calculated for both particles and then the particle selection procedure prohibiting double relaxation is completed for the remaining internal modes. Because electronic excitations are calculated for every collision, including electronic excitation in DSMC brings a high computational cost. A major reason for this cost is that Eqn. 3.11 requires searching over every electronic level up to J_{allow}. To minimize this

cost, a lookup table is created for each species as a function of the collision energy, E_c. At the beginning of a simulation, Eqn. 3.11 is solved over a set of collision energies to determine the level, J^*, where f_{max} occurs and the collision energy where the value of J^* changes. This array can then be accessed for an excitation event to quickly determine the value of f_{max} for the energy in that collision. An example of how J^* compares to the collision energy is plotted in Fig. 3.3 for atomic nitrogen's electronic levels simulated in CHIPS. The discretization of E_c is performed using 100,000 points from 95% of the 1st excited level's energy to 150% of the highest excited level, where the ground state is considered the 0th level. As seen in Fig. 3.3, the number of levels that must be searched through is reduced from 22 to 8. This reduction in computational cost is even more considerable when noting that most of the electronic levels can be represented by the first two values of J^*.

While Liechty's model covers the transition of electronic states due to particle collision, several mechanisms are still absent in either the CHIPS code or in the model itself. First, an accurate way to handle post-reaction electronic excitations is not available. Following precedent for how rotational and vibrational energy is assigned to the products of a chemical reaction, electronic states could be selected in the same manner, but this could lead to an overpopulation of the states. For example, dissociation of molecular species most often results in ground state atoms or a low probability of atoms in some excited state dependent on the excited state of the dissociating molecule [50]. On the other hand, the dissociative recombination process favors electronically excited states. In CHIPS, it is assumed that all chemical reactions result in ground state products to simplify this process. A second mechanism missing from the CHIPS code is the ability to model spontaneous emission where a particle de-excites from some electronic level and emits a photon. Finally, it must be taken into consideration that,

while Liechty's method simulates transitions, these excitations occur without regard for "forbidden" or "allowed" transitions. For a species, any level is free to transition to any other level in Liechty's model. Obviously, there are still improvements that can be made, but the current approach represents a simple and effective model for electronic excitation.

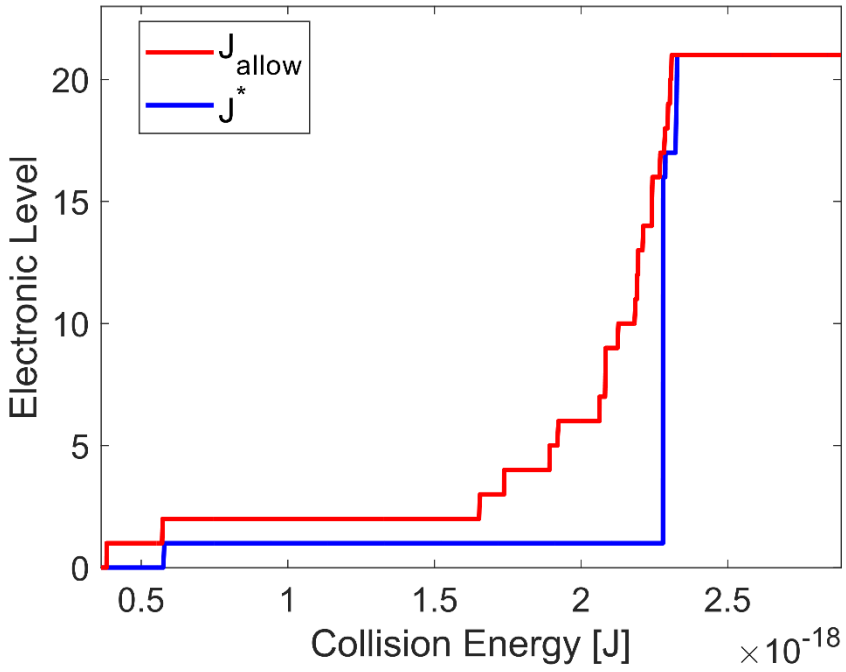

Figure 3.3 Comparison of the maximum allowed electronic level and the electronic level that determines f_{max} as a function of collision energy.

3.5.2 Free Electron and Electronic Temperature Calculations

Typically, in high temperature hypersonic simulations only two or three temperatures are modeled: T_{tr}, T_{rot}, and T_{vib}. In these cases, the free electron temperature, T_e, and the electronic temperature, T_{elec}, are assumed in equilibrium with one of the other temperatures. Because the CHIPS codebase includes the modeling of free

electrons and electronic excitation, separate temperatures for these modes can be defined to further represent nonequilibrium in the flow. The calculation of the free electron temperature is simple. While the free electrons are treated as bound to a pair ion assuming quasi-neutrality, they are still allowed their own velocity vector. T_e is determined from the translational temperature of the free electrons in each cell based purely on the kinetic energy associated with the velocity of the free electrons.

The calculation of the electronic temperature is not as straightforward. In the past, the electronic temperature has typically been calculated from the Boltzmann distribution using the ratio of populations of two specific states, such as the ground and first excited state [23][24]. While this is a valid approach for equilibrium conditions, it is likely that unphysical or unrealistic electronic temperatures can arise in non-equilibrium regions. In regions with a low number of simulated particles, the statistics are insufficient to appropriately represent the electronic temperature. Since CHIPS is able to record the entire electronic energy level distribution in each cell, a slightly improved option is available that makes use of more information to determine T_{elec}. This is done by comparing each level to all other levels for a particular species and then combining the species temperatures into a bulk electronic temperature. Equation 3.12 follows the electronic temperature equation formed by Liechty [49] and extends it to handle the entire excited level distribution. The electronic temperature for a single species is determined by comparing each electronic level and calculating the weighted average where each Boltzmann distribution ratio is weighted by number of particles in the two states being considered. In Eqns. 3.12 and 3.13, s is the species being considered, i and j are the current electronic levels, J_{max} is the number of excited states, E and g are the energy and degeneracy of the level respectively, and n is the number of particles in that state.

$$T^s_{elec_{i,j}} = \frac{E^s_{elec_i} - E^s_{elec_j}}{k_B ln\left(\frac{n^s_j g^s_i}{n^s_i g^s_j}\right)}\left(n_i + n_j\right) \quad [3.12]$$

$$T^s_{elec} = \frac{\sum_{i=1}^{Jmax}\sum_{j=i+1}^{Jmax} T^s_{elec_{i,j}}}{\sum_{i=1}^{Jmax}\sum_{j=i+1}^{Jmax}\left(n_i + n_j\right)} \quad [3.13]$$

These equations represent the ratio of two Boltzmann distributions for states i and j. Since the Boltzmann distributions are representations of equilibrium states, some difficulties arise in regions with a high degree of electronic non-equilibrium or a low resolution of the excited state populations, such as directly upstream of shock wave. In this region, the bulk of the particles originate from the freestream conditions at low temperatures. These temperatures are low enough that all of the simulated particles should be in the ground state. Near the shock front, high energy particles are present that have diffused from within the shock layer. These particles can strike a high velocity freestream particle which can lead to an electronic excitation. If this excited particle is the only particle not in the ground state, the electronic temperature is solely reliant on the comparison between that particle's excited state and all of the other particles in the ground state. As a result of the poor statistics in this event, the electronic temperature calculation from Eqns. 3.12 and 3.13 will produce unexpected or even unphysical values. In Eqn. 3.12, unphysical values will result from two scenarios. First, when the number of simulated particles in the i state is zero and second, when the ratio evaluated within the natural logarithm is one. These cases must be excluded in the electronic temperature calculation. For the shock scenarios studied in this dissertation, poor statistics are always encountered in the regions where the first free electrons are generated or where electronic

excitation begins. To mitigate the effect of these poor statistics on the T_e and T_{elec} calculations, a cut-off value for the minimum number of simulated particles in a sampling cell is set. In this dissertation, the cut-off value is determined to be five simulated particles (ensemble averaged) and the free electron or electronic temperature is set to zero when this condition is not met. In Chapter 8, the calculation of T_{elec} is revisited and improved.

CHAPTER 4

Preliminary CHIPS Nominal Simulations

4.1 OVERVIEW

Before a sensitivity study can be completed, a nominal simulation must be selected and tested. The nominal simulation is defined as the CHIPS simulation of some chosen scenario where the CHIPS input parameters for each model use values generally accepted by the DSMC and CFD communities. Some of these input parameters are varied in the following sensitivity analyses, but the nominal input values are contained within this range. For the nominal simulation to be relevant, it must reproduce a recently performed experiment that meets several criteria. First, the experiment must be rarefied enough to allow for its reproduction by DSMC without requiring excessive computational expense. Second, the experiment must occur in the high temperature hypersonic regime with a shock velocity greater than ~10 km/s so that charged particle physics and radiative emission are active. Third, the experiment must have clear data in a spectral range or ranges that are suitable for calibration. Finally, minimum experimental uncertainty should be present in the data. This last point is important because the information gained from a parameter calibration improves as the experimental uncertainty decreases. In this chapter, a simulation is chosen that serves as the nominal scenario of interest in the following detailed sensitivity analyses. In essence, this nominal

---

Higdon, K. J., Goldstein, D. B., and Varghese, P. L., "Sensitivity Analysis of Direct Simulation Monte Carlo Parameters for Ionizing Hypersonic Flows," *Journal of Thermophysics and Heat Transfer*, Vol. 32, No. 1, 2018, pp. 90-102.

Higdon, K. J., Goldstein, D. B., and Varghese, P. L., "Sensitivity Analysis of DSMC Parameters for an 11-Species Air Hypersonic Flow," *30th International Symposium on Rarefied Gas Dynamics*, AIP Conf. Proc. 1786, Victoria, B. C., July 2016.

D. B. Goldstein and P. L. Varghese supervised these projects and provided technical insight.

simulation represents the results of the chosen scenario using an input parameter set that the DSMC community has some degree of confidence in.

4.2 NOMINAL SHOCK SCENARIO #1

Considering the criteria set for the nominal simulation, the experimental results obtained in the Electric Arc Shock Tube (EAST) at NASA Ames were chosen as the first CHIPS nominal case and this corresponds to sensitivity analysis study #1 performed in Section 5.3 and Ref. [4]. Specifically, the nominal simulation reproduces Campaign 47, Shot 37 from a recent testing campaign which is a 10.26 km/s, 0.2 Torr shock in a synthetic air mixture [32]. The experimental conditions and CHIPS simulation parameters are listed in Table 4.1. This shock experiment is a well-documented and reliable case since it has also been the subject of a previous sensitivity analysis using an Eulerian solver [34]. Shot 37 was chosen because of its low pressure, which makes it reasonable to simulate with CHIPS, and more importantly because the experimental results have a relatively low uncertainty. In addition, these test conditions are within the flow regime where peak radiative heating occurs during lunar return missions for the crew exploration vehicle (CEV) [32].

Table 4.1 Nominal simulation inflow conditions and simulation parameters.

EAST Campaign 47 Shot 37		Simulation Parameters	
Shock velocity [km/s]	10.26	Domain Size [m]	1.0
Number density [#/m^3]	6.4377×10^{21}	Number of Cells	5000
Temperature [K]	300	Timestep [s]	1.6×10^{-8}
N_2 mole fraction [%]	79	f_{num} [#/m^3]	1.0×10^{17}
O_2 mole fraction [%]	21		

Nominal shock scenario #1 is completed using the input parameters and models described in Chapters 2 and 3, but with the omission of the electronic excitation model. Results of the nominal CHIPS simulation of EAST Shot 37 are presented in Fig. 4.1. Figure 4.1a shows the neutral particle number densities with respect to distance from the shock wave center. Diatomic particles become scarce behind the shock due to high temperature dissociation and atomic species N and O become dominant. Charged particle number densities are presented in Fig. 4.1b and bulk temperatures, including a separate free electron temperature T_e, are shown in Fig. 4.1c. When compared to the total number of particles, charged species are only a small fraction of the total number density. However, modeling this ionization is important to produce radiation and, later, comparisons to experimental measurements. Since there is only a small degree of ionization, the assumption of local charge neutrality is acceptable. As the number density of a particular species decreases, statistical noise begins to appear in the results. This occurs as the cell number density of a particular species approaches f_{num}, the chosen value for the number of real particles represented by each simulated particle. If more accurate results are desired, the number of simulated particles can be increased, or the simulation could be run longer to increase the number of ensemble average points. The drawback of either choice is a drastic increase in computational time. In Fig. 4.1, oxygen molecule and ion number densities become so small that there are only one or two simulated oxygen particles per cell downstream of the shock. In this region, most molecules have dissociated, resulting in a lack of diatomic particles that are able to represent the internal modes. This leads to large statistical fluctuations in the macroscopic rotational and vibrational temperatures. As the temperature equilibrates behind the shock, the number density of each species approaches its equilibrium value. As discussed in Section 3.4.3, this equilibrium may not exactly match the expected equilibrium

concentrations as the current backward reaction model cannot reproduce the equilibrium constant for all temperatures. However, comparison with analytic equilibrium results produces only minor discrepancies. In addition, it is important to point out that electronic excitation is not yet included in nominal simulation #1. Addition of electronic excitation will be explored in nominal simulation #2. While omission of the electronic excitation model affects the resulting temperatures, the maximum translational temperature reaches about 40,000 K which is significantly higher than the temperature range that most of the DSMC input parameters are calibrated to. These results reinforce the need for sensitivity analysis followed by uncertainty quantification since the input parameters are utilized far from their reference experimental measurements.

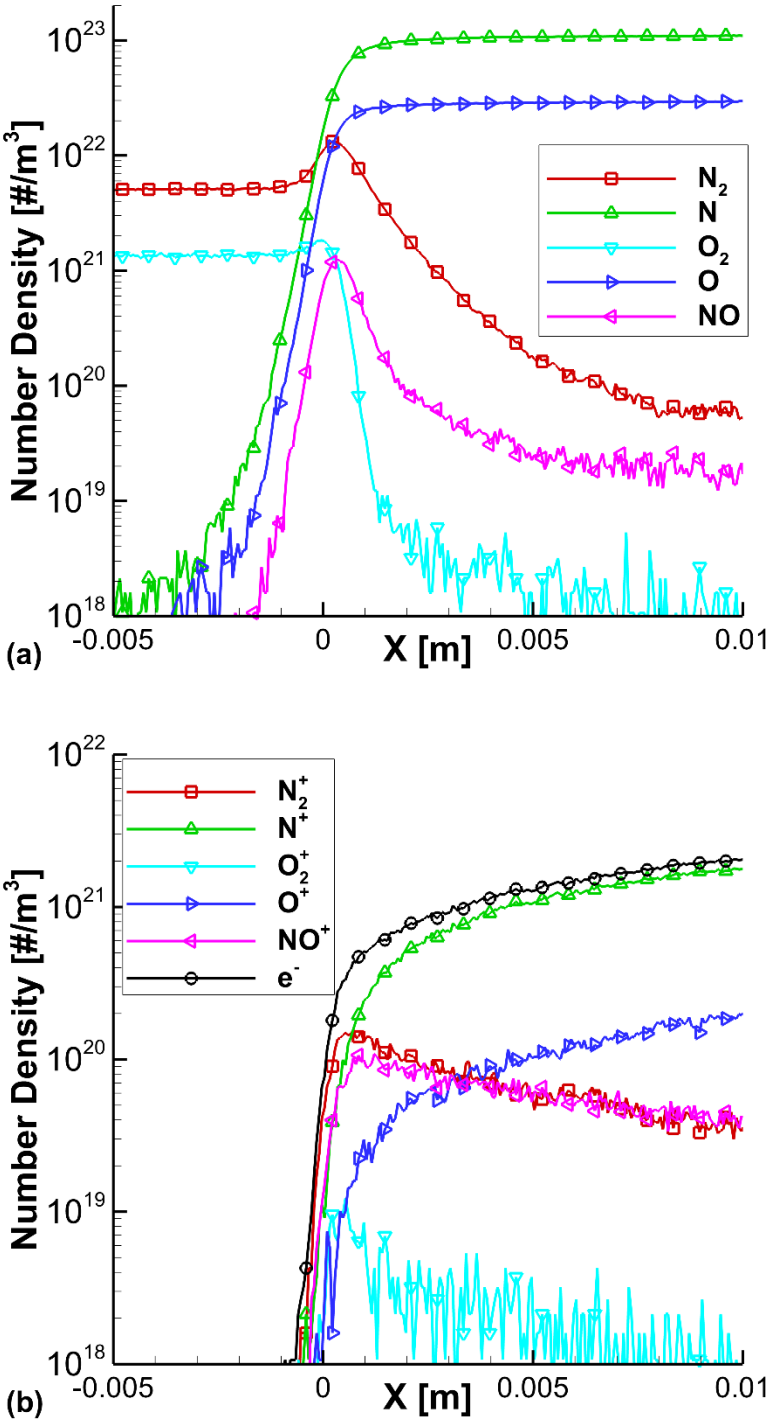
Number Density [#/m^3]
10^{23}
10^{22}
10^{21}
10^{20}
10^{19}
10^{18}
-0.005
0
0.005
0.01
X [m]
(a)
N_2
N
O_2
O
NO
Number Density [#/m^3]
10^{22}
10^{21}
10^{20}
10^{19}
10^{18}
-0.005
0
0.005
0.01
X [m]
(b)
N_2^+
N^+
O_2^+
O^+
NO^+
e^-

Figure 4.1

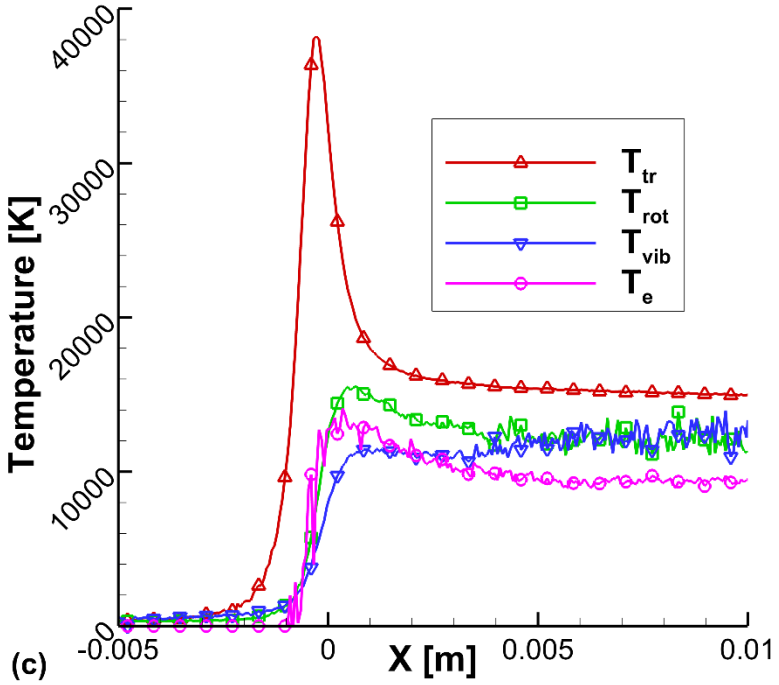

Figure 4.1 Nominal simulation #1 of EAST Campaign 47, Shot 37. *(a) Neutral particle number densities. (b) Charged particle number densities. (c) Bulk temperatures.*

4.3 CONVERGENCE STUDY

Due to the computationally intensive nature of the sensitivity analysis, results must be obtained with minimal computational effort for each shock simulation. Because confidence in the CHIPS simulation increases with the resolution, the goal is to reduce the computational expense without significantly sacrificing the accuracy of the results. As a study of convergence, the nominal CHIPS simulation parameters were modified to produce a satisfactorily converged and a severely under-resolved simulation (Table 4.2). These high and low-resolution cases are compared with the nominal simulation in Fig. 4.2. The number of simulated particles per cell in each simulation was always high enough to consistently represent the output macroparameters of interest. The nominal and

low-resolution simulations model 13 particles per cell in the freestream, which corresponds to ~340 particles per cell in the downstream. Because the high-resolution case is so expensive, it is performed using 8 simulated particles per cell in the freestream which still results in ~200 particles per cell in the post-shock region. This is more than sufficient to resolve most macroparameters that are calculated from the particles. Issues may still arise in calculating macroparameters from trace species, such as the number density of O_2^+ shown in Fig. 4.2b. Since this is a trace species, accurate results are much more difficult to obtain and require a much higher resolution than possible with the current computational time constraints. Fortunately, these trace species are not the subject of the following sensitivity analyses and are unlikely to contribute significantly to the results of these sensitivity studies.

Table 4.2 Simulation input parameters for the resolution study.

Simulation Parameters	Nominal	High Resolution	Low Resolution
Number of Cells	5000	50000	2500
Timestep [s]	1.6×10^{-8}	1.0×10^{-9}	4.0×10^{-8}
f_{num} [#/m^3]	1.0×10^{17}	1.6×10^{16}	3.2×10^{17}
Freestream Particles per Cell	13	8	13

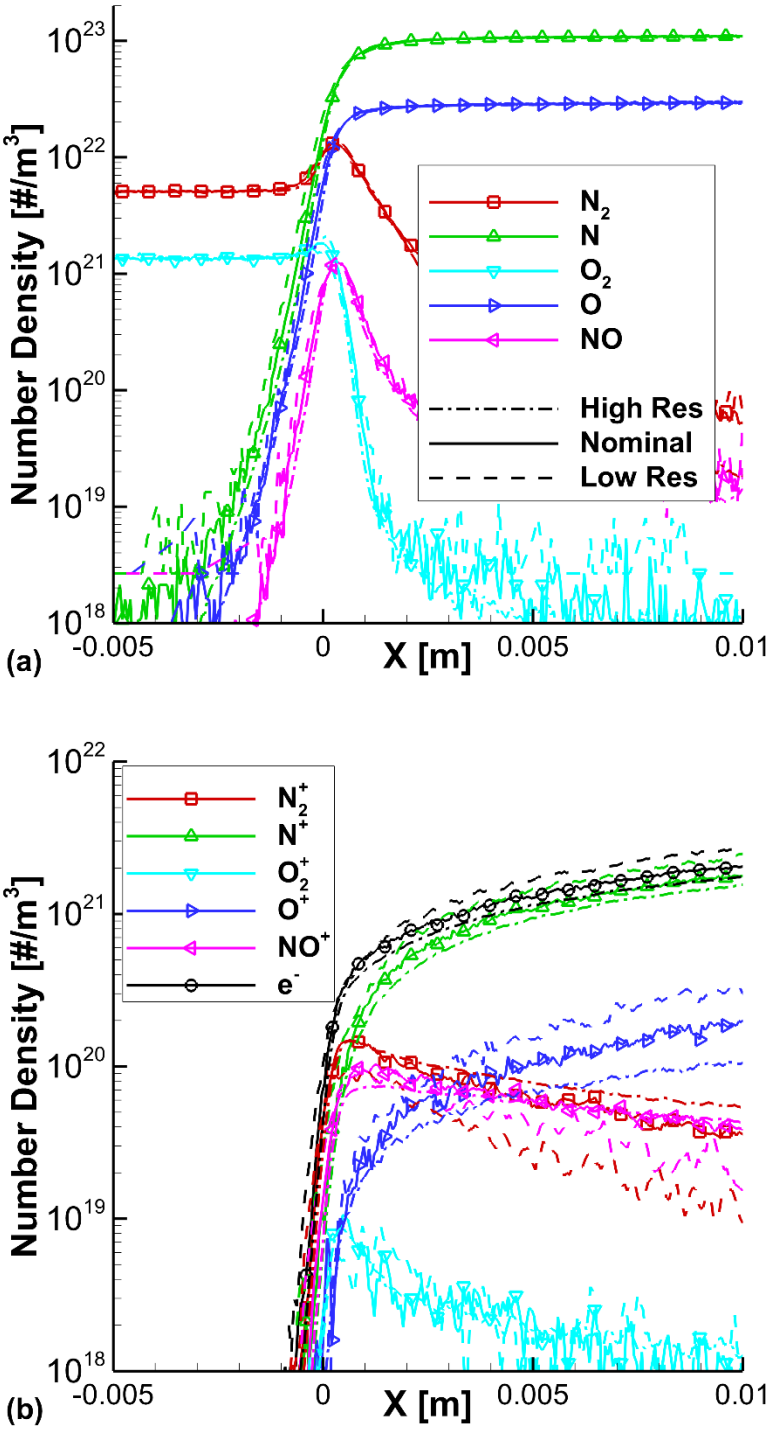
Number Density [#/m^3]
10^{23}
10^{22}
10^{21}
10^{20}
10^{19}
10^{18}
-0.005
0
0.005
0.01
X [m]
(a)
N_2
N
O_2
O
NO
High Res
Nominal
Low Res
Number Density [#/m^3]
10^{22}
10^{21}
10^{20}
10^{19}
10^{18}
-0.005
0
0.005
0.01
X [m]
(b)
N_2^+
N^+
O_2^+
O^+
NO^+
e^-

Figure 4.2

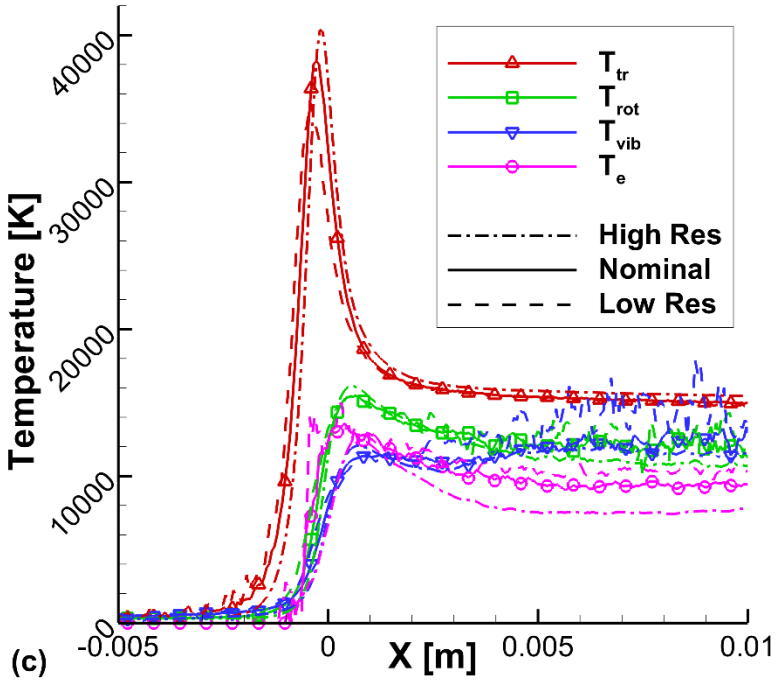

Figure 4.2 Comparison of high and low-resolution results to the nominal EAST Shot 37 simulation as a function of distance from the shock, low pass filtered for clarity. *(a) Neutral particle number densities. (b) Charged particle number densities. (c) Bulk temperatures.*

Resolution of the mean collision time and the mean free path was investigated simultaneously while performing the convergence study. In order to resolve the mean collision time of the particles, the collision timestep must be a fraction of the mean collision time. While resolving the collision time is desired to ensure accuracy, Fig. 4.3 shows that the simulation of free electrons introduces difficulty because the free electron collision time is at least an order of magnitude lower than the heavy particles. When analyzing the nominal simulation, the nominal timestep is found to be an order of magnitude larger than the mixture's mean collision time and two orders of magnitude larger than the free electron mean collision time in the post-shock region. This has some

negative effects on the results, especially in the simulation of macroparameters dependent on free electron collisions. For example, a noticeable discrepancy arises in Fig. 4.2c when comparing the nominal free electron temperature with the high-resolution case and is likely caused by modeling too few free electron collisions. Similar to the mean collision time, particle movement is resolved by ensuring that the cell size is a fraction of the mean free path. When comparing the actual mean free path to the nominal simulation in Fig. 4.4, the nominal simulation cell size is over an order of magnitude greater than the post-shock mean free path. The cell size in the nominal simulation was chosen to be small enough to obtain a shock thickness consistent with the high-resolution case. There is only a minor change in the shock thickness when comparing the translational temperature in Fig. 4.2c for the high resolution and nominal simulations. Even though the nominal simulation is clearly under-resolved in the interest of computational efficiency, comparison between the nominal and high-resolution results shown in Fig. 4.2 demonstrates that the nominal simulation is sufficient to reproduce the resolved results with an acceptable degree of consistency.

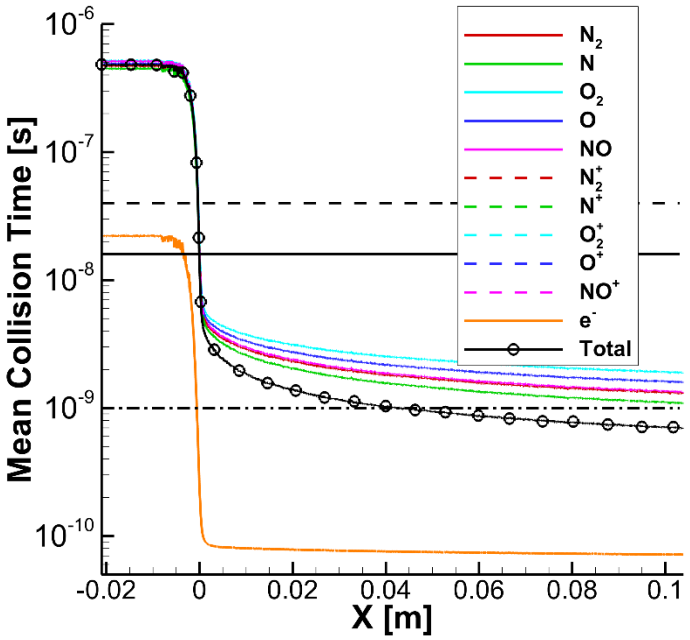

Figure 4.3 Mean collision time as a function of distance from the shock location. *The constant lines represent the high resolution (dash dot), nominal (solid), and low resolution (dashed) simulated timesteps.*

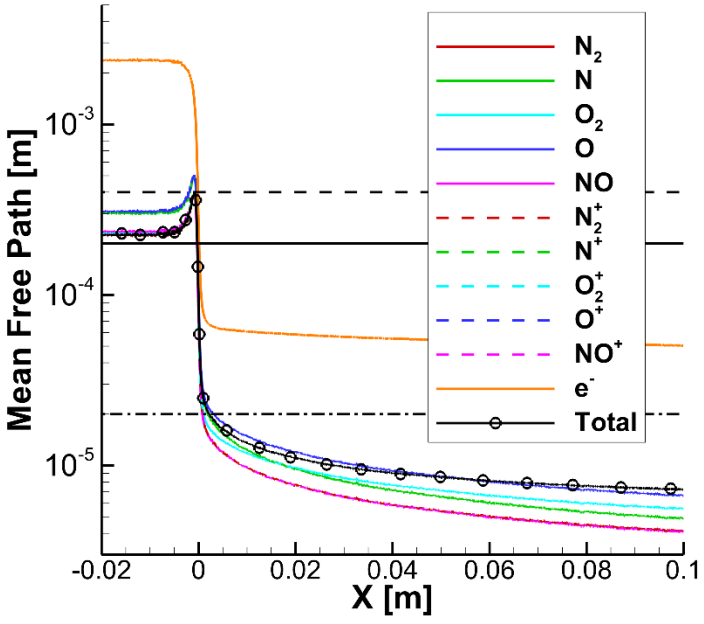

Figure 4.4 Mean free path as a function of distance from the shock location. *The constant lines represent the high resolution (dash dot), nominal (solid), and low resolution (dashed) simulated cell size.*

After studying the convergence of the nominal simulation, it is concluded that the results of the following sensitivity analyses would be the same if both the collision time and mean free path were completely resolved. In the shock region, the nominal simulation only demonstrates minimal error compared with the high-resolution simulation. Although noticeable discrepancies appear in the post-shock region, the results of a sensitivity study are unlikely to change since modifications of input parameters should affect the near-equilibrium region by simply shifting the macroparameters up or down. It is reasonable to assume that the sensitivity of the macroparameters to the various inputs would be measured nearly the same whether the nominal or high-resolution case was used in the sensitivity study. The primary method of comparing the input parameters is through a ranking based on sensitivity where the focus is on identifying the top 5-10 parameters. While the measured sensitivity value may change between the nominal and high-resolution cases, the ranking of the top parameters is unlikely to change. In addition to comparing with the high-resolution results, the low-resolution case reproduces the expected results without significant error, which demonstrates that the nominal simulation has adequate resolution. When comparing the nominal simulation to the low-resolution case, the most difficult feature to reproduce within the shock is the translational temperature spike. It is encouraging to see that this feature is reproduced well by the nominal simulation when compared to the high-resolution case. While there are some minor discrepancies between the nominal and high-resolution cases that may not be acceptable if a single simulation was run as a prediction, this small error is acceptable for a sensitivity analysis, especially considering that the differences between the nominal and high-resolution cases are negligible for the macroparameters studied in the following chapter.

4.4 NOMINAL SHOCK SCENARIO #2

The addition of an electronic excitation model is studied with a second preliminary sensitivity analysis, performed in Chapter 5 and Ref. [51]. Again, before the sensitivity analysis study #2 can be performed, a nominal simulation must be chosen. The hypersonic entry conditions of the previous shock scenario were selected which reproduces the same Campaign 47, Shot 37 experiment [32]. Figure 4.5a-c compares the number densities and temperatures before (dashed lines) and after (solid lines) the electronic excitation model was included in CHIPS. The addition of electronic excitation to the DSMC code has significant effects on the results of the 11-species air simulations. Since electronic energy levels offer another internal energy mode, it is expected that including electronic excitation should increase the level of ionization and decrease the translational temperature. When electronic excitation is modeled, the number density of the charged species is approximately an order of magnitude greater than when the electronic excitation model is omitted (Fig. 4.5b). This occurs because neutral particles can climb the electronic energy ladder when electronic excitation is included. As they reach higher electronic levels, the excited particles are carrying more energy and a collision that results in ionization is much more likely, even though the overall kinetic temperature is lower. On the other hand, ionization reactions must occur from the electronic ground state when electronic excitation is not included. Although the number density of electrons is much greater with electronic excitation included, the overall degree of ionization is still less than 10% and the Debye length remains sufficiently small. The assumption of quasi-neutrality is reasonable for the length scales of interest and each free electron can be moved with a paired ion to enforce this condition.

The effects of the electronic excitation model are also apparent in the translational temperature (Fig. 4.5c). Within the shock layer, the translational temperature peak is

approximately 8,000 K cooler with electronic excitation and downstream of the shock, the temperature difference is about 5,000 K. The reduction in the translational temperature with the electronic excitation model is due to the availability of an additional internal mode for particles to store energy. Kinetic energy of the particles is transferred into electronic excitation when high speed collisions occur. In the post-shock region, the internal temperatures equilibrate with each other quickly when electronic excitation is included while a large degree of nonequilibrium continues far downstream of the shock when the model is omitted. This observation provides support to the argument for the inclusion of electronic excitation because a high degree of nonequilibrium is not expected to persist far downstream of the shock. At the same time, rapid equilibration when the electronic excitation model is included is surprising. This will be explored further in Chapter 8.

In addition to analyzing the differences with and without electronic excitation, the high electronic temperature in Fig. 4.5c (solid cyan line) demonstrates the previously discussed issues with the electronic temperature calculation (Section 3.5.2). Upstream of the shock, it is expected that the electronic temperature should be at or near zero. While this is the case further upstream of 0.5 cm (not shown), the computed electronic temperature reaches values near 10,000 K as the freestream approaches the shock front. These high values are due to a small number of excited particles along with the relatively low number of simulated particles per cell in the upstream region. The excited particles in this region are attributable to collisions between freestream particles and atomic nitrogen or atomic oxygen that have diffused upstream. Low levels of atomic nitrogen are present up to 0.5 cm in front of the shock as seen in Fig. 4.5a.

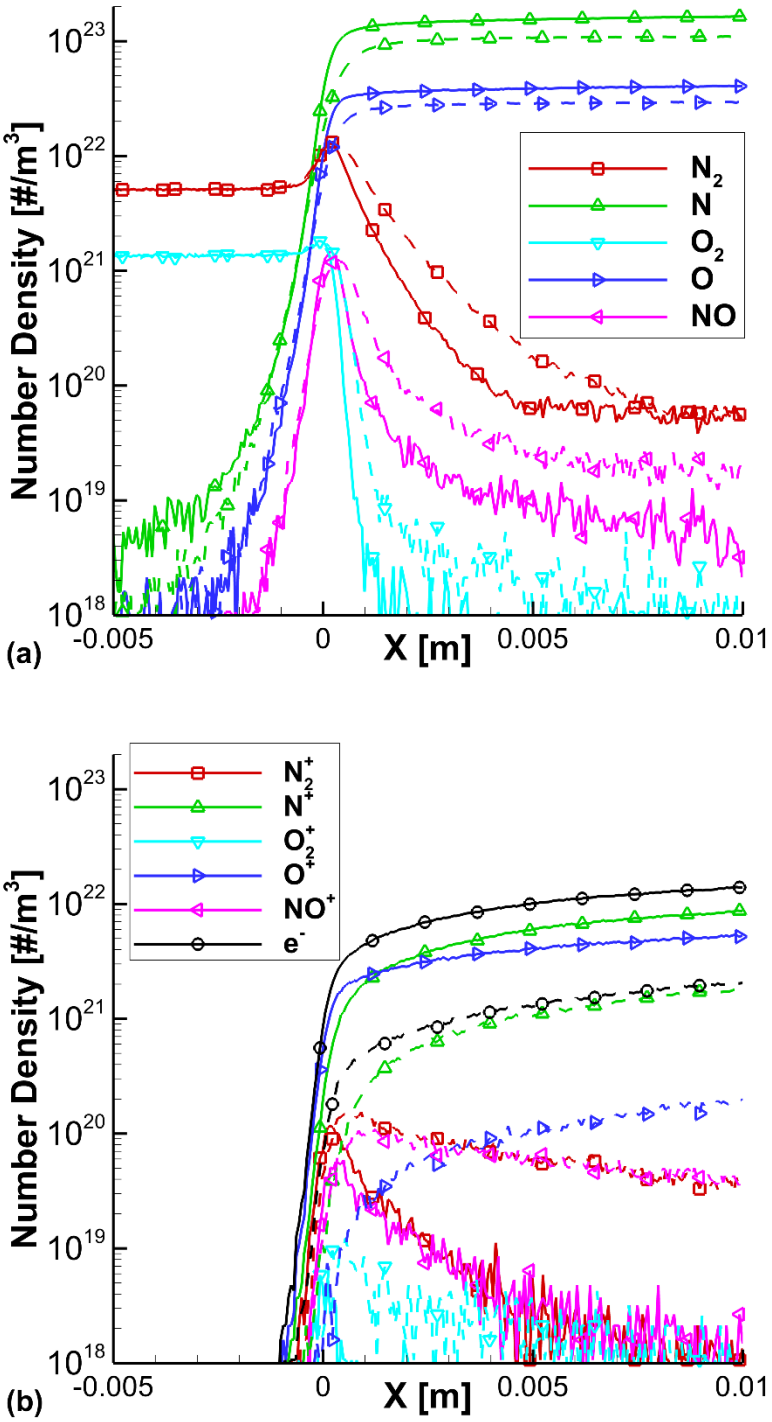
Number Density [#/m^3]
10^{23}
10^{22}
10^{21}
10^{20}
10^{19}
10^{18}
-0.005
0
0.005
0.01
X [m]
(a)
N_2
N
O_2
O
NO
N_2^+
N^+
O_2^+
O^+
NO^+
e^-
(b)

Figure 4.5

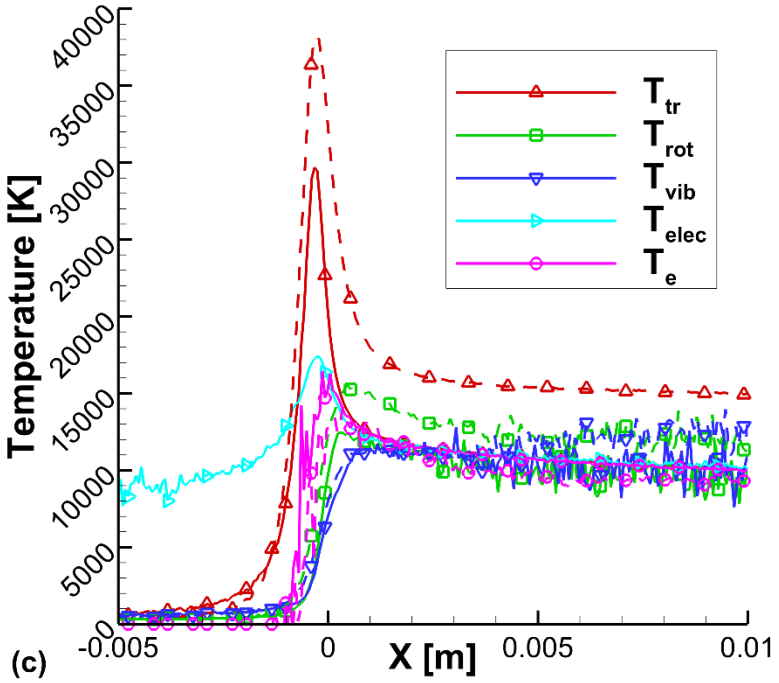

Figure 4.5 Simulation of EAST Shot 37 with (solid line) and without (dashed line) an electronic excitation model. *(a) Neutral particle number densities. (b) Charged particle number densities. (c) Bulk temperatures.*

CHAPTER 5

Preliminary Sensitivity Analyses

5.1 Overview

Now that nominal shock scenarios have been chosen, sensitivity analyses of the CHIPS input parameters are performed to investigate the influence of these input parameters on various important macroscopic quantities. Two preliminary sensitivity analyses are completed on CHIPS output data to identify models requiring improvement before a final sensitivity analysis can be performed with a linked CHIPS and radiative model. Much of the sensitivity analysis performed here is an extension of Strand's previous DSMC sensitivity analysis approach for 5-species air shocks [31]. The following sections detail the sensitivity analysis methodology and review the results of two separate analyses. The first sensitivity analysis is completed after the addition of an ionization model [4] and the second sensitivity analysis is performed following the inclusion of electronic excitation [51].

5.2 Methodology

5.2.1 Monte Carlo Sensitivity Analysis

In this dissertation, the physical system is investigated using a Monte Carlo global sensitivity analysis to rank the sensitivity of the DSMC simulation to each physical parameter. The sensitivity analysis reported in this research mimics a previous study

---

Higdon, K. J., Goldstein, D. B., and Varghese, P. L., "Sensitivity Analysis of Direct Simulation Monte Carlo Parameters for Ionizing Hypersonic Flows," *Journal of Thermophysics and Heat Transfer*, Vol. 32, No. 1, 2018, pp. 90-102.

Higdon, K. J., Goldstein, D. B., and Varghese, P. L., "Sensitivity Analysis of DSMC Parameters for an 11-Species Air Hypersonic Flow," *30th International Symposium on Rarefied Gas Dynamics*, AIP Conf. Proc. 1786, Victoria, B. C., July 2016.

D. B. Goldstein and P. L. Varghese supervised these projects and provided technical insight.

completed in Ref. [31] and much of the following methodology discussion is reiterated from Strand's work. Unlike a local sensitivity analysis where parameters are varied individually, a global sensitivity analysis varies multiple parameters simultaneously before each simulation to improve efficiency and investigate dependent relationships. Initially, the chosen simulation includes a set of nominal input parameters which have been determined by experiment, but also have some degree of uncertainty. Employing a Bayesian methodology, each parameter is assigned some prior probability that is determined by a combination of experimental uncertainty, alternate experimental results, and expert judgment. Considerations of parameters that have been extrapolated far from their experimental values or identifying physically incorrect quantities are examples where expert judgment is important. Typically, Gaussian or uniform prior distributions are applied to the nominal parameters. A Gaussian prior centered at the nominal value assumes that there is some confidence in its value. In contrast, a uniform prior assumes that there is no confidence in the nominal value.

Once prior distributions have been assigned, the parameter space is explored in a Monte Carlo fashion. All the input parameters are varied simultaneously as a large number of individual CHIPS simulations are performed in a global Monte Carlo sensitivity analysis. At the outset of each simulation, each parameter is independently varied by choosing a random value from its prior distribution. The simulation is completed using these chosen values and measurements of a specific quantity of interest (QoI) are recorded. Each simulation represents its own point in a (N+1)-dimensional parameter space where N is the number of input parameters and the final dimension of the N+1 space is the QoI. This QoI can be a scalar value or a set of vector values and is chosen to gauge the degree to which varying the input parameters affects the calculated result. The QoI is typically an output parameter that is experimentally measurable and

has a significant dependence on the physics of the simulation. Thus, from each point in parameter space a set of data are produced that includes the randomly selected parameter values and the QoI recorded from the simulation. After the Monte Carlo sampling is performed, the sensitivity of the QoI to each parameter is quantified. For a scalar QoI, a slice of the parameter space can be generated as a scatterplot of each parameter value vs. the QoI. An example of a sensitivity analysis scatter plot is shown in Fig. 5.1 where each point represents a completed simulation. In Fig. 5.1, the chosen QoI, translational temperature, responds to variations of an input parameter, the logarithm of the Arrhenius constant Λ. These scatterplots are used to examine the sensitivity of the QoI to each parameter through the calculation of the square of the Pearson correlation coefficient, r^2, and the mutual information, MI.

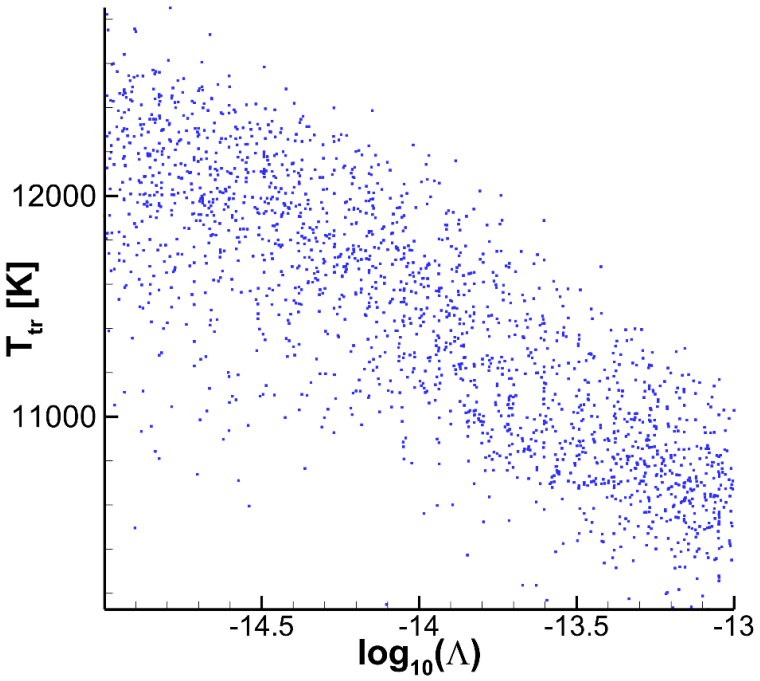

Figure 5.1 Scatterplot of a slice from the hypothetical parameter space where each point represents the results of a simulation.

5.2.2 Pearson Correlation Coefficient

The Pearson correlation coefficient is a measurement of the linear dependence of one variable upon another in a set of statistical points. In this dissertation, it will be used to quantify the dependence of the QoI upon each input parameter. Slices from the N+1 parameter space like the one shown in Fig. 5.1 are used to determine the correlation that a parameter has to a particular QoI. The correlation is calculated as

$$r = \frac{\sum_{i=1}^{N_{MC}}(X_i - \bar{X})(Y_i - \bar{Y})}{\sqrt{\sum_{i=1}^{N_{MC}}(X_i - \bar{X})^2}\sqrt{\sum_{i=1}^{N_{MC}}(Y_i - \bar{Y})^2}} \quad [5.1]$$

where N_{MC} is the number of Monte Carlo samples of the parameter space, X_i is the parameter value of the ith sample point, $\bar{X}$ is the mean of the parameter values, Y_i is the QoI value of the ith sample point, and $\bar{Y}$ is the mean of the QoI values. As the parameter value increases, the correlation, r, is positive if the QoI value increases or negative if the opposite is true. Only the overall sensitivity is important in this analysis so the square of the Pearson correlation coefficient, r^2, is used to rank the input parameters. The value of r^2 ranges from 0 to 1 where 0 corresponds to no linear relationship between the QoI and the input parameter and 1 corresponds to an exact linear dependence of the QoI to the input parameter. The most informative way to visualize the r^2 relationships is through a four-panel schematic reproduced from Strand's work [6]. Values of r^2 calculated from scatterplot projections of a sample simulation are shown in Fig. 5.2 using a hypothetical QoI and parameter value θ_1. The top left panel is an example of a dataset where r^2 approaches the lower limit of no correlation between the QoI and θ_1. The top right panel

exhibits dependence between the QoI and θ_1, but the value of r^2 is low because θ_1 has a much smaller effect on the QoI than other parameters in the simulation. In the bottom left panel, θ_1 has a strong enough effect on the QoI that the sensitivity of the QoI to other parameters is much smaller. The bottom right panel shows a correlation where the QoI is almost completely dependent on θ_1.

As mentioned earlier, the Pearson correlation coefficient is a linear measurement of the correlation between two quantities. Figure 5.3 demonstrates a case where there is a non-linear relationship between the QoI and θ_1. Even though there is quite clearly some dependence between the QoI and θ_1, the value of r^2 suggests no correlation is present between the QoI and θ_1. To capture the non-linearity of certain relationships a more sophisticated method to quantify sensitivity must be used.

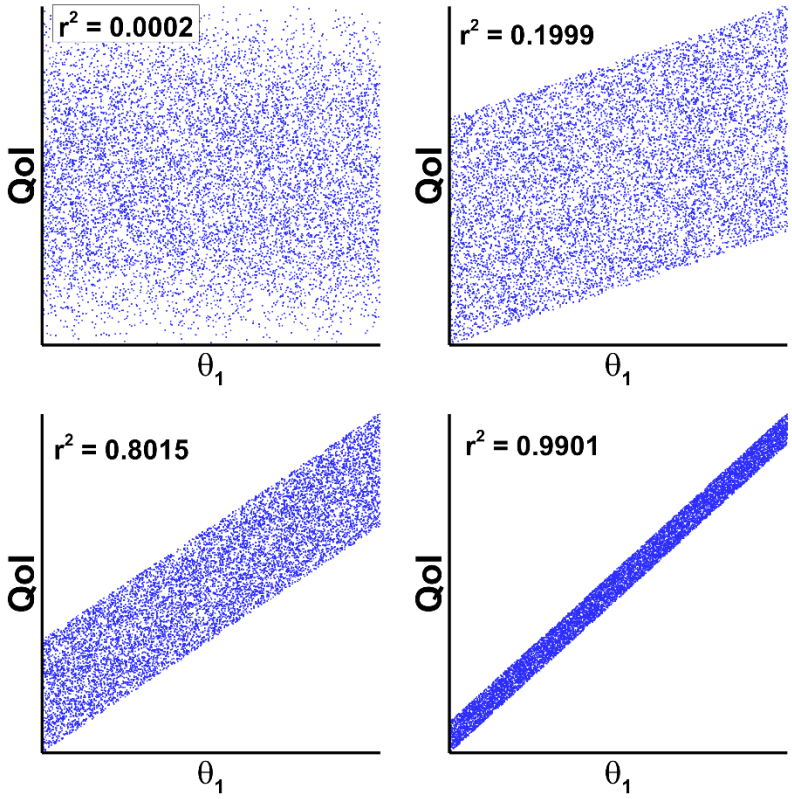

Figure 5.2 Scatterplots demonstrating various degrees of sensitivity to a parameter θ_1 for the square of the Pearson correlation coefficient. Sensitivities range from no relationship (top-left) to direct linear correlation (bottom-right).

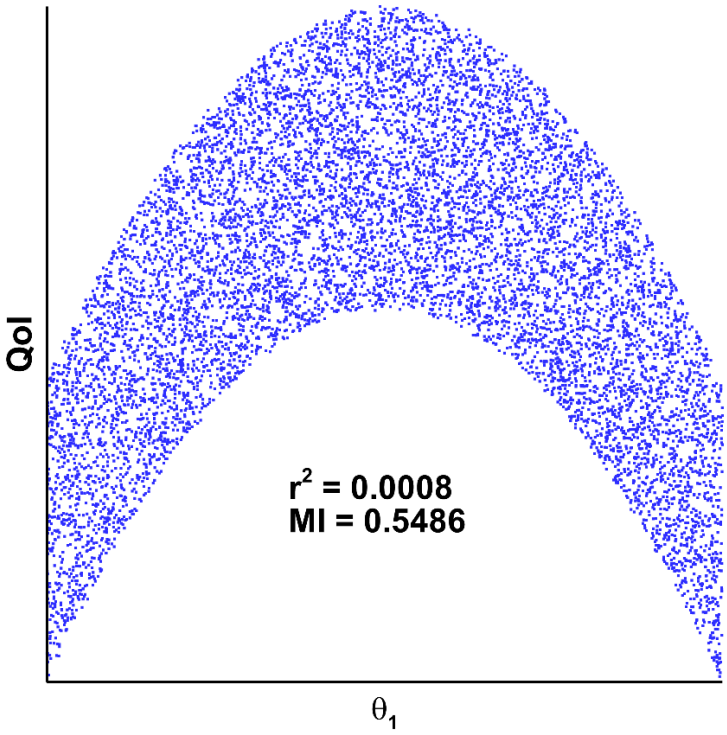

Figure 5.3 Scatterplot of a slice from a hypothetical parameter space where the dependence is non-linear.

5.2.3 Mutual Information

The mutual information is another measure of sensitivity used in this research and is superior to the square of the Pearson correlation coefficient in the sense that it can recognize non-linear correlations as shown in Fig. 5.3. The mutual information quantifies the difference between the joint probability distribution and the probability distribution when the QoI and parameter are assumed to be independent [52]. The mutual information between the QoI and a parameter value θ_1 is calculated as

$$MI = \int_{\theta_1} \int_{QoI} p(\theta_1, QoI) \left[ln \left(\frac{p(\theta_1, QoI)}{p(\theta_1) p(QoI)} \right) \right] d(QoI) d\theta_1 \qquad [5.2]$$

where $p(\theta_1, QoI)$ is the joint probability distribution function (PDF), $p(QoI)$ is the marginal PDF of the QoI, and $p(\theta_1)$ is the marginal PDF of the parameter. Since the mutual information also considers non-linear relationships, a value of zero guarantees that the parameter and the QoI are independent. The process to calculate the mutual information is shown in Figs. 5.4-5.7 following the work of Steuer et al. [53] and reproducing the schematics created by Strand [6].

First, the data are normalized so that they have a mean of zero and a standard deviation of one. These data are then divided into bins as in Fig. 5.4 and the number of data points in each bin are counted. Next, the 2-dimensional joint PDF is calculated using this histogram bin method by comparing the number of data points in each bin to the total number of data points. The 1-dimensional marginal PDF's for the QoI and parameter are calculated from the 2-dimensional joint PDF as shown in Fig. 5.5. These PDF's are then combined to create a hypothetical 2-dimensional joint PDF where the QoI is independent of the parameter (Fig. 5.6). Finally, as in the integrand of Eqn. 5.2, the joint PDF is combined with the hypothetical independent PDF. From the plot of the resulting mutual information in Fig. 5.7, the contributions of both the joint and independent PDFs are obvious. To compute a single value for the mutual information, the combined PDF is integrated over the parameter and QoI values.

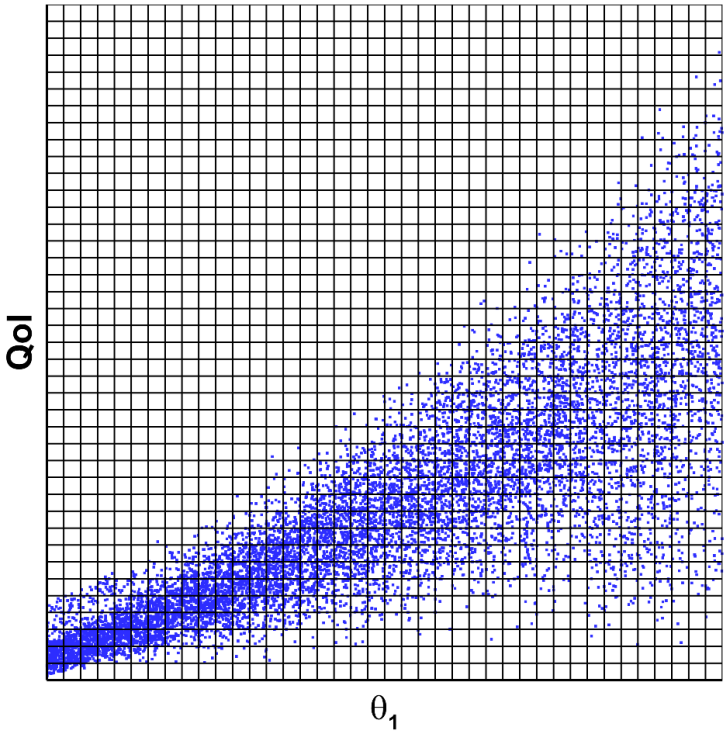

Figure 5.4 Histogram binning of a hypothetical Monte Carlo sensitivity analysis.

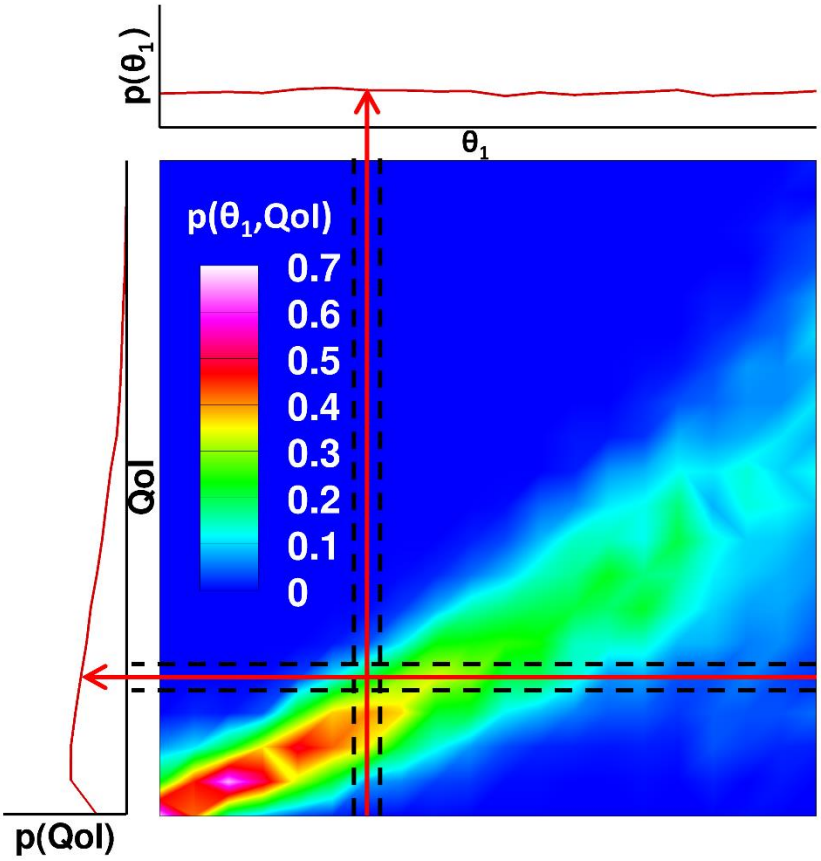

Figure 5.5 The 2-dimensional joint PDF calculated from the normalized scatterplot data is used to find the θ_1 and QoI marginal PDF's by integrating across each axis.

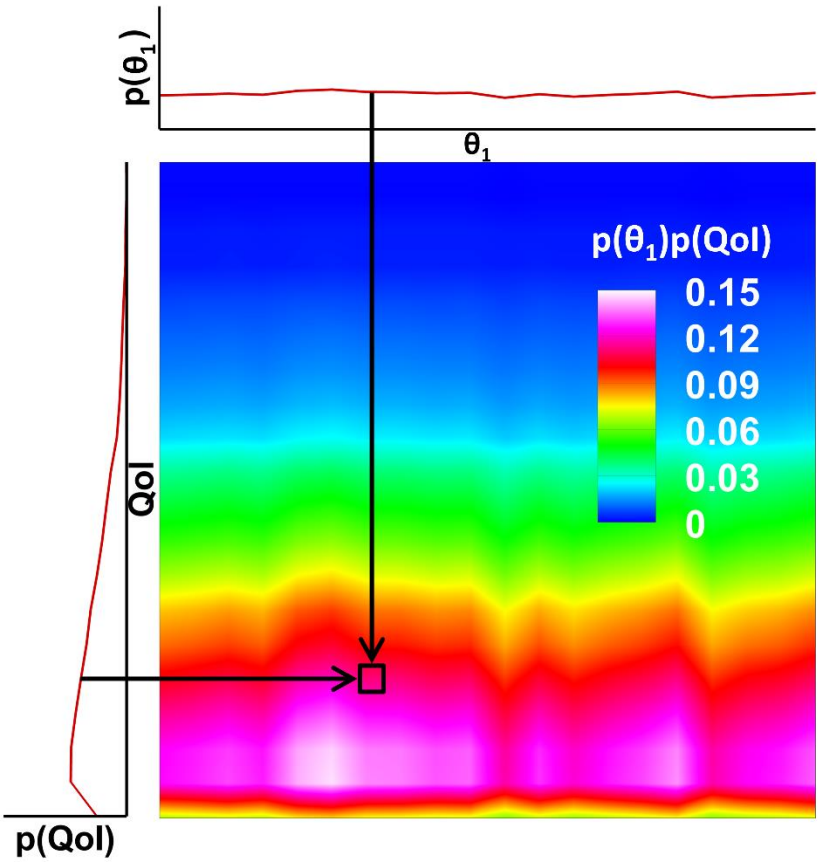

Figure 5.6 Creation of the 2-dimensional independent PDF by multiplication of the θ_1 and QoI marginal PDF's.

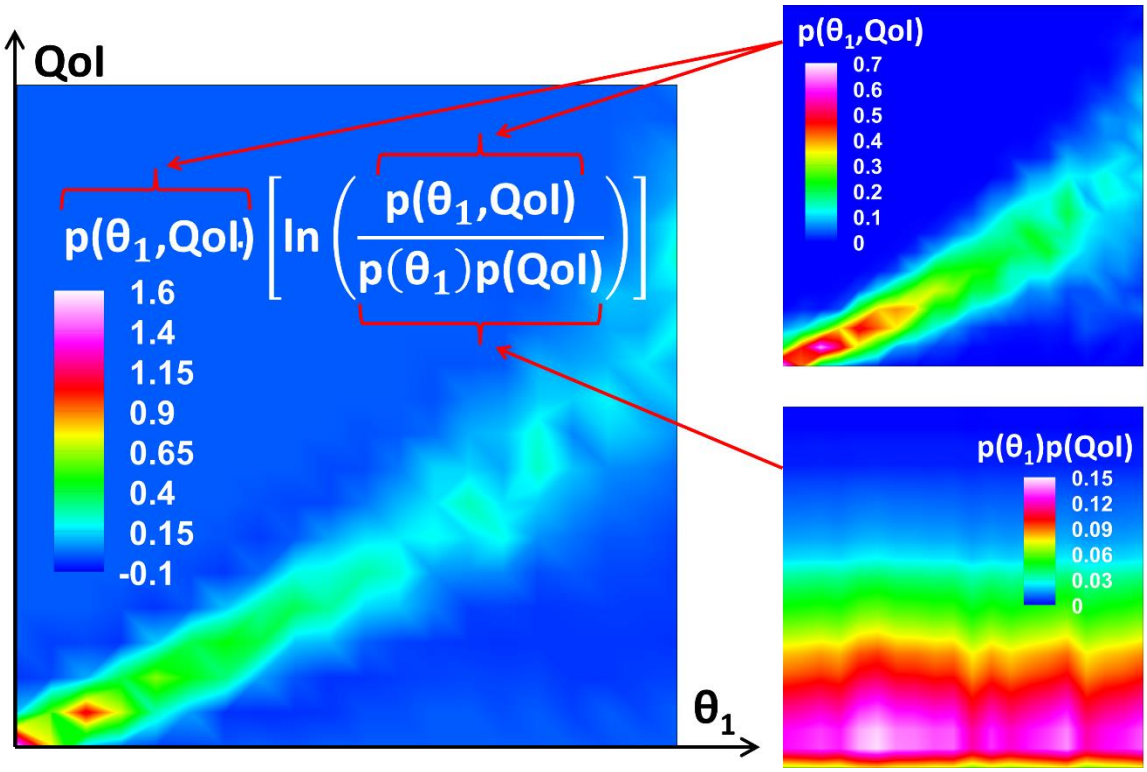

Figure 5.7 Visualization of the discrete mutual information points by combining the joint and independent PDF's where integration over this 2-dimensional space results in a single value for the mutual information.

5.2.4 Overall Sensitivity

These measures of sensitivity allow the input parameters to be ranked for a single QoI, but in shock simulations the QoI is typically a set of values as a function of distance from the shock front. As an illustrative example, consider the results of a sensitivity analysis where the translational temperature, T_{tr}, is recorded as the QoI. The colored lines in Figure 5.8a plot the results of T_{tr} as a function of distance from the shock for a large number of completed simulations. If a single location in x is chosen, the T_{tr} results of each simulation can be viewed as a function of each input parameter in a scatter plot. Following line (1), Fig. 5.8b shows this scatter plot where the input parameter on the x-

axis represents the logarithm of some reaction rate. The Pearson correlation coefficient is then calculated for this point and, following line (2) to Fig. 5.8c, this process can be repeated for each point in the x domain. When the QoI is a vector that varies over a specified domain, an overall sensitivity value is desired to rank the sensitivity of the QoI to each input parameter. To reduce the contributions of each point in the domain to a single overall sensitivity value, r^2 and MI values are first weighted by the variance of the QoI at each point. The variance for the example is represented in Fig. 5.8a by the black line. When the variance is multiplied by the Pearson correlation coefficient at each point, Fig. 5.8d is created (following lines (3a) and (3b)). This variance weighted sensitivity is then integrated over the entire domain to obtain a single overall sensitivity value [31]. From this integrated overall sensitivity value, a final ranking of the sensitivity of the QoI to each input parameter can be compiled and input parameters are compared in a bar chart where the overall sensitivities of the input parameter set are normalized by the highest value.

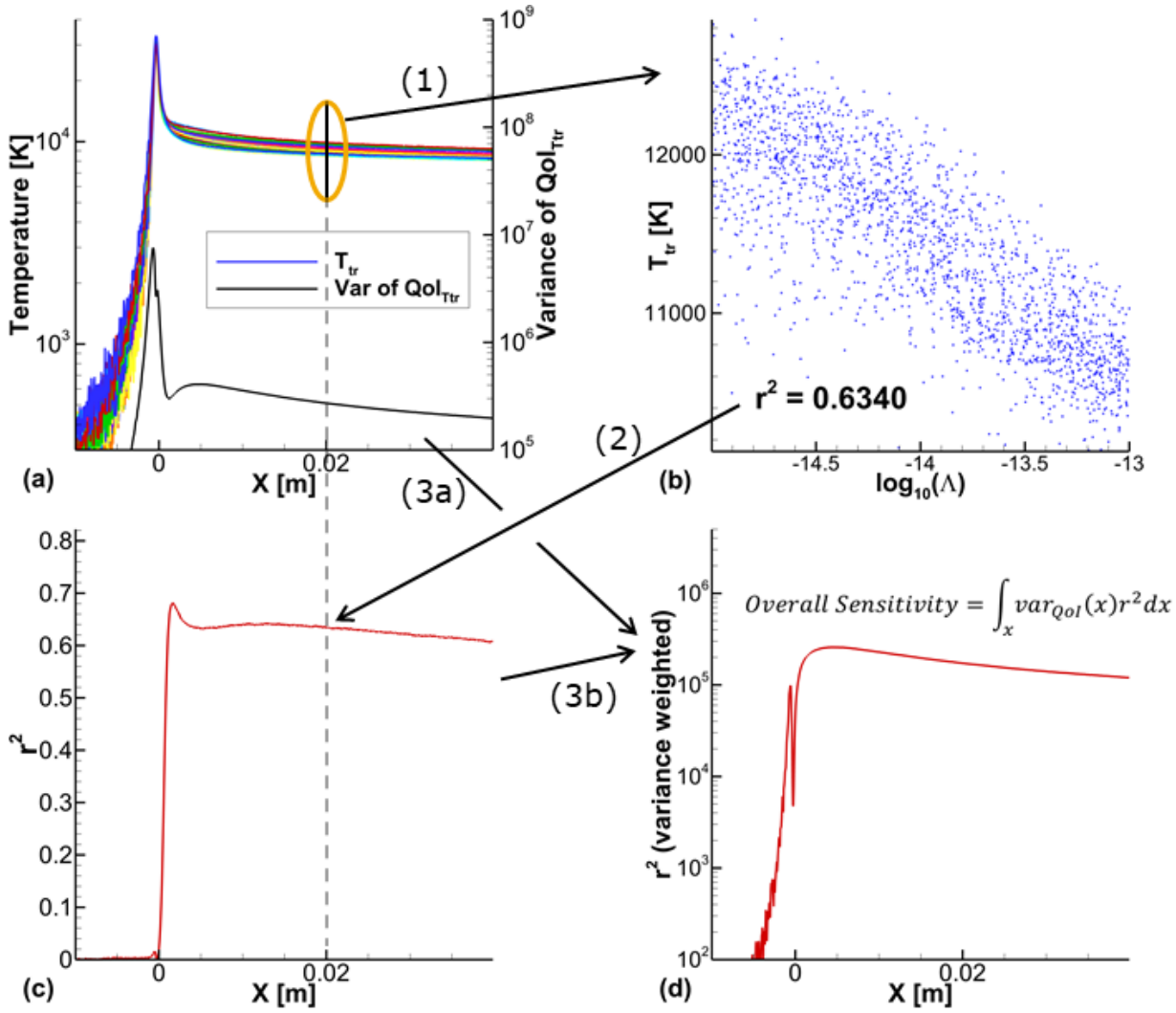

Figure 5.8 Map depicting the steps required to calculate an overall sensitivity value from the results of a global sensitivity analysis.

5.3 Sensitivity Analysis Study #1

A sensitivity analysis of the input reaction rates was performed based upon the nominal shock scenario #1 CHIPS simulation of the EAST Campaign 47, Shot 37 experiment discussed in the previous chapter (Section 4.2). This first sensitivity analysis is completed with charged particle collisions and chemical reactions, but without the

inclusion of the electronic excitation model. While the electronic excitation showed was shown in the previous chapter to be necessary, the completion of this sensitivity analysis occurred before the addition of the electronic excitation model. This preliminary study examines how the sensitivity analysis results can be interpreted and presented. It also serves as an investigation of the influence of ionization and charged particle interactions on the considered QoIs. Strand determined, in a previous sensitivity analysis, that the QoIs demonstrate a far greater sensitivity to the reaction rates than the other DSMC input parameters, therefore, these are the only parameters considered in this sensitivity analysis [6]. The sensitivity to each of the 53 reactions listed in Tables 3.2, 3.4, and 3.5 was considered by assigning a uniform prior distribution to the Arrhenius pre-exponential constant (A) over a range of plus/minus an order of magnitude. A uniform function is chosen as the prior distribution because there is little confidence in the reaction rate parameters and only epistemic uncertainties are considered. For the high temperatures experienced in the EAST simulation, these reaction rates are utilized far from their calibrated values. Of the three Arrhenius reaction rate parameters (Eqn. 2.4), the pre-exponential constant is the sole Arrhenius parameter chosen for study. The activation energy is considered reasonably well known and the constraints of the temperature exponent in the TCE chemistry model cause challenges to ensuring correctly modeled reaction rates. These challenges are explored thoroughly in Chapter 7. For each simulation instance in the sensitivity analysis, a random value for every forward reaction rate is chosen from its uniform prior. If a reaction rate from Tables 3.2, 3.4, or 3.5 has a backwards reaction rate listed, the randomly selected forward reaction rate is used to calculate the backward reaction rate from the equilibrium constant established by the ratio of the nominal forward and backward rates. In this way, 1,920 simulations of the Shot 37 conditions were performed with each simulation representing its own random

point in parameter space. While approximately 2,000 simulations are hardly enough data points to properly converge the sensitivity of every input parameter, the goal of this dissertation is to identify the top five or so most important input parameters. As discussed in Strand's sensitivity study of a lower speed 1D shock, these input parameters tend to separate themselves from the less important parameters even when substantially fewer simulations are completed [6]. Due to the computational cost of the sensitivity study, a less than optimal number of simulations must be performed. Each one of these simulations took approximately 36 minutes on 128 processors totaling 147,456 computer hours for the entire sensitivity analysis.

Results were obtained for several choices of the QoI, but here the focus is on the translational temperature, electron density, atomic nitrogen density, and atomic oxygen density. The translational temperature was chosen because its value is an important indicator of the type of chemistry expected to be present in a shock wave. The electron, N, and O densities were selected as candidate QoIs since they play key roles in the calculation of the radiation intensity that the shock wave produces. Previous analysis of the radiative heating by Johnston showed that the atomic line transitions of N and O contribute a significant portion of the radiative heat flux to the CEV [54]. In the EAST campaign, spatially and spectrally resolved shock layer radiance measurements were obtained for each experiment [2]. Since these data are a viable candidate for a calibration of DSMC input parameters, the QoIs are chosen to be closely related to a future calculation of radiative spectra. More specifically, EAST data for Shot 37 are available for the spectrally integrated radiative intensity for the 772-782 nm wavelength range as a potential calibration metric [32]. This range is dominated by the atomic oxygen triplet radiation and for this reason, the atomic oxygen density sensitivity is an important indication of reaction rates which are critical to a calibration to this feature. In the

following discussion of the sensitivity analysis, all four of these QoIs are actually vectors with the sensitivity of each reaction rate measured at multiple locations through the shock. The QoIs are tabulated at 1001 points uniformly spaced from 1 cm upstream of the shock to 4 cm downstream of the shock. This range was chosen to be within the distance that radiative intensity was measured during the Shot 37 experiment so that a future sensitivity analysis can be performed on radiative quantities. A single sensitivity value is obtained from this vector by integrating the variance weighted sensitivities and ranking each of the reaction rates using both the square of the Pearson correlation coefficient and the mutual information as described in the previous section.

5.3.1 Quantity of Interest: Translational Temperature

The first QoI investigated in the simulation of the EAST Shot 37 was the translational temperature. After calculating the square of Pearson correlation coefficient (r^2) and the mutual information (MI), Fig. 5.9 shows the sensitivity values of the five most sensitive reactions as a function of their x-location relative to the shock wave. The reactions listed in the legend of Fig. 5.9 are ordered by overall sensitivity. This type of plot is useful for understanding where $QoI_{T_{tr}}$ is sensitive to certain reaction rates in relation to the shock. As expected, the translational temperature is initially sensitive to the $N_2 + N_2 \rightleftharpoons N + N + N_2$ reaction as the nitrogen molecules begin to dissociate. Once atomic nitrogen begins to appear, the translational temperature is much more sensitive to the $N_2 + N \rightleftharpoons N + N + N$ reaction rate until most of the N_2 has dissociated. Further downstream, the translational temperature as it relaxes to equilibrium is sensitive to the $N + NO^+ \rightleftharpoons N^+ + NO$, $N + O \rightleftharpoons NO^+ + e^-$, and $N + N \rightleftharpoons N_2^+ + e^-$ reactions as ionization becomes a dominant process. The associative ionization reactions, $N + O \rightleftharpoons NO^+ + e^-$ and $N + N \rightleftharpoons N_2^+ + e^-$, are the source of the initial electrons and this process continues

downstream. For the high temperatures produced by the EAST shock tube, it was expected that the electron impact ionization reaction, $N + e^- \rightleftharpoons N^+ + e^- + e^-$, would occur frequently downstream of the shockwave. As identified previously by Park, this reaction should become increasingly important at high temperatures as the density of free electrons grows [44]. It could be inferred that the translational temperature should have the greatest sensitivity to these reactions in the downstream region, but this is not the case. Instead, $QoI_{T_{tr}}$ is most sensitive to the charge exchange reaction, $N + NO^+ \rightleftharpoons N^+ + NO$. To completely understand this result, the electron density QoI must be analyzed. This is the subject of the following section.

When comparing the r^2 and MI sensitivities for each reaction rate in Fig. 5.9, it is clear that the shapes of the curves are similar for most of the reactions. In addition, the ranking of the sensitivities at each x-location is nearly identical for either method of calculating the sensitivity. Although the magnitudes of r^2 and MI are similar in Fig. 5.9, typically these two methods are not expected to have comparable values. Figure 5.10 shows the variance weighted r^2 as a function of the distance from the shock location. A single overall sensitivity value is obtained following the previously established method that is used to rank the reaction rate sensitivities. The results of this ranking are shown in Fig. 5.11. The MI is not shown in Fig. 5.10 as it is qualitatively identical to r^2 and will not be plotted in these types of figures for the remainder of this dissertation, but the MI will continue to be represented in the overall sensitivity rankings for each QoI studied.

Even though the $N_2 + N \rightleftharpoons N + N + N$ reaction has a much higher peak than all other reactions in Fig. 5.10, the overall sensitivity in Fig. 5.11 is not much higher than the $N + NO^+ \rightleftharpoons N^+ + NO$ reaction. This is explained by considering the entire range of the variance weighted sensitivities. The dissociation reaction may have a much larger peak magnitude within the center of the shock, but its high sensitivity is short lived. The

charge exchange reaction does not have a large variance weighted sensitivity at any one x-location, but it is consistently the most sensitive parameter for much of the downstream portion. Care must be taken when analyzing these plots not to draw inappropriate conclusions based on relative sensitivities at a single x-location.

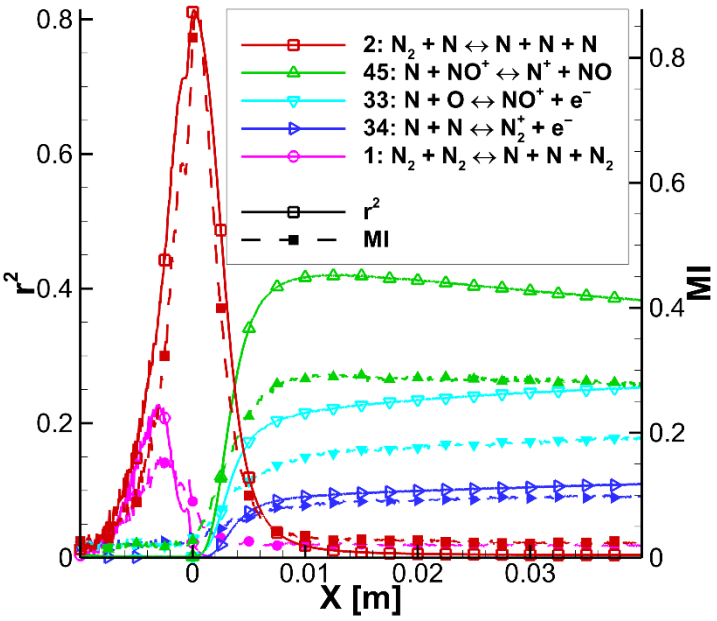

Figure 5.9 r^2 and MI sensitivities of the five most sensitive reaction rates when the translational temperature is the QoI ($QoI_{T_{tr}}$).

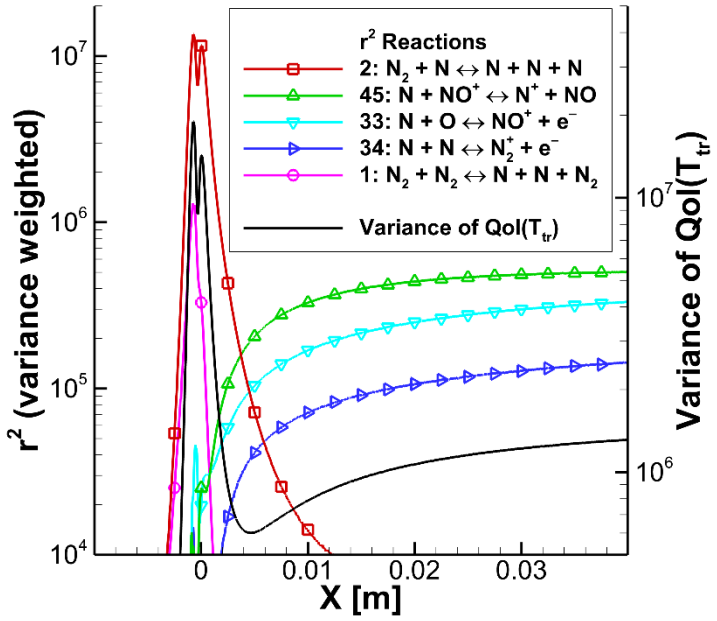

Figure 5.10 Variance weighted r^2 sensitivities of the five most sensitive reaction rates for $QoI_{T_{tr}}$, and the variance at each x-location for $QoI_{T_{tr}}$.

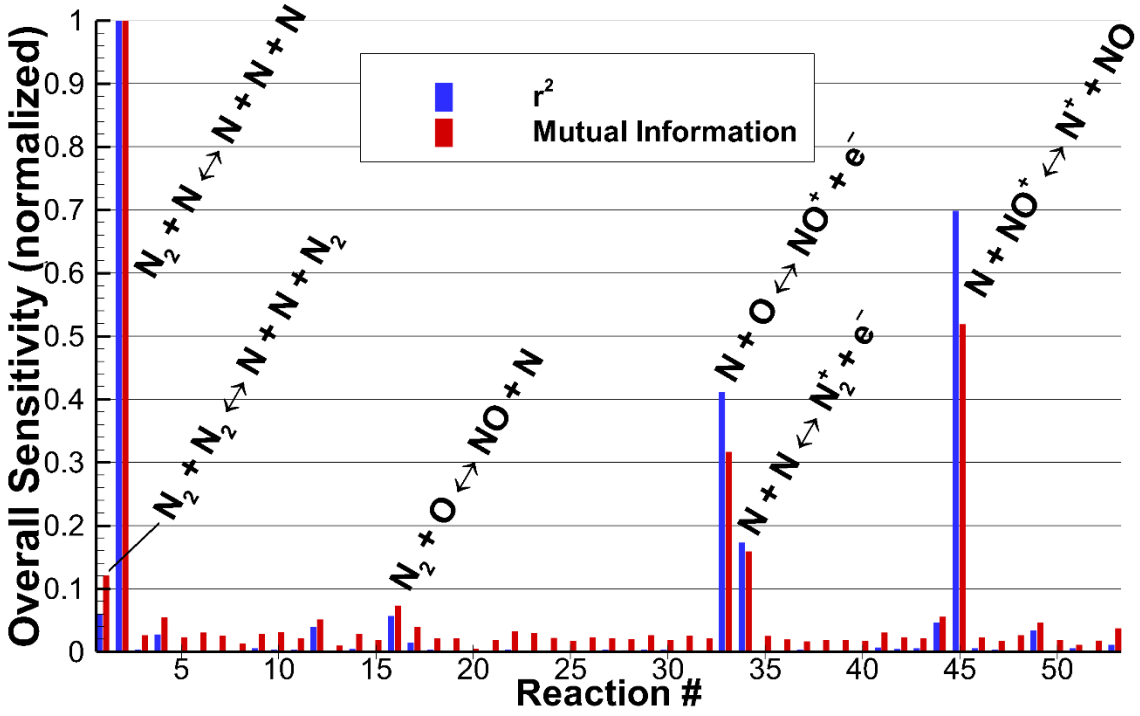

Figure 5.11 Normalized r^2 and MI overall, variance weighted sensitivities for $QoI_{T_{tr}}$.

5.3.2 Quantity of Interest: Free Electron Density

The electron density QoI provides a clearer description of the processes that result in the high sensitivity to the $N + NO^+ \rightleftharpoons N^+ + NO$ charge exchange reaction. Figure 5.12 maps the reaction progression which can be followed to demonstrate the importance of the $N + NO^+ \rightleftharpoons N^+ + NO$ reaction. In Fig. 5.13, the associative ionization reactions initially have the highest sensitivity, but this is short lived. After the first free electrons are formed by the associative ionization reactions $N + O \rightleftharpoons NO^+ + e^-$ and $N + N \rightleftharpoons N_2^+ + e^-$, both the forward and backward rates of these reactions are high enough that electrons are quickly created and then captured (#1 and #2 in Fig. 5.12). In order to prevent free electrons from being easily recaptured by the produced ions, the molecular ion products,

NO^+ and N_2^+, of the associative ionization reactions must be converted into other species through reactions. At the downstream conditions, the charge exchange reaction with the highest rate is $N + NO^+ \rightleftharpoons O + N_2^+$ (#3). This reaction only converts one associative ionization product into the other and therefore, does not stabilize the free electrons. The charge exchange reaction with the second fastest rate is $N + NO^+ \rightleftharpoons N^+ + NO$ (#4). Since the forward reaction converts NO^+ to N^+, the resulting NO quickly dissociates and the N^+ ion does not readily capture free electrons at these conditions, free electrons can be stabilized through this process. For this reason, the $N + NO^+ \rightleftharpoons N^+ + NO$ reaction has the greatest effect in the downstream region and QoI_{n_e} has the highest sensitivity to it. When comparing the variance weighted r^2 values in Fig. 5.14 to the raw values in Fig. 5.13, it is noticeable that the spike feature slightly upstream of the shock location is missing in Fig. 5.14. This feature disappears in Fig. 5.14 when the raw r^2 results are multiplied by the variance of the free electron density since the variance is low in the upstream region. This means that, while QoI_{n_e} in this region has an acute sensitivity to the associative ionization reactions, this sensitivity is minor compared to the sensitivity of QoI_{n_e} in the post-shock region.

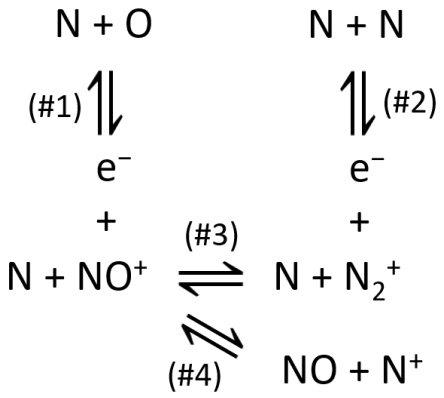

Figure 5.12 Reaction map demonstrating the importance of the $N + NO^+ \rightleftharpoons N^+ + NO$ charge exchange reaction to the free electron density.

Looking at the bar chart in Fig. 5.15 of the overall sensitivities, the results are unsurprising considering the previous analysis. As expected, the free electron density is sensitive to reaction $N + O \rightleftharpoons NO^+ + e^-$ and $N + N \rightleftharpoons N_2^+ + e^-$ as these reactions produce the first free electrons from the high concentration of atomic species behind the shock. Unexpectedly, QoI_{n_e} has almost no sensitivity to the electron impact ionization reaction $N + e^- \rightleftharpoons N^+ + e^- + e^-$. This supports the hypothesis that the flow is not hot enough and free electrons do not have a high enough energy to begin the electron cascade. In addition, the absence of an electronic excitation model restricts nitrogen atoms from accumulating electronic energy through electron impact excitation.

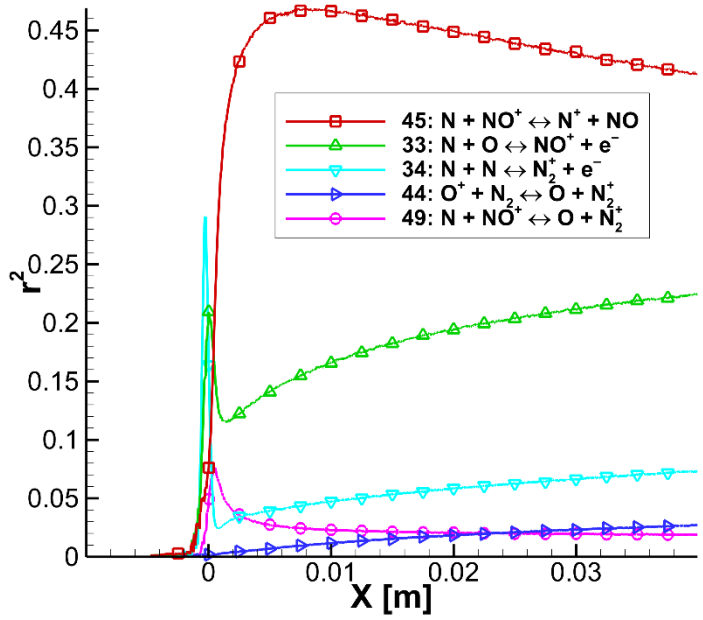

Figure 5.13 r^2 sensitivities of the five most sensitive reaction rates when the electron density is the QoI (QoI_{n_e}).

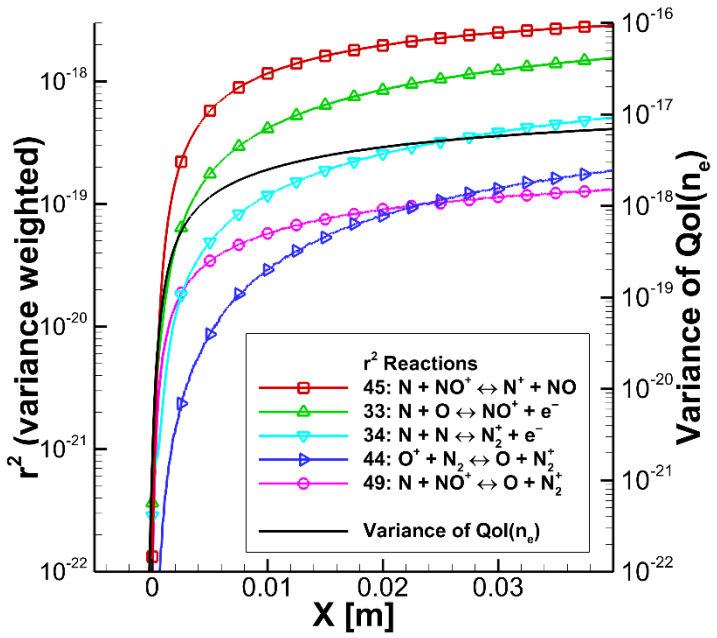

Figure 5.14 Variance weighted r^2 sensitivities of the five most sensitive reaction rates for QoI_{n_e}, and the variance at each x-location.

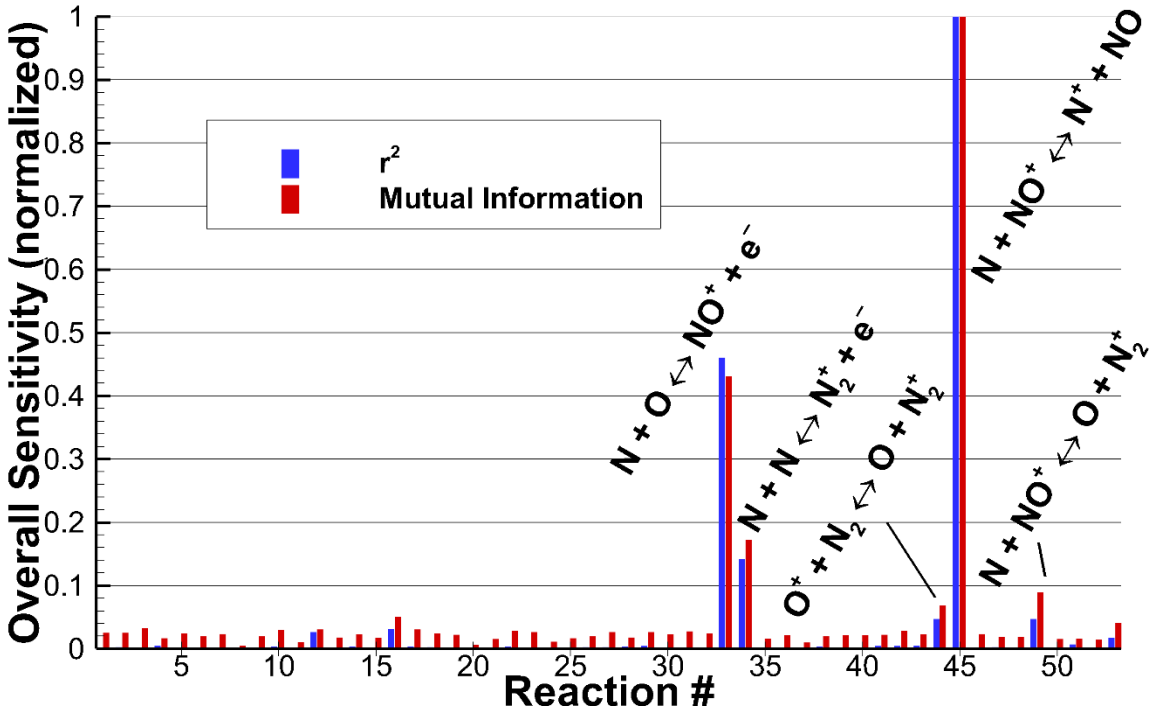

Figure 5.15 Normalized r^2 and MI overall, variance weighted sensitivities for QoI_{n_e}.

5.3.3 Quantity of Interest: Atomic Nitrogen Density

The next QoI considered is the density of atomic nitrogen. Since atomic line radiation is a large portion of the radiative heat flux, it is important to future calibrations to identify the reactions to which the atomic nitrogen density is sensitive. Figure 5.16 presents the top five reactions that QoI_{n_N} is sensitive to as a function of their x-location, Fig. 5.17 shows the variance weighted results, and Fig. 5.18 ranks the overall sensitivity of each reaction. Initially, the production of N by dissociation is the most sensitive reaction and further downstream, the ionization reactions discussed above take hold. The double hump in the sensitivity of the $N_2 + N \rightleftharpoons N + N + N$ dissociation reaction in Fig. 5.16 should be noted. Near the shock, the r^2 line reaches zero between the humps. In

actuality, this is occurring where the Pearson correlation coefficient, r, is crossing the x-axis from negative to positive or, in other words, switching from a negative correlation to a positive correlation. It turns out that the first hump is negligible when calculating the overall sensitivity and this is evident in Fig. 5.17 as the variance of QoI_{n_N} is low in this region. On the other hand, the mutual information approaches, but never reaches zero since the MI can never be negative. The MI value for $N_2 + N \rightleftharpoons N + N + N$ is much higher than calculated by r^2 when comparing the two measurements in Fig. 5.18. This may be occurring because the mutual information can capture nonlinearities in the correlation and/or the sensitivity of QoI_{n_N} to $N_2 + N \rightleftharpoons N + N + N$ is higher relative to the other reactions over the entire domain. Typically, minor differences in overall sensitivity of QoI_{n_N} between r^2 and MI are largely artifacts of the normalization scheme, but in this case the ranking of the overall sensitivities changes. A significant change in the ranking, such as seen with $N_2 + N \rightleftharpoons N + N + N$ in Fig. 5.18 is an indicator of possible non-linearity captured by the mutual information.

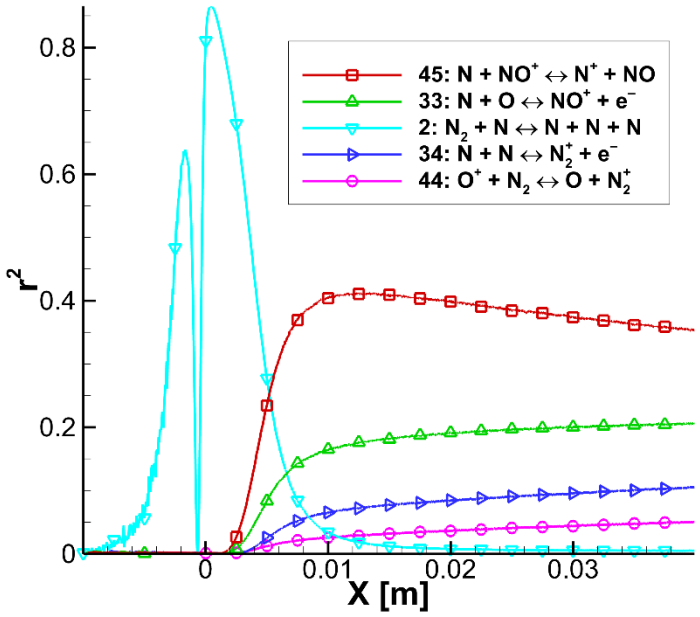

Figure 5.16 r^2 sensitivities of the five most sensitive reaction rates when the atomic nitrogen density is the QoI (QoI_{n_N}).

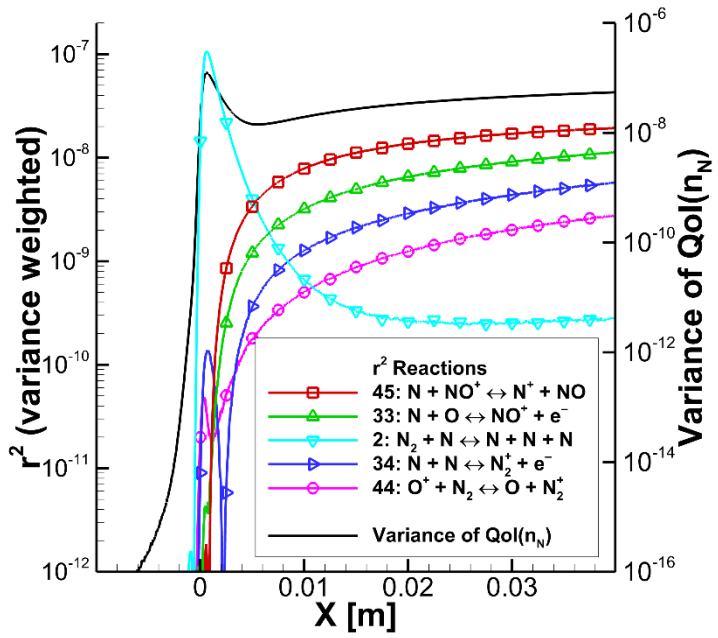

Figure 5.17 Variance weighted r^2 sensitivities of the five most sensitive reaction rates for QoI_{n_N}, and the variance at each x-location.

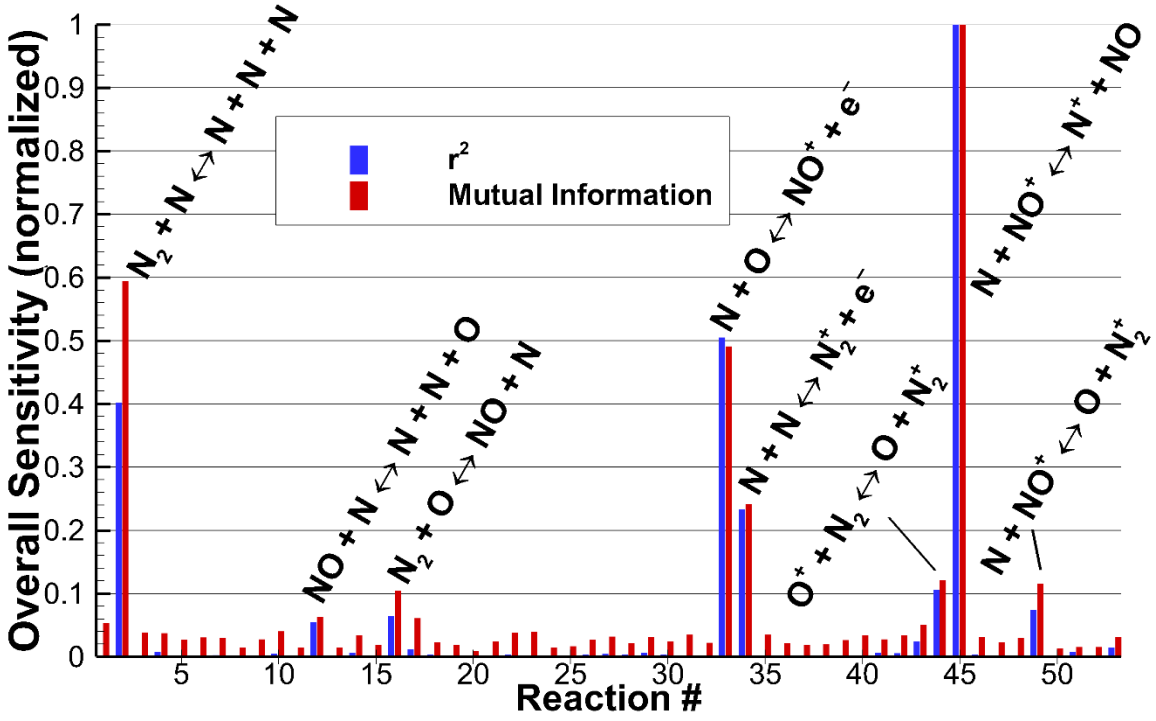

Figure 5.18 Normalized r^2 and MI overall, variance weighted sensitivities for QoI_{n_N}.

5.3.4 Quantity of Interest: Atomic Oxygen Density

The final QoI studied was the atomic oxygen density and the results are shown in Figs. 5.19-5.21. This sensitivity analysis also raises the same questions as the previous QoIs. Again, reactions $N + NO^+ \rightleftharpoons N^+ + NO$ and $N + O \rightleftharpoons NO^+ + e^-$ largely outweigh the sensitivities of the other reactions downstream of the shock. It is more interesting in this case to look at the r^2 sensitivity as a function of x in Fig. 5.19. In the shock region, the production of atomic oxygen relies heavily on the dissociation of nitrogen. The atomic nitrogen produced from dissociation then reacts with the diatomic oxygen molecules to produce NO and O. Notice how $N_2 + N \rightleftharpoons N + N + N$ again dips down to zero where the value of r crosses the x-axis at this point.

In order to obtain a better understanding of the reaction sensitivities in the active shock region, the sensitivity calculation was repeated for a modified x-range that only included the active shock region. Figures 5.22-5.24 show the sensitivities as a function of x-location from within the shock and the overall ranking of the sensitivities for this shortened region. As expected, QoI_{n_O} is most sensitive to $N_2 + N \rightleftharpoons N + N + N$ dissociation reaction near the shock. Surprisingly, the $O_2 + N \rightleftharpoons NO + O$ exchange reaction becomes the third most important reaction in this region. In addition, this reaction's sensitivity conveniently fills the gap in the $N_2 + N \rightleftharpoons N + N + N$ reaction's hump in Fig. 5.22. Even though this reaction is important for the shock region, it has a relatively small effect on any of the downstream results. For this reason, reaction $O_2 + N \rightleftharpoons NO + O$ is not a major factor in the overall sensitivity when the entire sensitivity analysis range is considered.

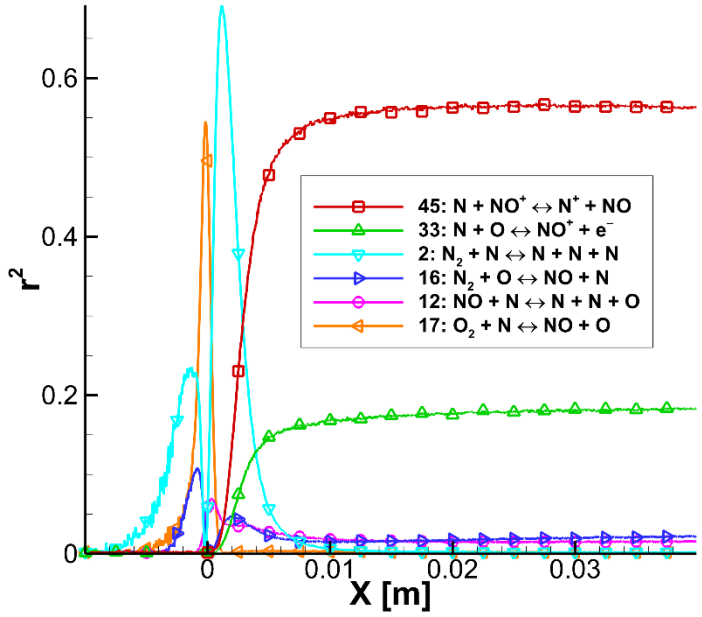

Figure 5.19 r^2 sensitivities of the six most sensitive reaction rates and reaction #17 when the atomic oxygen density is the QoI (QoI_{n_O}).

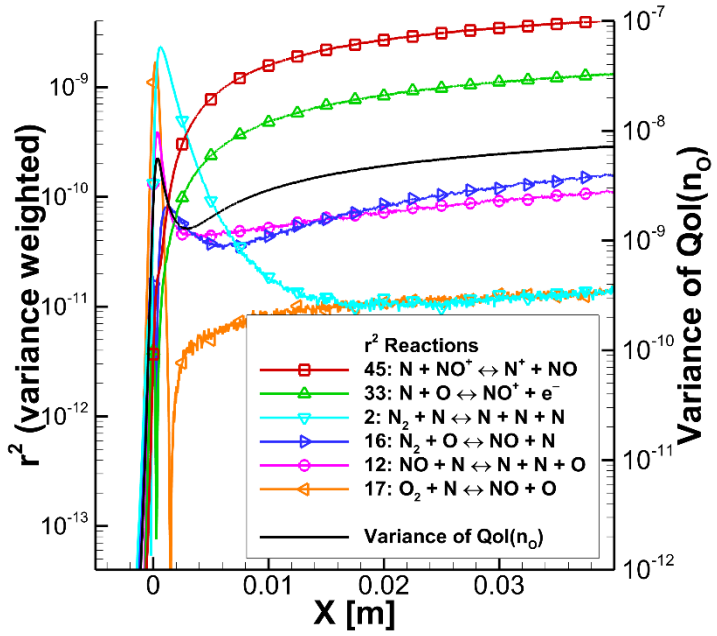

Figure 5.20 Variance weighted r^2 sensitivities of the six most sensitive reaction rates and reaction #17 for QoI_{n_O}, and the variance at each x-location.

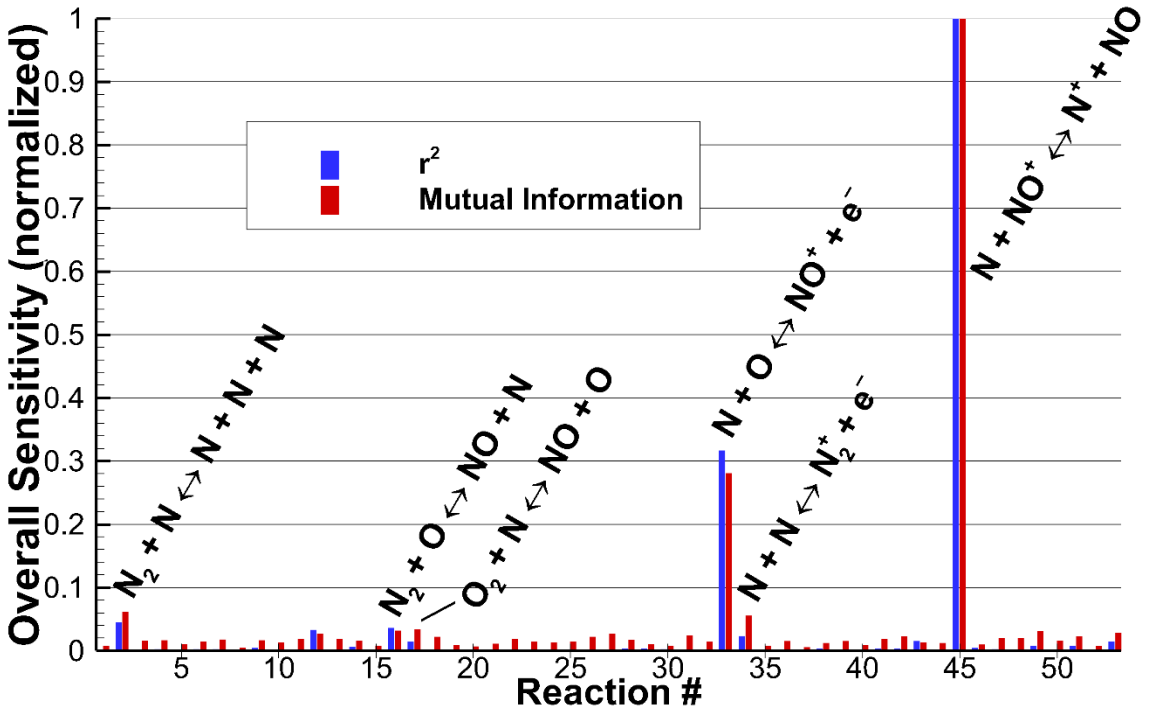

Figure 5.21 Normalized r^2 and MI overall, variance weighted sensitivities for QoI_{n_o}.

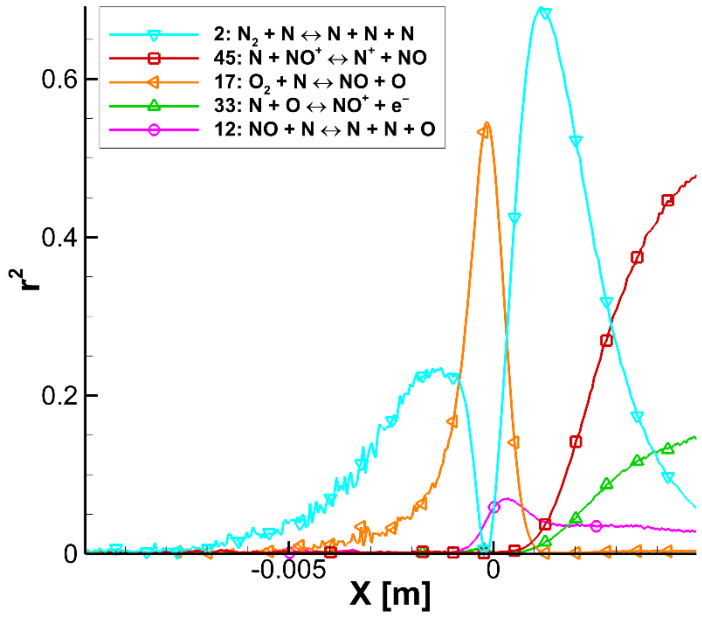

Figure 5.22 r^2 sensitivities of the five most sensitive reaction rates when QoI_{n_O} is defined over a modified range of x, concentrating in the active shock region.

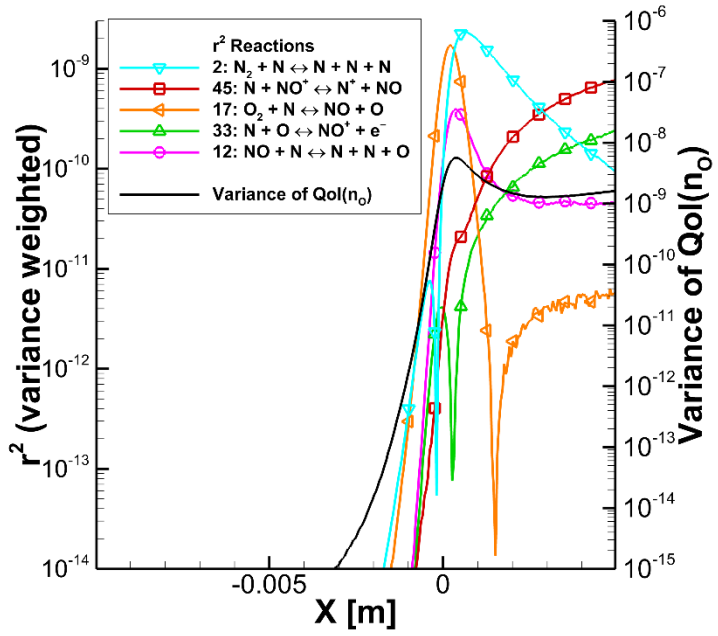

Figure 5.23 Variance weighted r^2 sensitivities of the five most sensitive reaction rates for QoI_{n_O}, and the variance at each x-location for the modified domain.

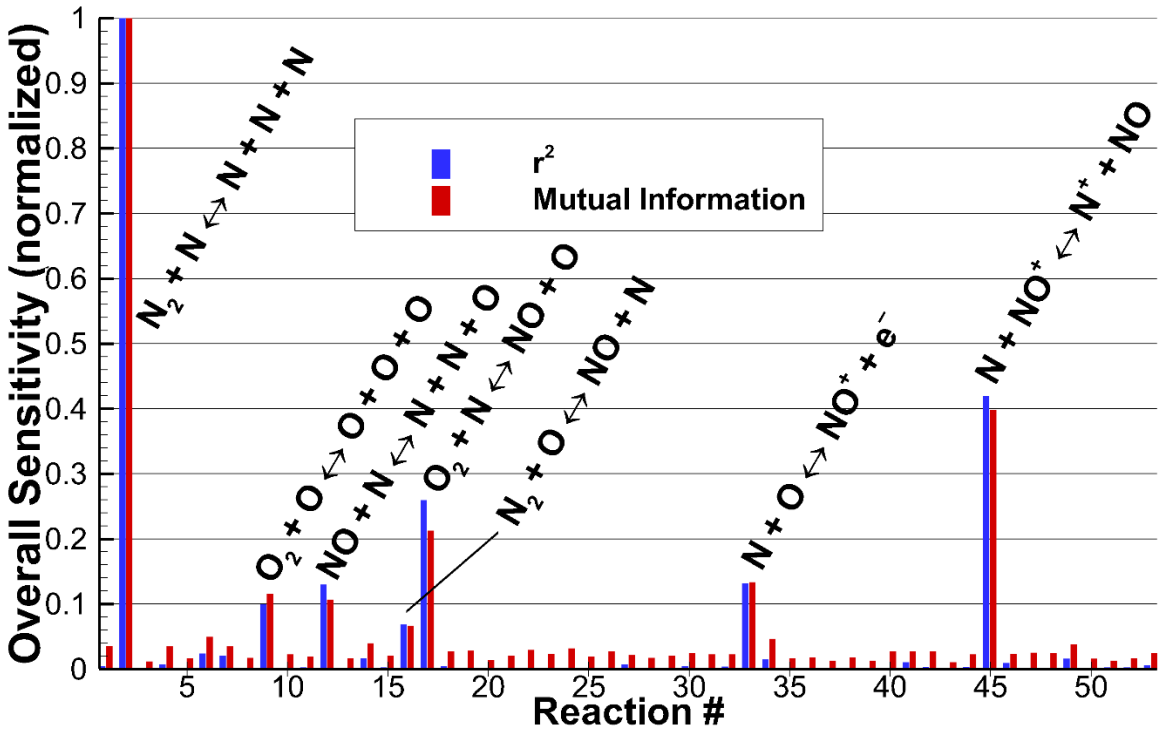

Figure 5.24 Normalized r^2 and MI overall, variance weighted sensitivities for QoI_{n_o} defined over a modified range of x.

5.3.5 Preliminary Conclusions

Based on the results of these four studies of differing QoIs, conclusions can be made about the most important reaction rates to this CHIPS simulation of EAST Shot 37 without electronic excitation. More importantly, observations about performing a sensitivity analysis of a shock wave can be used in the following studies. Understanding what information can be extracted from each figure type is important. The plots of r^2 as a function of x-location have the advantage of clearly demonstrating which reactions are most important at each location. This may be useful if an understanding of the most influential input parameters is desired for a specific region or feature. The variance

weighted r^2 plots may obscure this information since the variance may be low in this region compared to elsewhere in the domain. The r^2 figures also show where the r switches from a positive to negative correlation, but this is only visualized as a bounce off the x-axis. While the sign of r is not explicitly shown, it can be inferred through the understanding of the physics or the value can be determined from the sensitivity data (not shown here). The variance weighted r^2 plots have the advantage of displaying a more accurate representation of how each input parameter affects the QoI at each location. In addition, the variance weighted plots help visualize how the input parameters contribute to the overall sensitivity ranking over the domain. Finally, the variance data for each QoI are included on these plots which demonstrate the regions where high uncertainty in the QoI may be expected. Care must be taken when computing a variance weighted overall sensitivity. The calculated variance of a QoI is a measure of the range of values observed at that location, but in some cases, this variance could be high due to noise resulting from the simulation. Because DSMC is a particle method, noise is common in QoIs that are defined by a relatively small number of samples. An example of a QoI with significant statistical noise in the variance and the effect of this variance on the sensitivity results is discussed in the second preliminary sensitivity analysis.

The reactions to which each QoI is most sensitive to are compiled in Table 5.1 with their ranking. As demonstrated for QoI_{n_O}, the region of interest must be considered in ranking the reactions by overall sensitivity. The reactions that are important in the shock region may not be the same as those important for the downstream equilibrating region or vice versa. This is most obviously demonstrated by reaction $O_2 + O \rightleftharpoons O + O + O$. This reaction is within the top six reactions for the small modified region around the shock but is never within the top ten for any of the other QoIs. On the same note, the input parameter that produces the largest variance weighted value at a single point may

not be the most important parameter once the entire domain is considered. For example, $N_2 + N \rightleftharpoons N + N + N$ produces the largest variance weighted r^2 value in Fig. 5.17 for QoI_{n_N}, but holds the 3rd highest rank in Table 5.1. In addition, care must be taken to avoid generalizing the parameter rankings to other QoIs. For example, $N_2 + N \rightleftharpoons N + N + N$ has one of the top three largest sensitivities reactions for every QoI except for the QoI_{n_e}. When considering $N_2 + N \rightleftharpoons N + N + N$, QoI_{n_e} is nearly insensitive to modifications in its reaction rate.

Table 5.1 Ranking of the most sensitive reaction rates for sensitivity analysis #1.

#	Reaction	Sensitivity Rank									
		$QoI_{T_{tr}}$		QoI_{n_e}		QoI_{n_N}		QoI_{n_O}		QoI_{n_O} (mod)	
		r^2	MI	r^2	MI	r^2	MI	r^2	MI	r^2	MI
45	$N + NO^+ \rightleftharpoons N^+ + NO$	2	2	1	1	1	1	1	1	2	2
33	$N + O \rightleftharpoons NO^+ + e^-$	3	3	2	2	2	3	2	2	4	4
34	$N + N \rightleftharpoons N_2^+ + e^-$	4	4	3	3	4	4	6	4	12	9
2	$N_2 + N \rightleftharpoons N + N + N$	1	1	23	19	3	2	3	3	1	1
16	$N_2 + O \rightleftharpoons NO + N$	6	6	6	6	7	7	4	6	7	7
12	$NO + N \rightleftharpoons N + N + O$	8	9	7	10	8	8	5	9	5	6
49	$N + NO^+ \rightleftharpoons O + N_2^+$	9	10	5	4	6	6	10	7	11	11
17	$O_2 + N \rightleftharpoons NO + O$	11	11	20	9	11	9	9	5	3	3
44	$O^+ + N_2 \rightleftharpoons O + N_2^+$	7	7	4	5	5	5	25	38	23	30
9	$O_2 + O \rightleftharpoons O + O + O$	14	18	53	33	31	30	14	24	6	5
1	$N_2 + N_2 \rightleftharpoons N + N + N_2$	5	5	45	18	32	10	48	49	20	12

5.4 SENSITIVITY ANALYSIS STUDY #2

While the initial sensitivity analysis' purpose was to study the interpretation of the sensitivity results and investigate the influence of charged particle reactions, the first sensitivity analysis was completed without an electronic excitation model. In the previous

chapter, it was demonstrated that an electronic excitation model has a significant effect on the results and must be included for high speed hypersonic entry scenarios. A second sensitivity analysis of EAST Shot 37 is performed including this electronic excitation model in the CHIPS code and using the same input parameters and prior distributions as the previous sensitivity analysis (See nominal shock scenario #2, Section 4.4.). After deciding on prior distributions for the input parameters, the Monte Carlo sensitivity analysis is performed using approximately 2,000 simulations of Shot 37 that required about 150,000 computer hours on the Texas Advanced Computing Center supercomputer, Stampede. To study the importance of each input parameter, the translational temperature, electronic temperature, and electron density are analyzed as QoIs. Since the ability to measure radiative quantities in the simulation is not yet included at this point, these QoIs are chosen with a future sensitivity analysis to radiative quantities in mind. It is expected that each one of these QoIs will provide meaningful insight on what input parameters radiation may be sensitive to. In this analysis, the sensitivity of each QoI to the input reaction rates is ranked by both the Pearson correlation coefficient, r^2, and the mutual information, MI. Since the r^2 and MI ranking turn out nearly identical, similar to the previous sensitivity analysis, only the r^2 results are shown as a function of x-location, but both are included in the bar charts of the overall sensitivity.

5.4.1 Quantity of Interest: Translational Temperature

As with the first preliminary sensitivity analysis, the first QoI studied is the translational temperature, which will be designated again as $QoI_{T_{tr}}$. Figures 5.25 and 5.26 show the r^2 and the variance weighted r^2 values for the five most important reactions as a function of distance from the shock. Figure 5.26 also plots the variance of $QoI_{T_{tr}}$ on the right axis that is used to calculate the variance weighting. After integrating the variance

weighted r^2 values from x = –1 to 4 cm, the sensitivity of $QoI_{T_{tr}}$ can be compared for every reaction and the reactions can be ranked. The integration domain is chosen with future calibrations to EAST data in mind. The sensitivity of $QoI_{T_{tr}}$ to the reaction rates is most easily visualized by a bar chart as in Fig. 5.27 where the normalized overall sensitivity of each reaction is displayed. The results of Figs. 5.25-27 can be contrasted with the first preliminary sensitivity analysis (Figs. 5.9-11). Surprisingly, the list of the top five most important reactions includes the same reactions with one exception. The N + e^- ⇌ N^+ + e^- + e^- impact ionization reaction, unimportant in the first sensitivity analysis, becomes the most important reaction in the current sensitivity analysis. With the inclusion of an electronic excitation model being the only differentiator between the two sensitivity analyses, the importance of electronic excitation to this reaction becomes obvious and requires further study in the following chapters.

Considering Fig. 5.25 or 5.26 and looking from the freestream to downstream of the shock, the translational temperature is seen to be the most sensitive within the shock layer to the dissociation of N_2 through the N_2 + N_2 ⇌ N + N + N and N_2 + N ⇌ N + N + N reactions. These reactions have the greatest effect on the temperature spike of the translational temperature in Fig. 4.26c since the dissociation of N_2 is an endothermic process. As the shock is followed and the translational temperature of the particles spikes, ionization is initiated by the associative ionization reactions. The formation of the initial electrons is mostly due to the associative ionization reaction, N + O ⇌ NO^+ + e^-. Following closely after the production of the initial electrons, the electron impact ionization of atomic nitrogen, N + e^- ⇌ N^+ + e^- + e^-, begins. Since atomic nitrogen is the most common species downstream, along with the ionization and electron capture reactions being the primary mode of chemical heat transfer, $QoI_{T_{tr}}$ is the most sensitive to these two reactions downstream of the shock.

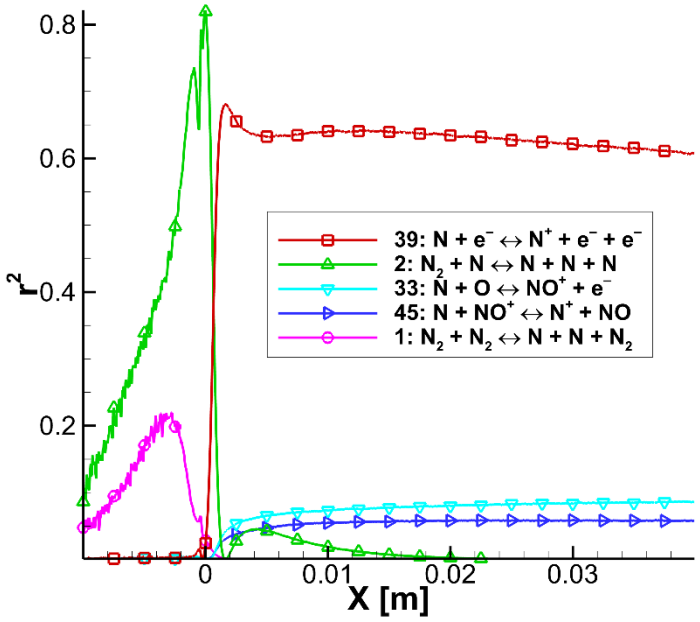

Figure 5.25 r^2 sensitivities of the five most sensitive reaction rates when the translational temperature is the QoI ($QoI_{T_{tr}}$).

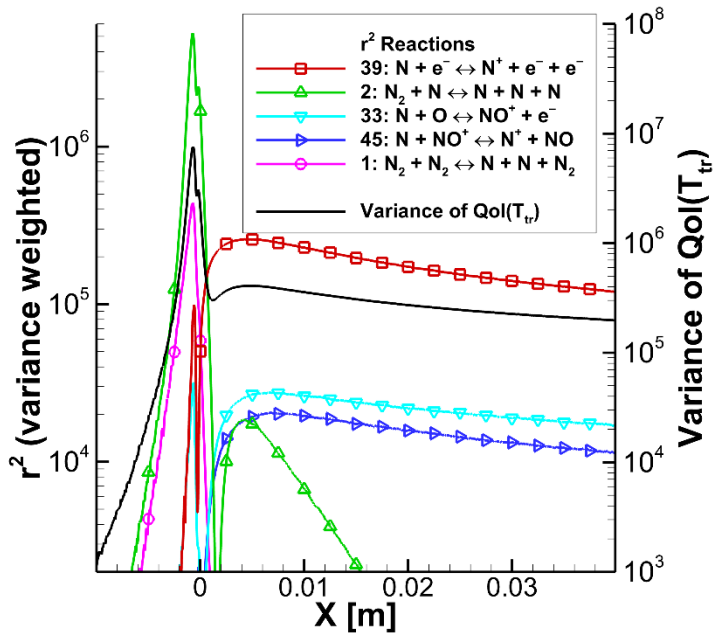

Figure 5.26 Variance weighted r^2 sensitivities of the five most sensitive reaction rates for $QoI_{T_{tr}}$, and the variance at each x-location.

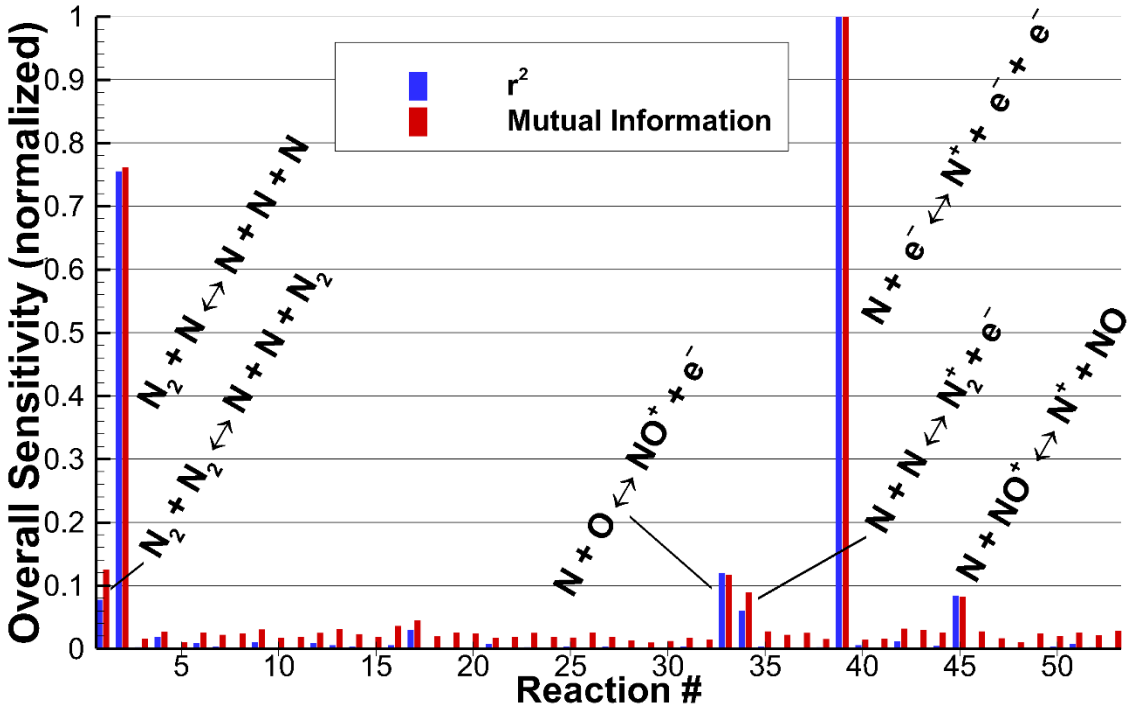

Figure 5.27 Normalized r^2 and MI overall, variance weighted sensitivities for $QoI_{T_{tr}}$.

5.4.2 Quantity of Interest: Electronic Temperature

The electronic temperature is also investigated as a quantity of interest ($QoI_{T_{elec}}$). Although there are still issues with the calculation of the electronic temperature upstream of the shock, the electronic temperature is an important quantity for future plans to complete a sensitivity study analyzing heat flux or radiance as a function of distance from the shock. Furthermore, the outcome of the $QoI_{T_{elec}}$ analysis provides a prediction of the radiative sensitivity results. Figures 5.28-5.30 plot the r^2 sensitivity along the domain and the overall sensitivity of $QoI_{T_{elec}}$. In the upstream region of Fig. 5.29, issues with the electronic temperature calculation are obvious and result in large amplitude oscillations of the computed variance. These fluctuations are an artifact of the electronic temperature

calculation (Eqn. 3.12) where a low number of simulated excited levels lead to unexpectedly high electronic temperatures. This problem carries an additional downside in that the simulated electronic temperature fluctuations obscure the important parameters in the upstream region by artificially weighting the upstream region due to the high variance of T_{elec}. It is likely that the variance of T_{elec} upstream of the shock would be small if the electronic temperature could be computed without distortion associated with very small sample sizes. Not many particles should be excited far upstream, and the temperature should be low. Despite the heavier variance weighting in this upstream region, Fig. 5.30 shows that the most sensitive reaction rates for $QoI_{T_{elec}}$ are still clearly distinguishable from the less important reactions. The variance does not influence the ordering of the most important reactions, but due to over-weighting the variance in the upstream region, it would be difficult to rank the reactions further down the list. This is most obvious when considering the MI as every input parameter demonstrates an unusually large overall sensitivity due to the upstream variance fluctuations.

From Fig. 5.30, $QoI_{T_{elec}}$ is most sensitive to the electron impact ionization reaction, $N + e^- \rightleftharpoons N^+ + e^- + e^-$. If Fig. 5.28 is considered and the region where this reaction is most important is identified, it is seen that this occurs shortly after ionization begins and downstream of the shock. $QoI_{T_{elec}}$ is most sensitive to the electron impact ionization reaction in this region because this reaction controls the electron cascade. As with the translational temperature, this reaction reduces the electronic temperature when its rate increases because it absorbs energy through the endothermic ionization reactions. In addition, the ionization reactions primarily remove bound electrons from the most excited states, thereby leaving a lower electronic temperature. The overall sensitivity of the electronic temperature to the impact ionization reaction is closely followed by two nitrogen dissociation reactions, $N_2 + N \rightleftharpoons N + N + N$ and $N_2 + N_2 \rightleftharpoons N + N + N_2$.

Upstream and within the shock, the correlation between the electronic temperature and dissociation reactions is negative because the reactions are reducing the amount of available energy. Moving into the post-shock region, the correlation between $QoI_{T_{elec}}$ and $N_2 + N \rightleftharpoons N + N + N$ becomes positive as it is easier to electronically excite atomic nitrogen than molecular nitrogen. While the importance of these two reactions makes sense when physically analyzed, it must be considered that their high ranking is, in some part, due to the high variance weighting in the upstream. Analyzing Fig. 5.29, the N_2 dissociation reactions have much higher correlation with the electronic temperature in the upstream region than the other reactions shown. Unexpectedly the charge exchange reaction, $N + NO^+ \rightleftharpoons N^+ + NO$, is the fourth most important reaction. To understand why this reaction has such a large effect on the DSMC results, the electron density is considered as a QoI.

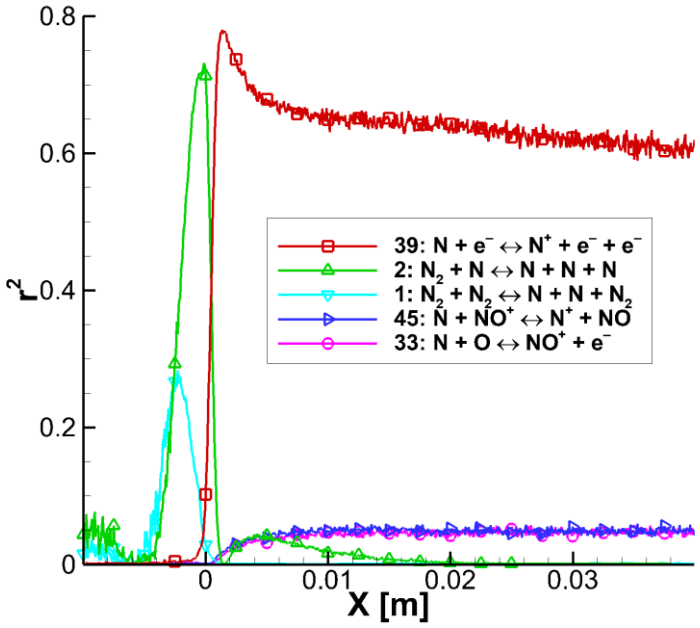

Figure 5.28 r^2 sensitivities of the five most sensitive reaction rates when the translational temperature is the QoI ($QoI_{T_{elec}}$).

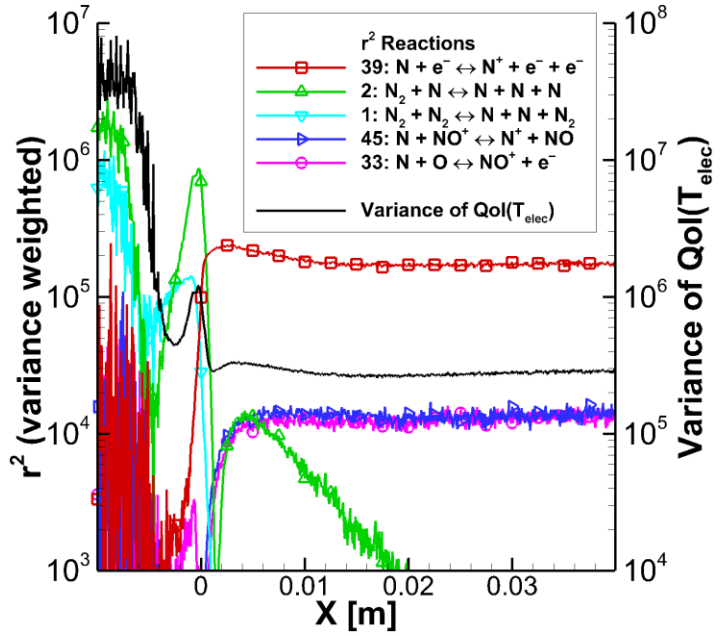

Figure 5.29 Variance weighted r^2 sensitivities of the five most sensitive reaction rates for $QoI_{T_{elec}}$, and the variance at each x-location.

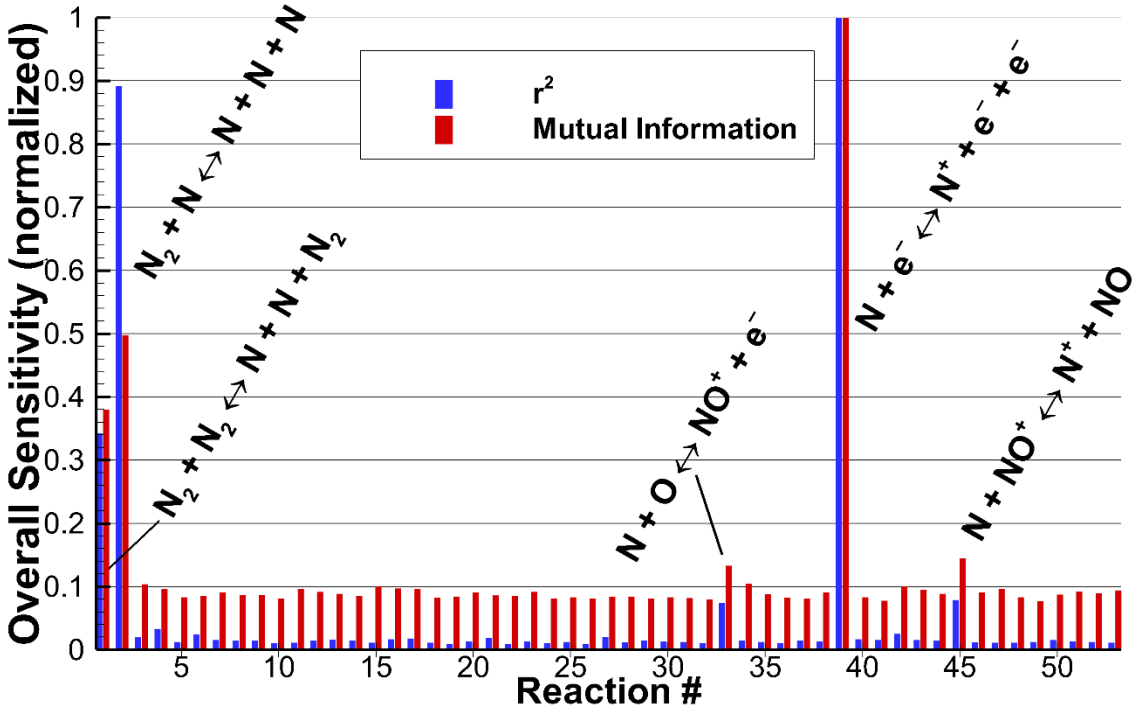

Figure 5.30 Normalized r^2 and MI overall, variance weighted sensitivities for $QoI_{T_{elec}}$.

5.4.3 Quantity of Interest: Free Electron Density

In addition to studying the electronic temperature as a means to understand the ionization process, the electron density quantity of interest, QoI_{n_e}, is a secondary prediction of how radiative quantities will be affected by the sensitivity analysis. Electron impact excitation plays an important role in the excitation of atomic particles within and downstream of the shock. Since an atomic spectral feature, for example the O I triplet at 777 nm, would be a suitable choice for future Markov Chain Monte Carlo calibrations, predicting the reaction rates that will affect these radiative quantities is of high importance. The sensitivity results are shown in Figs. 5.31-5.33 and can be compared with Figs. 5.13-15 from the previous sensitivity study. While both studies show

sensitivity to associative ionization reactions, the electron density is most sensitive to the nitrogen electron impact ionization reaction rate in the current study. As mentioned for the translational temperature QoI, this change in ranking between sensitivity studies can be attributed to the addition of an electronic excitation model. The electronic excitation model allows for collisions to excite particles to a higher energy state. As these particles excite to higher energy levels and begin to collide with other particles in high energy states, the total collision energy increases, meaning that colliding particles are more likely to ionize.

In addition to direct ionization reactions, the molecular nitrogen dissociation reaction is the next most important reaction and the reaction rate has a negative correlation with the electron density. This seems counterintuitive since the production of electrons in the electron cascade relies on atomic nitrogen. While this is true, the electron cascade requires much less atomic nitrogen than what is typically present in the simulated scenario even with the minimum nitrogen dissociation rate considered in the sensitivity analysis. Rather, the ionization reactions are much more reliant on the amount of energy available within and downstream of the shock. Since dissociation of molecular nitrogen by atomic nitrogen is a common endothermic reaction, reducing the dissociation rate actually increases the electron density.

Coming back to the charge exchange reaction, $N + NO^+ \rightleftharpoons N^+ + NO$, this reaction is found in Fig. 5.33 to be the fourth most important. As discussed in the previous sensitivity analysis, this charge exchange reaction does not have a direct path to ionization, making it difficult to trace the sensitivity of the QoI_{n_e} to it. Again, considering the reaction map in Fig. 5.12, a different charge exchange reaction, $N + NO^+ \rightleftharpoons O + N_2^+$, has a higher rate at the post-shock temperatures than the $N + NO^+ \rightleftharpoons N^+ + NO$ reaction. As NO^+ and N_2^+ are the products of associative ionization reactions and the reverse of

these reactions allows for the capture of free electrons, the charge exchange reaction with the highest rate ($N + NO^+ \rightleftharpoons O + N_2^+$) has no effect on QoI_{n_e}. However, the second charge exchange reaction ($N + NO^+ \rightleftharpoons N^+ + NO$) transfers the charge from NO^+ to N^+ and the atomic nitrogen ion does not as readily capture a free electron. In a sense, this charge exchange reaction stabilizes the free electron density and therefore, has a significant influence on QoI_{n_e}.

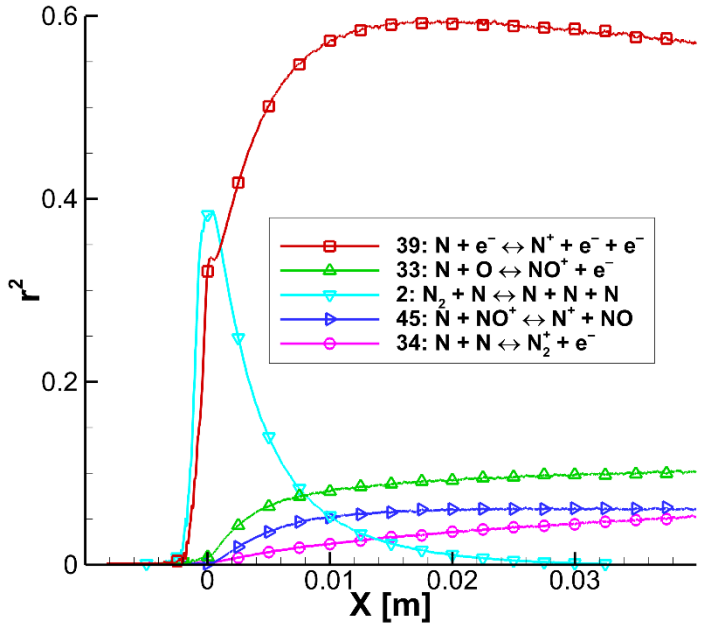

Figure 5.31 r^2 sensitivities of the five most sensitive reaction rates when the translational temperature is the QoI (QoI_{n_e}).

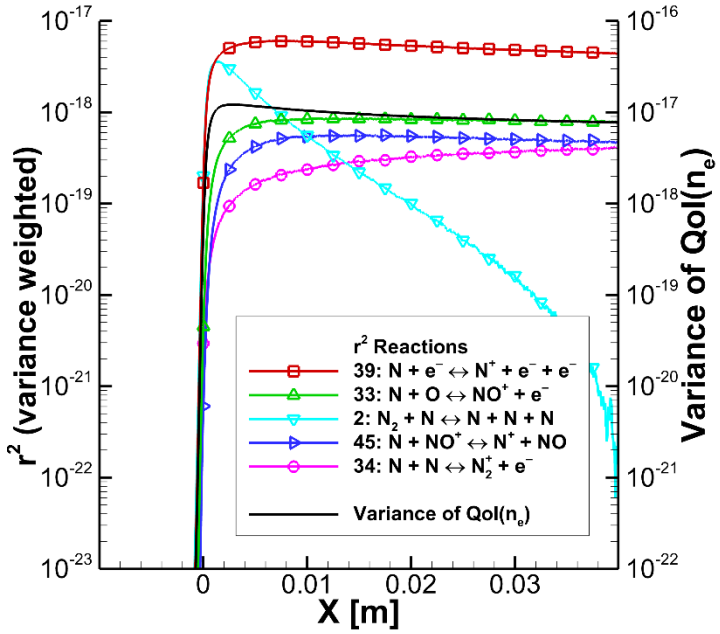

Figure 5.32 Variance weighted r^2 sensitivities of the five most sensitive reaction rates for QoI_{n_e}, and the variance at each x-location.

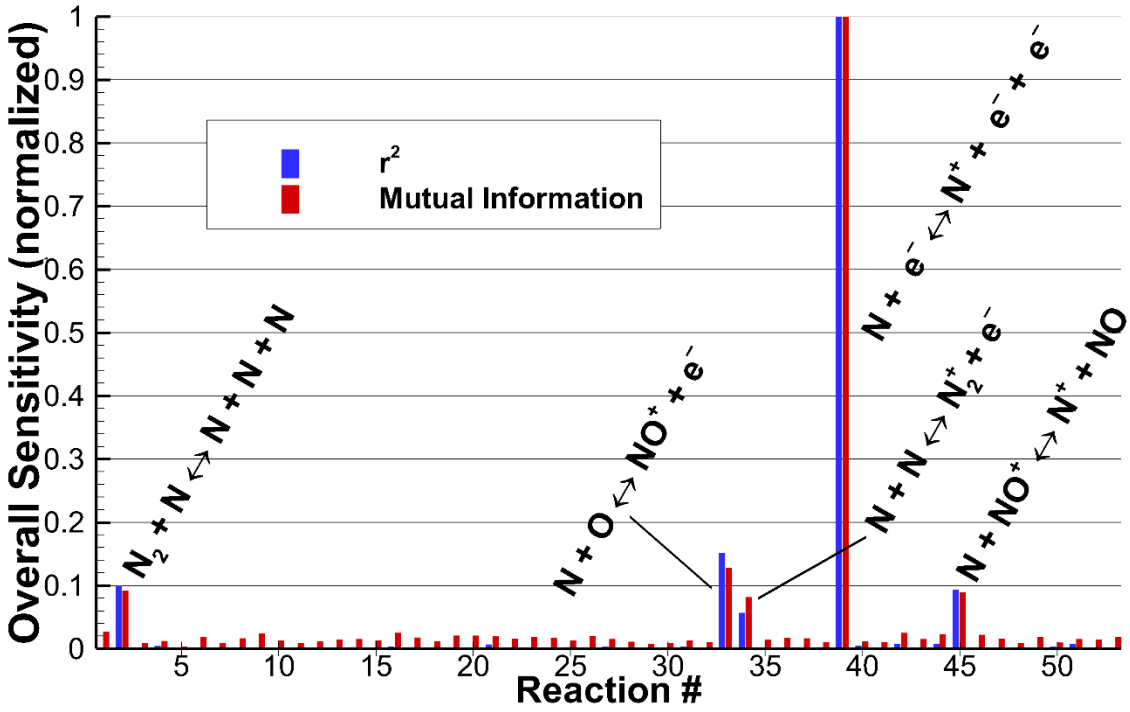

Figure 5.33 Normalized r^2 and MI overall, variance weighted sensitivities for QoI_{n_e}.

5.4.4 Preliminary Conclusions

Once the sensitivity analysis was completed, the results for the translational temperature, electronic temperature, and electron density were compiled into Table 5.2. The most important reaction for all three QoIs was the electron impact ionization reaction, $N + e^- \rightleftharpoons N^+ + e^- + e^-$, which determines the speed of the electron cascade and absorbs energy through its endothermic forward rate. This reaction was also determined to be the most important in an independent study by Miki, et al. focused on a sensitivity study of radiative heat flux [34]. The present sensitivity analysis is an improvement on the previous study of this case without electronic excitation. The inclusion of an

electronic excitation model resulted in a reaction ranking that was more dependent on ionization reactions, particularly the nitrogen electron impact ionization reaction. In addition to the electron impact ionization reaction, molecular nitrogen dissociation reactions and associative ionization reactions were found to play an important role for these three QoIs. Finally, this study reinforced the results of the previous sensitivity analysis that the charge exchange reaction, $N + NO^+ \rightleftharpoons N^+ + NO$, should be included in high temperature air simulations as it has effects on all three of the QoIs. These results lay the groundwork for the upcoming sensitivity analysis of radiative quantities from a high speed hypersonic shock simulation with CHIPS.

Table 5.2 Ranking of the most sensitive reaction rates for sensitivity analysis #2.

#	Reaction	Sensitivity Rank					
		$QoI_{T_{tr}}$		$QoI_{T_{elec}}$		QoI_{n_e}	
		r^2	MI	r^2	MI	r^2	MI
39	$N + e^- \rightleftharpoons N^+ + e^- + e^-$	1	1	1	1	1	1
2	$N_2 + N \rightleftharpoons N + N + N$	2	2	2	2	3	3
33	$N + O \rightleftharpoons NO^+ + e^-$	3	4	5	5	2	2
45	$N + NO^+ \rightleftharpoons N^+ + NO$	4	6	4	4	4	4
1	$N_2 + N_2 \rightleftharpoons N + N + N_2$	5	3	3	3	36	6
34	$N + N \rightleftharpoons N_2^+ + e^-$	6	5	24	6	5	5

While intuition and agreement with Miki, et al.'s results would support the conclusion that the $N + e^- \rightleftharpoons N^+ + e^- + e^-$ electronic impact ionization reaction is the most important for these QoIs, the physical models being used in the CHIPS code must still be analyzed to confirm that modeling error did not affect the sensitivity analysis results. First, the electronic excitation model used in CHIPS must be considered. Electronic excitation allows for particles to climb the energy ladder. This increases the potential for

an ionization event to occur as excited particles require less energy from an elastic collision or the other internal modes in order to surpass the ionization energy threshold. As explained in Section 3.5.1, the electronic excitation model does not strictly reproduce an experimental relaxation time and does not include spontaneous emission meaning that the excitation rate could be incorrect. This could lead to an overpopulation of excited states and, potentially, effect the results of the sensitivity analysis by increasing the ionization rate. A second modeling issue to be addressed is that the TCE reaction model currently being used in CHIPS has several shortcomings that may change the sensitivity analysis results. The most obvious error is the omission of several backward reaction rates, particularly, the backward reaction rate of $N + e^- \rightleftharpoons N^+ + e^- + e^-$. These missing reactions either were not previously available in Arrhenius form, or assumed to be unimportant. Because backward reactions are missing, it is guaranteed that the equilibrium composition downstream of the shock is incorrect. Since many of the missing backward reactions involve electron capture or charge exchange, the sensitivity results in the equilibrium region are likely to change following the addition of the backward reactions. A potential solution would be to fit Arrhenius form rates for the missing reactions, but there would still be errors in the backward reaction rate. In addition, the electronic energy of each colliding particle is currently allowed to participate in the TCE chemical reaction probability calculation. The TCE model is unable to appropriately handle this energy correctly and results in overpredictions of the chemical reaction rates. Solutions to the backward reaction modeling and TCE issues will be discussed in Chapter 7.

CHAPTER 6

Saturn Entry Simulation

6.1 Overview

On the completion of the preliminary sensitivity analyses, the focus of this chapter shifts to the development of radiation modeling with the CHIPS code. This is completed through the initial investigation of bow shock physics for Saturn entry probe scenarios and the influence of nonequilibrium phenomena on Saturn entry conditions [56]. Therefore, the purpose of this chapter is to employ models that are sufficient for a typical hypersonic entry DSMC simulation and identify the areas where improvement is required. The CHIPS code is used to simulate two rarefied hypersonic shock tube experiments on an 89%:11% hydrogen-helium mixture performed in the Electric Arc Shock Tube (EAST) at NASA Ames Research Center. This hypersonic shock wave situation is comparable to the stagnation line case experienced during Saturn entry scenarios. The CHIPS simulations are post-processed through the NEQAIR line-by-line radiation code to compare directly to the experimental results. Improved collision cross-sections, inelastic collision parameters, and reaction rates are determined for a high temperature DSMC simulation of a 7-species H_2-He mixture. Simulation results for 27.8 and 27.4 km/s shock waves are obtained at 0.2 and 0.1 Torr respectively and compared to measured spectra in the Vacuum Ultraviolet 120-165 nm (VUV), Ultraviolet/Visible 330-

---

Higdon, K. J., Cruden, B. A., Brandis, A. M., Liechty, D. S., Goldstein, D. B., and Varghese, P. L., "Direct Simulation Monte Carlo Shock Simulation of Saturn Entry Probe Conditions," *Journal of Thermophysics and Heat Transfer*, Vol. 32, No. 3, 2018, pp. 680-690.

B. A. Cruden and A. M. Brandis supervised the project and assisted with obtaining EAST data and NEQAIR simulations. D. S. Liechty guided development of electronic excitation models. D. B. Goldstein and P. L. Varghese provided technical insight.

500 nm (UV/Vis), Visible/Near Infrared 654-658 nm (Vis/NIR), and Near Infrared 1100-1600 nm (IR) ranges.

6.2 Introduction to Saturn Entry

Recent investigations of Saturn entry conditions have been spurred by the high priority listing of Saturn probe missions in the 2013-2022 Decadal Survey for planetary exploration and the Sept. 2017 entry and destruction of the Cassini probe [57]. In prior analysis of the uncertainty present in a CFD simulation of the Saturn entry conditions, it was found that radiative heating may account for up to 20% of peak heating of a blunt capsule with a large uncertainty [58]. To mitigate this uncertainty, shock tube tests in the EAST at NASA Ames Research Center were performed for a range of Saturn entry trajectory conditions [2]. These tests were performed in a hydrogen-helium mixture (89%:11% by volume) for a set of freestream velocities between 25 and 30 km/s and pressures between 0.1 and 0.5 Torr. These experiments showed that quantities in the post-shock region did not reach the expected equilibrium values and that radiative heating may not play a significant role. An induction period occurred in the experiments several centimeters behind the shock where radiance suddenly increased as the electron density increased. In addition, radiance in the VUV range was observed in the pre-shock regions, indicating the diffusion of excited hydrogen upstream of the shock. An attempt was made by Cruden and Bogdanoff to reproduce these observations with existing CFD tools [2]. While successful in modeling the electron number density through the shock, the continuum model grossly overpredicts the stagnation line radiance. The authors attributed this to the modeling of excited state populations by Boltzmann distributions. Also, the pre-shock radiation and the upstream diffusion of heated gas into the freestream were not

captured by the CFD model. To investigate these issues and further understand the physics, the CHIPS code is used to study Saturn entry scenarios.

6.3 High Temperature H_2-He Mixture Parameters

While available data from previous 11-species air DSMC simulations has been utilized in the past chapters, there have been only a few prior DSMC simulations of H_2-He mixtures and, as a result, little time has been spent developing a full set of accurate H_2-He high temperature collision parameters for standard DSMC models. The only DSMC simulations of an H_2-He mixture were performed for the Galileo Probe entry into Jupiter's atmosphere [59][60]. In Ref. [59], the VHS parameters were fit to high temperatures, but this fit was only performed for the H_2-He mixture and not the individual species. Even though extreme post-shock temperatures were experienced during the Jovian entry, neither publication included electronic excitation or chemistry models.

Besides the few simulations of H_2-He mixtures, several DSMC simulations involving either He or H_2 and its derivatives have been completed. Low temperature DSMC simulations with helium have been performed to model nanoscale mixed gas bearings [61] and microthrusters [62] where helium collision properties were determined for temperatures up to 300 K. DSMC simulations involving hydrogen have been completed for various scenarios, including low temperature supersonic arcjet flows [63], high temperature, low thrust arcjet flows [13][64][65], and H_2-O_2 detonation waves [66][67][68][69]. Reference [64] provides high temperature fits to H_2-H_2, H_2-H, H-H, and H-e^- VHS parameters, but relies on low temperature models for rotation and vibration, as do the other published DSMC simulations involving hydrogen. In addition, none of the studies on hydrogen or helium included electronic excitation. The inaccuracies in the few

published parameters become even more evident at the high temperatures experienced behind a hypervelocity shock. For this reason, improved DSMC parameters have been tabulated in this dissertation for a 7-species H_2-He mixture with a focus on high temperature simulation. These input parameters are used in the same CHIPS models discussed in Chapters 2 and 3.

6.3.1 VHS Elastic Collisions

For elastic collisions between two particles, previous VHS parameters were published by Bird [3], Haas and Milos [59], and Boyd [13]. The parameters provided by Bird are fit to low temperature data and are general values for H_2 and He in that they are collision partner independent. Haas and Milos published high temperature VHS parameters for an H_2-He mixture, but it is in the form of a single VHS fit specific to the expected viscosity of the Jovian atmosphere. Boyd provides the most complete set of the aforementioned publications by determining high temperature VHS fits for H_2-H_2, H_2-H, H-H, and H-e^-. In the present research, updated collision integral parameters provided by Palmer, et al. are utilized to obtain high temperature VHS fits [58]. For a collision pair (i, j), the viscosity collision integral, $\Omega_{ij}^{(2,2)}$, is calculated from these parameters (A, B, C, D) in Eqn. 6.1. The viscosity collision integral is then used in Eqn. 6.2 to determine the viscosity coefficient, μ_{ij}, of a neutral collision pair.

$$\Omega_{ij}^{(2,2)} = DT^{A[\ln(T)]^2+B\ln(T)+C} \quad [6.1]$$

$$\mu_{ij} = 2.6693 \times 10^{-6} \frac{\pi\sqrt{M_{ij}T}}{\Omega_{ij}^{(2,2)}} \quad [6.2]$$

Species specific VHS parameters for $\sigma_{T,ref}$ and ω were obtained for neutral-neutral and charge-neutral collisions by least squares curve fitting $\log(\mu_{ij})$ to the log of the VHS viscosity coefficient, $\mu_{ij,VHS}$, shown in Eqn. 6.3. This equation takes the form of the first approximation of the Chapman-Enskog viscosity coefficient for a VHS gas and is described by Bird [35].

$$\mu_{ij,VHS} = \frac{15\sqrt{2\pi m_r k_B} T^{\omega}}{2(5-2\omega)(7-2\omega)\sigma_{T,ref} T_{ref}^{(\omega-\frac{1}{2})}} \qquad [6.3]$$

The values of $\sigma_{T,ref}$ and ω to be used in Eqn. 6.3 when selecting a reference temperature of 1,000 K were determined by a curve fit to Eqn. 6.2 over the temperature range from 100 K to 10,000 K.

As discussed in Section 3.4.2, the VHS model used in the CHIPS code has difficulty reproducing charged particle cross-sections due to Coulombic forces. To handle these collisions, charge-charge cross-sections are assumed to be identical to the charge-neutral cross-sections while curve fits are completed for all other collision pairs. Table 6.1 compiles the fitted high temperature parameters for the H_2-He mixture where the VHS reference diameter, d_{ref}, is calculated from the reference cross-section. An example of one of the curve fits is shown in Figs. 6.1 and 6.2 for an H_2-H_2 elastic collision. Figure 6.1 compares the calculation of the viscosity coefficient with the current VHS fit to previous VHS parameters determined by Bird [3], Haas and Milos [59], and Boyd [13]. In addition, it shows the viscosity calculated from Eqns. 6.1 and 6.2 using parameters from Palmer's review of the viscosity coefficient [58]. Discrete points were selected from this line to determine the current fit shown in Fig. 6.1. The current fit begins diverging from Palmer's viscosity data at high temperatures and the difference grows as the

temperature increases. This error at very high temperatures is acceptable as evidenced in Fig. 6.2. The slope of the collision cross-section levels off at high temperatures so that the effect on simulations in this temperature range will be minimal.

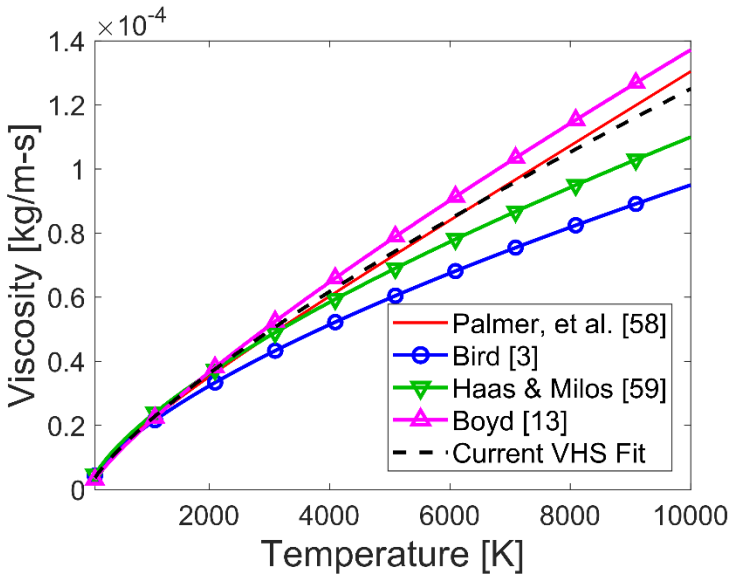

Figure 6.1 H_2-H_2 viscosity coefficient curve fit of VHS parameters to Palmer's empirical data and comparisons with other published VHS parameters.

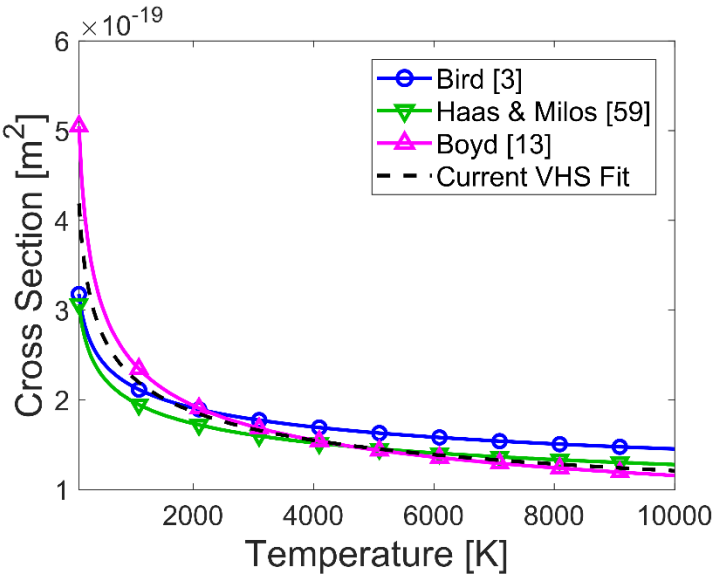

Figure 6.2 H_2-H_2 VHS cross-section for the current curve fit compared with other published VHS parameters.

Table 6.1 7-species H_2-He VHS cross-section parameters at T_{ref} = 1000 K.

d_{ref} [Å]	H_2	H	He	H_2^+	H^+	He^+	e^-
H_2	2.678	2.581	2.462	3.883	3.912	3.874	1.695
H	–	2.913	2.396	3.639	5.642	2.865	3.689
He	–	–	2.137	2.657	3.029	3.535	1.380
H_2^+	–	–	–	3.883	3.912	3.874	1.695
H^+	–	–	–	–	5.642	2.865	3.689
He^+	–	–	–	–	–	3.535	1.380
e^-	–	–	–	–	–	–	–

ω	H_2	H	He	H_2^+	H^+	He^+	e^-
H_2	0.770	0.927	0.775	0.907	0.880	0.982	0.400
H	–	0.825	0.859	0.905	1.006	0.912	0.831
He	–	–	0.759	0.761	0.974	0.855	0.510
H_2^+	–	–	–	0.907	0.880	0.982	0.400
H^+	–	–	–	–	1.006	0.912	0.831
He^+	–	–	–	–	–	0.855	0.510
e^-	–	–	–	–	–	–	–

6.3.2 Inelastic Collisions

When inelastic collisions involving H_2 occur, collision numbers for rotational, Z_{rot}, and vibrational, Z_{vib}, relaxation are calculated to determine the probability of a relaxation event. A review of vibrational collision number correlations is presented by Palmer, et al. [58], and a refit for the Millikan-White formula was provided [38]. These refit parameters will be used in the following simulations (Table 6.2). The modeling of rotational energy exchange is generally well developed in DSMC. Unfortunately, diatomic hydrogen is unlike any of the other molecular species typically modeled by DSMC. Usually, the probability of rotational exchange *increases* with increasing temperature and simulation of this trend is often handled with Parker's model for calculating the rotational collision number, Z_{rot} [37]. Experiments at low temperatures for diatomic hydrogen and a previous study by Boyd, however, have shown that the reverse trend is true for H_2 and the rotational collision number actually *decreases* with increasing temperature in the low temperature regime [63]. Boyd proposed a relationship between the rotational collision number and the temperature, but this model is only valid for low temperatures. Figure 6.3 presents a large set of collision numbers compiled from various sources by Takama and Suzuki for a moderate temperature range between 200 and 1500 K [70]. The data in this region are inconsistent and do not follow any identifiable trends so it is unclear whether this lack of consistency continues into high temperatures. For this reason, a temperature dependent model is not used in this dissertation and instead, a constant collision number, $Z_{rot} = 174$, is "fit" to the existing data. This fit agrees with a previous study by Willauer and Varghese which found that $Z_{rot} = 100$ reproduced the state-to-state relaxation of p-H_2 from initial conditions of

$T_{rot} = 700$ K and $T_{tr} = 300\,K$ relatively well [71]. Even, though the current Z_{rot} fit may be a poor representation of the rotational collision number, diatomic hydrogen dissociates relatively quickly in the high temperature flows simulated in this dissertation so accurate modeling of rotational relaxation may not be particularly important. As with the elastic collisions parameters, it is assumed that the same vibrational and rotational relaxation parameters can be utilized for H_2^+.

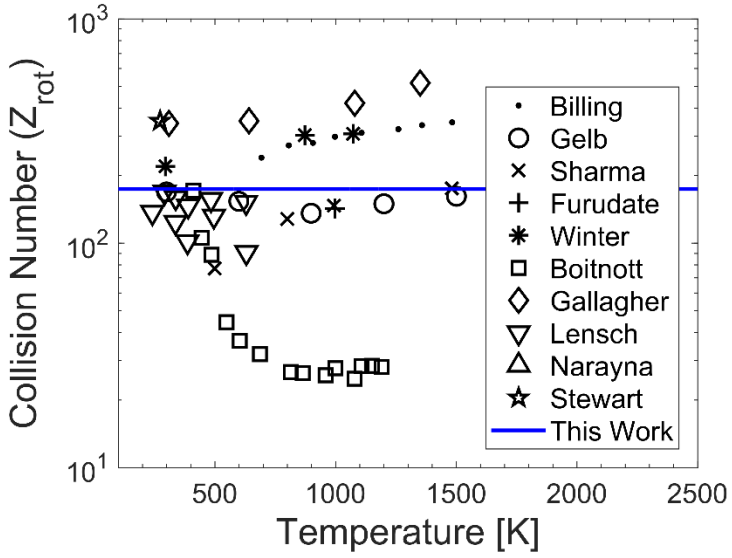

Figure 6.3 Rotational collision number curve fit to experimental and empirical data for H_2 compiled by Takama and Suzuki [70].

Table 6.2 Diatomic species vibrational parameters.

Collision Pair	a	b
H_2-H_2	65.110	0.006821
H_2-H	9.673	0.07250
H_2-He	69.971	0.004682

6.3.3 Arrhenius Reaction Rates

Forward reaction cross-sections for the H_2-He mixture are calculated in the TCE model [3][15] through Arrhenius reaction rates tabulated by Leibowitz [72]. Most continuum simulations calculate backward reaction rates, k_b, directly from published equilibrium constants, K_{eq}. However, the TCE model used in DSMC requires that the backward reaction rate be determined from the ratio of the forward rate to the equilibrium constant and then curve fitted to an Arrhenius form. The TCE model, therefore, misrepresents the backward reaction rate's complex dependence on temperature since it requires an Arrhenius form to calculate reaction cross-sections. In addition to restrictions imposed by the Arrhenius form, the TCE model also imposes limits on the upper and lower bounds of the Arrhenius temperature exponent, η. All of the backward reaction rates that are required for this set are termolecular recombination reactions where the TCE reaction probability equation in Ref. [3] can be simplified as

$$\left(\frac{\sigma_R}{\sigma_T}\right)_k = \frac{\sqrt{\pi} n_T \varepsilon \Lambda T_{ref}^{\eta}}{2\sigma_{ref}} \frac{\Gamma(\frac{5}{2} - \omega)}{\Gamma(\eta + \frac{3}{2})} \sqrt{\frac{m_r}{2k_B T_{ref}}} \left(\frac{E_c}{k_B T_{ref}}\right)^{\eta - 1 + \omega} \qquad [6.4]$$

where $\varepsilon = 1$ if $i \neq j$ or $\varepsilon = 2$ if $i = j$; m_r is the reduced mass of i and j; σ_{ref}, T_{ref}, and ω are the VHS parameters for species i and j; Λ and η are from the Arrhenius reaction rate equation; E_c is the total collision energy; and n_T is the number density of the third body. It must be noted that the activation energy, E_a, in the Arrhenius equation for the backward reaction is assumed to be zero which explains its omission from Eqn. 6.4. Since E_a is assumed to be zero, this reduces the number of available curve fit parameters to two, Λ and η.

Using the remaining Arrhenius equation parameters and Gordon and McBride's equilibrium constant curve fits (G&M) [73], a least-squares fit was performed on the log of the backward reaction rate which was calculated from the ratio of the forward rate and the G&M equilibrium constant. The complete set of forward and backward Arrhenius reaction rates is shown in Table 6.3. In order to obtain the most accurate backward Arrhenius rates, the recombination reactions were fit to a temperature range between 5,000 to 20,000 K unless otherwise noted. Figures 6.4 and 6.5 show the backward reaction rate and K_{eq} for the $H_2 + H_2 \rightleftharpoons H + H + H_2$ reaction. Relatively good agreement is obtained for both the G&M [73] and Park [74] equilibrium constants in the 5,000 to 20,000 K region of interest, but at higher temperatures the rate is severely overpredicted. The curve fits for the backward two-step ionization (electron capture) reactions suffer even more from the limitations of the TCE model. Consider the backward direction of the $H + H \rightleftharpoons H^+ + e^- + H$ reaction, which was also fit between 5,000 to 20,000 K (Figs. 6.6 and 6.7). In this temperature region, the backward reaction rate calculated from the equilibrium constant decreases rapidly as the temperature increases. Since the reaction probability must then decrease with increasing temperature, Eqn. 6.4 requires that the Arrhenius temperature exponent must satisfy $\eta < 1 - \omega$, leading to the limitation that $\eta < 0.175$ for the two-step electron capture reaction. In addition to this limit, the Arrhenius temperature exponent must be large enough that the gamma function input in the denominator of Eqn. 6.4 is greater than zero which requires that $\eta > -1.5$. This lower bound causes problems for fitting this two-step electron capture reaction because the "ideal" Arrhenius temperature exponent curve fit value is approximately –5.0. To address this issue, a value for η is specified for the reaction rates that does not satisfy the constraints of the TCE model. Although an Arrhenius temperature exponent of –1.5 would provide the best fit to the backward reaction rate, the reaction probability

calculated from Eqn. 6.4 would be zero at all temperatures. Instead, a minimum value was specified at $\eta = -1.0$ for all of the two-step electron capture reactions. This leaves just one parameter from Eqn. 6.4, the Arrhenius pre-exponential constant (Λ), to fit to the backward reaction rate and leads to the gross errors demonstrated in Figs. 6.6 and 6.7. Although recombination reactions are relatively rare and should not have a significant effect on the overall results, the poor reaction rate fitting may lead to discrepancies in the equilibrium concentration and could affect the species concentrations in nonequilibrium regions. Note that there are currently no reaction rates involving creation of H_2^+ meaning that this species will not occur unless a simulation is initialized with H_2^+. The ionization energy of H_2 is 15.42 eV which is not much higher than the 13.6 eV for H, but H_2^+ should only play a minor role as diatomic hydrogen is dissociated rapidly at the high temperatures simulated in this study. The difficulties of modeling backward reaction rates with the TCE model and solutions to these problems are the topic of the Chapter 7.

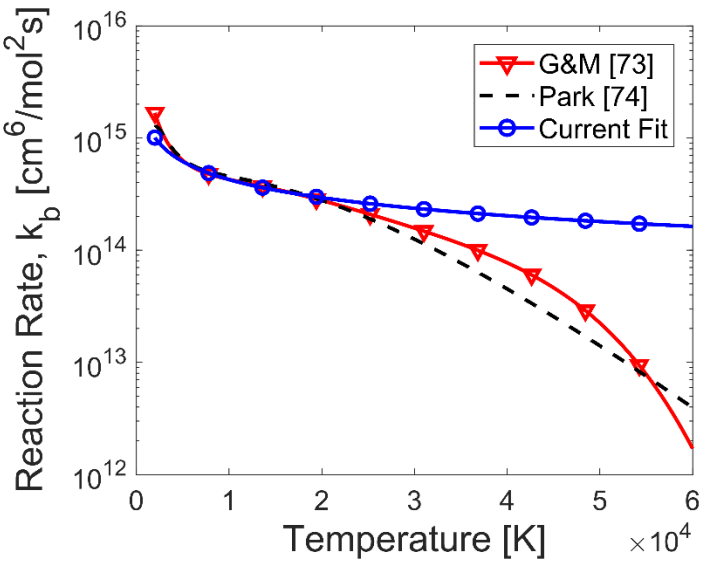

Figure 6.4 Current backward reaction rate curve fit compared to backward reaction rates calculated from the Park and G&M equilibrium constants for $H_2 + H_2 \rightleftharpoons H + H + H_2$.

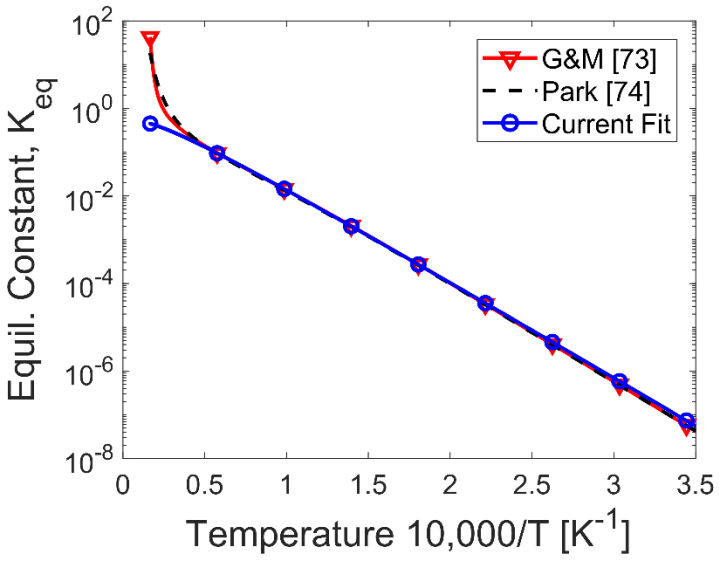

Figure 6.5 K_{eq} calculated from the curve fit compared with the G&M and Park K_{eq} expressions for $H_2 + H_2 \rightleftharpoons H + H + H_2$.

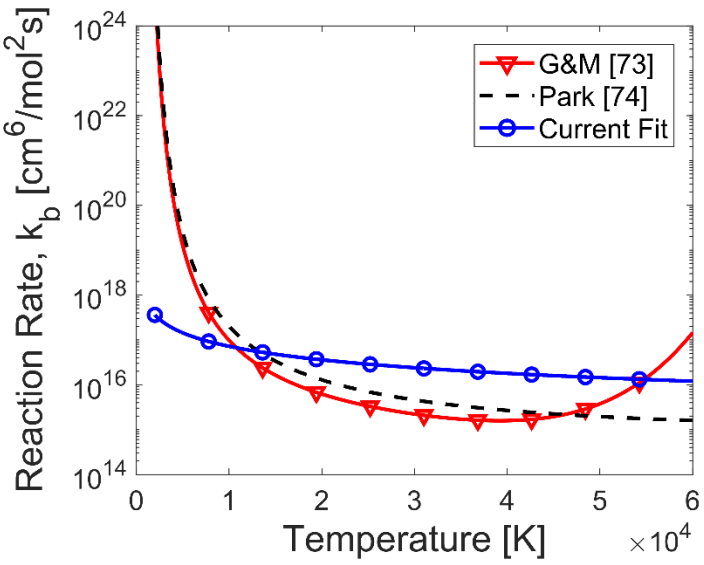

Figure 6.6 Current backward reaction rate curve fit compared to backward reaction rates calculated from the Park and G&M equilibrium constants for $H + H \rightleftharpoons H^+ + e^- + H$.

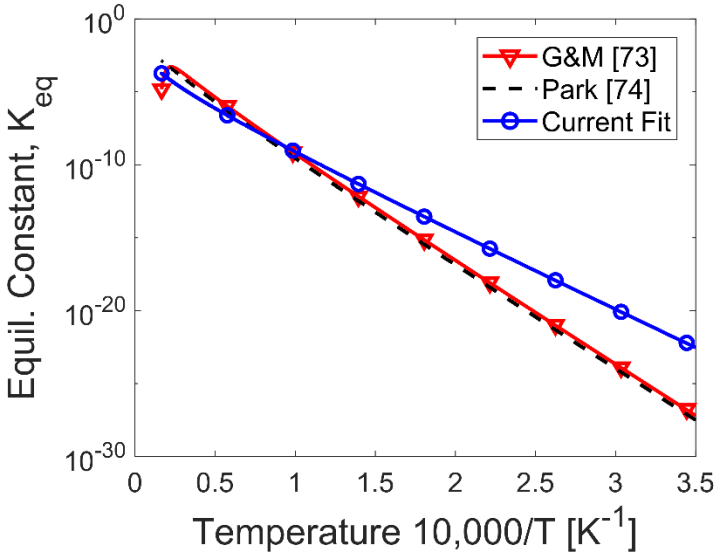

Figure 6.7 K_{eq} calculated from the curve fit compared with the G&M and Park K_{eq} expressions for $H + H \rightleftharpoons H^+ + e^- + H$.

Table 6.3 H_2-He mixture reaction rates.

#	Reaction	Forward Rate Coefficients			Backward Rate Coefficients		
		Λ [m^3/s]	η	E_a [10^{-19} J]	Λ [m^3/s]	η	E_a [10^{-19} J]
1	$H_2 + H_2 \rightleftharpoons H + H + H_2$	1.727×10^{-11}	-1.0	7.17358	1.6248×10^{-43}	-0.535	0.0
2	$H_2 + H \rightleftharpoons H + H + H$	1.386×10^{-10}	-1.0	7.17358	1.3040×10^{-42}	-0.535	0.0
3	$H_2 + He \rightleftharpoons H + H + He$	6.924×10^{-12}	-1.0	7.17358	6.5143×10^{-44}	-0.535	0.0
4	$H_2 + H_2^+ \rightleftharpoons H + H + H_2^+$	1.727×10^{-11}	-1.0	7.17358	1.6248×10^{-43}	-0.535	0.0
5	$H_2 + H^+ \rightleftharpoons H + H + H^+$	1.386×10^{-10}	-1.0	7.17358	1.3040×10^{-42}	-0.535	0.0
6	$H_2 + He^+ \rightleftharpoons H + H + He^+$	6.924×10^{-12}	-1.0	7.17358	6.5143×10^{-44}	-0.535	0.0
7	$H_2 + e^- \rightleftharpoons H + H + e^-$	1.386×10^{-10}	-1.0	7.17358	1.3040×10^{-42}	-0.535	0.0
8*	$H + H \rightleftharpoons H^+ + e^- + H$	1.024×10^{-19}	0.5	16.0293	1.9848×10^{-39}	-1.0	0.0
9*	$H + He \rightleftharpoons H^+ + e^- + He$	8.103×10^{-20}	0.5	16.0293	1.5706×10^{-39}	-1.0	0.0
10†	$H + e^- \rightleftharpoons H^+ + e^- + e^-$	3.790×10^{-17}	0.5	21.7866	1.2614×10^{-38}	-0.978	0.0
11*	$H + e^- \rightleftharpoons H^+ + e^- + e^-$	6.830×10^{-17}	0.5	16.0293	1.3228×10^{-36}	-1.0	0.0
12‡	$He + e^- \rightleftharpoons He^+ + e^- + e^-$	2.210×10^{-17}	0.5	39.3899	2.0319×10^{-39}	-0.989	0.0
13*	$He + e^- \rightleftharpoons He^+ + e^- + e^-$	3.720×10^{-17}	0.5	32.0449	5.2089×10^{-37}	-1.0	0.0

*Two-step process where particle is excited to first state and then immediately ionized by a second collision.
† Backward reaction curve fit between 5,000-25,000 K.
‡ Backward reaction curve fit between 5,000-40,000 K.

6.3.4 Electronic Excitation Levels

The calculation of electronic excitation is relatively straightforward for the model described in Section 3.5.1. Electronic level degeneracies and energy values were compiled from the NIST database [48]. Currently, this set is as complete as possible with the available information from NIST. Including the ground state, this set involves 40 levels for H, 22 levels for H_2, 192 levels for He, and 40 levels for He^+. Electronic excitation values for H_2^+ are not available as the excited electronic states are predissociated. In addition, electronic excitation of H^+ is not possible as it does not

contain an electron to excite. It also must be noted that in this chapter's application of the electronic excitation model, a separate electronic temperature calculation is not provided as these simulations occurred before this capability was added to the CHIPS code. For the scenarios simulated in this chapter, it is assumed that the *electronic* temperature is equivalent to the *free electron* temperature. The free electron temperature (T_e) is calculated from the translational temperature of the free electrons.

6.4 RADIATION MODEL

The macroscopic quantities output by the CHIPS code are useful in order to understand the composition of the flowfield and provide insight into the physics occurring throughout the shock, but radiative spectra are necessary to compare the simulation results to EAST experiments. To calculate the radiative spectra produced by each simulation, the CHIPS results are post-processed by passing the species number densities and the translational, rotational, vibrational, and electronic temperatures of the bulk fluid to the NEQAIR radiation solver [5]. Note that for the simulations performed in this dissertation, the electronic temperature passed to NEQAIR is assumed to be equal to the free electron temperature, as discussed in the previous section. NEQAIR then calculates the radiance along a line of sight for a uniform slab. The radiative spectra are obtained through a series of line-by-line calculations performed for the participating particle species. Multiple spectral broadening mechanisms are taken into account and spectral and spatial convolutions are included in the final results to mimic the smearing that occurs in experimental measurements. It should be noted that, quasi-steady state rates are not currently implemented in the NEQAIR simulations for H atoms. This omission will lead to an overestimate of the radiation for non-Boltzmann distributions of the H electronic state populations.

6.5 RESULTS

In this section, the results of the CHIPS/NEQAIR simulations of a 1-dimensional hypersonic shock tube are compared to two experiments performed in EAST. Due to the experimental setup constraints, high speeds, and high temperatures observed, data collected from this dissertation focused on spectral analysis of the flow, similar to the EAST experiments described in Chapter 1.

Table 6.4 Inflow conditions for the scenarios considered here.

Case	EAST Shot 25	EAST Shot 17
Shock velocity (km/s)	27.8	27.4
Number density (#/m^3)	6.44×10^{21}	3.22×10^{21}
Temperature (K)	300	300
H_2 mole fraction (%)	89	89
He mole fraction (%)	11	11

6.5.1 EAST Shot 25 Simulation

First, the CHIPS simulation of a Saturn atmospheric mixture of 89%:11% H_2-He was applied to simulate Shot 25 from the recent Campaign 56 in EAST for Saturn entry conditions [2]. The inflow conditions simulated in this scenario are listed in Table 6.4 and DSMC shock results are shown in Figs. 6.8 and 6.9 for EAST Shot 25 which had an initial pressure of 0.2 Torr and reached a shock velocity of 27.8 km/s. The output quantities are ensemble averaged as the CHIPS sampling domain moves with the shock and the shock location is defined as $X = 0$. Figure 6.8 shows the variation of particle number densities with respect to distance from the shock wave and Fig. 6.9 plots the total translational, rotational, vibrational, and free electron temperatures through the shock

wave. Diatomic hydrogen becomes scarce behind the shock due to high temperature dissociation and by approximately 1.5 cm, H_2 has completely dissociated. Statistical noise can be seen in the rotational and vibrational temperatures as the number density of H_2 approaches zero. These oscillations are a result of the rotational and vibrational temperatures being defined by a small number of simulated particles. Neither He^+ nor H_2^+ are produced in this scenario, but the number density of the atomic hydrogen ions and free electrons increases rapidly behind the shock and is on the order of the helium number density downstream as the flow approaches equilibrium. The free electron and atomic hydrogen ion number densities are identical in this simulation, so their lines overlay each other in Fig. 6.8. Charged species make up less than 10% of the total number of particles, but modeling this ionization is important for the calculations of radiation and comparisons to experimental measurements.

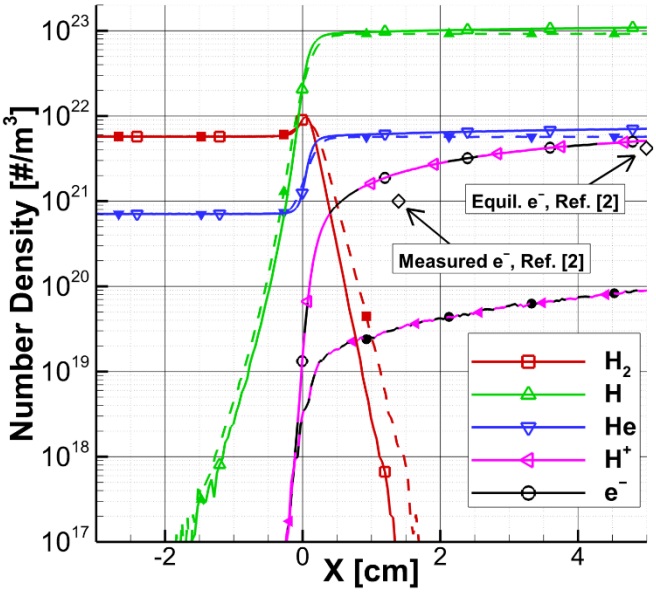

Figure 6.8 Simulated particle number densities including electronic excitation (solid line, empty symbols) and without electronic excitation (dashed line, filled symbols) relative to the shock location for EAST Shot 25.

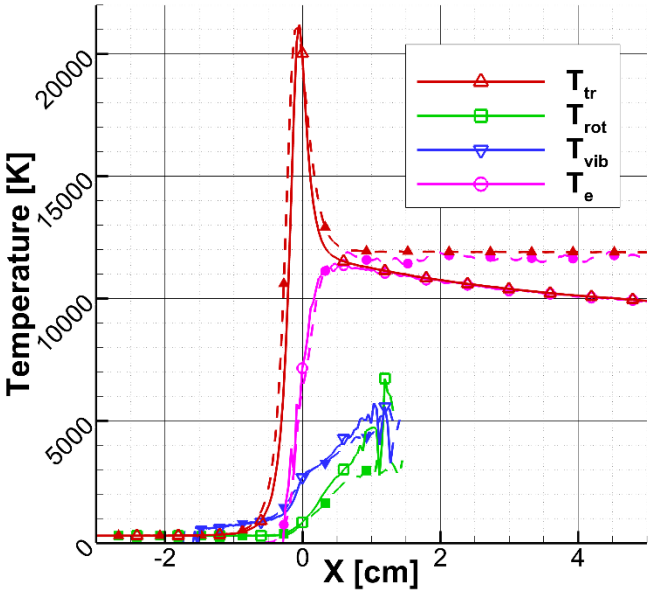

Figure 6.9 Simulated macroscopic temperatures including electronic excitation (solid line, empty symbols) and without electronic excitation (dashed line, filled symbols) relative to the shock location for EAST Shot 25.

In Ref. [2], Cruden and Bogdanoff estimated the free electron number density from Stark analysis and found the number density to be approximately 1.0×10^{21} m^{-3} at 1.4 cm behind the shock. This value is determined from a low resolution Balmer-γ line measurement with a large uncertainty. Cruden and Bogdanoff found that at about 3 cm, the free electron number density is increasing, but does not quite reach the equilibrium value of roughly 4.2×10^{21} m^{-3} by 5 cm. In Fig. 6.8, the free electron number density is seen to be slightly greater than the Ref. [2] value at 1.4 cm and increasing rapidly. By 5 cm, the free electron number density in Fig. 6.8 is already larger than the expected equilibrium value and Fig. 6.9 proves that equilibrium has not yet been reached at this point. The temperatures equilibrate to each other behind the shock, but the ionization process is still occurring, and the system has not yet reached full equilibrium by 5 cm behind the shock. The poor free electron number density comparison and overshoot of equilibrium can most likely be attributed to errors in the curve fitted backward reaction rates, particularly the free electron capture rates, and the misrepresentation of the corresponding equilibrium constant.

In addition to comparisons with analyses of the experimental results, the CHIPS simulation of Shot 25 can be directly equated to the experimental data by processing the output through NEQAIR to obtain emission spectra. Figs. 6.10-13 compare the experimental results to the convolved output from the radiation solver in the VUV, UV/Vis, Vis/NIR, and IR spectral ranges. All four ranges detect emission due to various transitions from excited atomic hydrogen states along with Lyman band emission from molecular hydrogen in VUV. The simulated molecular and Lyman-α emission in the VUV range (Fig. 6.10) occurs post-shock where pre-shock emission from heated H was expected upon comparison with the EAST results in Fig. 6.10. The Lyman-α emission occurs from the (2S→1S) transition in electronically excited H. Slight diffusion of atomic

H is seen upstream of the shock in Fig. 6.8. Although not definitive, this generally agrees with the observations of Lyman-α radiation in the pre-shock region, which Cruden and Bogdanoff [2] concluded was due to atomic hydrogen diffusing upstream of the shock. In Ref. [2], it was determined that optically thick radiation would be seen for atomic hydrogen number densities as low as 1.0×10^{18} m^{-3}. The CHIPS simulation predicts H number densities this large as far as 1.2 cm upstream of the shock suggesting again that this upstream H could be emitting if it is hot enough.

It is apparent in Figs. 6.10-13 that the simulated results currently overpredict the radiance throughout most of the measured region. In addition, the delayed radiative transition (or induction time) observed in the EAST experiments is not predicted in the simulation. Figure 6.13 shows drastic differences between the experimental and calculated emission from the near-IR Paschen lines and there seems to be little agreement between the two results. On the other hand, the simulated radiance in Figs. 6.11 and 6.12 seem to reproduce the correct magnitude and shape, but the simulated radiance occurs several centimeters before the experiment's radiance. Regardless, it is encouraging that the radiance measurements are of the correct shape and rough order of magnitude compared to the experimental data for these two ranges. The current discrepancies may be due to several factors including the omission of ambipolar diffusion, the use of assumed Boltzmann distributed electronic state populations for H atoms in NEQAIR, inaccurate high temperature data for the H_2-He mixture, or misrepresentation of the electronic temperature input into NEQAIR. The use of an incorrect electronic temperature input to NEQAIR is the most likely culprit in missing the upstream Lyman-α emission. As stated earlier, the simulated electronic temperature is determined from the kinetic energy of the electrons such that the *electronic* temperature and *free electron* temperature are assumed equal. Since free electrons are not found upstream of the shock

in the present simulations, the electronic temperature in this region is undefined. This representation of the electronic temperature does not take into account the fact that excited hydrogen has diffused upstream of the shock. With the implementation of a temperature model that combines both the kinetic electron energy and the excited states of the particles, NEQAIR should predict Lyman-α emission in this upstream region.

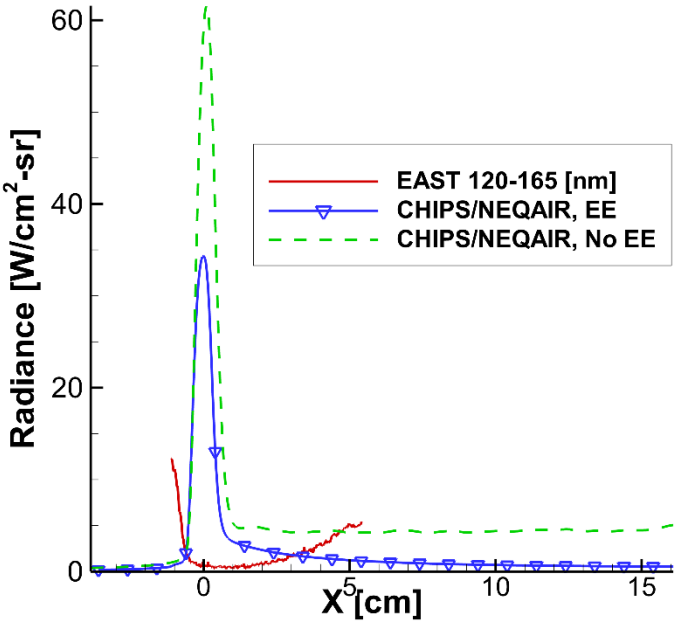

Figure 6.10 Simulated radiance with and without electronic excitation (EE) in the VUV range relative to the experimental data for EAST Shot 25.

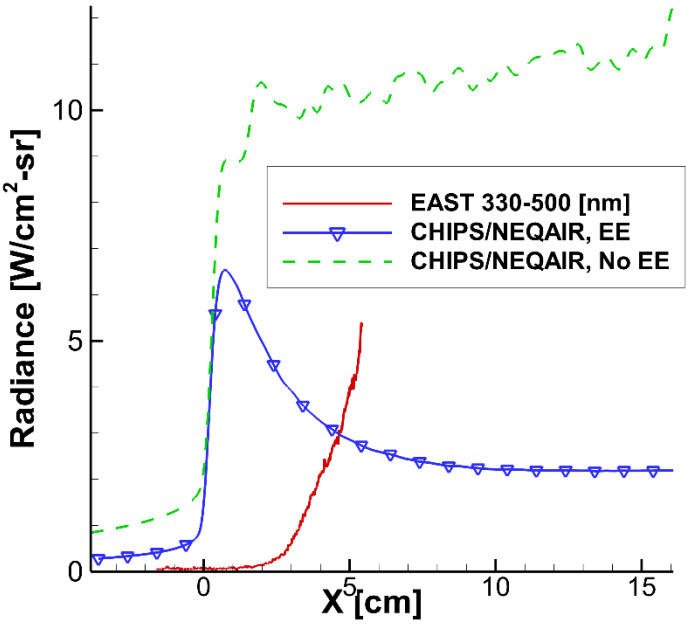

Figure 6.11 Simulated radiance with and without electronic excitation in the UV/Vis range relative to the experimental data for EAST Shot 25.

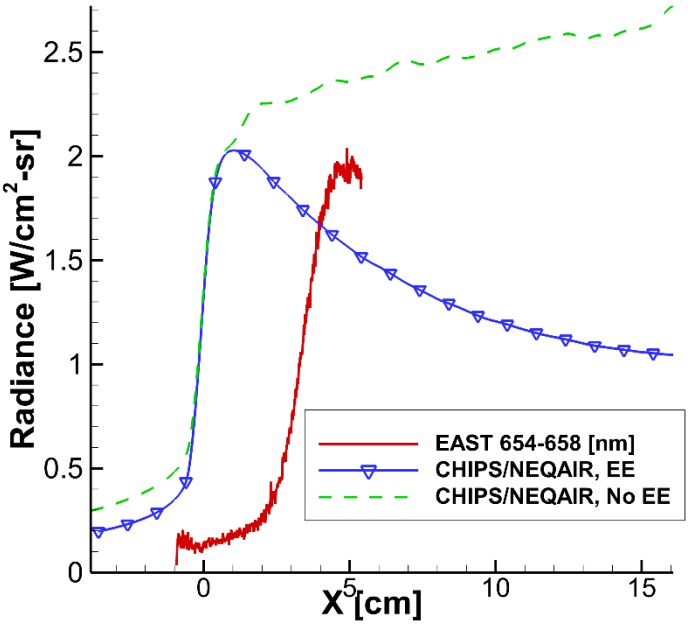

Figure 6.12 Simulated radiance with and without electronic excitation in the Vis/NIR range relative to the experimental data for EAST Shot 25.

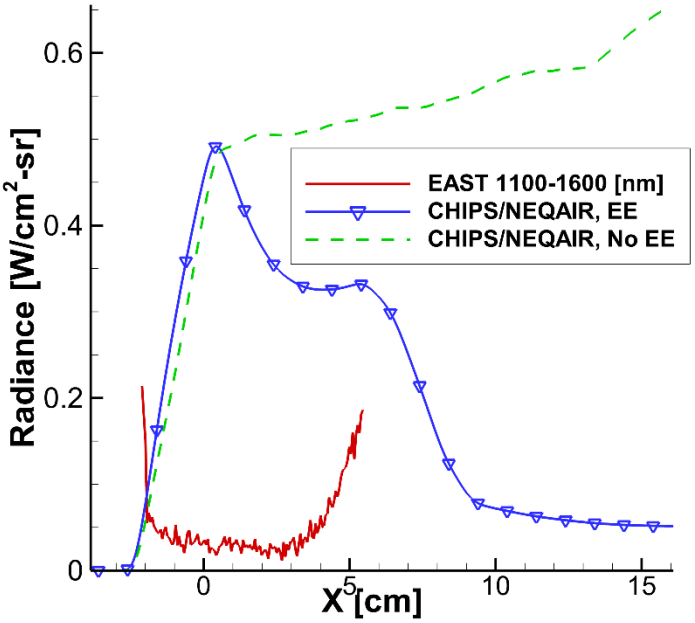

Figure 6.13 Simulated radiance with and without electronic excitation in the IR range relative to the experimental data for EAST Shot 25.

In order to demonstrate the importance of including electronic excitation in the CHIPS model for high temperature flows, Figs. 6.8-13 compare simulations with and without the electronic excitation model. The most drastic improvement is seen in Fig. 6.8 where the number density of the charged species has increased by nearly two orders of magnitude. In turn, this has an effect on the radiation produced by the NEQAIR code. In addition, the translational and free electron temperatures continue decreasing post-shock, presumably because the chemical reactions and electronic energy distributions continue to approach equilibrium. When comparing the effects on the radiance of including electronic excitation in the CHIPS code (Figs. 6.10-13), the improvement in the magnitude and shape of the downstream region of the emission calculation is encouraging.

6.5.2 EAST Shot 17 Simulation

To compare the results to a lower density experiment, the CHIPS model with electronic excitation is used to simulate Shot 17 from the same experimental campaign in the EAST shock tube. Figures 6.14 and 6.15 show the simulated number densities and temperatures as a function of the spatial location relative to the shock for a velocity of 27.4 km/s and initial gas pressure of 0.1 Torr. The length until complete dissociation of H_2 is nearly three times larger than for Shot 25 and no ions besides H^+ are present downstream. In this shot, Lyman-α measurements were used by Cruden and Bogdanoff [2] to calculate a constant free electron density of approximately 5.0×10^{20} m^{-3} from the shock front up to approximately 2.5 cm post-shock (not shown in Fig. 6.14), though the actual values may have been lower due to resolution limitations. In Ref. [2], the equilibrium free electron number density was determined to be 2.0×10^{21} m^{-3}. The simulated free electron number density in Fig. 6.14 is fairly consistent with the measured experimental number density, but demonstrates a gradually increasing trend that exceeds the 5.0×10^{20} m^{-3} electron density measure in Ref. [2] before 2.5 cm. This trend continues downstream and appears to be approaching the equilibrium free electron number density value calculated in Ref. [2]. Investigation further downstream showed, however, that the free electron number density eventually surpasses the equilibrium value, and this is again attributed to the incorrect backward reaction rates. As was seen in Shot 25, atomic hydrogen diffuses upstream of the shock, but in this case the diffusion distance is much longer. To support the previous claim that this hydrogen is hot and the source of the Lyman-α band emission seen in the simulations, the translational temperature of H is plotted in Fig. 6.15. The pre-shock temperature of atomic hydrogen is between 20,000-25,000 K and is hot enough to electronically excite the hydrogen, indicating again that an improved representation of the electronic temperature should produce more accurate

results in modeling the Lyman-α radiance. The low number of simulated particles leads to significant statistical noise in the pre-shock temperature profiles for atomic hydrogen and free electrons. A similar effect is seen in the rotational and vibrational temperature profiles of H_2 nearing complete dissociation.

After post-processing the CHIPS results with NEQAIR and convolving the radiance with the instrument line functions, simulated emission profiles for the VUV, UV/Vis, and Vis/NIR wavelengths were produced (Figs. 6.16-18). As in Shot 25, the magnitude of the radiance does not agree with the experimentally measured values. In the VUV range (Fig. 6.16), the width of the spike is comparable to the measured radiance, although this computed peak again occurs at the shock front instead of in the pre-shock region. The onset of modeled radiance in the UV/Vis range seems to follow the same trend as the experimental data, but a shift in where emission begins is again seen. Similarities between the simulation and experiment are more difficult to determine in the Vis/NIR range, but the radiance increases at the shock front for both sets.

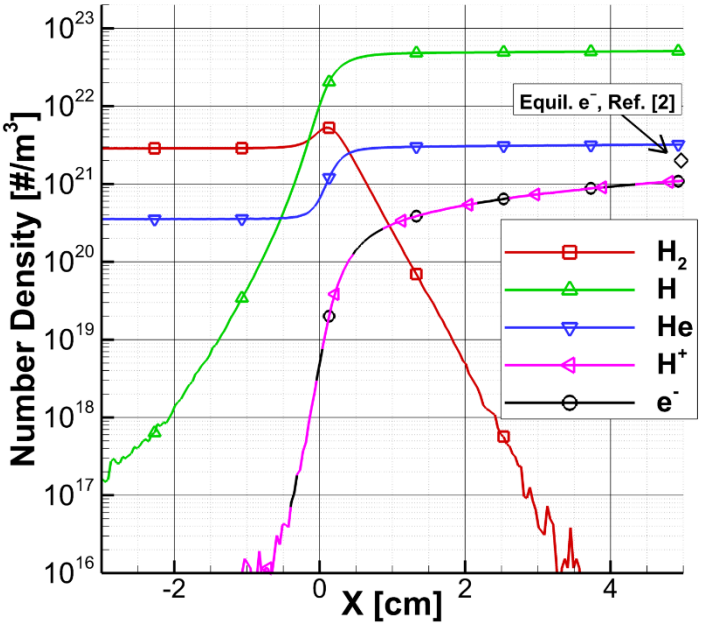

Figure 6.14 Simulated particle number densities relative to the shock location for EAST Shot 17.

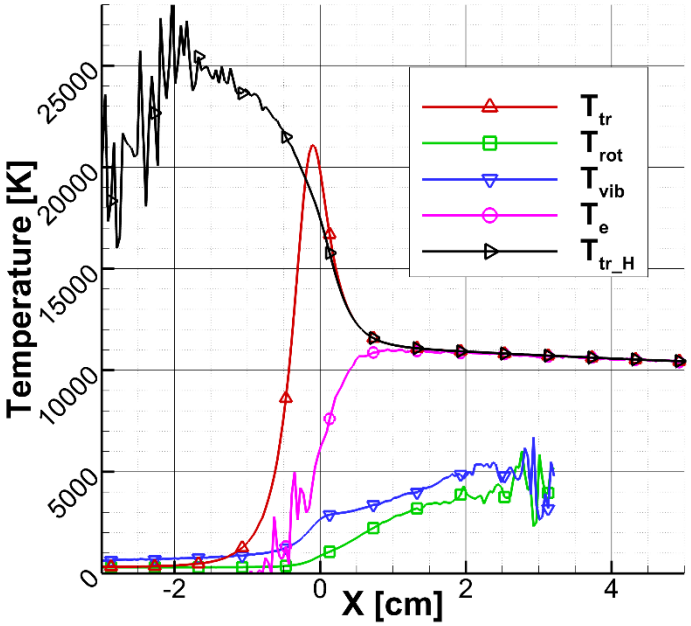

Figure 6.15 Simulated macroscopic temperatures relative to the shock location for EAST Shot 17.

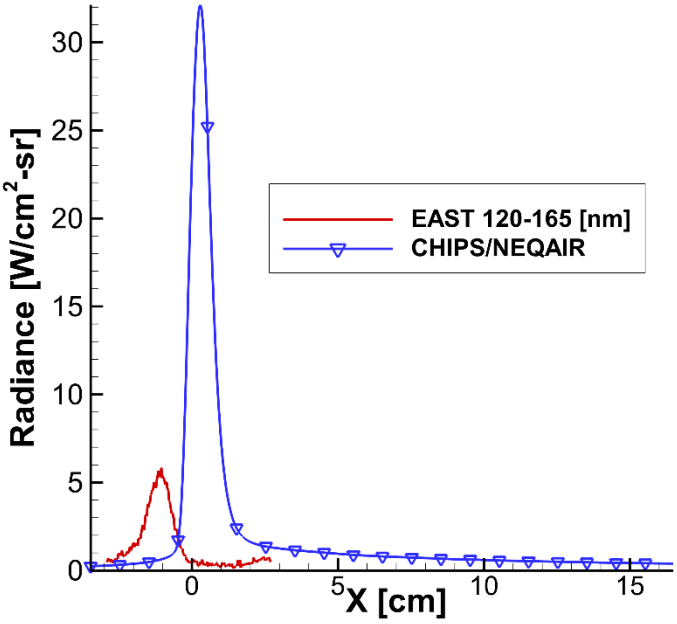

Figure 6.16 Radiance in the VUV range relative to the shock location for EAST Shot 17.

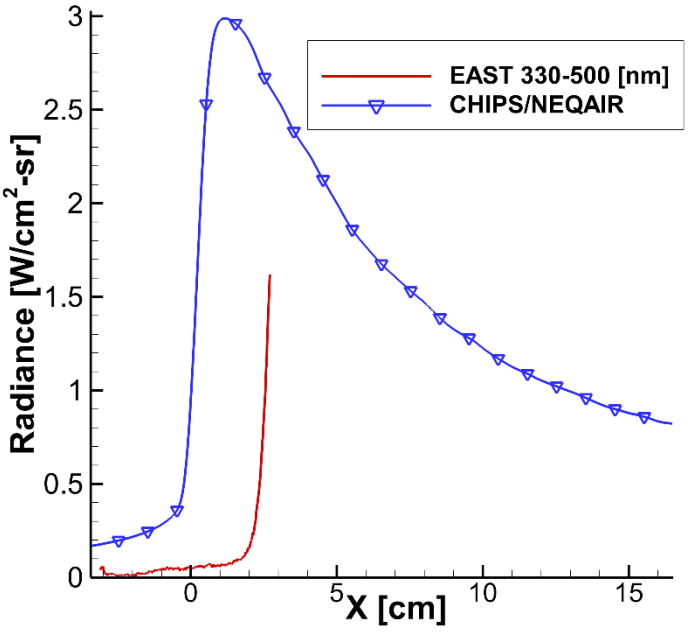

Figure 6.17 Radiance in the UV/Vis range relative to the shock location for EAST Shot 17.

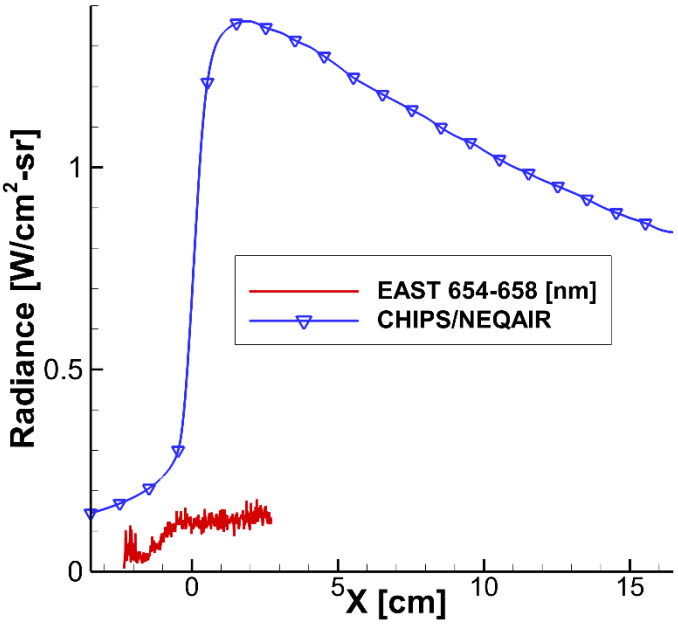

Figure 6.18 Radiance in the Vis/NIR range relative to the shock location for EAST Shot 17.

It is obvious from these results that significant improvements must be made in order to compare DSMC simulations with the experimental data. One potential source of error is that the electronic temperature used in these CHIPS simulations is assumed to be equivalent to the free electron temperature. Another potential source of error arises through the method of passing this temperature to NEQAIR, where the code then calculates the excited state distributions. As NEQAIR assumes Boltzmann distributions at the passed temperature, it effectively removes the nonequilibrium information obtained through the CHIPS simulation. These two complications are explored in Chapter 8. In addition, difficulties in simulating the correct backward reaction rates were identified as a cause of error in the Saturn simulations. It was found that the backward reaction rate curve fits were unable to accurately match the reaction rates calculated from the

equilibrium constant. It is likely that incorrect reaction rate modeling affected both the CHIPS and NEQAIR results. To improve the modeling of backward reaction rates in DSMC, the following chapter introduces a new reaction rate model.

CHAPTER 7

DSMC Chemistry Modeling

7.1 Overview

Completion of the nominal simulations in Chapter 4, preliminary sensitivity analyses in Chapter 5, and Saturn simulations in Chapter 6 demonstrated various ways in which the results of the CHIPS simulations of ionizing, hypersonic shock waves are affected by chemical reactions. Information gained from these results can now be put to use in the improvement of several CHIPS models. First, the significant difference in the two nominal simulations and sensitivity analysis studies due to the inclusion of an electronic excitation model needs further examination. The effect of electronically excited states on the ionization rate must be understood due to the high ranking of ionization reactions in the sensitivity analysis results. In the preliminary conclusions of Chapter 5, it was also postulated that the backward reaction model plays an important role in simulating several reactions, such as electron capture reactions. The importance of backward reaction modeling was again highlighted in the Saturn entry simulations when the free electron number density was greater than the expected equilibrium concentration. One issue with the current backward reaction model is that the chemical reaction set is missing several backward reaction rates that are likely to prevent the correct equilibrium composition from forming. All these concerns involving the CHIPS chemistry model are investigated in the current chapter.

7.2 Arrhenius Chemistry

Before the chemistry models used in DSMC can be analyzed, a brief overview of Arrhenius chemistry is required. Let us consider a reaction with N_r reactants that results in N_p products,

$$\sum_{i=1}^{N_r}(\alpha_i X_i) \rightleftharpoons \sum_{j=1}^{N_p}(\beta_j X_j) \qquad [7.1]$$

$$\alpha_r = \sum_{i=1}^{N_r}\alpha_i - 1 \qquad [7.2]$$

$$\beta_p = \sum_{j=1}^{N_p}\beta_j - 1 \qquad [7.3]$$

where X_i is any reacting molecular species, α_i and β_j are stochiometric constants, and the forward reaction in Eqn. 7.1 proceeds from left to right. The forward reaction rate, k_f, is represented in modified Arrhenius form by the equation

$$k_f(T) = \Lambda_f T^{\eta_f} exp\left(-{E_{a_f}}/{k_B T}\right) \qquad \left[\frac{1}{s}\left(\frac{cm^3}{mol}\right)^{\alpha_r}\right] \qquad [7.4]$$

where Λ_f is the pre-exponential constant, η_f is the temperature exponent, and E_{a_f} is the activation energy. The activation energy is the minimum energy required for the reaction to occur and is typically fairly well known for a specific reaction. The constants, Λ_f and η_f, are parameters that are adjusted to fit experimental or calculated forward reaction rates as a function of temperature. It is not uncommon to find differing values of these constants in the literature. The equilibrium constant, K_{eq}, is defined as

$$K_{eq}(T) = \frac{k_f(T)}{k_b(T)} \tag{7.5}$$

where k_b is the backward reaction rate. The equilibrium constant is defined such that detailed balance, or more specifically, the law of mass action is satisfied [75]. This allows the equilibrium constant to be represented as

$$\begin{aligned} K_{eq}(T) &= \frac{\prod_j^{N_p} (n_j)^{\beta_j}}{\prod_i^{N_r} (n_i)^{\alpha_i}} \\ &= \frac{\prod_j^{N_p} (Q_j)^{\beta_j}}{\prod_i^{N_r} (Q_i)^{\alpha_i}} V^{(\alpha_r - \beta_p)} exp\left(-\Delta H^\circ / k_B T\right) \quad \left[\left(\frac{mol}{cm^3}\right)^{(\beta_p - \alpha_r)}\right] \end{aligned} \tag{7.6}$$

with n_i and Q_i defined as the number density and total partition function of the current species, ΔH° as the enthalpy of the reaction from reference temperature 298.15 K, and V as the volume. Typically, the equilibrium constant is determined from high order partition functions or ab initio calculations and then the backward reaction rate is calculated by rearranging Eqn. 7.5.

7.3 Total Collision Energy Chemistry Model

Since DSMC is a particle method where chemistry must be applied on a per collision basis, the modified Arrhenius reaction rate equation cannot be used in its current form. Instead, methods have been proposed to utilize the properties of the colliding particles in order to produce the Arrhenius rate. The most widely used method for performing forward reactions with Arrhenius rate chemistry in DSMC is the Total Collision Energy (TCE) model [3][15], briefly discussed in Section 2.3.2. Other common

chemistry methods exist, such as the quantum-kinetic (Q-K) model [35] or the use of molecular dynamics/quasi-classical trajectory (MD/QCT) calculations [76], to perform chemistry in DSMC, but they do not apply Arrhenius rate equations and will not be discussed here.

When two particles are selected to collide in a chemically active DSMC simulation, a probability for each possible reaction must be determined. In the TCE model, the reaction probability is calculated from the energy contained in the colliding particles. This includes the relative translational energy of the colliding particles and the contributing internal energy of each individual particle. Once the reaction probabilities are calculated, they are each compared to a previously drawn random number to determine if a reaction takes place. If a reaction is selected to occur, the reaction products are created and the total relative translational and internal energies of the reactants, less the enthalpy of reaction, $\Delta H°$, are redistributed to the products using the Borgnakke-Larsen model [25]. While this seems straightforward, there have recently been misunderstandings with the assumptions and limitations of the TCE model that will be discussed in the following sections.

7.3.1 TCE Model Derivation

First, a brief analysis of the TCE model's derivation is required. In Bird's 1994 book [3], the derivation of the TCE model begins with the distribution functions for the relative translational and internal energy of the colliding particles (pg. 104-5, 126). While this is a valid starting point, the derivation of the distribution function for internal energy must be considered to understand the underlying assumptions in the TCE model. The subsequent summary follows Hinshelwood's derivation of the distribution function for

internal energy [77]. Hinshelwood begins by defining a momentum coordinate, p, and its corresponding energy, ε, for some motion in a coordinate, x.

$$p = mx, \quad \varepsilon = \frac{1}{2}mx^2 \tag{7.7}$$

Every different coordinate, x, describes a separate degree of freedom such as a directional velocity (translational), angular momentum (rotational), etc. This representation of momentum and energy follows from classical mechanics where each degree of freedom contributes a single quadratic ("square") term to the energy. It is important to note that, from the equipartition theorem, each individual degree of freedom that is quadratic in energy contributes equally to the total energy in thermal equilibrium. It can be shown that this quantity is

$$\bar{\varepsilon} = \frac{1}{2}k_B T \tag{7.8}$$

where $\bar{\varepsilon}$ is the average energy that the single degree of freedom possesses at equilibrium.

Now consider a series of quantized energy states $\varepsilon_i = \varepsilon_1, \varepsilon_2, \ldots, \varepsilon_M$ where the probability of a particle being in state j is defined by the Boltzmann distribution as

$$\frac{N_j}{N} = \frac{exp\left(-{}^{\varepsilon_j}/_{k_B T}\right)}{\sum_{i=1}^{M} exp\left(-{}^{\varepsilon_i}/_{k_B T}\right)} \tag{7.9}$$

with N_j being the number of particles in state j. This fraction can be converted from the quantum to the classical theory by following Hinshelwood and the number of particles, dN, with momentum between p and $p + dp$ is found to be

$$\frac{dN}{N} = \frac{\varepsilon^{-\frac{1}{2}} exp\left(-{}^{\varepsilon}/_{k_B T}\right) d\varepsilon}{\sqrt{\pi k_B T}} \qquad [7.10]$$

which is true regardless of the type of energy, translational or internal. If a particle with ζ degrees of freedom is now considered, there are ζ different quadratic terms that contribute to the fraction of molecules where the total energy, E, is between E and $E + dE$. By combining and integrating each term, this fraction becomes

$$\frac{dN}{N} = \frac{1}{(\pi k_B T)^{\frac{1}{2}\zeta}} \int_0^E \int_0^E \dots \varepsilon_1^{-\frac{1}{2}} exp\left(-{}^{\varepsilon_1}/_{k_B T}\right) d\varepsilon_1 \times \varepsilon_2^{-\frac{1}{2}} exp\left(-{}^{\varepsilon_2}/_{k_B T}\right) d\varepsilon_2 \dots \\ \dots [E - (\varepsilon_1 + \varepsilon_2 \dots)]^{-\frac{1}{2}} exp\left(-{}^{[E - (\varepsilon_1 + \varepsilon_2 \dots)]}/_{k_B T}\right) dE \qquad [7.11]$$

where the energy in the final term, ε_ζ, is replaced by rearranging

$$E = \varepsilon_1 + \varepsilon_2 + \cdots + \varepsilon_\zeta \qquad [7.12]$$

After integrating Eqn. 7.11, the distribution of E is found to be

$$f_{\left(E/k_BT\right)} = \frac{\left(E/k_BT\right)^{\frac{\zeta}{2}-1} exp\left(-E/k_BT\right)}{\Gamma\left(\frac{\zeta}{2}\right)} \quad [7.13]$$

which has been normalized by k_BT. This is the distribution function for the internal energy in a molecule with ζ degrees of freedom and is the starting point in Bird's 1994 book [3].

Following Bird's derivation, the reaction cross-section, σ_R, for two colliding particles A, B with a total collision energy, E_c, is assumed to take the form

$$\sigma_R = \begin{cases} 0 & if\ E_c < E_a \\ \sigma_T C_1 (E_c - E_a)^{C_2} (1 - E_a/E_c)^{\zeta_I + 3/2 - \omega_{A,B}} & if\ E_c > E_a \end{cases} \quad [7.14]$$

where C_1 and C_2 are constants to be determined, σ_T is the total collision cross-section, and

$$\zeta_I = \sum_{i=1}^{N_{\zeta_A} + N_{\zeta_B}} \frac{\zeta_i}{2} \quad [7.15]$$

which is the total contribution of the internal degrees of freedom of each particle. In Eqn. 7.15, N_{ζ_A} and N_{ζ_B} are the number of contributing internal degrees of freedom from particles A and B. Note that calling ζ_I the "average degrees of freedom" is a common misconception in the DSMC community because the two in the denominator of Eqn. 7.15 originates from the assumption that ε is a square term (Eqn. 7.7), not from averaging the degrees of freedom between colliding particles A and B. Also, the total collision energy

(Eqn. 7.16) is determined from the sum of the relative translational energy of the colliding particles, E_{tr}, and the internal energy of each contributing internal mode, E_{int}.

$$E_c = E_{tr} + \sum_{i=1}^{N_{\zeta_A}+N_{\zeta_B}} E_{int_i} \quad [7.16]$$

After determining the constants in Eqn. 7.14 by considering the Variable Hard Sphere (VHS) model [15] collision frequency and comparing with the modified Arrhenius equation (Eqn. 7.4), the reaction probability for binary collisions with $E_c > E_a$ is found to be

$$P_{react} = \frac{\sigma_R}{\sigma_T}$$

$$= \frac{\sqrt{\pi}\left(1+\delta_{A,B}\right)\Lambda T_{ref_{A,B}}^{\eta}}{2\pi d_{ref_{A,B}}^2 \left(k_B T_{ref_{A,B}}\right)^{\eta-1+\omega_{A,B}}} \frac{\Gamma\left(\zeta_I + \frac{5}{2} - \omega_{A,B}\right)}{\Gamma\left(\zeta_I + \eta + \frac{3}{2}\right)} \sqrt{\frac{m_r}{2k_B T_{ref_{A,B}}}} \frac{\left(E_c - E_a\right)^{\eta+\zeta_I+\frac{1}{2}}}{E_c^{\zeta_I+\frac{3}{2}-\omega_{A,B}}} \quad [7.17]$$

In Eqn. 7.17, the VHS parameters for the colliding particles (A, B) are d_{ref}, T_{ref}, and ω. Also, $\delta_{A,B}$ is one when $A = B$ and zero otherwise. This is the final form of the TCE model and is used to calculate the reaction probability for each possible reaction that a pair of colliding particles can undergo.

7.3.2 Limitations Due to Model Requirements

In the TCE model, the reaction probability calculated from Eqn. 7.17 is solely dependent on the properties of the colliding particles being considered. While this is advantageous for simulating a non-equilibrium flow, there are various limitations that

must be considered when utilizing the TCE model. Analysis of the relationships between the contributing internal degrees of freedom, ζ_I, the VHS temperature-viscosity exponent, $\omega_{A,B}$, and the Arrhenius temperature exponent, η in Eqn. 7.17 identifies some of these limitations. In order for Eqn. 7.17 to produce the expected or, in some cases, realistic trends, these parameters must satisfy various constraints. First, the reaction probability must tend to zero as E_c approaches E_a since a nonzero reaction probability at the activation energy is unphysical. This leads to the requirement that the Arrhenius temperature exponent must satisfy $\eta > -\zeta_I - 1/2$ and represents the lower limit for η. If this requirement is not met, the reaction probability approaches infinity when $E_c = E_a$ and is clearly unphysical. The upper limit of η is not as easily defined and previous publications have identified the upper limit from Eqn. 7.17 to be $\eta < \omega_{A,B} - 1$ [3][36]. This limit is intended to be set so that the reaction probability approaches zero as E_c approaches infinity. Analysis of Eqn. 7.14 yields a different result for this upper limit. Since it is desired that $\sigma_R \to 0$ when $E_c \to \infty$, the value of C_2 must be negative so that the term $(E_c - E_a)^{C_2}$ appears in the denominator. In the original derivation of Eqn. 7.17, it was found that $C_2 = \eta - 1 + \omega_{A,B}$ and leads to the conclusion that the upper limit is actually $\eta < 1 - \omega_{A,B}$. If η is greater than this limit, the reaction rate increases monotonically towards infinity as the collision energy increases instead of decreasing back to zero. In summary, the Arrhenius temperature exponent must satisfy

$$-\zeta_I - 1/2 < \eta < 1 - \omega_{A,B} \qquad [7.18]$$

which represents the hard limits of the η values. If these constraints are met, the reaction probability will be zero when $E_c = E_a$, increase to some maximum probability as E_c

increases, and then decrease back to zero as E_c approaches infinity. An example of the expected trend is shown by the $\eta = -1.5$ case in Fig. 7.1 for the dissociation reaction $O_2 + N_2 \rightleftharpoons O + O + N_2$ which represents the reaction probability as a function of collision energy for the published value of the Arrhenius temperature exponent. Only the rotational modes are considered in this case with the parameters used in this calculation listed in Tables 7.1 and 7.2 [3][44][48].

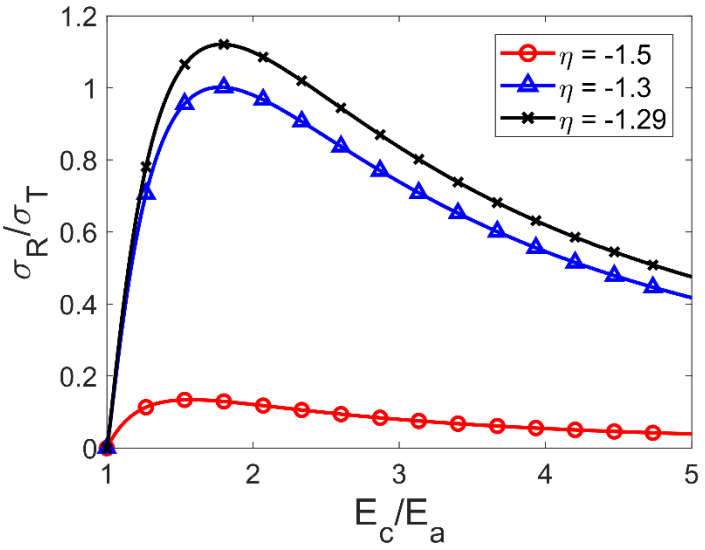

Figure 7.1 TCE reaction probability as function of the collision energy for various values of η in the O_2 dissociation reaction, $O_2 + N_2 \rightleftharpoons O + O + N_2$.

Table 7.1 Arrhenius rate reactions and equilibrium constants used in this chapter.

Reaction	Forward Arrhenius Rate, k_f [m^3/molec-s]			Backward Arrhenius Rate, k_b [m^3/molec-s]	
$O_2 + N_2 \rightleftharpoons O + O + N_2$	$3.321 \times 10^{-9} T^{-1.5} \exp(-59400/T)$				
$O + N_2 \rightleftharpoons N + NO$	$1.069 \times 10^{-12} T^{-1.0} \exp(-37500/T)$			$4.059 \times 10^{-12} T^{-1.359}$	
Park's equilibrium constant, K_{eq} [47]	A_1	A_2	A_3	A_4	A_5
$O_2 + N_2 \rightleftharpoons O + O + N_2$	0.967940	0.891310	0.729100	-3.955500	0.006488

Table 7.2 Species model parameters used in this chapter.

Species i	N_2	N	O_2	O	NO
VHS reference diameter, d_{ref_i} [m]	4.17×10^{-10}	3.00×10^{-10}	4.07×10^{-10}	3.00×10^{-10}	4.20×10^{-10}
VHS temperature exponent, ω_i	0.74	0.8	0.77	0.8	0.79
Characteristic rotational temperature, θ_{rot} [K]	2.88	–	2.07	–	2.44
Characteristic vibrational temperature, θ_{vib} [K]	3390	–	2270	–	2740
Electronic energy levels	Ref. [48]	–	Ref. [48]	–	Ref. [48]

While it seems like the identification of the correct upper limit extends the range of possible η values compared to previous publications, in some cases approaching this limit may be detrimental to reproducing the correct Arrhenius rate. A parametric study where η was varied over the range of Eqn. 7.18 showed that, for some reactions, Eqn. 7.17 produces maximum reaction probabilities greater than one even if Eqn. 7.18 is satisfied. This can occur beginning at some value of η and extends until the previously

determined upper limit is reached. Probabilities greater than one cannot be accounted for in the current form of the TCE model and will result in discrepancies between the actual and simulated Arrhenius rate. Although probabilities greater than one are unphysical, they may be acceptable in certain collision energy ranges with minor adverse effects on the simulated Arrhenius rate. For example, consider the previously mentioned O_2 dissociation reaction. The upper limit for this reaction, using the parameters listed in Tables 7.1 and 7.2 and according to Eqn. 7.18, is $\eta = 0.245$, but Fig. 7.1 shows that the reaction probability will reach values greater than one when $\eta \gtrsim -1.3$. Now consider the case in Fig. 7.1 where $\eta = -1.29$. The reaction probability is realistic for $E_c < 1.4E_a$, but the probability is greater than one from 1.4 to $2.5E_a$. The region where the reaction probability is greater than one is concerning because the appropriate number of reactions will not be modeled. But, this should have a negligible effect on the simulated Arrhenius rate since a reaction this energetic is rare and it is unlikely, for most simulated scenarios, that a highly energized molecule would survive previous collisions without dissociating. If an even larger value of η is used, more of the probability curve will be larger than one and, at some point, effects on the simulated reaction rate will be felt. Unfortunately, this means that in addition to satisfying Eqn. 7.18, each reaction must be individually considered to determine if the reaction probability is greater than one for substantial portions of the collision energy range significant to the intended DSMC application. The effect on the Arrhenius rate can be studied by initializing a single DSMC cell in equilibrium at some temperature of interest, counting the number of accepted reactions (without performing the reactions/collisions), and comparing the simulated DSMC reaction rate to the expected Arrhenius rate.

7.3.3 Solutions for Satisfying Model Requirements

Arrhenius reaction rate values are typically compiled from published curve fits of ab initio or experimental results. As might be expected, these Arrhenius rates are published without regard for the limitations of the TCE model, so it is not unusual to encounter Arrhenius temperature exponent values that violate the constraints of the TCE model. The standard approach to using these reaction rates with TCE is to refit the Arrhenius parameters, Λ and η, to the original Arrhenius rate over the temperature range of interest, while constraining η to values compatible with the TCE model. While this avoids introducing errors through the TCE model, the simulated reaction rate may no longer be as accurate as the original Arrhenius rate. As an alternative to refitting the Arrhenius rate equation for certain cases, the VHS parameters could be refit so that $\omega_{A,B}$ is small enough to allow for a larger η value. While the effects of changing $\omega_{A,B}$ are much more difficult to predict, sensitivity analysis results for a high temperature reacting heat bath DSMC simulation have shown that results may be much more sensitive to reaction rate parameters than VHS parameters [78]. This is most likely due the relatively small variation of the VHS cross-section with temperature as high temperatures are reached [56].

While the approach of refitting parameters provides a simple solution, another method is available to remedy a subset of the issues with the Arrhenius temperature exponent. The derivation of the TCE model (Eqn. 7.17) assumes that the total collision cross-section, σ_T, is equivalent to the VHS cross-section, σ_{VHS} [3]. This approximation is valid for a pair of colliding particles as long as the total reaction probability of all the possible reactions for that pair is small, meaning that the reaction cross-section, σ_R, is much less than σ_{VHS}. This is typically true at low temperatures, but at high temperatures where dissociation and ionization are likely, the reaction cross-section can become large.

The reaction cross-section can even become greater than σ_{VHS} which will result in reaction probabilities greater than one as shown in Fig. 7.1. As previously discussed, reaction probabilities greater than one will result in an incorrect simulated Arrhenius rate. To calculate the appropriate total cross-section and avoid reaction probabilities greater than one, Strand and Goldstein proposed the modification

$$\sigma_T = \sigma_{VHS}\left(1 + \sum_{i=1}^{N_R}\left(\frac{\sigma_R}{\sigma_{VHS}}\right)_i\right) \quad [7.19]$$

where N_R is the number of possible reactions for the selected reaction pair and $(\sigma_R/\sigma_{VHS})_i$ is the reaction probability calculated from Eqn. 7.17 for each reaction, i [31]. The reaction probability for each reaction is now

$$P_{react_i} = \frac{\sigma_{VHS}}{\sigma_T}\left(\frac{\sigma_R}{\sigma_{VHS}}\right)_i \quad [7.20]$$

and the new total cross-section is also used to find the product of the total cross-section and the relative speed, $\sigma_T c_r$, which is compared to the maximum, $(\sigma_T c_r)_{max}$, to determine if a potential collision occurs. This method guarantees that the total reaction probability will not surpass one. It addresses the case where $\eta < 1 - \omega_{A,B}$, but the reaction probability is greater than one, essentially extending the limits of η to its true restrictions identified in Eqn. 7.18. One downside of including the reaction cross-section in the total cross-section is that the reaction probabilities must be calculated for each *potential* collision before it is accepted, thereby adding computational expense. Without this method, reaction probabilities were only calculated for *accepted* collisions. The other

downside is that $(\sigma_T c_r)_{max}$ can become prohibitively large. As presented by Bird [3][35], $(\sigma_T c_r)_{max}$ is used to calculate the number of potential collisions to consider at each timestep. For large values, many potential collisions must be considered. This can quickly cause a simulation to become intractable due to the sheer number of potential collisions that must be considered. An appropriate compromise for this issue is to limit Eqn. 7.17 for an individual reaction probability by selecting a maximum value, such as $P_{react_i} = 1$ which represents the case where $\sigma_{R_i} = \sigma_{VHS}$. This approach is taken in the CHIPS code and allows for improvement to the reaction modeling, but reduces the computational hit incurred by extreme values of the reaction probability.

7.3.4 Limitations Due to Model Assumptions

In addition to limitations on the TCE model parameters, the derivation of the TCE model has underlying assumptions that must be met. The derivation of the internal energy distribution (Eqn. 7.13) by Hinshelwood assumes that each degree of freedom depends quadratically on its coordinate [77]. The equipartition theorem then states that each quadratic degree of freedom contributes to an average energy of $1/2k_BT$ (Eqn. 7.8). The Borgnakke-Larsen model [25] also originates from the same internal energy distribution function and the effects of its underlying assumptions on the model have been analyzed in previous publications [79][80][81]. While much effort has been spent on the Borgnakke-Larsen model, the limitations of the TCE model due to the assumptions inherent to Eqn. 7.13 have been largely overlooked. When using the TCE model, the following restrictions must be considered.

First, the quadratic corollary to the equipartition theorem states that each degree of freedom used in the TCE model must correspond to a square term representing an average energy of $1/2k_BT$. While classical statistical mechanics restricts the degrees of

freedom used in Eqn. 7.13 to integer values [75][82], non-integer values can potentially be used as long as they satisfy the previous statement by returning the equivalent fraction of the average energy. As an example, consider the modeling of continuous rotational energy in a standard DSMC simulation. When either using the Borgnakke-Larsen model [25] to redistribute internal energy after a collision or initializing a particle entering the simulation, the internal energy is randomly selected from Eqn. 7.13 for a given temperature. Hypothetically, if the molecular species being assigned energy has a non-integer value for the rotational degrees of freedom, such as $\zeta_{rot} = 2.5$, the correct internal energy distribution and average energy of $2.5 \times 1/2k_BT$ will be produced from Eqn. 7.13. In turn, the non-integer degrees of freedom will have no effect on the reproduction of the correct Arrhenius rate by the TCE model. However, the TCE model will fail to reproduce the Arrhenius rate if the degrees of freedom and average internal energy do not match.

The second assumption contained within the equipartition theorem is that equipartition is only valid for classical statistical mechanics which requires that energy distributions are continuous. In DSMC simulations, rotational energy is typically modeled as continuous since most simulations are performed for temperatures where the rotational modes are fully excited. On the other hand, the vibrational modes are not yet fully excited for the temperatures modeled in most DSMC scenarios. It is common for DSMC simulations to be completed with quantum models for electronic and vibrational modes, such as the quantum simple harmonic oscillator (SHO) for vibration. If internal energy for certain modes are modeled discretely, these modes cannot contribute to the total collision energy used to calculate the reaction probability in Eqn. 7.17 without introducing some degree of error into the simulated reaction rate.

Figure 7.2 demonstrates the resulting error when including quantum internal energy in the TCE calculation. In Fig. 7.2, the same dissociation reaction as investigated previously (Tables 7.1 and 7.2) is considered, but this time both rotation and vibration are included in TCE where the vibrational modes are modeled with the discrete SHO. To obtain the Arrhenius rate simulated by DSMC, a single cell is filled with two million particles per species where the particles are initialized in equilibrium at the temperature of interest. During a timestep, the reaction probability is calculated for particles selected to collide, but collisions are never carried out. Instead, the number of accepted reactions is counted. Two timesteps are completed per simulation where the purpose of the first timestep is to obtain the correct total cross-section so that the appropriate number of potential collisions are considered. In the second timestep, the number of reactions are counted and this result is ensemble averaged over 16 instances of this simulation to obtain an accurate simulated Arrhenius rate. When comparing the DSMC results (Δ symbols) with the exact Arrhenius rate, a slight overshoot in the simulated reaction rate is observed at low temperatures. This error occurs because the discrete spacing in vibrational levels is important when the temperature is on the order of the characteristic vibrational temperature or lower. The value of the effective vibrational degrees of freedom is calculated as

$$\zeta_{vib} = \frac{2\theta_{vib}}{T_{vib}(e^{\theta_{vib}/T_{vib}} - 1)} \qquad [7.21]$$

where T_{vib} is the vibrational temperature and θ_{vib} is the characteristic vibrational temperature of the molecule. The SHO, and therefore, Eqn. 7.21 approaches the classical limit as the temperature becomes much larger than the characteristic vibrational

temperature. This causes the difference between the simulated and exact rate to decrease with increasing temperature. While the effects on the simulated reaction rate for this reaction are relatively small, these effects become more pronounced as the characteristic temperature or a molecule's vibrational complexity increases. This effect has been documented in a previous publication by Gimelshein, et al. where the simulated rate for a CO_2-CO_2 reaction is twice as fast as the expected rate [83]. While Gimelshein, et al. correctly pointed out that discrete representations of internal energy cannot be used in the TCE model, this was not attributed to the underlying assumptions of classical mechanics in the TCE model's derivation.

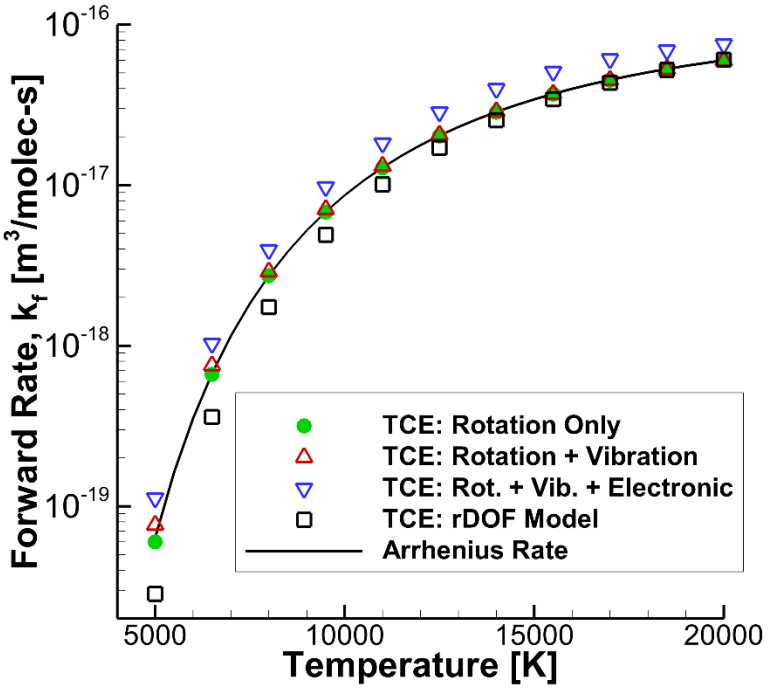

Figure 7.2 Comparison of the exact forward reaction rate for $O_2 + N_2 \rightleftharpoons O + O + N_2$ with DSMC using the TCE model with various internal mode contributions and with the rDOF model.

In the same publication, Gimelshein, et al. suggests a curve fitting method to adjust the Arrhenius parameters, Λ and η, so that discrete models can contribute to the total collision energy. This method has the distinct advantage of including the contributions of internal energy from all participating internal modes. In some cases, the energy contribution from the vibrational or electronic modes is arguably the most important for determining the reaction probability. For example, dissociation reactions rely heavily on the vibrationally excited state of the dissociating molecule and chemical models have been developed to address this dependence such as the Vibrationally Favored Dissociation model [36][84], although this model may suffer from the same discrete modeling issue as TCE. Since the curve fitting method addresses the errors from both discrete energy distributions and the resulting non-quadratic degrees of freedom, this may appropriately correct the TCE reaction probability. It is unclear whether this method has any unintended effects on non-equilibrium modeling, but it is difficult to obtain non-equilibrium cross-sections for comparison.

In addition to satisfying the equipartition theorem and being continuous, internal energy distributions used in the TCE model must follow the form of Eqn. 7.13. A somewhat common, yet unpublished, method that will be designated the reaction degrees of freedom model (rDOF) has been propagated through the DSMC community. The intention of the rDOF model is to correct the total collision energy by only including the internal energy modes that contribute to the specific reaction rate. In theory, this approach has the advantage of improving the realism for some reactions since not all available degrees of freedom may contribute to the reaction rate in a real particle collision [75]. To apply this theory, Eqn. 7.16 was modified such that

$$E_c = E_{tr} + \frac{\zeta_{react}}{\zeta_I} \sum_{i=1}^{N_{\zeta_A}+N_{\zeta_B}} E_{int_i} \qquad [7.22]$$

where ζ_{react} is the contributing degrees of freedom for the specific reaction. In addition, Eqn. 7.17 is calculated from ζ_{react} instead of using ζ_I from Eqn. 7.15. This approach seems to be allowed because the purpose of multiplying the contributing internal energy by the ratio of the degrees of freedom is to effectively scale the average energy for ζ_{react} and, therefore, would satisfy the equipartition theorem. In practice however, the rDOF model fails since the direct scaling of the internal energy for a selected reaction degrees of freedom value does not produce the correct internal energy distribution that is expected for those degrees of freedom. This failure occurs because the scaling is applied to the internal energy of the particles participating in individual collisions. In a DSMC simulation, the internal energy of the individual particles represents a collection of values randomly selected from equilibrium internal energy distribution functions (Eqn. 7.13) for each classical degree of freedom. To change the degrees of freedom represented by a simulated species, the particles must be reinitialized using the new degrees of freedom. For this reason, the scaled collision energy in the rDOF model produces the incorrect Arrhenius rate when used in the TCE model because the incorrect number of collisions are accepted for reaction. This occurs even though the TCE model is calculating the "correct" reaction probability for the scaled collision energy and degrees of freedom values.

In order to demonstrate the errors produced by the rDOF model, consider the same O_2 dissociation reaction as the previous section (Tables 7.1 and 7.2). Only the rotational modes are considered so that $\zeta_I = 2$ and an assumed reaction degrees of

freedom is set to $\zeta_{react} = 1$. Figure 7.3 shows the internal energy distributions calculated from Eqn. 7.13 for the original TCE case $\zeta = 2 \times \zeta_I = 4$ and the rDOF case $\zeta = 2 \times \zeta_{react} = 2$. To calculate the third line, representing the rDOF model, the rotational energy for a large number of particles was selected from the internal energy distribution for $\zeta = 4$. The rotational energy of each particle was then scaled following the second term on the right-hand side of Eqn. 7.22 where $\zeta_I = 2$ and $\zeta_{react} = 1$. The resulting internal energy distribution is plotted in Fig. 7.3 by the line with the ∇ symbols. This line would coincide with the $\zeta = 2$ case if the rDOF method were able to correctly modify the internal energy. Even though these lines do not match, they both will result in an average internal energy of $k_B T$ showing that the rDOF method satisfies equipartition. The resulting errors in the simulated Arrhenius rate occur because the rDOF model considers too many or too few reactions when compared to the correct distribution. Using this same example, Fig. 7.2 compares the forward rate simulated by the rDOF model in DSMC to the exact rate calculated from the Arrhenius equation in Table 7.1. Again, only the rotational modes are considered in the rDOF model. While it may seem that the rDOF model predicts the correct rate at high temperatures, this is not true for every reaction. The effect of ζ_{react} largely depends on its relationship to ζ_I, the Arrhenius parameters for the reaction, and the species involved in the reaction. In some cases, the effect of ζ_{react} is more pronounced at high temperatures and can even overpredict the reaction rate. While the simulation of the O_2 + N_2 reaction with the rDOF model shown in Fig. 7.2 still satisfies the TCE limitations set in Eqn. 7.18, this may not be the case for every reaction and would lead to further discrepancies between the simulated and exact rates.

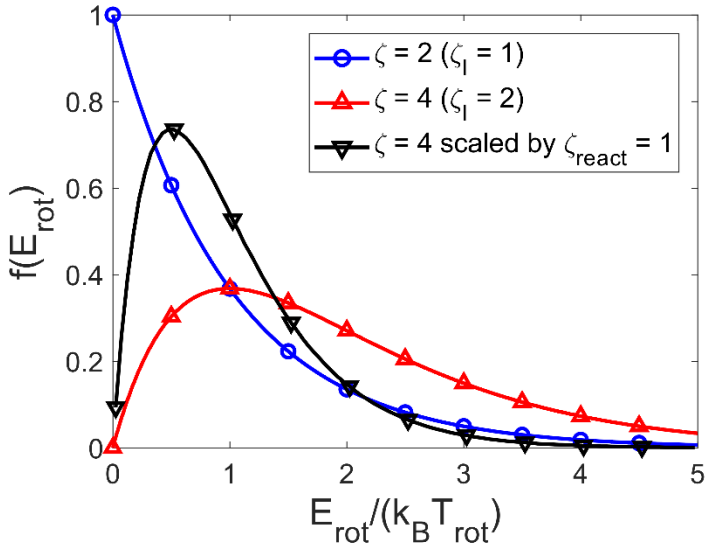

Figure 7.3 Analytic internal energy distribution functions for $\zeta = 2$ and 4 and rDOF model distribution function scaled from $\zeta = 4$ by a selected ζ_{react} value.

One final problem with of the TCE model remains to be discussed. The derivation of Eqn. 7.17 involved an integration over all collision energies, from the activation energy to infinity. In the past, most DSMC simulations assumed that the enthalpy of the reaction is equal to the activation energy of the forward rate, where the forward rate is defined as the endothermic side of the reaction. In turn, the activation energy for a backward reaction is then set to zero. These assumptions lead to errors in modeling the correct amount of energy absorbed or released in each reaction since the enthalpy of reaction is not typically equal to the activation energy. If the correct enthalpy of reaction is used, the TCE model may still encounter problems if this enthalpy is greater than the activation energy. Since a reaction cannot occur unless the collision energy is greater than both the enthalpy of reaction and the activation energy, the enthalpy of reaction is the minimum collision energy required in this case. Because Eqn. 7.17 was derived assuming

that any collision energy greater than the activation is allowed, collisions with energy between the activation energy and enthalpy of reaction values would result in a reaction probability of zero. This leads to an under-simulation of the reaction rate. While, in reality, this scenario is not physical as the activation energy must always be greater than or equal to the enthalpy of reaction, modifications of the Arrhenius rate for several reactions have violated this requirement in an attempt to fit rates that were previously incompatible with the TCE model.

7.3.5 Solutions for Satisfying Model Assumptions

While there are many underlying assumptions and restrictions, the TCE model is still applicable to many DSMC scenarios if the appropriate limitations are taken into account. Consider a standard chemically reactive DSMC simulation where rotational energy is modeled by a continuous distribution and vibrational energy is modeled by the discrete SHO. From the previously mentioned limitations, the vibrational energy model is not compatible with the TCE model. To appropriately address this issue and ensure that the correct Arrhenius rate is modeled, contributions from the vibrational modes of the colliding particles must be excluded from the calculation of Eqns. 7.15 and 7.16. The collision energy and contributing degrees of freedom, for this case, now depend solely on the rotational and relative translational values. The resulting collision energy is compared with the activation energy, then it and the contributing degrees of freedom values are used in Eqn. 7.17 to calculate the reaction probability. This means that the "total" collision energy used in the TCE model is no longer defined as the *total* energy of the colliding particles. Note, though, that now the collision energy calculated for the TCE model is no longer equal to the *total* energy that is used to determine the post-collisional states from the Borgnakke-Larsen model. Figure 7.2 demonstrates that the correct

reaction rate is simulated by DSMC when only the rotational mode is included to calculate the TCE probability. While this approach allows the TCE model to reproduce the correct Arrhenius rate, information from the vibrational modes no longer influences which particles react. It is not difficult to perceive situations where this result is troublesome as molecules in excited vibrational states will now react at the same rate as molecules in the vibrational ground state. With this in mind, it may be worthwhile in some cases, to purposely ignore the minor reaction rate error so that the vibrational modes contribute to determining which particles react. While it is likely that only slight errors in the reaction rate will be present for diatomic molecules simulated at high temperatures, problems may arise as the molecular complexity is increased. This approach cannot be extended to electronic excitation modeling since the observed errors are much greater for the much more widely spaced quantum electronic levels. The effects of including the electronically excited state energy in the TCE model can be seen for the O_2 dissociation reaction in Fig. 7.2. For this reaction, the rate is overpredicted by an even larger margin than the case with rotational and vibrational energy contributing to the TCE mode. On a large scale, it was found that the ionization rates were severely overpredicted when the electronic energy was included in the TCE model. It is likely that this problem resulted in an overprediction of ionization in the second nominal simulation and sensitivity analysis (Chapters 4 and 5).

7.4 Modeling Backward Reactions

If forward reactions are simulated by the TCE model, backward reactions must also be modeled in order to reproduce the equilibrium constant, K_{eq}, defined in Eqn. 7.5. Since DSMC simulations model chemical reactions on a per collision basis, the equilibrium constant cannot be directly calculated from Eqn. 7.6. Instead, the backward

reaction rate, k_b, must be represented by determining a reaction probability for each collision pair, similar to forward reactions. There are several current methods for calculating the backward reaction probability discussed in the following section. A new method developed in this dissertation is presented in Section 7.4.2.

7.4.1 Current Backward Reaction Models

The most common method for addressing backward reactions in DSMC is to reuse the TCE model, which requires that the backward reaction rate takes the Arrhenius form [3]. Since equilibrium constants, and not backward reaction rates, are published in most cases, the backward reaction rates must be fit to the Arrhenius form by rearranging Eqn. 7.5. As previously discussed in Section 7.3.4, the activation energy for backward reactions is typically set to zero when using the TCE model. This leaves only the pre-exponential constant, Λ_b, and the temperature exponent, η_b, to represent the backward reaction rate. Now both the forward and backward rate are represented by Arrhenius equations meaning that the equilibrium constant must also have this form. In actuality, the equilibrium constant typically has a more complex dependence on temperature than the Arrhenius form. To mitigate the errors caused by representing the equilibrium constant with an Arrhenius form, backward reaction rates are often strategically fit to the expected temperature range of the DSMC simulation. Even then, discrepancies in the reaction rate may still be evident and, in some cases, are egregious outside of the fit temperature range. The restrictions on the TCE model laid out in Section 7.3.2 must also be considered, increasing the difficulty in accurately matching the backward reaction rate to an Arrhenius form.

Due to the difficulties of simulating backward reactions with the TCE model, Boyd has proposed an improved approach to modeling these reactions [36][85]. Instead

of calculating a reaction probability based on the properties of each collision pair, a constant reaction probability in each DSMC cell is calculated for each reaction from the temperature of the cell. While this approach only allows for nonequilibrium to occur on the cell scale for backward reactions, this should have a negligible effect on the overall nonequilibrium of the simulation because backward reactions are relatively rare in the thermal nonequilibrium regions of typical DSMC applications. Boyd's method takes advantage of Eqns. 7.4-6 to determine the backward rate by assuming that the activation energy of the backward reaction is zero. The backward rate is then found to be

$$k_b(T) = \Lambda_f T^{\eta_f} \frac{\prod_i^{N_r} (Q_i)^{\alpha_i}}{\prod_j^{N_p} (Q_j)^{\beta_j}} V^{(\beta_p - \alpha_r)} \qquad \left[\frac{1}{s}\left(\frac{cm^3}{mol}\right)^{\beta_p}\right] \qquad [7.23]$$

where the reactant and products are defined from the forward direction (Eqn. 7.1). The reaction probability is then determined from the collision frequency, $\nu_{A,B}$, of the collision pair A and B as

$$P_{react} = \Lambda_f T^{\eta_f} \frac{\prod_i^{N_r} (Q_i)^{\alpha_i}}{\prod_j^{N_p} (Q_j)^{\beta_j}} V^{(\beta_p - \alpha_r)} \times \frac{n_B}{\nu_{A,B}} \qquad [7.24]$$

where n_B is the number density of the collision pair species used in the calculation of $\nu_{A,B}$. The temperature, T, and the total partition function, Q, for each species are calculated based on the cell temperature where the total partition function is determined from the translational, rotational, vibrational and electronic partition functions for that

particular species. If the reaction being considered is a recombination reaction, Eqn. 7.24 must also be multiplied by the number density of the third body.

In theory, this method should accurately represent the backward reaction rate and, therefore, reproduce the equilibrium constant. In practice, this is much more difficult than it seems. The calculation of the partition functions can become complex when a high degree of accuracy is desired. High order partition functions for each mode, coupling between rotation and vibration, temperature and density cut-offs for electronically excited levels, and a large number of input parameters all contribute to this complexity [75]. If low order partition functions are used, errors in the backward reaction rate may become an issue, especially at high temperatures. Also, additional parameters could be required even for these low order partition functions. Rotational, vibrational, or electronic partition function parameters may be essential to calculate an accurate total partition function for a species, regardless of whether those modes are included in the DSMC simulation. Even if low order partition functions are used, the partition functions for a species must be calculated in every cell where that species can potentially react. This process must be repeated at every timestep. For a large number of cells, the computational cost quickly increases, but has little benefit to the overall result since backward reactions are typically infrequent. In addition, the assumption that the backward reaction's activation energy is zero creates the same problems that the TCE model faces.

7.4.2 Improved Backward Reaction Model

To address the issue of accuracy, the following model for backward reactions simulated in DSMC is proposed. This model is similar to Boyd's method and is contained within the derivation of the backward reaction rate (Eqn. 27 in Ref. [85]). The proposed model calculates the backward reaction rate from Eqns. 7.4 and 7.5 as

$$k_b(T) = \frac{\Lambda_f T^{\eta_f} exp\left(-{E_{a_f}}/{k_B T}\right)}{K_{eq}(T)} \quad [7.25]$$

where T is calculated from the cell temperature and the backward reaction probability is then defined as

$$P_{react} = \frac{\Lambda_f T^{\eta_f} exp\left(-{E_{a_f}}/{k_B T}\right)}{K_{eq}(T)} \times \frac{n_B}{\nu_{A,B}} \quad [7.26]$$

where Eqn. 7.26 should be multiplied by the number density of the third body for a recombination reaction. Instead of calculating the equilibrium constant, K_{eq}, from partition functions, the equilibrium constant can be calculated from previously published curve fits. These published equations are fit to high order partition functions or ab initio calculations over a range of temperatures for each individual reaction and are generally considered accurate representations of the equilibrium constant. For example, if Park's equilibrium constant curve fit [47] is used, Eqn. 7.26 becomes

$$P_{react} = \frac{\Lambda_f T^{\eta_f} exp\left(-{E_{a_f}}/{k_B T}\right)}{\exp\left[\frac{A_1}{Z} + A_2 + A_3 \ln(Z) + A_4 Z + A_5 Z^2\right]} \times \frac{n_B}{\nu_{A,B}} \quad [7.27]$$

In Park's equilibrium constant equation, A_i are coefficients and $Z = 10{,}000/T$. Other than Park's curve fits, equilibrium constant values have been published in several sources with varying degrees of accuracy, including Gupta's curve fits [86] or the Gibbs free

energy approach applied in the NASA Chemical Equilibrium with Applications code [87].

Unlike the TCE model and Boyd's model, this approach does not require that the backward reaction rate's activation energy be equal to zero. Instead, the backward activation energy of a reaction, E_{a_b}, is defined as

$$E_{a_b} = E_{a_f} - \Delta H° \qquad [7.28]$$

where ΔH is the enthalpy of the forward reaction and E_{a_f} is the forward rate's activation energy. As DSMC is a particle method, this backward activation energy is important to calculate since the reaction is not allowed to occur for collisions that do not have enough energy. This means that Eqn. 7.26 is used when $E_c > max\left(E_{a_b}, -\Delta H°\right)$ and $P_{react} = 0$ otherwise. Care must also be taken so that the enthalpy removed from the system, when a reaction proceeds in one direction, is equivalent to the enthalpy added to the system when the reaction happens in the opposite direction. For example, energy is removed from the total collision energy for an endothermic dissociation reaction, but when the corresponding recombination reaction occurs, the same amount of energy is added to the total collision energy.

Eqn. 7.26 is actually a special case that assumes $E_{a_b} \ll k_B T$ which is typically a valid assumption for most reactions in DSMC simulations. If the backward reaction's activation energy is significant or the simulated temperature is low enough, a correction term must be included. This correction term is derived by starting from Eqn. 7.13 and considering the collision energy, E_c [3]. When the VHS model is used, the distribution integrated over all collision energy values, normalized to $k_B T$ is

$$f\left(\frac{E_c}{k_B T}\right) = \frac{1}{\Gamma\left(\zeta_I + \frac{5}{2} - \omega_{A,B}\right)}\left(\frac{E_c}{k_B T}\right)^{\zeta_I + \frac{3}{2} - \omega_{A,B}} exp\left(-\frac{E_c}{k_B T}\right) \quad [7.29]$$

where ζ_I is determined from Eqn. 7.15. By integrating from E_{a_b} to infinity, the fraction of collisions with $E_c > E_{a_b}$ is found to be

$$\frac{dN}{N} = \frac{\Gamma\left(\zeta_I + \frac{5}{2} - \omega_{A,B}, E_{a_b}/k_B T\right)}{\Gamma\left(\zeta_I + \frac{5}{2} - \omega_{A,B}\right)} \quad [7.30]$$

with the numerator defined as an incomplete gamma function. When $E_{a_b} \ll k_B T$, Eqn. 7.30 approaches one and can be ignored, but otherwise, this ratio must be calculated directly and applied to the reaction probability by dividing Eqn. 7.26 by Eqn. 7.30. A simplification of Eqn. 7.30 can be made when $E_{a_b} \gg (\zeta_I + 3/2 - \omega_{A,B}) k_B T$, but this is generally not the case for backward reactions [75]. Note that, like the TCE model, the degrees of freedom used to calculate Eqn. 7.30 must correspond to the energy modes that contributed to determining if $E_c > E_{a_b}$. In addition, for the rare case where $-\Delta H° > E_{a_b}$, the backward activation energy in Eqn. 7.30 should be replaced by $-\Delta H°$ since the minimum collision energy for a reaction to be possible is now defined by the enthalpy of reaction. Finally, this correction should not be applied when $max\left(E_{a_b}, -\Delta H°\right) < 0$ as the correction factor will result in unintended modifications of the reaction rate.

The approach developed for the proposed backward reaction model can also be adopted to improve Boyd's model. While the original derivation of Boyd's model assumed that the enthalpy of reaction is equal to the forward activation energy, this simplification is not necessary. Instead, the exponential terms from the Arrhenius forward rate (Eqn. 7.4) and the equilibrium constant (Eqn. 7.6) should not cancel and should

appear in Eqns. 7.23 and 7.24. Since it is now possible for the backward activation energy to be nonzero, the correction factor in Eqn. 7.30 should also be applied where necessary. Finally, it must be noted that neither Boyd's or the proposed model guarantee that the reaction probability will be less than one. While probabilities greater than one will result in errors modeling the backward reaction rate, it is unlikely that these errors negatively affect the simulation results. Since both models rely on cell temperature, it is reasonable to expect that the mixture has been fully reacted before the cell temperature corresponding to a probability of one is reached. On the other hand, probabilities greater than one resulting from the TCE model are possible at much lower temperatures due to the reliance on collision energy to calculate the probability.

7.5 Backward Reaction Model Comparisons

7.5.1 Reaction Rate Comparison

With the introduction of a new backward reaction model, several assessments of its relationship to the old models must be completed. Figure 7.4 compares the backward reaction rate for the Zeldovich reaction, $O + N_2 \rightleftharpoons N + NO$, calculated from each of the three models to the exact backward reaction rate. The backward rate for each model is determined from a DSMC simulation following the same method applied in Section 7.3. Here, the "exact" backward rate is considered to be the ratio of the forward rate over the equilibrium constant curve fit, both determined by Park [47]. The equilibrium constant is determined from detailed calculations of the partition functions and curve fit over some temperature range. The equilibrium constant, and therefore the backward reaction rate, is only considered accurate within this temperature range. Park's equilibrium constant was curve fit with five temperature points between 2,000 and 10,000 K. Although Park states that the fit diverges only slightly at high temperatures [47], Gupta has shown these errors

can be large for some reactions [86]. The parameters used to calculate the forward rate and equilibrium constant are listed in Table 7.1. Since the equilibrium constant is a function of density at high temperature due to temperature cutoffs for the atomic electronic partition functions, the current equilibrium constant is selected to correspond to the number density of the scenarios modeled [86].

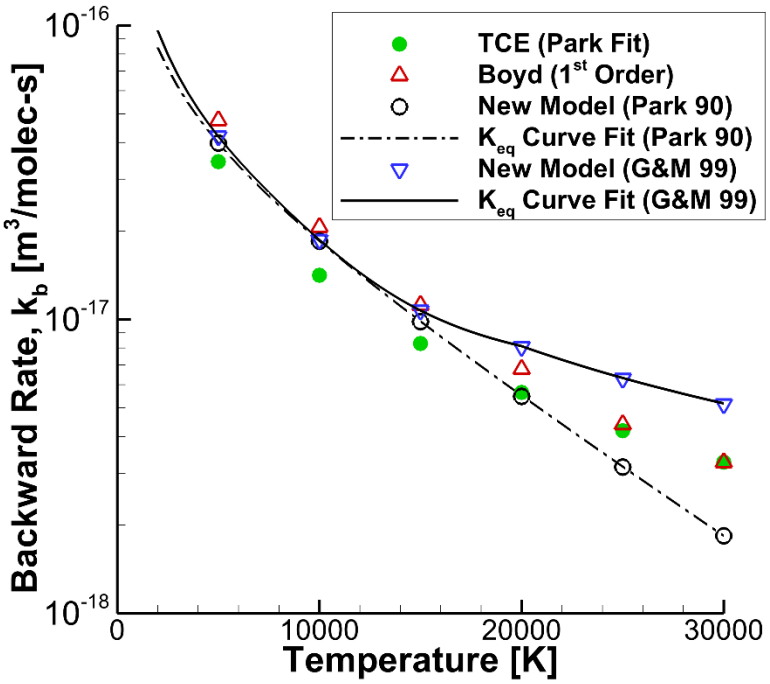

Figure 7.4 Comparison of the exact backward reaction rate for $O + N_2 \rightleftharpoons O + NO$ with DSMC using the TCE model, Boyd's model, and the proposed model.

First, the TCE model using a backward rate in Arrhenius form (Table 7.1), specifically fit to Park's parameters, is compared with the exact rate [88]. The Arrhenius form for the TCE reaction rate was fit to the temperature range between 10,000 and 20,000 K but is intended to reproduce the entirety of Park's curve fit. Even within this range, the TCE model displays noticeable error and above 20,000 K the error grows

dramatically with increasing temperature. This degree of error is expected since the Arrhenius equation cannot appropriately reproduce the complex dependence of the equilibrium constant on temperature and the Arrhenius parameters are constrained by the TCE model. Figure 7.4 also compares Boyd's approach (Eqn. 7.24) using first order partition functions with the exact rate. The exact partition function for translational, rigid rotor for rotational, SHO for vibrational, and quantum electronic partition functions are used here [85]. In order to reproduce Park's equilibrium constant, parameters for the partition functions were obtained from Refs. [85] and [47] (Table 7.2). Even when using Park's parameters, Fig. 7.4 shows that minor errors are evident below 20,000 K. It must be noted that above 20,000 K, Boyd's model is not expected to match with Park's. In this region, it is likely that Boyd's model is more accurate, but without calculating high order partition functions, a conclusion about the accuracy in this temperature range cannot be made. Finally, the backward reaction rate calculated by the proposed model is compared to the exact rate by directly using Park's equilibrium constant (Eqn. 7.27). As shown in Fig. 7.4, the simulated backward rate reproduces the exact backward rate identically for the entire temperature range.

A second test of the proposed model was conducted for the backward reaction rate calculated from the equilibrium constant curve fit determined by Gordon and McBride (G&M) [87]. The work published by G&M provides a large set of piecewise curve fits between 200 and 20,000 K where each equilibrium constant is fit using the enthalpy and entropy of the participating species. The advantage of using the G&M equilibrium constants is that they are commonly used in computational fluid dynamics (CFD) simulations. In addition, the curve fits are easily applied by following the approach detailed in Ref. [89] and using the curve fit and enthalpy data available in the *thermo.inp* file located in the NASA Chemical Equilibrium with Applications (CEA)

code [90]. Unfortunately, these curve fits are difficult to extrapolate because they tend to become unstable. For example, the G&M curve fit for the $O + N_2 \rightleftharpoons O + NO$ reaction is shown in Fig. 7.5. Above 20,000 K, the equilibrium constant quickly trends towards zero. This leads to unphysical results when the G&M equilibrium constant is used in Eqn. 7.26 as a large backward reaction probability is calculated, resulting in unexpected backward reactions at temperatures above 20,000 K. Typically, CFD simulations set the backward reaction rate to zero outside of the G&M curve fit's valid range. For CFD this is a reasonable strategy, but fluctuations in the DSMC cell temperature make this occurrence more likely. As an alternative to setting the backward reaction probability to zero, a reasonable extrapolation of the G&M equilibrium constant can be performed. As the equilibrium constant is approximately linear on a semi-log plot vs $1/T$, a least squares regression fit can be performed on the G&M equilibrium constant at high temperatures (Fig. 7.5). A continuous extrapolation of the equilibrium constant is obtained by shifting this least squares fit so that the extrapolation begins at the highest valid temperature of the G&M curve. An example of the G&M fit combined with the extrapolation is demonstrated in Fig. 7.5. This equilibrium constant was used to determine the G&M backward reaction rate shown in Fig. 7.4. The same equilibrium constant was then applied with the proposed backward reaction model. As seen in Fig. 7.4, the proposed model again reproduces the backward reaction rate exactly. The same extrapolation method could be applied to the lower bound of the G&M curve fit, but it may be more accurate to use Boyd's model and calculate the partition functions directly at these low temperatures, instead of using a least squares approximation, since low order partition functions should be sufficient. In the scenarios modeled in this dissertation, calculation of the lower G&M temperature bound is not an issue as temperatures this low will not be experienced.

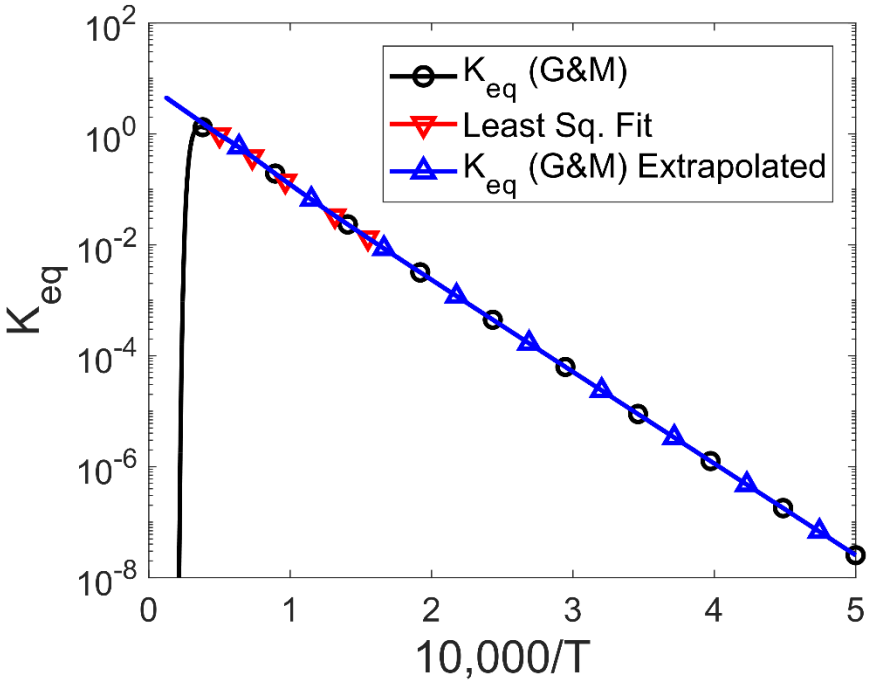

Figure 7.5 Analysis of the Gordon and McBride (G&M) equilibrium constant as a function of temperature.

7.5.2 1-Dimensional Shock Comparison

To demonstrate the importance of modeling backward reaction rates correctly in an ionizing, hypersonic shock, each of the models is used to simulate the EAST experiment examined in Chapter 4. This scenario reproduces the conditions of a lunar return trajectory at 10.26 km/s and pressure of 0.2 Torr using a synthetic air mixture of 79% N_2 and 21% O_2. The CHIPS code was used to simulate these conditions three separate times, applying the TCE model, Boyd's model with first order partition functions, and the proposed model for simulating backward reactions. The same parameters as in the previous CHIPS simulations were used for the forward reaction rates

and for the backward rates if the TCE model is used (Tables 3.2, 3.4, and 3.5). The proposed model calculates the backward reactions from the Gordon and McBride equilibrium constants and uses the high temperature extrapolation described in the previous section [87]. The results of comparing these models are plotted in Fig. 7.6a-c. It also should be noted that the TCE model was used to simulate forward reactions and the rotational and vibrational modes were included in the TCE total collision energy, even though a discrete vibrational distribution is used. As mentioned in Section 7.3.4, the inclusion of discrete vibrational energy in the TCE calculations should not lead to significant errors in this case because the temperatures modeled are typically higher than the characteristic vibrational temperatures of 11-species air molecules and the molecules involved in this mixture are diatomic. However, in this iteration of the EAST scenario simulation, the electronic energy is not allowed to contribute to the forward reaction rate, unlike previous simulations completed in Chapters 4 and 5. This is due to the significantly discrete nature of electronic excitation. Removing electronic excitation from consideration has a noticeable effect when comparing Fig. 7.6a-c with Fig. 4.5a-c, resulting in a perceptible increase in the temperatures and decrease in the ionized particle number densities.

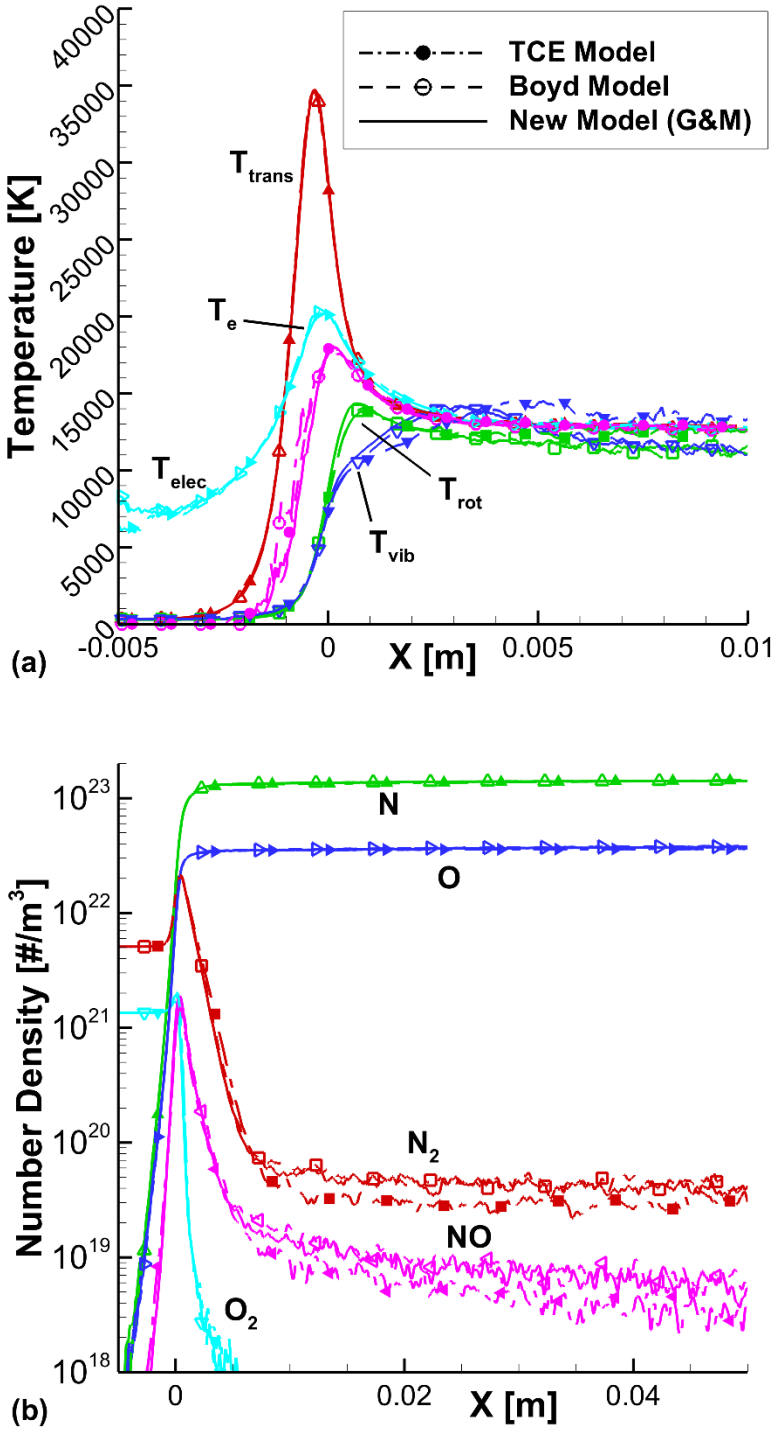
TCE Model
Boyd Model
New Model (G&M)
Temperature [K]
40000
35000
30000
25000
20000
15000
10000
5000
0
T trans
T e
T elec
T rot
T vib
-0.005
0
X [m]
0.005
0.01
(a)
Number Density [#/m3]
10^23
10^22
10^21
10^20
10^19
10^18
N
O
N2
NO
O2
0
0.02
X [m]
0.04
(b)

Figure 7.6

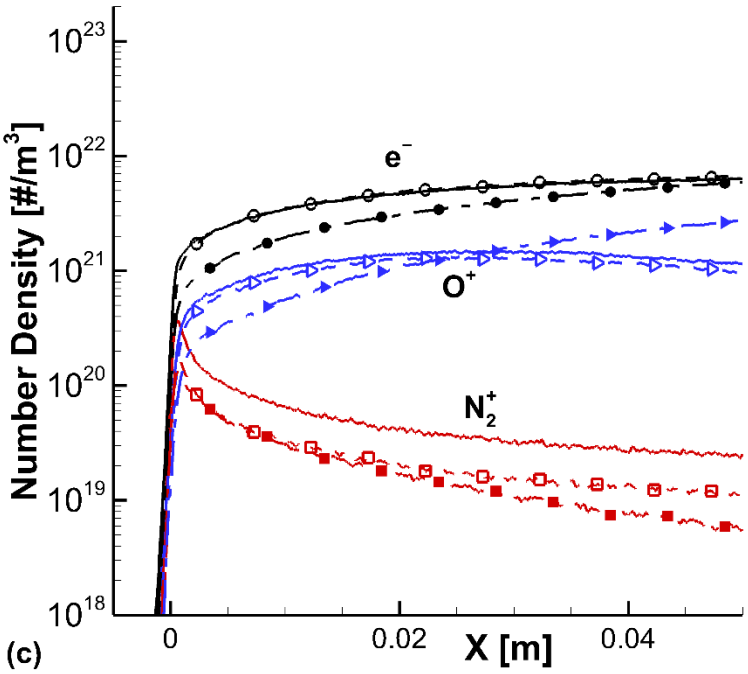

Figure 7.6 Comparison of the TCE (dash-dotted line, solid symbols), Boyd's (dashed line, open symbols), and the proposed (solid line) models for CHIPS simulations of EAST Shot 37. *(a) Bulk temperatures. (b) Neutral particle number densities. (c) Charged particle number densities.*

When comparing the results from using the different backward reaction models, several discrepancies can be identified. In Fig. 7.6a, the simulated temperatures from the three models agree well, except for the vibrational temperature. The TCE model predicts a slightly higher vibrational temperature downstream of the shock than the other two models, which are in good agreement with each other. This is likely due to the TCE model reproducing an incorrect recombination rate which leads to the slight underprediction of N_2 and O_2 as seen in Fig. 7.6b. Again, the proposed model and Boyd's model are in relatively good agreement for all the neutral particle number densities. The charged particle number densities are compared in Fig. 7.6c where the number densities of N^+, O_2^+, and NO^+ are removed for clarity. This figure demonstrates substantial

disagreement between the models, especially for the TCE model. When using the TCE model, the number density of O^+ is continuously increasing downstream of the shock while O^+ increases initially and then decreases further downstream when using Boyd's or the proposed model. This occurs because Arrhenius form reaction rates are not available in the current literature for O^+ electron capture reactions. In fact, several electron capture and reverse charge exchange reactions are missing from the TCE reaction set (Table 3.5). These reactions could be fit to an Arrhenius form, but this attempt is likely to be a wasted effort because of the difficulty in fitting charged reactions to an Arrhenius form within the TCE model's constraints. Both the proposed model and Boyd's model produce similar charged particle number densities, with the exception of N_2^+. This difference is likely a result of using first order partition functions in Boyd's model. As the complexity of the colliding particles increases, this simplification will result in greater error.

While the discrepancies between predictions from the three backward reaction models does not seem to be extreme for an ionizing, hypersonic shock case, this would not be true in every instance. For example, if a cold entry vehicle body were place behind the shock, it would force the temperature to equilibrate quickly to some low temperature value. This equilibration would require a much larger number of backward reactions, especially electron capture reactions. In this case, the chosen backward reaction model would have a greater influence on the results.

7.5.3 Model Analysis

These comparisons demonstrate several advantages of using the equilibrium constant curve fits instead of low order partition functions, but also raises some important items to consider. The proposed method can only simulate the backward reaction rate with the same accuracy of the equilibrium constant used in Eqn. 7.26. Care must be taken

to use equilibrium constants that are valid in the expected temperature range. If large errors in the equilibrium constant are anticipated for the simulated temperatures, Boyd's model may be more appropriate. However, this should not typically detract from the use of the proposed model because high accuracy equilibrium constants are easily obtained for most temperature ranges of interest. If equilibrium constants for a specific reaction are completely unavailable, Boyd's model is necessary. Another consideration is that these three models have differing requirements for compiling rates from different sources. The forward and backward reactions rates used in the TCE model *must* correspond to each other since the backward rate is curve fit to the forward rate and a specific equilibrium constant. For both the TCE and proposed models, the forward rate and equilibrium constant should be a matching pair. Compiling the forward rate and equilibrium constant from separate sources risks errors in the backward rate since the activation energy should be identical for both equations. While this is a requirement, activation energy values are relatively well known and should deviate only slightly between different sources, meaning that mixing forward rates and equilibrium constants from different sources should not typically result in large errors. Boyd's model has an advantage in this regard since only the forward rate is required.

When considering computational cost, both the proposed method and Boyd's model using low order partition functions provide significant improvement compared to the TCE model, resulting in a 1.8x speedup of a 0-dimensional relaxation simulation with similar results for other DSMC simulations. The efficiency of the proposed method and Boyd's model have comparable computational cost depending on the order of the partition functions used in Boyd's method. Conclusions on the overall computational efficiency for a full DSMC simulation of a reacting mixture are not as clear when comparing the two models. The required number of calculations per cell scales with the

number of reactions for the proposed method, whereas the number of calculations per cell scales with the number of simulated species for Boyd's model. Implementations of both Boyd's and the proposed methods could potentially increase computational efficiency from look-up tables or parametric curve fits calculated on the fly since the rate of each reaction is only a function of cell temperature.

The greatest advantage for the proposed method is that, while it is new for DSMC, this method is a standard approach used in continuum modeling and can make use of the same equilibrium curve fits. In addition, Gordon and McBride have published a large database of parameters required to calculate the equilibrium constant that is readily available [87]. Since this database is commonly used in CFD, the proposed backward reaction method reduces the number of discrepancies encountered when attempting to match with continuum simulations or to interface between the continuum and rarefied regimes.

CHAPTER 8

Final Nominal Simulation

8.1 Overview

In anticipation of the final sensitivity analysis completed in this research, one last nominal simulation of an Earth entry scenario must be completed. The chosen scenario for this nominal simulation is nearly identical to the scenario studied in Chapter 4, but the CHIPS code now includes the backward reaction model developed in the previous chapter. In addition to applying the new backward reaction model, several additional advancements to the CHIPS code are detailed in this chapter. These improvements address key shortcomings identified in the previous sensitivity analyses and simulations.

The poor agreement with EAST experimental results, observed in Chapter 6, would not be sufficient for the final sensitivity analysis. In order for the sensitivity analysis to be meaningful, the combined CHIPS/NEQAIR simulations must compare relatively well with the EAST experimental measurements. Accompanying the improvements to the CHIPS code, the method for post-processing the CHIPS code with NEQAIR is enhanced. These changes aim to avoid difficulties identified in Chapter 6 when calculating radiative quantities from CHIPS results. By applying these improvements to the CHIPS/NEQAIR nominal simulation, results can be directly compared with the EAST experimental data.

8.2 Model Improvements

8.2.1 Elastic Collision Parameters

In previous CHIPS simulations, the heavy particle elastic collision parameters used in the Variable Hard Sphere (VHS) model were not collision partner specific and did not treat neutral-ion collisions separately (Table 3.1) [15]. Only the electron-heavy

VHS collision parameters were collision partner specific, but even these interactions required an additional model to capture resonances in the cross-sections and ignored Coulombic forces between charged-charged collisions (Table 3.3). While these simplifications, discussed in Section 3.4.2, are not expected to cause significant errors in the hypersonic scenarios of interest, improved VHS parameters have been published recently by Swaminathan-Gopalan and Stephani [18]. The curve fits performed by Swaminathan-Gopalan and Stephani minimize the error in the first and second collision integrals, thereby obtaining a best fit approximation of the viscosity and diffusion coefficients. While there are still errors in these best fits due to the limitations of the VHS model, the published parameters are a significant improvement over the VHS parameters used in previous CHIPS simulations.

Table 8.1 summarizes the collision partner specific VHS parameters published in Ref. [18] for elastic collisions between heavy particles. These parameter fits ranged between 1,000 and 20,000 K with a reference temperature of 273 K. Separate fits were completed in Ref. [18] for neutral-electron collisions and are compiled in Table 8.2. These fits require piecewise functions for N_2 and O_2 due to complex quantum mechanical phenomena, but the CHIPS code is currently unable to handle the piecewise VHS parameters. Instead, the high temperature functions of the piecewise fits for N_2 and O_2 are chosen to represent their collisions with electrons (Table 8.2). Because the updated VHS fits include the expected resonance peaks in the N_2-e^- and NO-e^- cross-sections, the separate resonance calculations discussed in Section 3.4.2 are removed from the CHIPS code. Finally, charged-charged collisions can be determined from a Coulombic attractive or repulsive potential, but the VHS model is unable to reproduce these collision integrals. To handle these interactions, VHS collision parameters from the charged-neutral interactions are used to represent the charged-charged collisions (Table 8.1). As charged-

charged interactions are assumed to be rare, it is expected that choosing the VHS parameters from charged-neutral interactions will have little effect on the results. While this assumption is similar to the approach employed in previous DSMC simulations, accurate modeling of charged-charged interactions may be necessary for some important reaction equilibria, such as simulating the correct electron capture rate, and can be improved in future work.

Table 8.1 Heavy Particle VHS elastic collision parameters for 11-species air with $T_{ref} = 273$ K.

d_{ref} [Å]	N_2	N	O_2	O	NO	N_2^+	N^+	O_2^+	O^+	NO^+
N_2	3.618	3.531	3.225	2.884	3.856	9.523	3.486	3.480	3.296	3.562
N	3.531	3.278	3.219	3.333	3.423	4.517	8.040	2.944	5.008	3.020
O_2	3.225	3.219	3.469	3.230	3.578	2.804	2.638	7.186	2.472	2.810
O	2.884	3.333	3.230	3.195	3.205	2.863	5.286	2.852	7.367	2.877
NO	3.856	3.423	3.578	3.205	3.690	3.137	3.046	3.105	2.848	8.491
N_2^+	9.523	3.486	3.480	3.296	3.562	9.523	3.486	3.480	3.296	3.562
N^+	4.517	8.040	2.944	5.008	3.020	4.517	8.040	2.944	5.008	3.020
O_2^+	2.804	2.638	7.186	2.472	2.810	2.804	2.638	7.186	2.472	2.810
O^+	2.863	5.286	2.852	7.367	2.877	2.863	5.286	2.852	7.367	2.877
NO^+	3.137	3.046	3.105	2.848	8.491	3.137	3.046	3.105	2.848	8.491

ω	N_2	N	O_2	O	NO	N_2^+	N^+	O_2^+	O^+	NO^+
N_2	0.652	0.720	0.672	0.671	0.721	1.000	0.605	0.603	0.602	0.604
N	0.720	0.760	0.719	0.762	0.746	0.833	1.000	0.612	0.930	0.614
O_2	0.672	0.719	0.668	0.715	0.685	0.622	0.613	1.000	0.610	0.620
O	0.671	0.762	0.715	0.768	0.715	0.617	0.897	0.621	1.000	0.616
NO	0.721	0.746	0.685	0.715	0.702	0.607	0.606	0.609	0.601	1.000
N_2^+	1.000	0.605	0.603	0.602	0.604	1.000	0.605	0.603	0.602	0.604
N^+	0.833	1.000	0.612	0.930	0.614	0.833	1.000	0.612	0.930	0.614
O_2^+	0.622	0.613	1.000	0.610	0.620	0.622	0.613	1.000	0.610	0.620
O^+	0.617	0.897	0.621	1.000	0.616	0.617	0.897	0.621	1.000	0.616
NO^+	0.607	0.606	0.609	0.601	1.000	0.607	0.606	0.609	0.601	1.000

Table 8.2 Neutral-electron VHS elastic collision parameters for 11-species air with $T_{ref} = 273$ K.

Species	Temperature Range [K]	d_{ref} [Å]	ω
N_2	7400–20000	3.282	0.738
N	5000–20000	2.385	0.684
O_2	10300–20000	1.480	0.505
O	5000–20000	0.739	0.292
NO	5000–20000	2.912	0.730

8.2.2 Chemical Reaction Rates

Investigation of the Total Collision Energy (TCE) model in the previous chapter identified several limitations. Since the CHIPS code still uses the TCE model to calculate forward reaction rates, these limitations need to be addressed. First, the energy modes that contribute to the total collision energy must be represented by continuous distributions. In the CHIPS code, the rotational mode is continuous, but the vibrational and electronic modes are modeled by discrete distributions. While, in the CHIPS code, it is technically incorrect to calculate the total collision energy including the internal energy in the vibrational and electronic levels of the colliding particles, omitting the energy from these levels can result in unintended consequences.

For example, consider a simulation where the vibrational and electronic energy of the colliding particles cannot contribute to the total collision energy used to calculate the reaction rates. This leaves only the energy from the relative velocity of the colliding particles and their rotational energy to contribute toward the TCE reaction rate calculation. In the hypersonic scenarios modeled in this dissertation, dissociation and ionization reactions are important to the temperature and mixture composition, but these reactions require a substantial amount of total energy in order to surpass the activation

energy minimum. In this example, colliding particles may have more than enough energy in their vibrational or electronic modes, but these same particles will have no chance of reacting if the sum of their energy from the relative velocity and rotational energy is not greater than the activation energy. Essentially, this would mean that any energy in the vibrational or electronic modes are "invisible" to the TCE model, resulting in an underprediction of the reaction rates.

A compromise is applied in the CHIPS code. Because high temperatures are expected for the hypersonic simulations performed in this dissertation, it is reasonable to include vibration energy in the TCE calculation of the forward reaction rates. Although the vibrational mode is modeled with the discrete simple harmonic oscillator, the temperatures are high enough that the distribution is approximately continuous. While the vibrational energy can be included in the TCE model in this case, the electronic energy levels are still too widely spaced to be included in the reaction calculations. In the simulations performed in Chapters 4, 5, and 6, the electronic energy was allowed to contribute to the TCE model. This likely resulted in an overprediction of reaction rates, as was the case in Fig. 7.2, and may be one cause of the drastic increase in the ionization rates when compared before and after the addition of an electronic excitation model (Figs. 4.5b and 6.8). While removing the electronic energy contribution to the TCE model will eliminate the identified errors in overpredicting the reaction rates, this may also introduce errors by making the electronic mode "invisible" to the TCE model. This could result in an underprediction of the forward reaction rates. At this time, the underprediction is hypothetical and, for this reason, the current CHIPS code does not include electronic excitation in the calculation of forward reaction rates. In the future, solutions to including the electronic energy of colliding particles in the reaction probability calculations should be investigated.

The second TCE model limitation that must be addressed is the choice of Arrhenius reaction rates that fall within the restriction of the TCE model (Section 7.3.2). In analyzing the reaction rates used for the previous CHIPS simulations, it was found that several of the reaction rates are incompatible with the TCE model. A comprehensive study of reaction rates for hypersonic entry in air was completed by Cruden and Brandis where an improved reaction rate set was suggested [91]. Ideally, these reactions rates could be used directly in the CHIPS code, but some of the Arrhenius rates are also incompatible with the TCE model. In this dissertation, each one of the reactions was individually studied to determine whether it met the TCE model requirements and, if it did not, every effort was made to replace the reaction with a similar rate when possible. The completed set for the CHIPS code is listed in Tables 8.3-5. It must be reiterated that while an individual reaction rate may or may not currently be within the limitations of the TCE model used in the CHIPS code, this will not always be true. As discussed in Chapter 7, the TCE model's limitations depend on the specific VHS parameters and the internal modes that contribute to the reaction probability calculation. These parameters could change from one code to the next, requiring a reevaluation of each reaction rate to ensure that the TCE model's limitation are satisfied.

Table 8.3 Neutral particle dissociation, recombination, and exchange reaction rates.

#	Reaction	Forward Rate Coefficients			Reference
		Λ [m^3/s]	η	E_a [10^{-19} J]	
1	$N_2 + N_2 \rightleftharpoons N + N + N_2$	1.162×10^{-8}	−1.6	15.63	[91]
2	$N_2 + N \rightleftharpoons N + N + N$	4.982×10^{-8}	−1.6	15.63	[91]
3	$N_2 + O_2 \rightleftharpoons N + N + O_2$	1.162×10^{-8}	−1.6	15.63	[91]
4	$N_2 + O \rightleftharpoons N + N + O$	4.982×10^{-8}	−1.6	15.63	[91]
5	$N_2 + NO \rightleftharpoons N + N + NO$	1.162×10^{-8}	−1.6	15.63	[91]
6	$O_2 + N_2 \rightleftharpoons O + O + N_2$	3.321×10^{-9}	−1.5	8.215	[91]
7	$O_2 + N \rightleftharpoons O + O + N$	1.661×10^{-8}	−1.5	8.215	[91]
8	$O_2 + O_2 \rightleftharpoons O + O + O_2$	3.321×10^{-9}	−1.5	8.215	[91]
9	$O_2 + O \rightleftharpoons O + O + O$	1.661×10^{-8}	−1.5	8.215	[91]
10	$O_2 + NO \rightleftharpoons O + O + NO$	3.321×10^{-9}	−1.5	8.215	[91]
11	$NO + N_2 \rightleftharpoons N + O + N_2$	3.819×10^{-13}	−0.5	10.30	[92]
12	$NO + N \rightleftharpoons N + N + O$	7.638×10^{-13}	−0.5	10.30	[92]
13	$NO + O_2 \rightleftharpoons N + O + O_2$	3.819×10^{-13}	−0.5	10.30	[92]
14	$NO + O \rightleftharpoons N + O + O$	7.638×10^{-13}	−0.5	10.30	[92]
15	$NO + NO \rightleftharpoons N + O + NO$	3.819×10^{-13}	−0.5	10.30	[92]
16	$N_2 + O \rightleftharpoons NO + N$	2.989×10^{-16}	0.0	5.281	[91]
17	$O_2 + N \rightleftharpoons NO + O$	1.494×10^{-20}	1.0	0.4515	[91]

Table 8.4 Charged particle dissociation and recombination reaction rates.

#	Reaction	Forward Rate Coefficients			Reference
		Λ [m^3/s]	η	E_a [10^{-19} J]	
18	$N_2 + N_2^+ \rightleftharpoons N + N + N_2^+$	1.162×10^{-8}	−1.6	15.63	[91]
19	$N_2 + N^+ \rightleftharpoons N + N + N^+$	4.982×10^{-8}	−1.6	15.63	[91]
20	$N_2 + O_2^+ \rightleftharpoons N + N + O_2^+$	1.162×10^{-8}	−1.6	15.63	[91]
21	$N_2 + O^+ \rightleftharpoons N + N + O^+$	4.982×10^{-8}	−1.6	15.63	[91]
22	$N_2 + NO^+ \rightleftharpoons N + N + NO^+$	1.162×10^{-8}	−1.6	15.63	[91]
23	$O_2 + N_2^+ \rightleftharpoons O + O + N_2^+$	3.321×10^{-9}	−1.5	8.215	[91]
24	$O_2 + N^+ \rightleftharpoons O + O + N^+$	1.661×10^{-8}	−1.5	8.215	[91]
25	$O_2 + O_2^+ \rightleftharpoons O + O + O_2^+$	3.321×10^{-9}	−1.5	8.215	[91]
26	$O_2 + O^+ \rightleftharpoons O + O + O^+$	1.661×10^{-8}	−1.5	8.215	[91]
27	$O_2 + NO^+ \rightleftharpoons O + O + NO^+$	3.321×10^{-9}	−1.5	8.215	[91]
28	$NO + N_2^+ \rightleftharpoons N + O + N_2^+$	3.819×10^{-13}	−0.5	10.30	[92]
29	$NO + N^+ \rightleftharpoons N + O + N^+$	7.638×10^{-13}	−0.5	10.30	[92]
30	$NO + O_2^+ \rightleftharpoons N + O + O_2^+$	3.819×10^{-13}	−0.5	10.30	[92]
31	$NO + O^+ \rightleftharpoons N + O + O^+$	7.638×10^{-13}	−0.5	10.30	[92]
32	$NO + NO^+ \rightleftharpoons N + O + NO^+$	3.819×10^{-13}	−0.5	10.30	[92]

Table 8.5 Ionization, electron impact dissociation, and charge exchange reactions.

#	Reaction	Forward Rate Coefficients			Reference
		Λ [m^3/s]	η	E_a [10^{-19} J]	
33	$N + O \rightleftharpoons NO^+ + e^-$	8.800×10^{-18}	0.0	4.404	[47]
34	$N + N \rightleftharpoons N_2^+ + e^-$	3.321×10^{-17}	0.0	9.319	[47]
35	$O + O \rightleftharpoons O_2^+ + e^-$	1.827×10^{-17}	0.0	11.13	[47]
36	$N_2 + e^- \rightleftharpoons N + N + e^-$	4.980×10^{-6}	−1.6	15.63	[44]
37	$NO + e^- \rightleftharpoons N + O + e^-$	1.451×10^{-9}	−0.5	10.30	This work
38	$N + e^- \rightleftharpoons N^+ + e^- + e^-$	4.00×10^{-12}	−0.25	23.28	This work
39	$O + e^- \rightleftharpoons O^+ + e^- + e^-$	1.00×10^{-12}	−0.25	21.88	This work
40	$N_2 + N^+ \rightleftharpoons N + N_2^+$	1.162×10^{-23}	1.47	1.813	[91]
41	$N_2 + O^+ \rightleftharpoons O + N_2^+$	1.511×10^{-18}	0.36	3.148	[91]
42	$O + O_2^+ \rightleftharpoons O_2 + O^+$	6.642×10^{-18}	−0.09	2.485	[91]
43	$NO + O^+ \rightleftharpoons O_2 + N^+$	2.325×10^{-25}	1.9	3.673	[91]
44	$O_2 + NO^+ \rightleftharpoons NO + O_2^+$	3.985×10^{-17}	0.41	4.501	[91]
45	$N + NO^+ \rightleftharpoons O + N_2^+$	1.196×10^{-16}	0.0	4.901	[91]
46	$O + NO^+ \rightleftharpoons O_2 + N^+$	1.661×10^{-18}	0.5	10.66	[91]
47	$N + O_2^+ \rightleftharpoons O_2 + N^+$	1.445×10^{-16}	0.14	3.949	[91]
48	$N_2 + O_2^+ \rightleftharpoons O_2 + N_2^+$	1.644×10^{-17}	0.0	5.619	[91]
49	$N + NO^+ \rightleftharpoons N_2 + O^+$	5.646×10^{-17}	−1.08	1.767	[91]
50	$O + NO^+ \rightleftharpoons N + O_2^+$	1.196×10^{-27}	0.29	6.710	[91]
51	$NO + N^+ \rightleftharpoons N + NO^+$	2.989×10^{-18}	0.57	0.0	[91]

In Ref. [91], the NO dissociation reactions are analyzed and updated by Cruden and Brandis. After calculating the reaction probabilities as a function of collision energy using the suggested Arrhenius rates, the probability was found to be greater than one for a significant range of collision energy in each NO dissociation reaction. This results in an underprediction of the reaction rate in the CHIPS code. Unfortunately, the NO dissociation rates provided by several other sources, including Park 1990 [47], were also unable to be reproduced correctly by the TCE model used in CHIPS. The reaction rates published by Gupta [86] are allowed with the TCE model, but it was found that the rates published by Park and Menees [92] provide the best match with the updated values in

Ref. [91]. Note that a small shift in the activation energy was made in order to be in line with the activation energy used in Ref. [91]. The Arrhenius rates from these sources are compared in Fig. 8.1 for the dissociation of NO by a molecule, NO + M ⇌ N + O + M. For electron impact dissociation reactions, the same multiplication factor as Ref. [91] was used. That is, the NO dissociation rate for collisions with molecules is multiplied by 3,800 to come up with the electron impact dissociation rate. Regrettably, analysis of this rate shows that it always results in dissociation probabilities greater than one, meaning that underprediction of the electron impact dissociation rate of NO is unavoidable. In addition to NO dissociation, the N_2 electron impact dissociation reaction rate suggested in Ref. [91] cannot be used in the TCE model due to its large Arrhenius temperature exponent, η. A comparison of various rates in Ref. [91] points to Park's 1993 reaction rate for N_2 electron impact dissociation as the second-best option. This rate is compatible with the TCE model, so it is used in the CHIPS code [44].

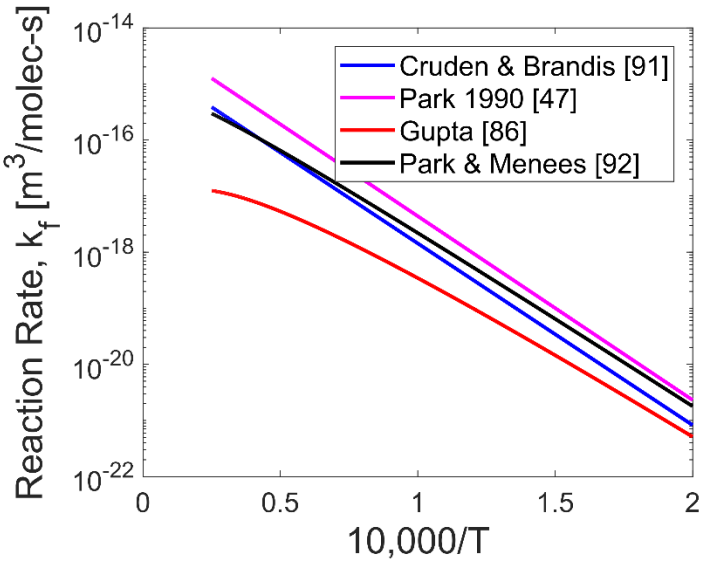

Figure 8.1 Comparison of Arrhenius reaction rates for the NO dissociation reaction with any molecule, NO + M ⇌ N + O + M.

Dissociation reactions were not the only reactions whose rates fell outside of the accepted TCE model range as several ionization reaction rates encountered the same difficulties. All three associative ionization reactions in Ref. [91] have η values that are too large. While Cruden and Brandis conclude that the Park 1990 [47] rates are not ideal, they are presently fit using η values of zero which allows these rates to be used with the TCE model. The atomic nitrogen and atomic oxygen electron impact ionization reaction rates suggested in Ref. [91], compiled from Park 1993 [44], are also outside of the valid TCE range for η. In fact, N and O electron impact ionization Arrhenius rates similar to the suggested rate in Ref. [91] and fit within the limitations of the TCE model could not be found. Alternate electron impact ionization rates published by Wilson [93] were used in previous DSMC simulations by Boyd [85]. These rates are fairly accurate when compared with Ref. [91] in Figs. 8.2 and 8.3, but the activation energy is significantly lower than both the enthalpy of the reaction and the other published rates. As discussed in Section 7.3.4, the simulated reaction rate using the TCE model will be underpredicted when the activation energy is lower than the enthalpy of reaction, meaning that these rates cannot be used in this research. For the electron impact ionization reactions, the rates used in the previous CHIPS simulations originate from Bird, but it is unclear how Bird determined these rates [19]. While the $O + e^- \rightleftharpoons O^+ + e^- + e^-$ rate compares well to Ref. [91], it is not usable in the TCE model due to the reaction probability being greater than one for most of the possible collision energies. In addition, the $N + e^- \rightleftharpoons N^+ + e^- + e^-$ rate is underpredicted by several orders of magnitude. Since all the published rates are unusable in the current model, it was decided that creating new electron impact reaction rates was the appropriate course of action. The $N + e^- \rightleftharpoons N^+ + e^- + e^-$ and $O + e^- \rightleftharpoons O^+ + e^- + e^-$ rates listed in Table 8.5 use the activation energy from Ref. [91] and *assume* a

temperature exponent of -0.25. This value of η is within the acceptable TCE range while avoiding the limiting value of -0.5. The reaction rates are then compared with the rates published in Ref. [91] and the Arrhenius constant is used to shift the rate within reasonable agreement between 5,000 and 40,000 K (Figs. 8.2 and 8.3). This Arrhenius constant fit is performed while also ensuring that the reaction probability is nowhere above one for the possible collision energy values. Finally, the $O_2 + NO^+ \rightleftharpoons NO + O_2^+$ charge exchange reaction rate in Ref. [91] is slightly underpredicted using the current CHIPS code, but no other options are available, and it is unlikely that the slight underprediction will have noticeable effect on the results.

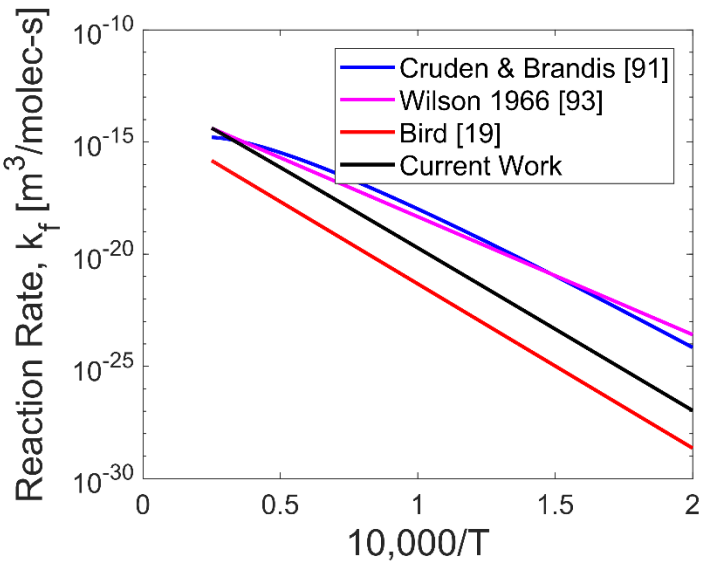

Figure 8.2 Comparison of Arrhenius reaction rates for the $N + e^- \rightleftharpoons N^+ + e^- + e^-$ reaction.

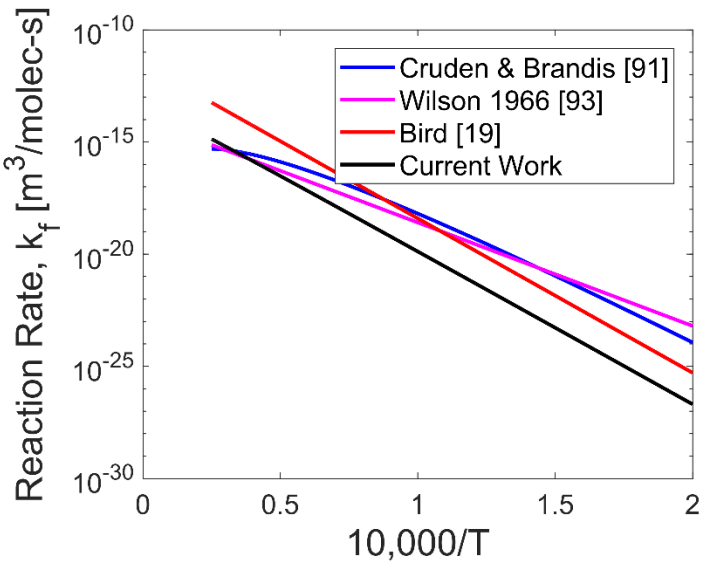

Figure 8.3 Comparison of Arrhenius reaction rates for the $O + e^- \rightleftharpoons O^+ + e^- + e^-$ reaction.

Now that the forward reaction rate set is completed, the backward reaction rate model is considered. The previous CHIPS simulations also used the TCE model for backward reactions. Since published rates for several backward reactions were not available, these rates were missing from the scenarios modeled earlier in this dissertation. With the introduction of the new backward reaction model detailed in Chapter 7, the TCE model is no longer needed for backward reactions and all backward reactions can now be simulated. The equilibrium constants and enthalpies of formation published by Gordon and McBride are used in the CHIPS code to calculate backward reaction probabilities [87].

8.2.3 Electronic Excitation Model

8.2.3.1 Electronic Relaxation Rate

The introduction of the electronic excitation model in Section 3.5.1 stated that an advantage of Liechty's model is its ability to simulate a non-equilibrium electronic level distribution without the need for individual excitation cross-sections [24]. While this simplicity is certainly an advantage, the general nature of the model leads to difficulties in accurately reproducing individual excitation rates. These individual excitation rates can be drastically different when processes such as allowed and forbidden transitions are accounted for. In Ref. [24], Liechty's electronic excitation model was shown to reproduce the transition rates with reasonable accuracy but was only analyzed for equilibrium conditions. When applying this electronic excitation model to nonequilibrium hypersonic conditions simulated with CHIPS, the electronic levels are overpopulated in the nonequilibrium regions of the flow. This is a symptom of the model's assumption that every particle collision can result in an electronic excitation. Essentially, this is the equivalent of using an electronic collision number where $Z_{elec} = 1$. In the course of this dissertation, it has become obvious that this electronic relaxation rate is incorrect.

The electronic excitation model implemented from Liechty's work employs the Borgnakke-Larsen [25] method to select excitations from particle collisions. This approach is similar to how rotational and vibrational energy transfer is handled in the CHIPS code. For both of these internal energy modes, a relaxation rate is defined by a collision number, Z, which represents the number of collisions to reach equilibrium. This collision number is usually fit to experimental or theoretical data to reproduce the relaxation time as a function of temperature. In the case of rotational and vibrational levels, the relaxation time is typically generalized so that the collision number is independent of the current state of the colliding particles. For electronic excitation,

experimental or theoretical results for a general electronic relaxation time are not available. This is partially due to the difficulty in defining a relaxation rate general enough to describe the individual transitions rates of each electronic level.

In the past, DSMC electronic excitation models have used several different electronic collision numbers and these approaches are reviewed in Chapter 1. Typically, state- and temperature-independent electronic collision numbers are defined for each species, but more recently, Burt and Josyula proposed a state- and temperature-specific collision number approach [21]. While this method has the potential to improve the electronic excitation model's accuracy, it requires intricate calculations in each cell that would be difficult to extend to the unsteady simulations performed in the CHIPS code. With this in mind, a state- and temperature-independent collision number method is employed in the CHIPS code.

In the CHIPS code, the electronic collision number, Z_{elec}, for each collision pair is determined from a combination of physical intuition, collision numbers published in other DSMC simulations, and comparisons with radiative results. Previous collision numbers were published by Bird where heavy particles colliding with other heavy particles were assigned a collision number on the order of ~O(100-1,000) and excitations by free electrons were given a collision number on the order of ~O(10-100) [19]. When using these values of Z_{elec} in the CHIPS code and comparing with experimental radiative results, the electronic excitation rate appears to be underpredicted. New Z_{elec} values have been assumed based off intuition and confirmed with the radiative results in the following sections. For excitations by heavy particles, Z_{elec} is defined to be 250 and for excitations by free electrons, Z_{elec} is set as 2. These values agree with intuition as the free electrons are expected to be much more efficient at excitation than heavy particles. In the CHIPS simulations, the probability of an excitation event occurring is defined as

$$P_{elec} = \frac{1}{Z_{elec_{i,j}}} \quad [8.1]$$

for the excitation of species i by j. While the choice of Z_{elec} in the current simulations are relatively arbitrary, this is a simple starting point where the sensitivity study completed in the following chapter should give more insight into selecting appropriate values. In the future, Z_{elec} values for individual transitions and/or a temperature dependent relationship for Z_{elec} could be determined from published cross-sections. For example, the work by Huo, et al. provides a database of electron impact cross-sections for a partially ionized gas [94].

8.2.3.2 Electronic Temperature

Various different methods for calculating the electronic temperature have been covered in this thesis (Section 3.5.2), but each of these approaches has had difficulty representing a nonequilibrium electronic distribution as a temperature. This conclusion is supported by the unexpected presence of a high electronic temperature far upstream of the shock in the nominal simulations (Section 4.4) and the large statistical fluctuations observed in the sensitivity study of electronic temperature (Section 5.4.2). The previous attempts to calculate the electronic temperature relied on the direct calculation of the temperature from the Boltzmann distribution. This involved the comparison of either the energy populating two pre-selected states or the average temperature from comparing every populated state. In nonequilibrium portions of the simulation or regions where the number of excited particles is low, these electronic temperature calculations can result in unrealistically large or small temperatures. While a nonequilibrium or statistically sparse

electronic temperature is difficult to properly define, the following approach provides an improvement over the previously used methods.

The intention of the previously used electronic temperature calculation, where each populated state is compared, was to incorporate the information of the entire electronic distribution (Eqn. 3.13). Although this is accomplished, the method is too sensitive to statistical fluctuations associated with very small numbers of excited states in cells with a low number of excited particles or to unphysical temperatures that result from assuming a Boltzmann distribution. As an alternative, the CHIPS code now calculates the electronic temperature of each species in a cell by performing a linear least squares fit to the Boltzmann distribution. The ratio of populations of two states is given by

$$\frac{n_i}{n_j} = \frac{g_i \exp(-E_{elec_i}/k_B T)}{g_j \exp(-E_{elec_j}/k_B T)} \qquad [8.2]$$

where n is the number density, g is the degeneracy, and E_{elec} is the electronic energy in state i or j. Assuming that T is the electronic temperature and rearranging Eqn. 8.2, the electronic temperature can be calculated directly from two states as

$$\left[ln\left(\frac{n_j}{g_j}\right) - ln\left(\frac{n_i}{g_i}\right)\right] = -\frac{E_{elec_i} - E_{elec_j}}{k_B T_{elec}} \qquad [8.3].$$

By inspection of Eqn. 8.3, T_{elec} can be related to the slope of a so-called Boltzmann plot, i.e. a plot of the logarithm of the degeneracy normalized state population versus state energy. This has a slope

$$s = -\frac{1}{k_B T_{elec}} = \frac{ln\left(\frac{n_2}{g_2}\right) - ln\left(\frac{n_1}{g_1}\right)}{E_2 - E_1} \quad [8.4]$$

that defines the electronic temperature. In a simulated cell, each species may have several excited electronic energy levels. To determine the electronic temperature of these species, a linear least squares regression of the species' excited population is performed by minimizing the sum of the squared residuals

$$R = \sum_{i=1}^{N_G} \left[ln\left(\frac{n_i}{g_i}\right)_{DSMC} - ln\left(\frac{n_i}{g_i}\right)_{fit} \right]^2 \quad [8.5]$$

where N_G is the number of populated levels, $(n_i/g_i)_{DSMC}$ is the simulated population normalized by degeneracy at each level, and $(n_i/g_i)_{fit}$ is the normalized population related to the Boltzmann distribution at the fit temperature. By performing a least squares regression, the electronic temperature calculation is less sensitive to individual over- or underpopulated excited states.

Although determining the electronic temperature via a linear least squares fit is an improvement over the previous models, there are still difficulties when calculating an electronic temperature from a species that has very few electronically excited particles. In this case, large electronic temperatures can still result, but some of these inappropriate temperatures can be avoided. By setting a minimum number of particles for each species that acts as a threshold before the electronic temperature is calculated, many of the temperature fluctuations can be ignored. In the CHIPS code, this minimum is 5 particles excited out of the ground state. Another problem to be aware of is the effect of modeling a large number of excited states. Each excited state is treated as a separate point in the

linear least squares fit. This means that in the least squares fit, the highest excited state is weighted the same as the ground state regardless of how many particles populate each state. This could skew curve fit to the electronic temperature calculation in favor of the higher lying states even though more particles are populating the lower levels. In the future, it would be beneficial to weight each level based on the number of simulated particles.

8.3 Radiation Model

In Chapter 6, radiation was obtained from CHIPS results for hypersonic entry scenarios into the hydrogen-helium Saturn atmosphere. To obtain radiative quantities, the number densities and temperatures calculated from the CHIPS simulations were passed to the NEQAIR line-by-line radiation code [5]. The line of sight radiative predictions at each simulated point were performed for several spectral ranges and compared to experimental measurements from the NASA Electric Arc Shock Tube (EAST) [2]. Although simulated radiance was successfully obtained by post-processing CHIPS with NEQAIR, comparisons with the experimental data demonstrated that improvements were required (Chapter 6). In addition, it is expected that simulating radiation for an 11-species air hypersonic scenario will present new challenges due to additional physics present in high temperature air flows.

8.3.1 Nominal EAST Experiments

Now that the CHIPS code is able to simulate radiation with the assistance of NEQAIR, the nominal simulation choice is revisited. Unlike the previous hypersonic air simulations that did not include radiation calculations (Chapter 4), the nominal simulation chosen for the final sensitivity analysis must consider the availability of experimental radiation data. The experiments performed in the EAST facility are prime candidates for

a nominal simulation due to their extensive review. Brandis and Cruden have analyzed each of these experiments and identified several benchmark cases that produced results with minimal experimental error [1]. A group of these benchmark experiments performed at an initial pressure of 0.2 Torr are clustered near a shock speed of 10.3 km/s and are summarized in Table 8.6. Since these conditions are rarefied enough for DSMC, require ionization modeling, and a large set of data over several experiments is available, this scenario is well suited for a final sensitivity analysis. This set of experimental data also includes Campaign 47, Shot 37 which was the subject of the previous nominal lunar return simulations and sensitivity analyses. When selecting a nominal simulation, only a single shock speed can be reproduced by the CHIPS code even though five separate speeds were recorded in the set. To obtain the best comparison with all of the experimental data, the average of the shock speeds in Table 8.6 is taken to select a nominal shock speed of 10.28 km/s.

Table 8.6 Summary of benchmark EAST experimental data near 10.3 km/s and 0.2 Torr.

Campaign	Shot	Shock Speed [km/s]	Camera
50	57	10.25	IR
47	37	10.26	Vis/NIR
50	29	10.29	VUV & UV/Vis
57	16	10.3	VUV
47	33	10.32	UV/Vis

In each of the EAST experiments, measurements were taken in the VUV, UV/Vis, Vis/NIR, and IR spectral regions. While all of these regions were recorded in each Shot, only the cameras that provided reliable, well resolved data are listed in Table 8.6. The

final nominal simulation will be compared to these camera measurements after post-processing the CHIPS results with NEQAIR. In order to directly compare with the experiments, the convolution functions listed in Table 8.7 are applied to the radiation calculation in the NEQAIR code. For more details about the convolution functions and their application, refer to Chapter 1 or to Ref. [33].

Table 8.7 Convolution function parameters used for the spectral ranges simulated with NEQAIR [1].

Spectral Range	Optical Resolution Function	d_{opt_1}	d_{opt_2}	w_g	w_l	d_{gate}
VUV	Triangular	0.041	–	0.026	0.063	0.514
UV/Vis	Triangular	0.041	–	0.021	0.004	0.257
Vis/NIR	Triangular	0.041	–	0.063	0.015	0.109
IR	Trapezoidal	0.313	0.128	0.141	–	0.513

8.3.2 CHIPS Interconnect with NEQAIR

In addition to choosing the nominal simulation, radiative results must be obtained by NEQAIR from a CHIPS simulation reproducing a hypersonic shock in air. Previously, emission spectra were calculated from NEQAIR for a hydrogen-helium mixture (Chapter 6), but significant errors were observed when comparing with the experimental data and several improvements were suggested. One of the potential improvements identified in Chapter 6 addresses how the CHIPS results are passed to the NEQAIR code. In the Saturn entry case, the electronic temperature was assumed to be equal to the free electron temperature. At the completion of a CHIPS simulation, the free electron temperature was sent to the NEQAIR code, along with the translational, rotational, and vibrational temperatures and the species number densities at each sample point. The NEQAIR code

then used these quantities to calculate the radiative outputs. With the improved electronic temperature calculation detailed in Section 8.2.3.2, the simulated electronic temperature can now be used in place of the free electron temperature when passing CHIPS results to the NEQAIR code. While this is an improvement over using the free electron temperature, this approach still results in unnecessary calculations.

Using the standard NEQAIR settings, the electronic temperature passed to NEQAIR, or the free electron temperature in the Saturn case, is used to calculate the populations of the excited states for each species. The excited state populations are assumed by NEQAIR to follow some distribution based on the electronic temperature. This distribution could be Boltzmann, Quasi-Steady State, etc. depending on which mode NEQAIR is set to run. The emission and absorption coefficients are then calculated from the excited state distributions and these coefficients are used to determine the radiative transport, resulting in simulated radiance at each line of sight. When using the CHIPS code with NEQAIR, the first step is in fact redundant and introduces errors into the radiative results. In the CHIPS code, excited state populations are directly available. By determining an electronic temperature, passing it to NEQAIR, and then recalculating the state populations in NEQAIR, significant nonequilibrium information is lost. For the final sensitivity analysis and nominal simulation, a different version of the NEQAIR code is employed where the excited state distributions are passed directly to NEQAIR, completely omitting the first step. Although this approach has its obvious advantages, extra effort is required to ensure that data are sent from CHIPS to NEQAIR in the appropriate format.

8.3.3 Electronic State Grouping and Ungrouping

When the electronic level populations for each species are passed to the NEQAIR code from CHIPS, each level modeled in the NEQAIR code must be accounted for. This includes 334 electronic levels for atomic nitrogen and 479 levels for atomic oxygen for example. Accurately modeling each one of these excited states is impossible without an extremely large number of simulated particles. In addition, the excitation probability calculated from Liechty's model may become so small that populating the level would be unlikely. Instead of modeling each level individually in the CHIPS code, this issue is solved by grouping the excited states. The grouping substantially increases the computational efficiency of the CHIPS simulation and allows for better statistics describing each excited state. This same grouping approach has been commonly applied in many DSMC and CFD simulations [49][95][96].

In the CHIPS code, electronically excited states for 11-species air are modeled according to the groups suggested in NEQAIR. The grouped excited state's energy and degeneracy are determined from a weighted average of the electronic levels contained in the group. The group's energy is defined as

$$E_G = \frac{\sum_{i=1}^{N_G} g_i E_i}{g_G} \qquad [8.6]$$

where E_i and g_i are the energy and degeneracy of N_G excited states contained in the group G and the degeneracy of the group is determined as

$$g_G = \sum_{i=1}^{N_G} g_i \qquad [8.7].$$

While this seems to be a valid solution, groupings must be chosen carefully. If the levels are grouped without consideration for the important transitions that define the spectral ranges of interest, certain radiative contributors could be suppressed. For example, if both the upper and lower excited states for a specific bound-bound transition are grouped into a single level, nonequilibrium between these states is impossible. This results in an incorrect prediction of radiative emissions from that spectral line.

Although modeling the grouped electronic levels is straightforward, ungrouping the excited states so that they can be passed to NEQAIR is more difficult. In previous publications, ungrouping was performed by calculating the number density of the excited states contained in a group from the Boltzmann distribution at the free electron temperature [96][95]. In this method, the number density of an ungrouped level is calculated from the Boltzmann distribution as

$$n_i = \frac{n_G g_i \exp\left(-\frac{E_i - E_G}{k_B T_e}\right)}{\sum_{i=1}^{N_G} g_i \exp\left(-\frac{E_i - E_G}{k_B T_e}\right)} \qquad [8.8]$$

where the denominator is the electronic partition function of the states contained in the group. There are several drawbacks to this approach. First, the normalization factor of the Boltzmann distribution is determined only from the excited states contained in the group. While this conserves mass, as the number density is distributed from the grouped level to the ungrouped levels, it does not conserve energy unless the ungrouping is performed at equilibrium [96]. Even though this method does not exactly conserve energy, the error is nearly negligible for the excited state distributions and has no effect on the simulation as ungrouping is a post-processing step. The second negative characteristic of this

ungrouping method, particularly for DSMC, is its reliance on a free electron temperature. In nonequilibrium regions, the free electron temperature may not accurately describe the electronically excited populations. In highly nonequilibrium regions where the free electron temperature is subject to statistical fluctuations caused by a small number of simulated free electrons, this method has been observed to severely misrepresent the electronic populations. In addition, there may be regions where no free electrons are simulated by DSMC, but particles are electronically excited. These regions encounter the same problems just discussed as they require Eqn. 8.8 to be calculated from a different temperature, such as the translational temperature.

In this research, an alternative ungrouping method is proposed that avoids using any explicitly determined temperatures. Similar to the new electronic temperature fitting approach detailed in Section 8.2.3.2, the representation of the ratio of two Boltzmann distributions as a line is utilized (Eqn. 8.4). While a linear least squares regression could be employed to fit the grouped excited state distributions for each species, complexity in the distribution can be captured with a polynomial least squares curve fit. The slope of the curve fit, s_G, at the grouped level's energy is used to define each ungrouping by

$$n_i = \frac{g_i}{g_G} n_G \exp\left(s_G (E_i - E_G)\right) \qquad [8.9]$$

where the slope can be related to the temperature characterizing this group of excited states. It should be noted that, like Eqn. 8.8, this approach does not conserve energy exactly. In nonequilibrium regions, the populations of the grouped levels may not be linearly distributed on a Boltzmann plot and instead might be split into distinct subsets of energy levels that follow separate trends. The advantage of the polynomial curve fit is

that it can capture the trend of each subsection. Figure 8.4 shows a distribution that was sampled from the CHIPS code within the nonequilibrium region of a shock (filled blue circles). Because complex physical processes are occurring in this region, the excited state distribution can no longer be described by a single line (Boltzmann distribution). This distribution plotted in Fig. 8.4 demonstrates the separation of the atomic nitrogen electronic level populations into three distinct groups. The first group is defined by the ground state. As N_2 dissociation begins to occur within the shock, the ground state of atomic nitrogen is populated since only ground level particles can result from reactions in the current model. The beginning of electronic excitation within the shock creates the second group from the 1st excited state to approximately the 3rd grouped excited state near $E = 1.6 \times 10^{-18}$ J. Since the slope of this group is shallower, the excitation process to these levels is likely driven by the high energy kinetic interactions that occur within the shock. The final group, from the 5th to the highest excited level, seems to be depleted. This is either a result of ionization reactions or due to a delay in populating the highest levels as a result of the time required to build enough energy to populate these states. A similar nonequilibrium distribution structure has been observed in atomic nitrogen by Panesi, et al. and was attributed to depletion from the upper states by ionization and spontaneous emission [97]. In their work, upper state populations trended towards the Saha distribution computed from the free electron temperature.

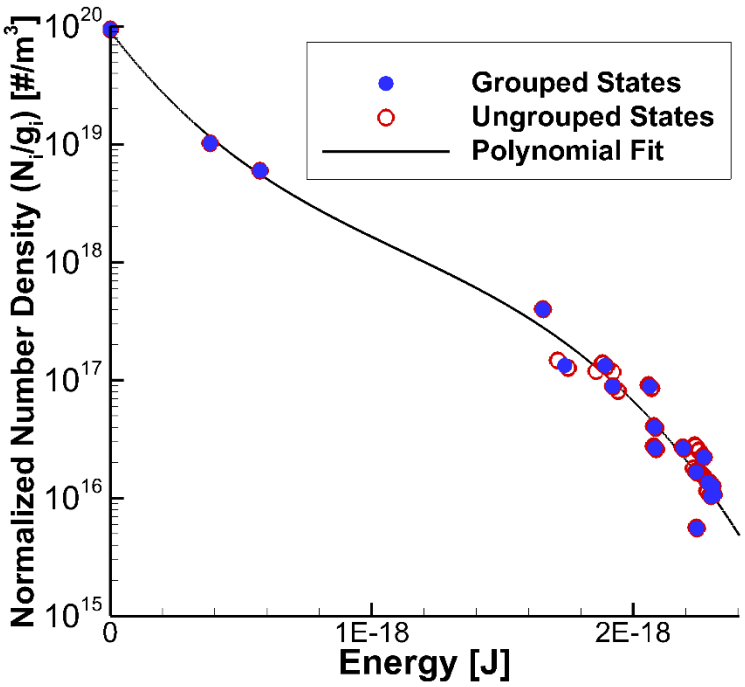

Figure 8.4 Ungrouping and curve fit of atomic nitrogen excited states within a nonequilibrium shock region.

While the atomic nitrogen population shown in Fig. 8.4 is likely the most complex distribution encountered in the CHIPS code, a range of less intricate distributions are expected. The polynomial fit approach must be able to accurately handle cases where only a few excited states are populated. This poses a problem for the polynomial curve fitting method since overfitting can occur when using a high order polynomial. Because each curve fit cannot be analyzed manually, the polynomial fitting routine must automatically determine the polynomial's order to avoid overfitting. In the CHIPS code, a 3rd order polynomial is considered when there are more than 15 populated levels, a 2nd order polynomial is possible when there are more than 10 populated levels, and only a linear fit is allowed when 10 or fewer levels are populated. In addition, even when a higher order polynomial fit is possible, the fits are calculated in increasing order.

If the standard deviation does not decrease by some preset amount, the previously checked polynomial order is used. Figure 8.4 demonstrates an example of a 3rd order fit to the atomic nitrogen level population. Upon analyzing the curve fits throughout the shock for each species, good agreement with the populations was observed. One caveat of the polynomial fitting method is that if only a single excited state is present in a cell, curve fitting is not possible. To handle this occurrence, the ungrouping is determined from Eqn. 8.8. In this approach a temperature must be selected for the Boltzmann distribution. When available, the electronic temperature is used, but otherwise the translational temperature is applied. Now that an ungrouping method is defined, Fig. 8.4 shows the electronic levels ungrouped by the polynomial fit's slope (open red circles).

Resolving electronic state distributions is much more difficult than resolving the bulk temperatures or number densities of individual species. Difficulties with poor statistics in the modeling of electronic distributions have already been discussed, but the statistics can be improved by effectively increasing the number of simulated particles. While adding more particles to the simulation incurs a computation penalty, the electronic distribution statistics can instead be improved by increasing the size of the sampling cells. Since increasing the sampling cells would be detrimental to accurately representing gradients in the temperature and number density outputs, a second sampling grid was created in the CHIPS simulation that stores and outputs the quantities that are intended for NEQAIR. This "NEQAIR" sampling grid is treated in the exact same manner as the original sampling grid where both grids move in lockstep with the unsteady shock wave. Files are then written from this sampling grid to be passed to the NEQAIR code where line of sight radiation from each sampling grid point is calculated. This second sampling grid reduces the noise in the radiative results by providing NEQAIR with better defined electronic state populations.

8.4 EAST NOMINAL SIMULATION

After improving the CHIPS models and radiation calculations obtained from NEQAIR, a final nominal simulation is performed which aims to reproduce the EAST experiments summarized in Table 8.6. Since only a single scenario can be selected to represent the nominal simulation, a freestream pressure of 0.2 Torr and a shock velocity of 10.28 km/s, determined from the average velocities in Table 8.6, are simulated in the CHIPS code. The full inflow conditions, including CHIPS simulation parameters, are listed in Tables 8.8 and 8.9. In this simulation, the updated CHIPS input parameters for the VHS and TCE chemistry models in this chapter are used. For the sets of model parameters not updated in this chapter, the values from Chapters 2 and 3 are used.

Table 8.8 Nominal simulation inflow conditions.

EAST Scenario	
Shock velocity [km/s]	10.28
Number density [#/m^3]	6.4377×10^{21}
Temperature [K]	300
N_2 mole fraction [%]	79
O_2 mole fraction [%]	21

Table 8.9 Nominal simulation CHIPS simulation parameters.

Simulation Parameters		Sampling Grid Parameters	
Collision Cell Size [m]	2.0×10^{-4}	Cell Size [m]	7.5×10^{-5}
Number of Cells	5000	Number of Sampling Cells	1000
Timestep [s]	8.0×10^{-9}	NEQAIR Cell Size [m]	4.0×10^{-5}
f_{num} [#/m^3]	1.0×10^{17}	Number of NEQAIR Cells	100
		Number of Ensemble Samples	6000

Results of the temperatures and number densities calculated from the nominal CHIPS simulation are presented in Fig. 8.5a-c. The nominal case was run twice, first with the electronic collision number values discussed in Section 8.2.3.1 (solid lines) and second without the electronic collision number, assuming $Z_{elec} = 1$ (dashed lines). As the selected scenario has similar conditions to the previously performed nominal lunar return cases in Chapter 4, the results are comparable. Figure 8.5a plots the neutral particle number densities and Figure 8.5b shows the charged particle number densities as a function of distance from the shock location. As the freestream nitrogen and oxygen molecules encounter the shock, dissociation begins and rapidly accelerates within the shock. After the onset of dissociation, the flow is energetic enough that ionization reactions are initiated. The first free electrons in the flow are created by associative ionization reactions. Once enough free electrons are formed, electron impact ionization reactions contribute to the creation of additional free electrons and the number density of charged particles rises quickly. Downstream of the shock, chemistry slows, and the concentration of each species approaches equilibrium. In Figs. 8.5a and 8.5b, chemical

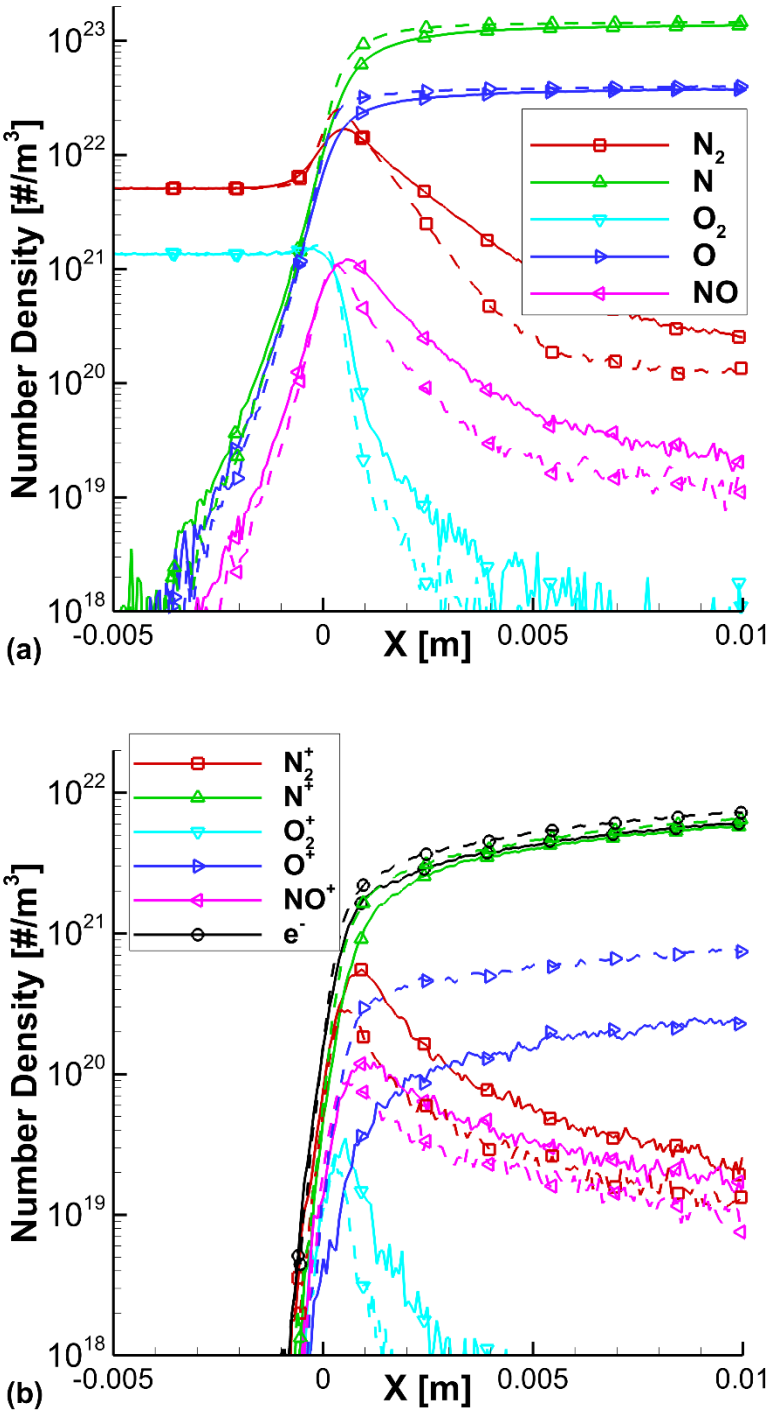
Number Density [#/m^3]
10^{23}
10^{22}
10^{21}
10^{20}
10^{19}
10^{18}
-0.005
0
0.005
0.01
X [m]
(a)
N_2
N
O_2
O
NO
N_2^+
N^+
O_2^+
O^+
NO^+
e^-
(b)

Figure 8.5

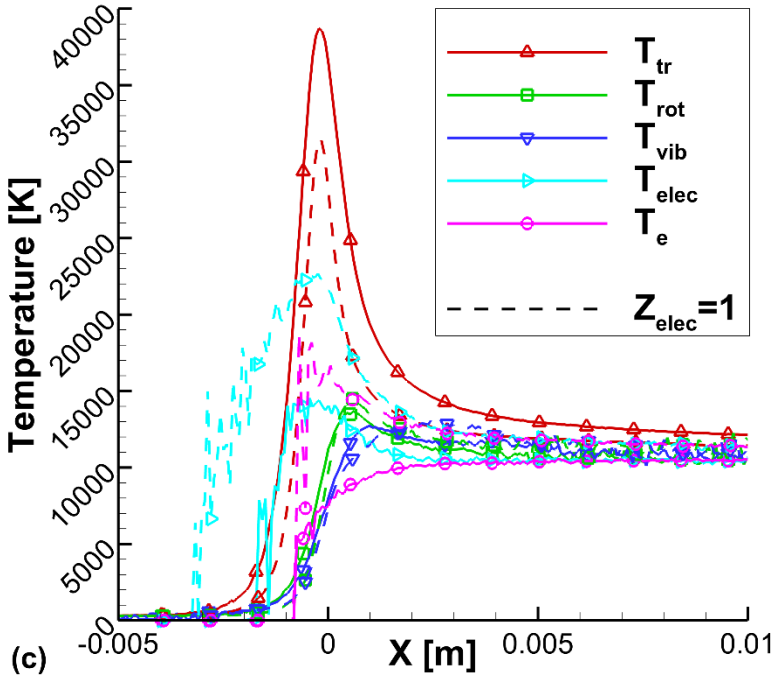

Figure 8.5 Simulation of EAST experiments with specific electronic relaxation numbers (solid line) and with $Z_{elelc} = 1$ (dashed line). (a) Neutral Particle number densities. (b) Charged particle number densities. (c) Bulk temperatures.

relaxation is still occurring at $X = 1$ cm, but the concentrations are approaching their final equilibrium.

In Fig. 8.5c, five separate temperatures are observed in the CHIPS results. Within the shock, significant nonequilibrium is present between the various temperatures. The translational temperature initially spikes to 40,000 K, but quickly relaxes toward equilibrium as kinetic energy is transferred to internal energy modes or absorbed by endothermic chemical reactions. The rotational and vibrational temperature trail behind the translational temperature as energy first enters the rotational mode and then the vibrational mode. As equilibrium with the translational temperature is approached, the statistics of these internal temperatures becomes poorer because most of the diatomic

molecules have been dissociated. The opposite resolution problem occurs for the free electron temperature. The creation of the first free electrons occurs within the shock from ionization reactions. Initially, the statistics are poor, resulting in unphysical temperature spikes, until more ionization reactions have occurred. Many of the statistical fluctuations have been avoided in the CHIPS simulation by only calculating the free electron temperature after five simulated particles are present in a sampling cell. Using this threshold, the free electron temperatures shown in Fig. 8.5c are mostly free of large statistical fluctuations. The free electron temperature is in significant nonequilibrium with the translational temperature into the downstream region. While it may be assumed that the free electrons equilibrate quickly due to the high collision frequency of the electrons, it is likely the case that free electron temperature is kept out of equilibrium by the continuous ionization and capture reactions taking place. In fact, the free electron temperature is typically modeled by assuming that $T_e = T_{vib}$ since electrons exchange energy with electronic and vibrational modes more efficiently [47]. Finally, the electronic temperature in Fig. 8.5c is calculated by using the new curve fitting method. As with the free electron temperature, the minimum number of simulated particles required to calculate the electronic temperature is set to five. The minimum is applied to each individual species' electronic temperature calculation so that an unphysical electronic temperature calculated from one species does not skew the overall electronic temperature result. The electronic temperature shown in Fig. 8.5c increases rapidly at the shock front. Because the electronic collision number is much lower for collisions involving free electrons ($Z_{elec} = 2$) than for collisions with heavy particles ($Z_{elec} = 250$), the electronic temperature begins equilibrating to the free electron temperature once the ionization process begins. Compared to previous CHIPS simulations involving electronic excitation, the electronic temperature calculated here shows improvement since the new least

squares regression is less sensitive to outliers in the excited state population. Also, the minimum particle threshold eliminates the problem of high electronic temperatures calculated far upstream of the shock based on a small sample of excited states.

It must be noted that the temperatures in Fig. 8.5c do not fully equilibrate by 1 cm. It is difficult to say whether the persistence of nonequilibrium is correct for a hypersonic shock of this speed. While it is generally assumed that the temperatures equilibrate relatively quickly behind a shock, there is a complex set of processes in an electronically excited and ionizing shock that could slow the approach to equilibrium. If this observed nonequilibrium is a result of error in the CHIPS calculations, there are several causes that might be identified. First, the omission of electronic energy contributions to the reaction probability could slow equilibration by forcing energy to be depleted from the excited states through inelastic collisions instead of by ionization reactions. Another possibility is that the post-reaction assignment of energy to the products of a reaction may be incorrect. If this is the cause, energy could be over- or under-assigned to an internal mode which would force the flow away from equilibrium at every reaction. In addition, the equilibration of the rotational mode is slower than expected and previous simulations have found that the rotational temperature equilibrates with the translational temperature more quickly [47][97]. Finally, an energy transfer process that is not modeled in the current research, such as spontaneous photon emission, may be important.

The nominal simulation was run a second time, with the original electronic collision number model form proposed by Liechty, so that the effects of different assumptions can be quantified [24]. The dashed lines in Fig. 8.5a-c show the results when $Z_{elec} = 1$ for all collisions. In Fig. 8.5a, the neutral number densities within the shock are mainly unchanged, but in the post-shock region the rate that diatomic molecules

dissociate increases. Differences are more apparent in Fig. 8.5b where the overall number density of charged particles is larger, and a significant increase is seen in the ionization rate of atomic oxygen. The most obvious changes are seen in the temperatures plotted in Fig. 8.5c. The peak of the translational temperature spike drops nearly 10,000 K when the electronic collision number is set to unity. This coincides with a significant increase in the electronic temperature. This is expected since setting $Z_{elec} = 1$ means that every collision could possibly result in an electronic excitation event; this drives the flow toward equilibrium much faster. Because thermal equilibration is accelerated as internal modes are populated, the dissociation and ionization processes occur more rapidly. A high electronic temperature is also computed further upstream of the shock. Since electronic excitation events are now more probable, this is most likely due to a combination of electronically excited particles diffusing into the freestream or collisions between freestream particles and diffused shock particles that result in an excitation.

Once the nominal scenario is completed with the CHIPS code, the results are passed to NEQAIR. Four separate spectral ranges are simulated in NEQAIR and the results are compared with the EAST experimental results in Figs. 8.6-9. The spectral ranges studied here include the VUV (170-178 nm), UV/Vis (328-496 nm), Vis/NIR (480-890 nm), and IR (840-1250 nm) ranges with the corresponding experiments listed in Table 8.6. The experimental data requires some modification to be directly compared with the CHIPS/NEQAIR simulations. In the CHIPS/NEQAIR results, the shock location is tracked based on the halfway point of the normalized pressure jump. On the other hand, the shock location in the EAST experiments can only be inferred from the radiative results. Because the shock location in the EAST experiments is subjective, identifying a shock front consistent with the CHIPS simulations is difficult. Adding to the difficulty, the shock location is not synchronized between cameras. This means that a well-defined

shock location from one spectral region cannot be used to locate the shock in a separate region. For each experimental data set, the data must be shifted manually over the X domain relative to the CHIPS/NEQAIR results. Attempts can be made to match significant spectral features from the experiments with the simulated results, but there is no guarantee that matching these features is exact. In addition, the presence of the driver gas contact surface in the shock tube will eventually contaminate the results. The NEQAIR simulations cover a 4 cm domain that was chosen to roughly match the valid domain of the EAST experiments. While some of the experiments produced valid data outside of this range, interference from the contact surface in the EAST experiments is generally avoided by truncating the results at 4 cm. When the contact surface obviously affected the experimental data in a region less than 4 cm, these data were removed.

Simulations for each spectral range were completed with the NEQAIR code and the convolved results are compared to the EAST experiments in Figs. 8.6-9. The NEQAIR simulations were also completed for the case where the electronic collision number was assumed to equal one. Figure 8.6 plots the results of the VUV spectrum between 170 – 178 nm which is dominated by the atomic nitrogen transition from the 3s ^{2}P to the 2p^3 ^{2}P excited state. In the experiments, a radiance peak occurs due to high nonequilibrium temperatures within the shock that cause excitation of the atomic nitrogen, leading to bound-bound emission. As the temperatures equilibrate, the radiance from nonequilibrium atomic nitrogen decreases until the point where emissions are a result of the equilibrium transition rate. Post-shock, this equilibrium radiance increases slightly with the number density until chemical equilibrium is obtained.

The CHIPS/NEQAIR simulations are comparable with the general trend observed in the experiments, but a few discrepancies can be identified. While the simulated radiance peak in the nonequilibrium shock region seems to reproduce the experiments

well and the dip in the radiance is observed, the subsequent rise after the dip is not simulated. Instead, the simulated VUV radiance monotonically decreases weakly with distance from the shock. This may indicate that the simulated states of the emitting atomic nitrogen are relaxing to equilibrium slower than the experiment. To determine the analytic equilibrium radiance from the pre-shock conditions, the NASA Chemical Equilibrium with Applications (CEA) code was used [98]. The equilibrium temperature and chemical concentrations were determined by running the CEA code in shock tube mode and then these results were processed by the NEQAIR code to determine the equilibrium radiance for the spectral range. The dashed black line in Fig. 8.6 compares the analytic equilibrium radiance with the simulation and experiments. The experimental measurements appear to reach an equilibrium value slightly above the analytic equilibrium radiance. This discrepancy will be discussed when analyzing the UV/Vis spectral range. When comparing the simulated radiance with the expected equilibrium radiance, the correct radiance is produced by the simulation from approximately 0.5 – 1.5 cm, but the simulated radiance then diverges from the analytic equilibrium. This is an unintended consequence of the convolution that is applied in NEQAIR to mimic the experimental smearing. Since the simulation only produced data up to 3 cm, the convolution is reducing the radiance as the end of the data is approached. This effect is not visible in the experimental data because the measured data has been *truncated* to remove the contact surface and typically extends much further post-shock. In the future, this negative affect could be eliminated by simulating further behind the shock and truncating the result when unrealistic convolution affects are observed. In addition, a slight gradual increase of the simulated radiance is observed in front of the shock. This is also an artifact of the smearing due to the convolution function. In actuality, no radiance is present in this upstream region before convolving the NEQAIR results but, unlike the

post-shock convolution problem, this is a desired result as the experiments were unlikely to measure any pre-shock radiation either. Although the nominal simulated case has some discrepancies with the experiments, the CHIPS/NEQAIR results using $Z_{elec} = 1$ overpredicts the VUV radiance in Fig. 8.6 by as much as an order of magnitude.

Another process that may influence the simulated results is spontaneous emission. While spontaneous emission is modeled in NEQAIR to determine bound-bound emission from the excited state populations, it is not currently modeled by the CHIPS code. Including spontaneous emission in CHIPS could be important for reproducing the correct relaxation rate and excited state populations and, therefore, the correct radiance calculated from NEQAIR. In the VUV range considered here, the radiative lifetime of the atomic nitrogen 3s ^{2}P state to the 2p^3 ^{2}P state is as short as 10 ns which is comparable to the nominal simulation timestep and likely shorter than the collisional relaxation time through deexcitation by particle impact. Although this is true for the atomic nitrogen transition measured in this spectral range, the radiative lifetime of the other transitions considered in this research is typically an order of magnitude or more longer and so the corresponding simulated spectra would be less influenced by including spontaneous emission in CHIPS.

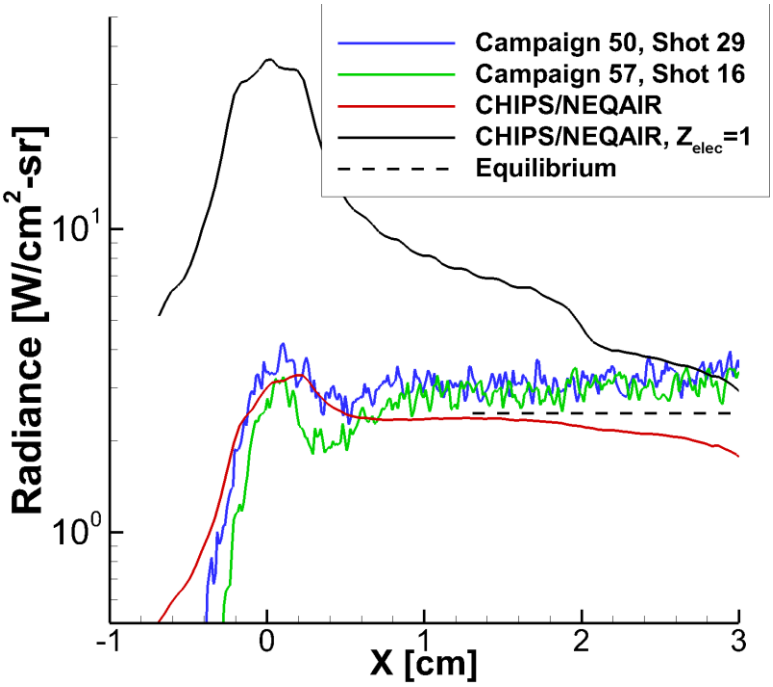

Figure 8.6 Simulated radiance with and without an electronic relaxation number in the VUV range (170-178 nm) relative to the EAST experimental data.

Figure 8.7 compares the UV/Vis spectral range from 328 – 496 nm with two independent EAST experiments. The initial spike observed in the radiance measurements is primarily a result of the N_2^+ 1st negative $\left(B^2\Sigma_u^+ \rightarrow X^2\Sigma_g^+\right)$ and N_2 2nd positive $(C^3\Pi \rightarrow B^3\Pi)$ emissions. As dissociation occurs within the shock, the emission from these transitions decreases until an equilibrium region occurs downstream of the shock. This region is dominated by bound-free continuum emission resulting from free electron capture by N^+. In addition, some atomic line emissions of nitrogen are present. The analytic equilibrium radiance was again plotted in Fig. 8.7. In this case, the experimental equilibrium is significantly larger than the expected equilibrium calculated from the freestream conditions. This could be a result of several uncertainties in the experimental measurements. The increased radiance could be due to contamination in the flow or boundary layer effects that developed along the shock tube wall. Inaccurate measurement

of the shock velocity could be a cause of the discrepancy as the radiance is strongly dependent on the shock velocity. In the experiments, the shock is also decelerating as it travels down the shock tube, meaning that the gas has seen higher shock speeds than the velocity measured at the test section. Most likely, a combination of these factors contributes to the discrepancy between the simulations and experimental data.

The CHIPS/NEQAIR simulation predicts a radiance peak, but the radiation trails off further from the shock. As in the VUV spectrum, the analytic equilibrium is matched post-shock, but suddenly decreases as the end of the simulated data is approached. This is again likely a result of the convolution affects previously discussed. Another source of error in the simulated equilibrium could potentially originate from misrepresenting the concentration of free electrons and N^+ in the downstream region. Since the bound-free radiation is proportional to the product of the e^- and N^+ number densities, error in the number density by a factor of two will results in error in the radiance by a factor of four. When considering that the accepted nitrogen electron impact ionization reaction rates are incompatible with the TCE model and a poorly fit new reaction rate had to be created (Section 8.2.2), it is reasonable to expect that the number density of N^+ is not accurate. When considering the simulation with $Z_{elec} = 1$, the results again overpredict the peak within the shock by an order of magnitude. However, in Fig. 8.7 the radiance for this case quickly converges with the other CHIPS/NEQAIR simulation in the post-shock region. This observation furthers the conclusion that the radiance in this region depends on the N^+ number density since the N^+ number density plotted in Fig. 8.5b is similar for both cases.

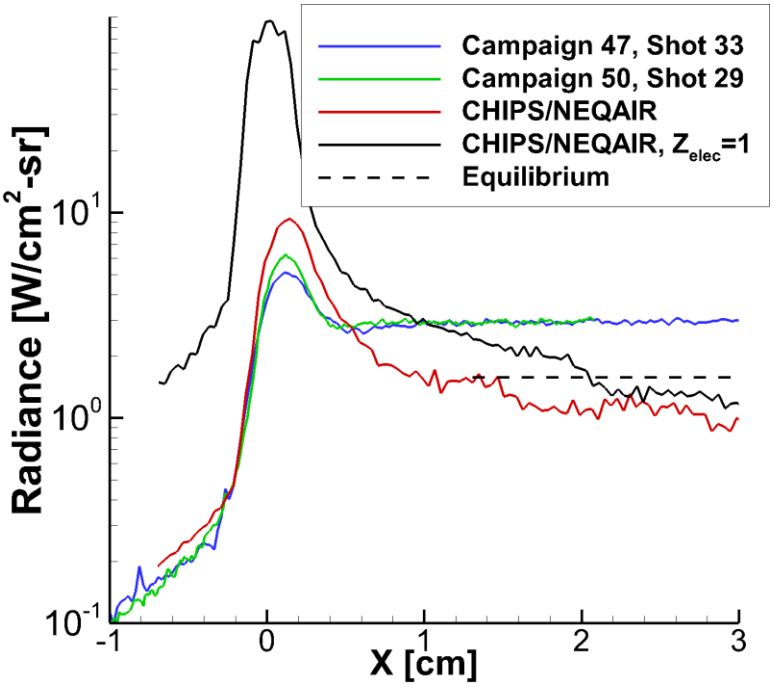

Figure 8.7 Simulated radiance with and without an electronic relaxation number in the UV/Vis range (328-496 nm) relative to the EAST experimental data.

In Fig. 8.8, the Vis/NIR range from 480-900 nm is studied by comparing with the Campaign 47, Shot 37 EAST experiment. The emissions observed in this region are mainly attributed to N and O bound-bound transitions while the bound-free background continuum is less of a factor. The simulated CHIPS/NEQAIR radiance shows a peak within the shock, but a radiance peak is not present in the EAST data. Instead, a short-lived plateau is observed within the shock, followed by a second increase in radiation intensity that leads to the equilibrium radiance. As with the previous spectral ranges, the nominal simulation compares well with the analytic equilibrium while the experimental results overpredict equilibrium. While the current simulation predicts a small peak within the shock, a dip is observed that may indicate the correct physics are being modeled. Again, the peak occurs in the nonequilibrium region where the CHIPS model could be

incorrectly predicting the excitation rate. To support this hypothesis, the CHIPS/NEQAIR simulation with $Z_{elec} = 1$ results in a much larger peak in the shock that dominates any other spectral feature. Since this peak seems to increase when the collision number is equivalent to $Z_{elec} = 1$, raising the N and O electronic collision number in the nominal simulation may eliminate the nonequilibrium peak.

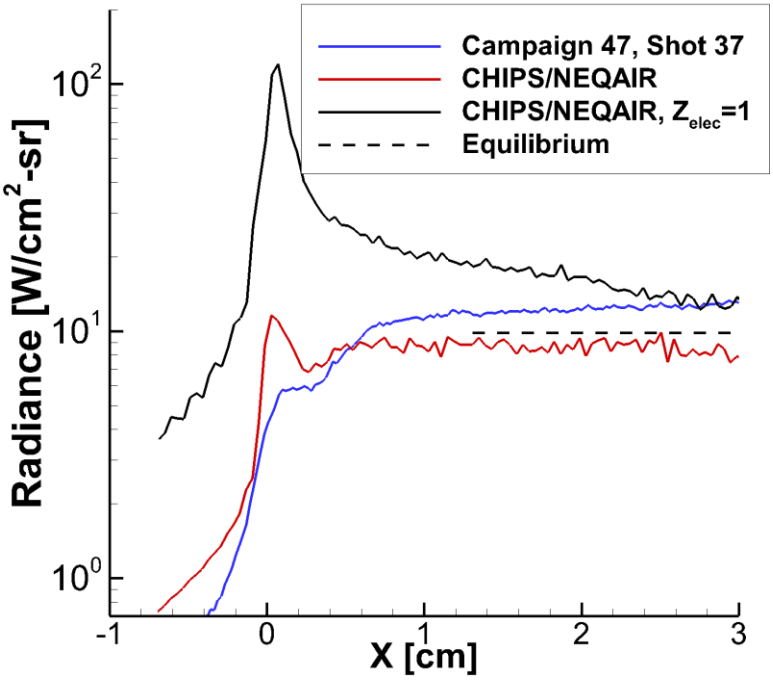

Figure 8.8 Simulated radiance with and without an electronic relaxation number in the Vis/NIR range (480-890 nm) relative to the EAST experimental data.

Finally, results for the IR spectral range from 840 – 1250 nm are compared in Fig. 8.9. Like the Vis/NIR spectrum, the IR radiance is mostly a result of N and O bound-bound emissions. The EAST experimental results and the CHIPS/NEQAIR simulations show similar trends and seem to converge to the same radiance value at the end of the domain. However, the simulated radiance increases to the equilibrium value too rapidly.

This is in agreement with the observations from the previously discussed spectral ranges, reinforcing the conclusion that the current rate of electronic excitation may be too fast. This could potentially be solved by using larger electronic collision numbers in the CHIPS simulation. In this case, the experimental radiance measurements underpredict the analytic equilibrium, but the radiance is still increasing and seems to be approaching the correct equilibrium. As in the previous comparisons, the simulation with $Z_{elec} = 1$ model severely overpredicts the radiance.

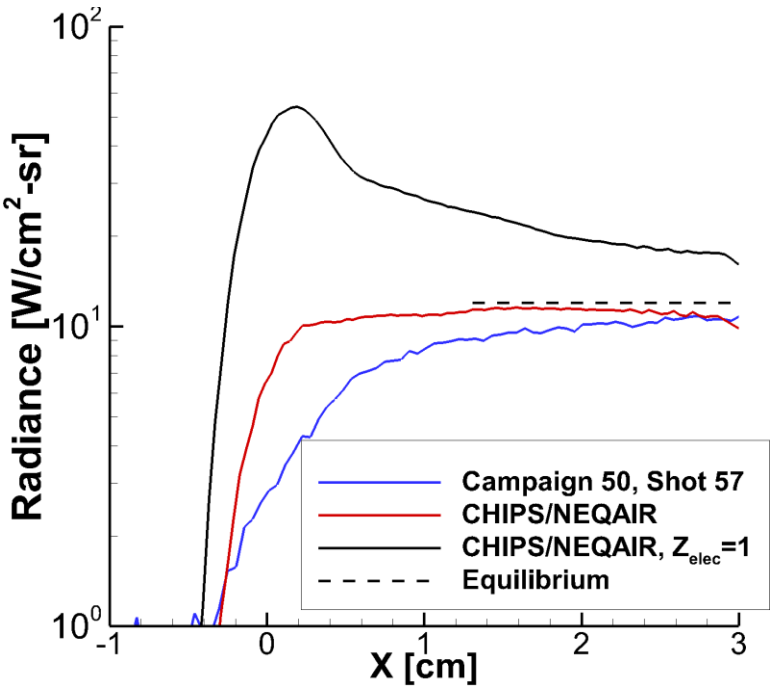

Figure 8.9 Simulated radiance with and without an electronic relaxation number in the IR range (840-1250 nm) relative to the EAST experimental data.

Although the nominal simulation identified additional improvements that can be made to better reproduce experimental radiation measurements, the radiation results produced from the CHIPS/NEQAIR codes are a significant improvement from the

simulations performed for the Saturn entry case (Chapter 6). This is primarily a result of new and updated CHIPS models, both for performing the initial DSMC simulation and for passing results to NEQAIR. From the analysis of the simulated radiation, it is clear that accurate electronic collision numbers are integral to reproducing the EAST data. With electronic collisions numbers added to the CHIPS code, the simulations were able to reproduce the general structure and were well within an order of magnitude of the expected radiance for each of the spectral ranges. Of course, without appropriate experimental measurements to support the choice of the electronic collision numbers, these favorable comparisons have benefitted from the ability to arbitrarily select the electronic collision numbers used in the CHIPS code. While this may be the case, the following sensitivity analysis will help determine which electronic collision numbers are important for each spectral range.

The comparisons of the analytical equilibrium results to the experimental radiance demonstrated that uncertainties in the measurements can play a significant role in matching the simulation and experiment. While these uncertainties are not addressed in this dissertation, future comparisons with experimental radiance would benefit from calibration studies where both simulation and experimental uncertainties are quantified. Since the following sensitivity analysis does not rely on comparisons with experimental results, the chosen nominal simulation is still relevant for future simulations of the chosen scenario.

CHAPTER 9

Final Sensitivity Analysis

9.1 Overview

Upon completion of the nominal CHIPS/NEQAIR simulation for a lunar return Earth entry scenario, a final sensitivity study of CHIPS input parameters is performed. The intention of this sensitivity study is to identify the important CHIPS input parameters that influence some quantity of interest. While previous preliminary sensitivity studies in this dissertation were only able to consider CHIPS outputs as quantities of interest, the addition of the NEQAIR code allows for the sensitivity of radiative quantities to be analyzed. Because simulated radiative results can be directly compared with the EAST experiments, understanding the sensitivity of the CHIPS code will help improve future attempts at reproducing the experimental data. To aid this effort, the sensitivity rankings can be used to identify input parameter values that would benefit from further investigation and indicate which CHIPS models may need improvement.

9.2 Sensitivity Analysis Study

The global Monte Carlo sensitivity analysis completed in this chapter follows the same methodology discussed in Chapter 5. Both the square of the Pearson correlation coefficient, r^2, and the mutual information, MI, are calculated at each $x-$location to measure the sensitivity of some quantity of interest, QoI, to CHIPS input parameters. An overall sensitivity is obtained for each QoI by multiplying the variance of the QoI with the sensitivity measures at each point and integrating over the domain. The input parameters are then ranked by the QoI's overall sensitivity to each parameter. In this study, 57 different potential QoIs from the CHIPS code and 4 radiative QoIs from the NEQAIR code are recorded. Of these QoIs, the following analysis focuses on the VUV,

UV/Vis, Vis/NIR, and IR radiance QoIs resulting from post-processing the CHIPS simulations with the NEQAIR code. In addition, the translational temperature and free electron number density QoIs from the CHIPS simulations are investigated. The results of the other 55 QoIs are listed in Appendix A but are not analyzed. To complete the sensitivity analysis, 2,250 simulations were performed, totaling approximately 130,000 computer hours on the Stampede2 supercomputer at the Texas Advanced Computing Center and the Cedar computer cluster at NASA Ames Research Center. Upon analyzing the results, it was found that the r^2 and MI rankings for the most important input parameters are nearly the same. To ensure clarity, the MI results are not included in the figures that plot the sensitivity as a function of x, but are included in the overall sensitivity comparisons.

In this sensitivity study, only select input parameters from the CHIPS code are studied. While the inputs parameters used in the NEQAIR code, such as the instrument line shape parameters, may carry significant uncertainty, investigation of the sensitivity of the radiative quantities of interest to these parameters is outside the scope of this dissertation. Previous investigations of the NEQAIR sensitivity and uncertainty have been performed in Refs. [99] and [100]. The CHIPS input parameters considered in the sensitivity analysis are restricted to forward reaction rates and the electronic collision numbers for each species. These input parameters are selected from uniform prior distributions before each simulation. For the forward reaction rates, only the Arrhenius pre-exponential constant, Λ, is studied as in the previous sensitivity analyses (Chapter 5). In addition, the backward reaction rate is modified correspondingly which preserves the equilibrium constant. Prior distributions for 51 reaction rates are centered at the nominal value listed in Tables 8.3-5 and the reaction number listed corresponds to the parameter numbers shown in the following figures. The prior distribution used for the forward

reaction rates ranges from plus/minus an order of magnitude. The next 20 parameters studied in the sensitivity analysis are species specific electronic collision numbers, Z_{elec}, with the nominal values and minimum and maximum values listed in Table 9.1. Since the electronic collision numbers for collisions with heavy particles are expected to be larger than for collisions with free electrons, the range of the uniform distribution is shifted accordingly. These parameters are numbered starting from 52 so that they can be related to the figures created in this chapter. Since both the reaction rate and Z_{elec} input values are investigated over several orders of magnitude (Table 9.1), each value is randomly selected from the uniform prior distribution over the base ten logarithm of this range. By using the base ten logarithm, the input parameter range is adequately explored without bias towards larger values.

Unfortunately, the restrictions of the TCE model discussed in Chapter 7 may have unintended consequences for the sensitivity analysis. While most of the nominal parameters satisfy the TCE model restrictions, increasing the Arrhenius pre-exponential constant could result in the reaction probability surpassing one for a significant portion of the collision energy values expected in the simulation. Since the Arrhenius pre-exponential constant is randomly varied over a wide range, a selected value that results in reaction probabilities greater than one could lead to an underprediction of the reaction rate. Although this could potentially affect the sensitivity analysis, it is unlikely that this problem is severe. Studying the reaction rates in Chapter 8 showed that only two of the nominal rates currently used in the CHIPS code result in reaction probabilities greater than one. This means that nearly the entire range of randomly selected values that are lower than the nominal value are acceptable for use in the TCE model. When the reaction rate is selected from the uniform prior to be higher than the nominal value, probabilities greater than one may result. This occurrence is uncommon though, as most reaction rates

either have a significant buffer between the nominal Λ value and the value where the TCE model fails or the maximum value from the uniform prior is not larger than the Λ value where the TCE model fails.

As in the preliminary sensitivity analyses performed in Chapter 5, other CHIPS input parameters such as the internal relaxation constants, VHS parameters, etc. are not included in the current sensitivity analysis. A previous sensitivity analysis performed by Strand demonstrated that these input parameters are less correlated than reaction rates for nonionizing hypersonic shock conditions [6]. This conclusion is extrapolated to the ionizing hypersonic shocks simulated in this dissertation because it is necessary to complete the current sensitivity analysis: the CHIPS simulations are computationally expensive, and the computational time is limited. By eliminating these input parameters from the sensitivity study, the results of the sensitivity analysis are expected to converge at a quicker rate, making it easier to identify the most important input parameters from fewer CHIPS simulations.

Table 9.1 Nominal species specific electronic collision number values and sensitivity analysis bounds.

#	Species	Collision Partner	Nominal Value	Uniform Prior	
				Minimum	Maximum
52	N_2	Heavy	250	100	1000
53	N	Heavy	250	100	1000
54	O_2	Heavy	250	100	1000
55	O	Heavy	250	100	1000
56	NO	Heavy	250	100	1000
57	N_2^+	Heavy	250	100	1000
58	N^+	Heavy	250	100	1000
59	O_2^+	Heavy	250	100	1000
60	O^+	Heavy	250	100	1000
61	NO^+	Heavy	250	100	1000
62	e^-	–	2	1	500
63	N_2	e^-	2	1	500
64	N	e^-	2	1	500
65	O_2	e^-	2	1	500
66	O	e^-	2	1	500
67	NO	e^-	2	1	500
68	N_2^+	e^-	2	1	500
69	N^+	e^-	2	1	500
70	O_2^+	e^-	2	1	500
71	O^+	e^-	2	1	500
72	NO^+	e^-	2	1	500

The simulation performed in the previous chapter serves as the nominal case for this sensitivity analysis. Besides the input parameters selected from the prior distributions, all other input parameters are identical to those used to obtain the results in Chapter 8. Additional parameters are also required for the sensitivity analysis. When studying QoIs resulting from the CHIPS code, 1000 uniformly spaced locations are analyzed between approximately ½ cm upstream to 2.5 cm downstream of the shock. Since the simulated NEQAIR sampling grid is sparser, 100 uniformly spaced points are studied over, roughly, the same range. While fewer points are used to calculate the overall sensitivity values for the radiative QoIs, this will not have a discernable effect on

the meaning of the results since the same sampling domain is used. The sampling domain is strategically chosen to bias measurement of the QoI's sensitivity to the nonequilibrium processes occurring within the shock. In addition, reducing the domain improves the relevance of the sensitivity rankings to stagnation point simulations where a blunt body is present behind the shock, truncating the equilibrium region.

9.2.1 Quantity of Interest: Translational Temperature

Similar to the preliminary sensitivity analyses, the first QoI studied is the translational temperature ($QoI_{T_{tr}}$). The five most important input parameters are plotted as a function of distance from the shock for the Pearson correlation coefficient, r, in Fig. 9.1. In this sensitivity study, plots of the signed r values as a function of $x-$location, in addition to plots of r^2, are used to help understand the underlying physics. When the correlation is positive, increasing or decreasing the input parameters causes the QoI to move in the same direction. A negative correlation causes the opposite effect. Figure 9.2 shows the variance of $QoI_{T_{tr}}$ (right axis) that is used to calculate the variance weighted r^2 at each location (left axis). After integrating over the domain, an overall sensitivity value for each input parameter is obtained. The overall sensitivities, normalized by the largest value, are compared in Fig. 9.3 as a bar chart.

Figures 9.1 and 9.2 can be analyzed to determine which input parameters the translational temperature is sensitive to in different regions of the shock. Within the shock, where the translational temperature peaks, the dissociation of N_2 has the greatest impact. This is expected since freestream is composed of 79% N_2 and dissociation is an endothermic reaction. Since the correlation is negative for each input parameter (Fig. 9.1), the translational temperature decreases when these reaction rates increase. This occurs because absorption of kinetic energy through the chemical process of breaking the

N_2 bond has a significant impact on the translational temperature. Dissociation of N_2 takes place through various reactions, but the translational temperature is most sensitive to the $N_2 + N \rightleftharpoons N + N + N$ reaction rate. When considering that the dissociation of N_2 creates two atomic nitrogen particles, N quickly becomes the most common particle and, therefore, the most likely to transfer energy. In addition to simple dissociation, the $N_2 + O \rightleftharpoons NO + N$ Zeldovich reaction is important. Although this reaction does not absorb as much energy as dissociation, the translational temperature is likely also sensitive to this Zeldovich reaction through its creation of additional atomic nitrogen that can then cause a dissociation reaction. Downstream of the shock, the $NO + N^+ \rightleftharpoons N + NO^+$ charge exchange reaction becomes important by affecting the rate of electron capture, slowing the relaxation rate of the translational temperature. The importance of this charge exchange reaction is analyzed in the following section.

These figures were likewise created for the translational temperature in Chapter 5 from the preliminary sensitivity analyses. Several conclusions can be drawn when contrasting the results. Foremost, the results of this sensitivity analysis match the first preliminary analysis (without electronic excitation) closely (Figs. 5.9-11). In both cases, the $N_2 + N \rightleftharpoons N + N + N$ and $NO + N^+ \rightleftharpoons N + NO^+$ reactions are the most important and follow parallel trends throughout the shock. This conclusion was preserved even though a significant update to the Ref. [6] $NO + N^+ \rightleftharpoons N + NO^+$ reaction rate was adopted from Ref. [91] (Chapter 8). While the first two reactions are the same, comparing Fig. 9.3 with the results from the first preliminary analysis demonstrates that ionization reactions play a much smaller role in defining the translational temperature in this later study. This change is partially due to the reduction in the sensitivity analysis domain that removed part of the downstream equilibrium region. When comparing with the second preliminary sensitivity analysis (with electronic excitation) in Chapter 5 (Figs. 5.25-27), the second

preliminary sensitivity analysis is dominated by the electron impact ionization of atomic nitrogen while the current analysis shows no sensitivity to the reaction. This reinforces the conclusion that the second preliminary sensitivity analysis suffered from an overprediction of ionization reactions either because electronic energy was allowed to contribute to the TCE model reaction probability, the electronic excitation model used $Z_{elec} = 1$, or both.

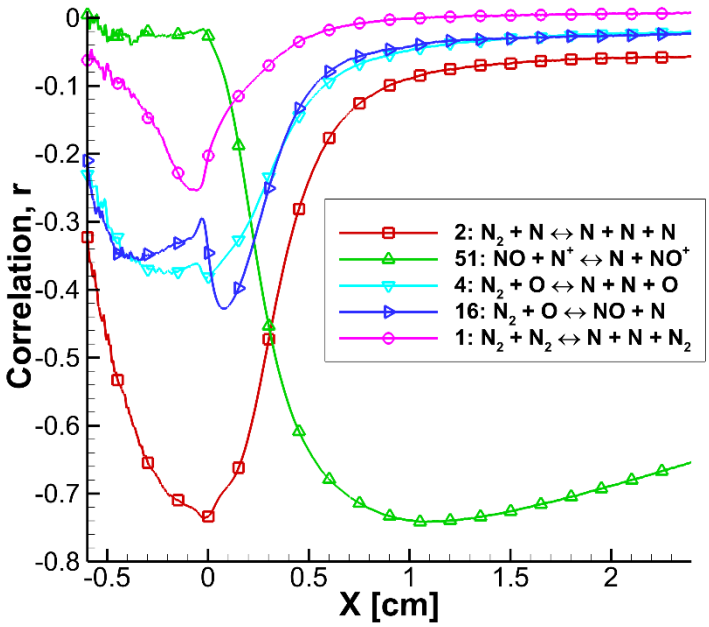

Figure 9.1 Pearson correlation coefficient of the five most sensitive reaction rates when the translational temperature is the QoI ($QoI_{T_{tr}}$).

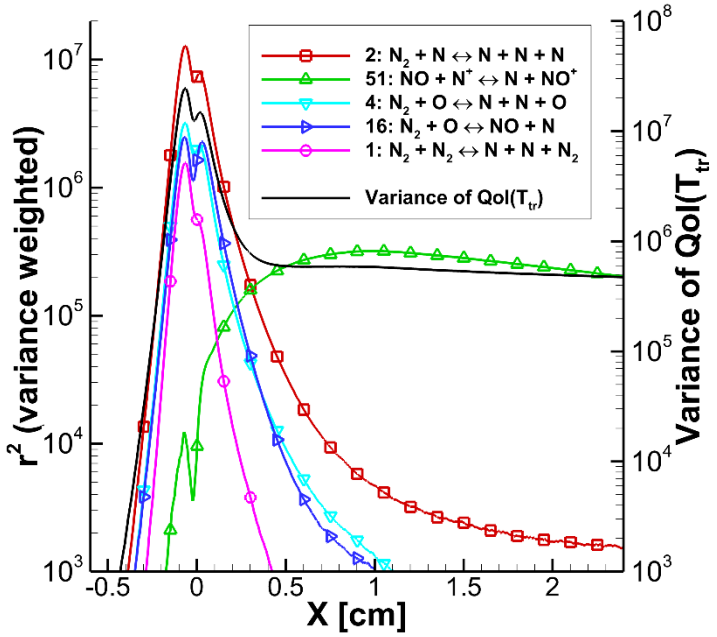

Figure 9.2 Variance weighted r^2 sensitivities of the five most sensitive reaction rates for $QoI_{T_{tr}}$, and the variance at each x −location.

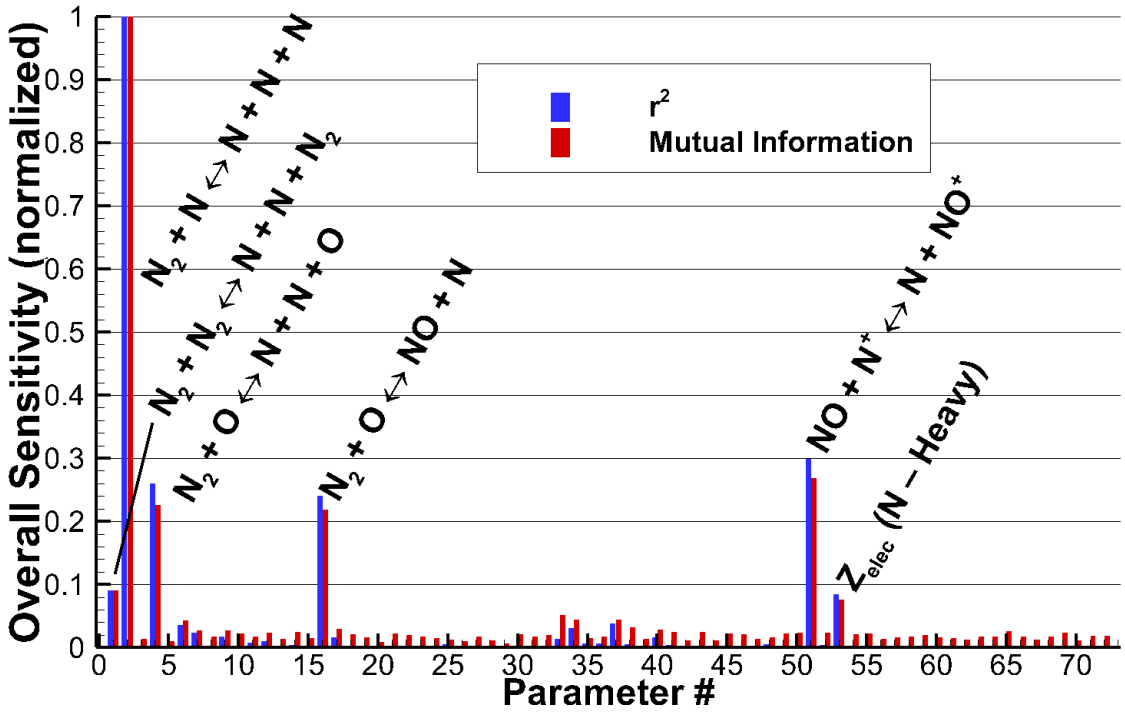

Figure 9.3 Normalized r^2 and MI overall, variance weighted sensitivities for $QoI_{T_{tr}}$.

9.2.2 Quantity of Interest: Free Electron Number Density

In order to understand the pathways leading to ionization of the flow, Figs. 9.4-6 plot the sensitivity of the free electron number density (QoI_{n_e}) to each input parameter. Figures 9.4 and 9.5 show the correlation between the five most important parameters and the free electron number density. Looking through the shock, associative ionization reactions initially have the highest correlation as they provide the first electrons. Interestingly, the $N + N \rightleftharpoons N_2^+ + e^-$ reaction is initially more important than the $N + O \rightleftharpoons NO^+ + e^-$ reaction and seems to be the source of the first major contribution of free electrons in the flow. Moving into the post-shock region, the importance of associative ionization drops off and the $NO + N^+ \rightleftharpoons N + NO^+$ reaction controls the free electron number density. As discussed in Chapter 5, this reaction is especially important for free electrons due to its ability to stabilize the free electrons. The backward charge exchange reaction, where the ion NO^+ is formed into N^+, results in fewer NO^+ so free electrons are less likely to be captured by the backward form of the $N + O \rightleftharpoons NO^+ + e^-$ associative ionization reaction. The backward form of the $N + e^- \rightleftharpoons N^+ + e^- + e^-$ reaction is the only reaction in the current set where N^+ can capture an electron. While free electron capture by this reaction is confirmed by the negative correlation in Fig. 9.4, the rate of capture is not significant enough to drive the free electron number density. In fact, Fig. 9.6 demonstrates that the free electron number density is dominated by these five reaction rates without much contribution of the other rates.

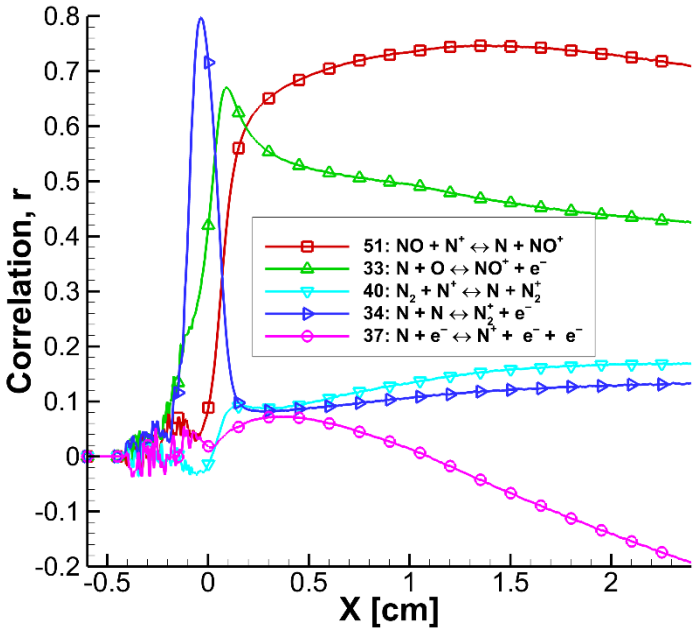

Figure 9.4 Pearson correlation coefficient of the five most sensitive reaction rates when the free electron number density is the QoI (QoI_{n_e}).

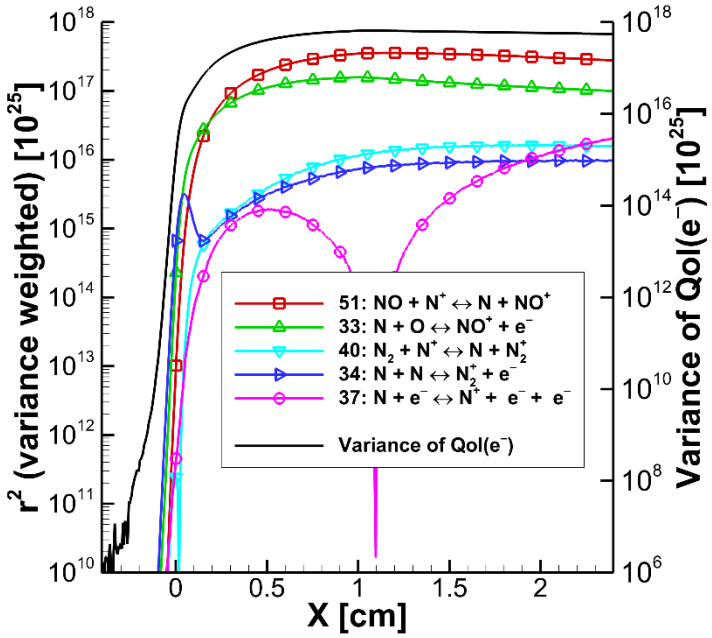

Figure 9.5 Variance weighted r^2 sensitivities of the five most sensitive reaction rates for QoI_{n_e}, and the variance at each x −location.

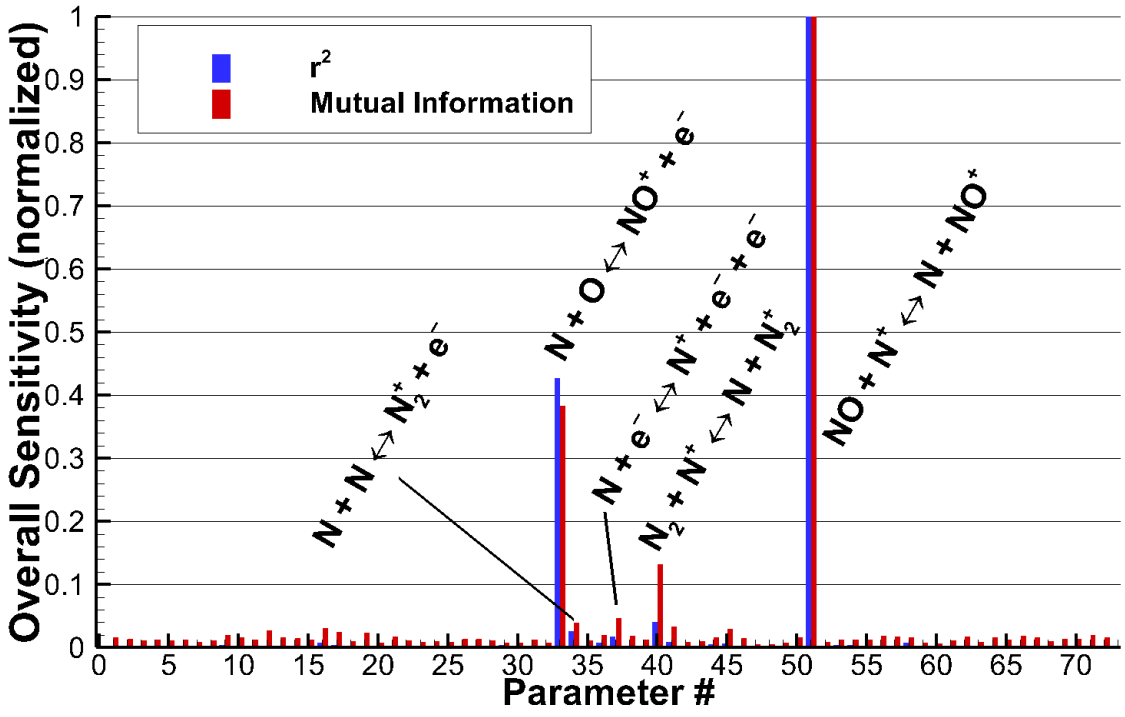

Figure 9.6 Normalized r^2 and MI overall, variance weighted sensitivities for QoI_{n_e}.

9.2.3 Quantity of Interest: VUV Radiance

Now that two QoIs from the CHIPS simulation have been analyzed, the focus is shifted to understanding the effect of CHIPS input parameters on the simulation of radiative spectra obtained from the NEQAIR code. The first radiative QoI studied is the radiance in the VUV spectral range from 170 – 178 nm (QoI_{VUV}). Figures 9.7 and 9.8 plot the Pearson correlation coefficient as a function of distance from the shock for the top five most important input parameters. Within the shock region, where nonequilibrium is the strongest, the atomic nitrogen electronic collision numbers, Z_{elec}, for collisions with both free electrons and heavy particles are the most important. Since the radiance peak observed in the shock region (Fig. 8.6) is most affected by the input parameters, the

variance shown if Fig. 9.8 is also high in this region. When calculating the overall sensitivity from the variance weighted correlations and comparing them in Fig. 9.9, the atomic nitrogen electronic collision numbers are the most important parameters. This is expected since the radiance of this portion of the spectrum arises primarily from atomic nitrogen bound-bound transitions. Surprisingly, the value of r is positive for $Z_{elec}(N - e^{-})$ meaning that the radiance decreases as the atomic nitrogen electronic collision number with free electrons decreases. This result is counter-intuitive since the number of excitation events increases for lower Z_{elec} values. In addition, it was expected that a higher excitation rate would lead to more radiative transitions. One possible explanation is that, while free electron excitations are more likely to occur for a lower Z_{elec} value, the bombardment of atomic nitrogen by the electrons causes more deexcitations and drives the flow toward equilibrium. This hypothesis is supported by the nominal simulation results of Fig. 8.5c which show that the free electron temperature is much cooler than the heavy particle translational temperature. With the limited information from the nominal simulation and sensitivity analysis results, confirmation of this hypothesis is outside the scope of the current research. On the other hand, the correlation is negative for atomic nitrogen electronic excitation by heavy particles, $Z_{elec}(N - Heavy)$ which is the expected result. As the number of heavy particle excitation events increases, the VUV radiance also increases.

Downstream of the shock, the flow approaches equilibrium and the sensitivity of the VUV radiance to the electronic collision number rapidly declines. The origins of the post-shock sensitivity ranking must be viewed from two perspectives, locally and globally. First the local perspective is studied for the post-shock parameters that demonstrate high correlation with the radiance. In the post-shock region, the VUV spectrum becomes most sensitive to the associative ionization reactions involving atomic

nitrogen. These reactions have a negative correlation with the VUV radiance (Fig. 9.7) which indicates that the radiance increases as the rate of the reactions decline. One explanation of the sensitivity is that, reducing the rate of the $N + N \rightleftharpoons N_2^+ + e^-$ and $N + O \rightleftharpoons NO^+ + e^-$ reactions, decreases the ionization of atomic nitrogen at each $x-$location. Because more neutral N atoms are present, the potential for VUV emission increases. While the creation/destruction of atomic nitrogen is directly related to the sensitivity of VUV emissions to associative ionization reactions, the large negative correlation of the $N_2 + N \rightleftharpoons N + N + N$ reaction within the shock indicates that a more complex process may influence the radiance. Although increasing the rate of this reaction produces more atomic nitrogen, the absorption of energy through the endothermic forward reaction reduces the available energy of the flow at that $x-$location, thereby producing fewer electronically excited states. This logic can be extrapolated to understand the sensitivity on a global scale.

From the sensitivity results in Fig. 9.7 and 9.8, it seems that input parameters can be ranked independently based on the physics occurring at a certain $x-$location. Although the input parameters do indeed contribute to a QoIs sensitivity at a specific location, the surrounding domain also contributes to this ranking, especially in a shock wave simulation where information propagates mostly in one direction. Because the initial nonequilibrium processes within a shock largely define the post-shock composition and relaxation to equilibrium, measurements at locations in the post-shock region are significantly influenced by the physics occurring upstream. For example, the VUV radiance was found to have a strong negative correlation to the associative ionization reactions downstream of the shock. In the nonequilibrium shock region, the associative ionization reactions beginning the ionization process mostly occur in the endothermic forward direction, absorbing energy. By increasing their rate, more reactions that absorb

energy take place within the shock which drives the flow toward equilibrium faster than the nominal rate. Since the flow within the shock is now closer to equilibrium, every point that follows will also be nearer to equilibrium. This leaves less energy for electronic excitation events and results in a lower VUV radiance. Considering this, one possibility for the negative correlation downstream of the shock is that the root cause for the decline in VUV radiance stems from the increased associative ionization rate within the shock region. Even when a simpler inference seems obvious, e.g. the negative correlation is caused by the destruction of atomic nitrogen, scenarios comparable to this one make it difficult to determine the physics determining a QoI's sensitivity to an input parameter.

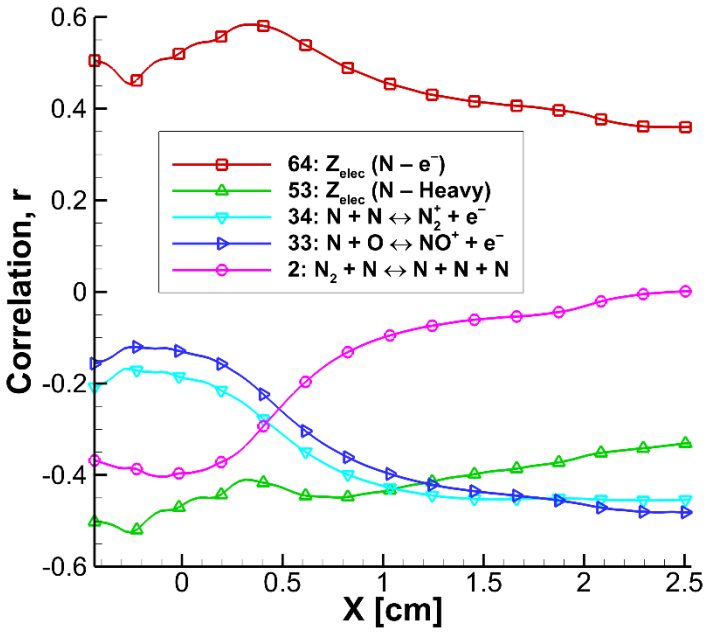

Figure 9.7 Pearson correlation coefficient of the five most sensitive reaction rates when the VUV radiance is the QoI (QoI_{VUV}).

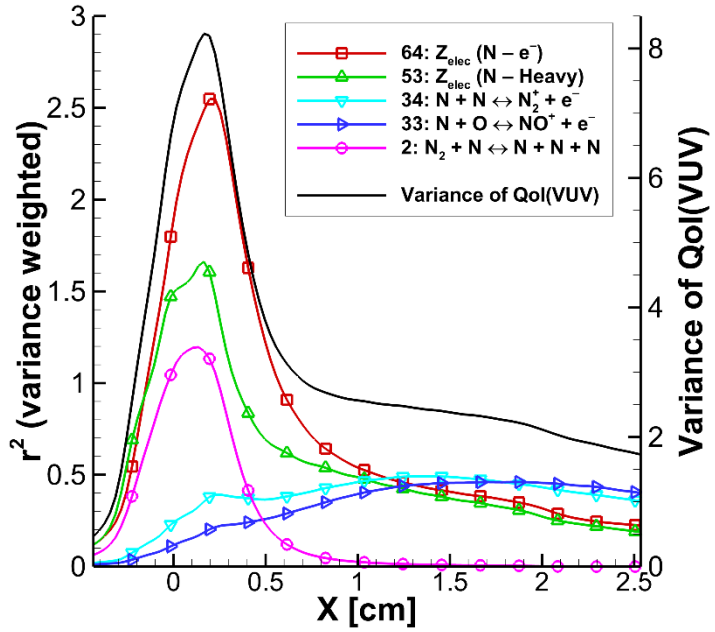

Figure 9.8 Variance weighted r^2 sensitivities of the five most sensitive reaction rates for QoI_{VUV}, and the variance at each x −location.

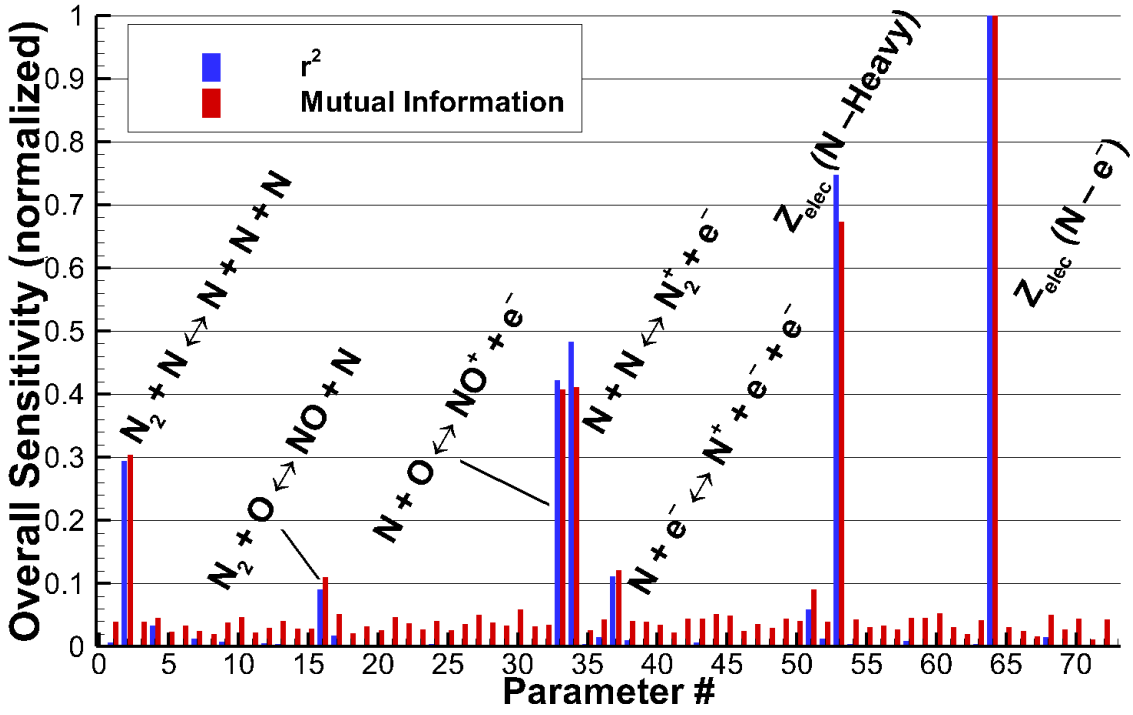

Figure 9.9 Normalized r^2 and MI overall, variance weighted sensitivities for QoI_{VUV}.

9.2.4 Quantity of Interest: UV/Vis Radiance

The second radiative QoI studied is the UV/Vis radiance from the 328 – 496 nm spectral range, $QoI_{UV/Vis}$, where the results are plotted in Figs. 9.10-12. Since the UV/Vis spectral range relies on emissions from N_2 and N_2^+, several of the top five input parameters shown in Figs. 9.10 and 9.11 involve one of these particles. The most important input parameter is $Z_{elec}(N_2^+ - e^-)$, but the electronic collision number for N_2 is only the 7th most important. The correlation shows that the UV/Vis radiance increases with a smaller electronic collision number which indicates that for this shock speed, N_2^+ is responsible for more of the emissions than N_2. In support of this conclusion, the UV/Vis radiance is second most sensitive to the $N + N \rightleftharpoons N_2^+ + e^-$ reaction. Behind the shock, the $N + N \rightleftharpoons N_2^+ + e^-$ reaction has a negative correlation due to the electron capture reaction removing N_2^+ from the flow and lowering the radiance. However, this negative correlation could also be a result of the global effects discussed in the previous section. Within the shock, the forward $N + N \rightleftharpoons N_2^+ + e^-$ reaction absorbs energy and potentially has a greater effect on the UV/Vis radiance than the production or removal of N_2^+. The same global effect could also be the cause of the negative correlation seen in Fig. 9.10 for the $N_2 + N \rightleftharpoons N + N + N$ and $N_2 + O \rightleftharpoons NO + N$ reactions.

While bound-free emission from atomic nitrogen ion capture of free electrons was expected to contribute to the post-shock equilibrium radiance, the variance shown in Fig. 9.11 is small, indicating that the downstream region is relatively unaffected by the input parameters studied here. The bound-free continuum emission relies on the concentrations of N^+ and e^-, but these concentrations are relatively unaffected by the shock physics as the flow approaches equilibrium. Instead, the equilibrium concentrations are defined by the equilibrium constants for each reaction and the freestream conditions. Since these parameters are constant for each simulation in the sensitivity analysis, large discrepancies

in the post-shock region are not expected. In support of this conclusion, Fig. 9.12 shows that the UV/Vis radiance is uncorrelated with the atomic nitrogen electron impact ionization reaction (input parameter #37).

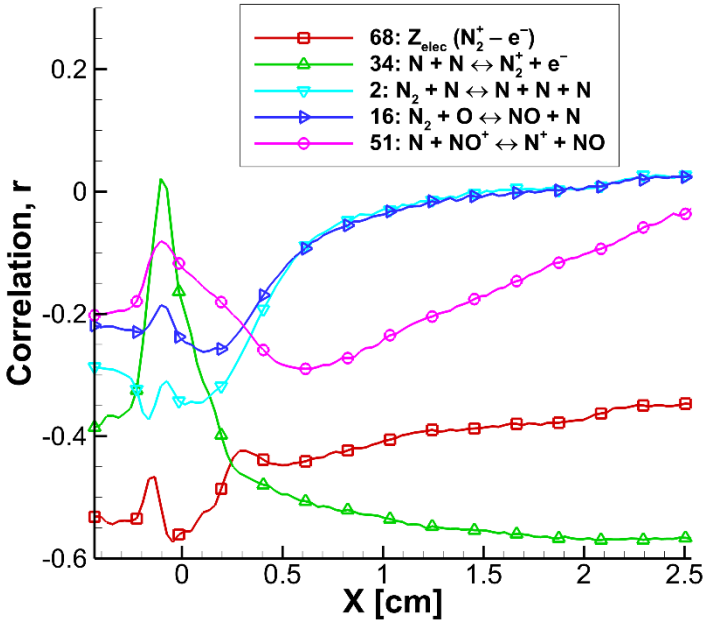

Figure 9.10 Pearson correlation coefficient of the five most sensitive reaction rates when the UV/Vis radiance is the QoI ($QoI_{UV/Vis}$).

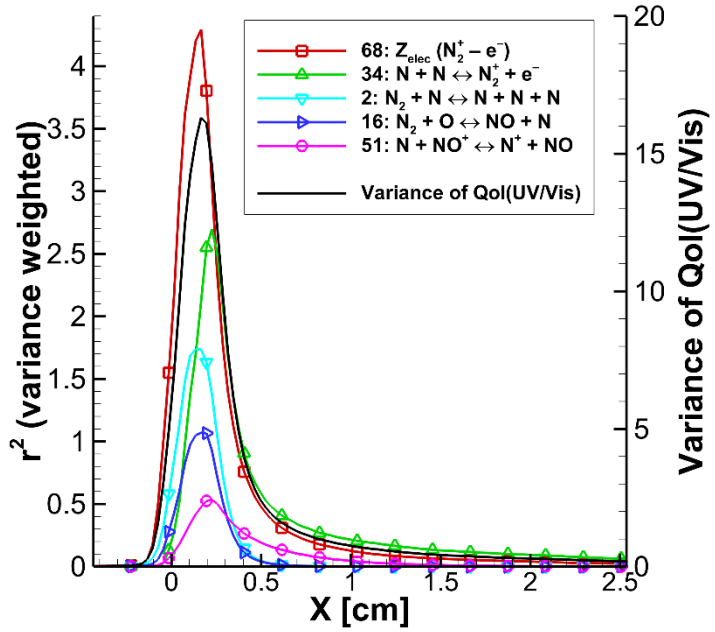

Figure 9.11 Variance weighted r^2 sensitivities of the five most sensitive reaction rates for $QoI_{UV/Vis}$, and the variance at each x −location.

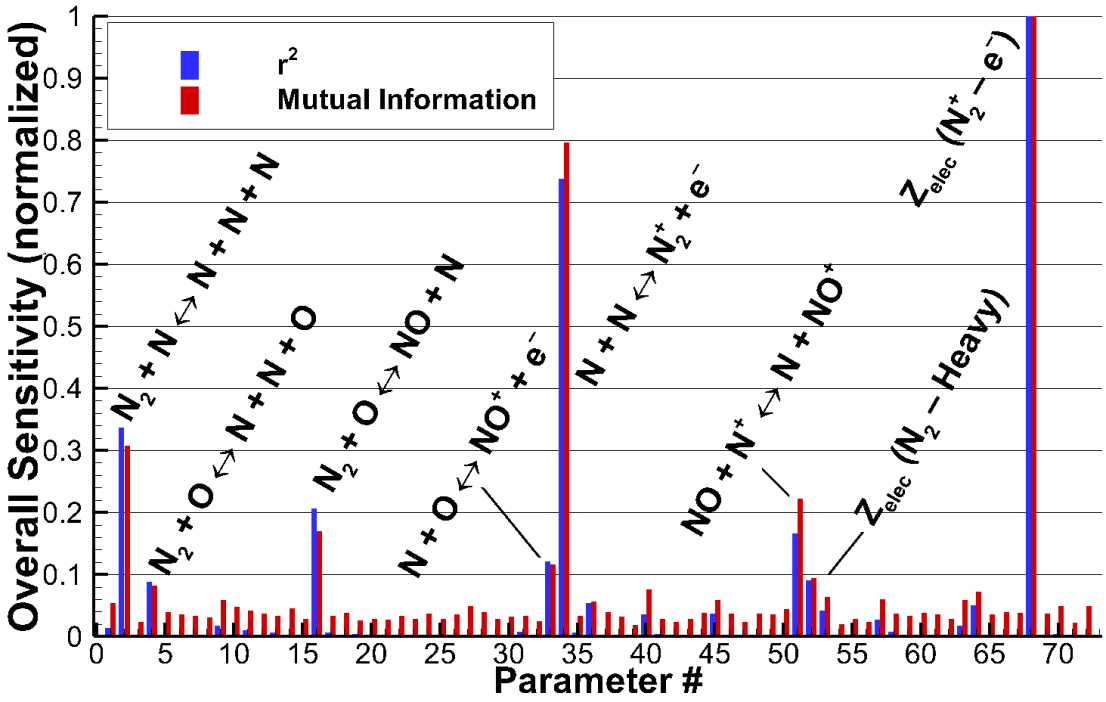

Figure 9.12 Normalized r^2 and MI overall, variance weighted sensitivities for $QoI_{UV/Vis}$.

9.2.5 Quantity of Interest: Vis/NIR Radiance

The next spectral range studied in Figs. 9.13-15 covers the 480 – 890 nm Vis/NIR band, $QoI_{Vis/NIR}$. Unlike the previous radiative QoIs discussed, the sensitivity of the Vis/NIR spectrum seems relatively straightforward. As discussed in Chapter 8, the emissions that occur in this spectrum are mostly the result of N and O bound-bound transitions. Because both of these species are important, it is unsurprising that the N + O $\rightleftharpoons$ $NO^+ + e^-$ reaction is the most sensitive. The forward form of this reaction removes both N and O, as well as absorbing energy from the flow, resulting in a strong negative correlation. The same is true, to a lesser degree, for the N + N $\rightleftharpoons$ $N_2^+ + e^-$ reaction. Figure 9.15 shows that the Vis/NIR radiance is sensitive to multiple electronic collision numbers, particularly near the shock. In this region, a radiance spike was observed in the nominal simulation that did not appear in the experimental measurements (Fig. 8.8). From the sensitivity results, it appears that this spike is due to some combination of $Z_{elec}(N - Heavy)$, $Z_{elec}(N - e^-)$ and, to a lesser extent, $Z_{elec}(O - e^-)$. The correlation results in Fig. 9.13 point to $Z_{elec}(N - Heavy)$ being too small or $Z_{elec}(N - e^-)$ and $Z_{elec}(O - e^-)$ being too large as the sources of this discrepancy. With a few adjustments of the electronic collision numbers, the simulations may be able to reproduce the same trends observed in the EAST experiment.

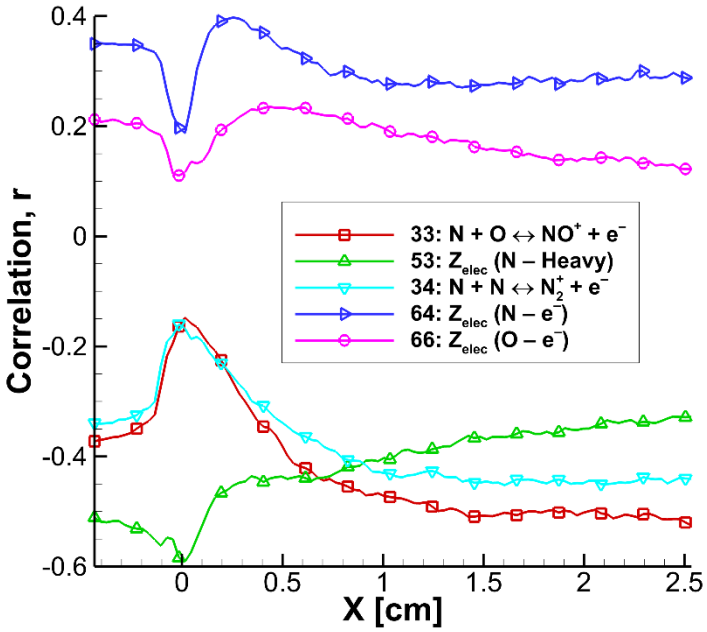

Figure 9.13 Pearson correlation coefficient of the five most sensitive reaction rates when the Vis/NIR radiance is the QoI ($QoI_{Vis/NIR}$).

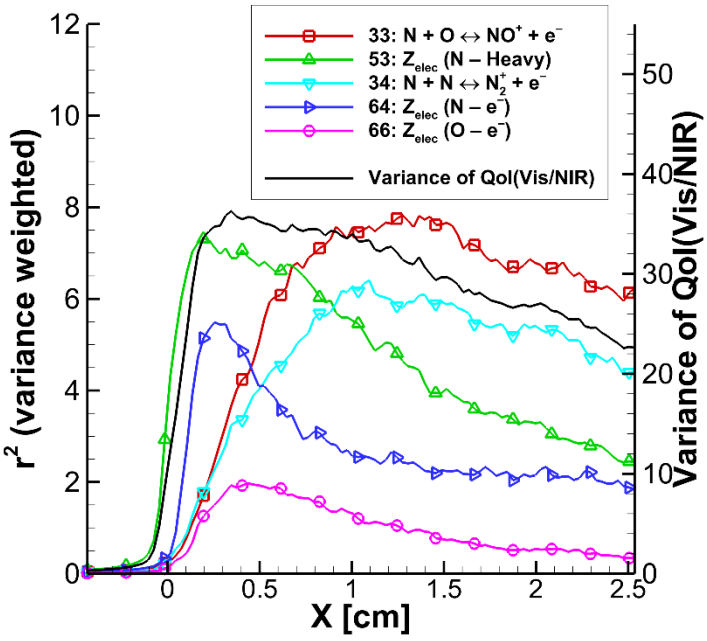

Figure 9.14 Variance weighted r^2 sensitivities of the five most sensitive reaction rates for $QoI_{Vis/NIR}$, and the variance at each x −location.

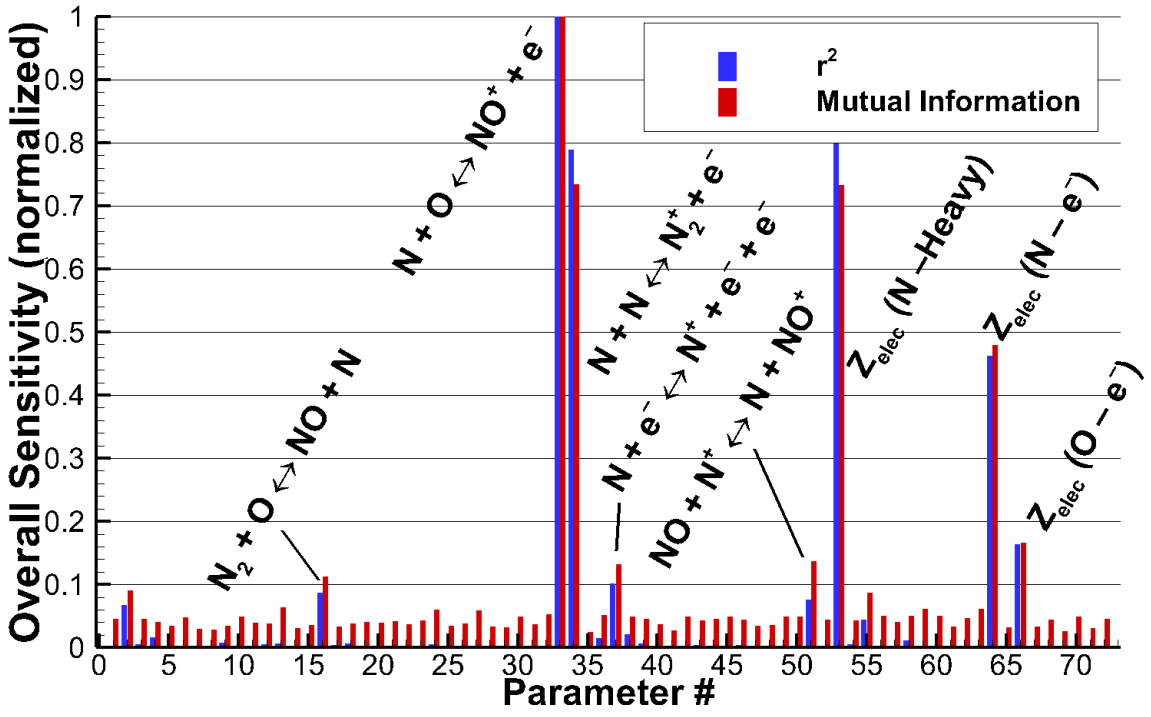

Figure 9.15 Normalized r^2 and MI overall, variance weighted sensitivities for $QoI_{Vis/NIR}$.

9.2.6 Quantity of Interest: IR Radiance

The final radiance QoI studied in this sensitivity analysis concerns the IR spectral range from 840 – 1250 nm, QoI_{IR}. Similar to the Vis/NIR range, the IR radiance is dominated by atomic nitrogen and oxygen spectral lines. Due to the parallels between the two spectral ranges, the results of the overall sensitivity rankings for each input parameter shown in Fig. 9.18 are nearly identical to Fig. 9.15. While the order of the sensitivities is slightly different when comparing the two QoIs, the sensitivities as a function of distance from the shock also demonstrate similar trends (Figs. 9.16 and 9.17). The qualitative differences seen in the pre-shock region when comparing Fig. 9.16 to Fig. 9.13 are an artifact of the spatial convolution. When considering that the variance is low in the pre-

shock region, these differences have no effect on the overall ranking. This is obvious when comparing Fig. 9.17 to Fig. 9.14 as they are nearly identical in shape.

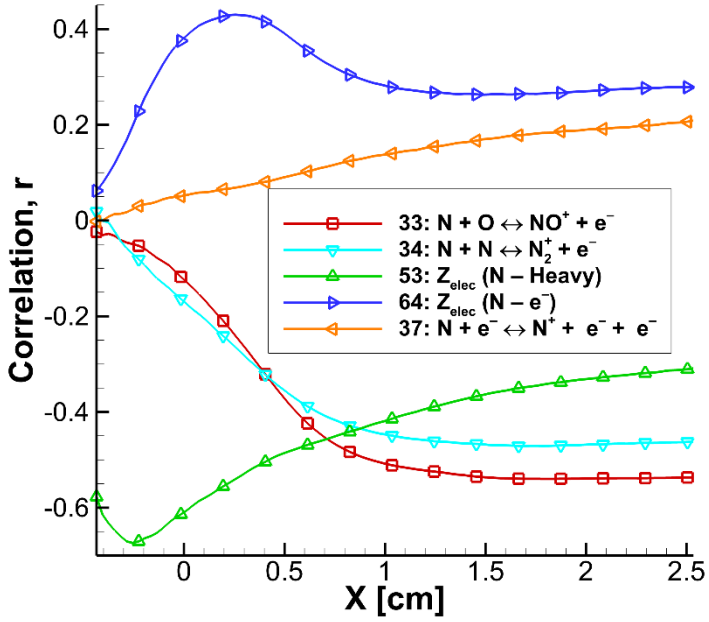

Figure 9.16 Pearson correlation coefficient of the five most sensitive reaction rates when the IR radiance is the QoI (QoI_{IR}).

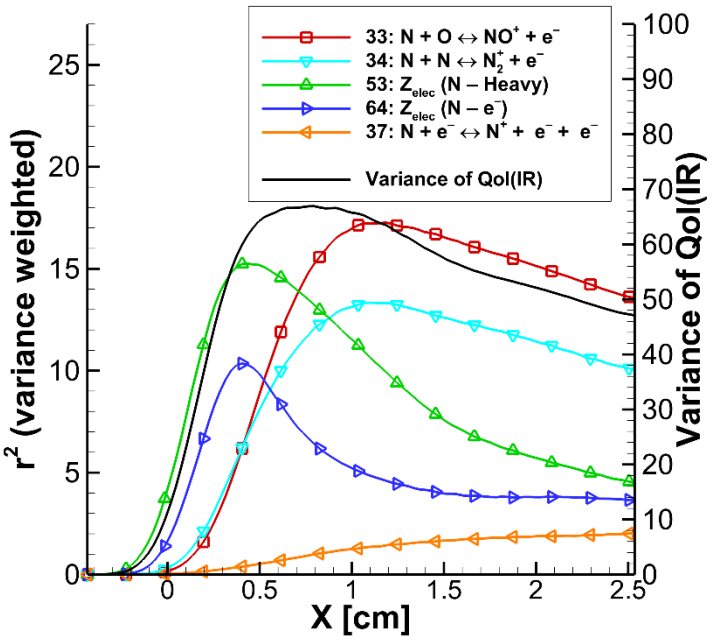

Figure 9.17 Variance weighted r^2 sensitivities of the five most sensitive reaction rates for QoI_{IR}, and the variance at each x −location.

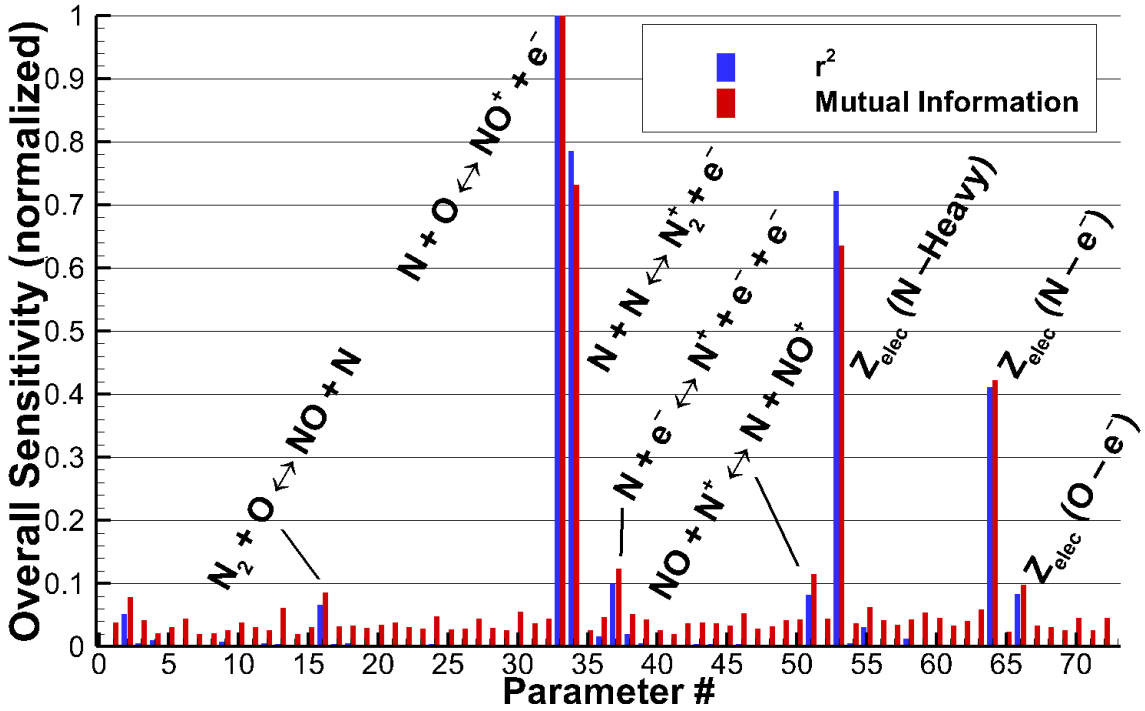

Figure 9.18 Normalized r^2 and MI overall, variance weighted sensitivities for QoI_{IR}.

9.3 CONVERGENCE

Sensitivity analysis convergence must be addressed to demonstrate that the results of the previous section represent the true ranking of the most important input parameters. Since a Monte Carlo sensitivity analysis is performed, the results are expected to converge with $\sqrt{N}$ where N is the number of samples. In this study 2,250 simulations were completed, representing the same number of Monte Carlo samples. While this number is substantially less than the number of samples required to adequately converge the r^2 and MI results for all 72 input parameters, this sensitivity study is only concerned with determining the top five or so input parameters that each QoI is sensitive to. In addition, it is not necessary to converge the value of r^2 and MI for each input parameter, only their ranking relative to the other input parameters. Complete convergence of the input parameter ranking is intractable within a reasonable computational time.

In order to demonstrate that the previous sensitivity analysis results were appropriately converged, a simple study is performed where the Pearson correlation coefficient results were recomputed using half of the samples. Figures 9.19 and 9.20 compare the translational temperature sensitivity analysis results when all and half of the Monte Carlo samples are used to calculate the r values. When calculating both the raw correlation coefficient value (Fig. 9.19) and determining the ranking of each input parameter (Fig. 9.20), no changes in the results are apparent. While the input parameter rankings are not consistent for every input parameter, the ranking of the top seven most important parameters is unchanged. The same convergence study was also performed on the IR radiance sensitivity results, with the correlation values plotted in Fig. 9.21 and the rankings plotted in Fig. 9.22 comparing the cases with all and half of the Monte Carlo samples. Again, the correlation values for the top five most important input parameters in Fig. 9.21 are nearly identical for both cases. When comparing the rankings, the top four

parameters are unchanged, but the rankings of the next tier of input parameters has shifted slightly. In particular, the overall sensitivity value for $Z_{elec}(O - e^{-})$ has halved which reduces its overall ranking from 6th to 10th. This demonstrates that when determining the most important input parameters for an under-converged case, care must be taken in making conclusions about parameters with overall sensitivity values that have not significantly separated from the bulk of the parameters. On the other hand, this study has shown that the sensitivity analysis results are sufficiently converged to determine the most important input parameters when their sensitivity values have significantly separated from the majority of the input parameters.

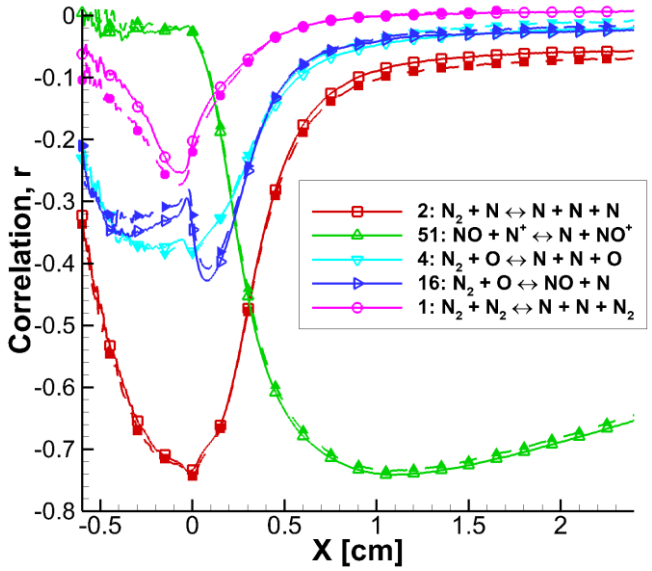

Figure 9.19 Pearson correlation coefficient of the five most sensitive reaction rates using all (solid line, open symbols) and half of the samples (dashed line, solid symbols) when the translational temperature is the QoI ($QoI_{T_{tr}}$).

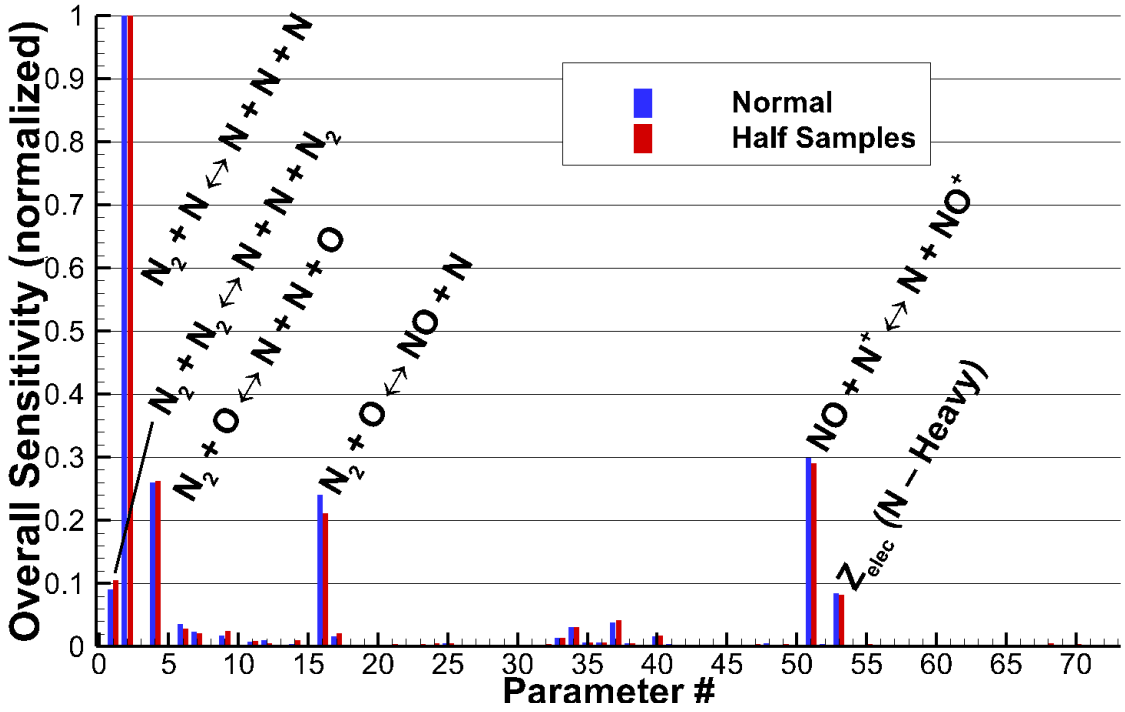

Figure 9.20 Normalized r^2 overall, variance weighted sensitivities for $QoI_{T_{tr}}$ calculated from all and half of the samples.

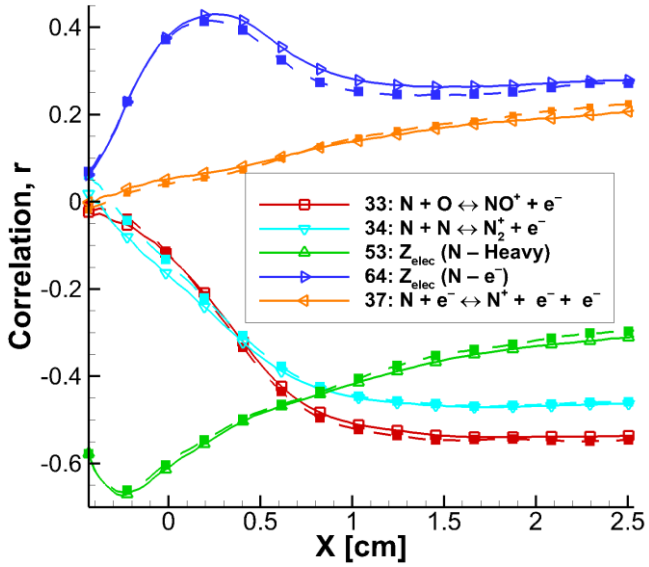

Figure 9.21 Pearson correlation coefficient of the five most sensitive reaction rates using all (solid line, open symbols) and half of the samples (dashed line, solid symbols) when the IR radiance is the QoI (QoI_{IR}).

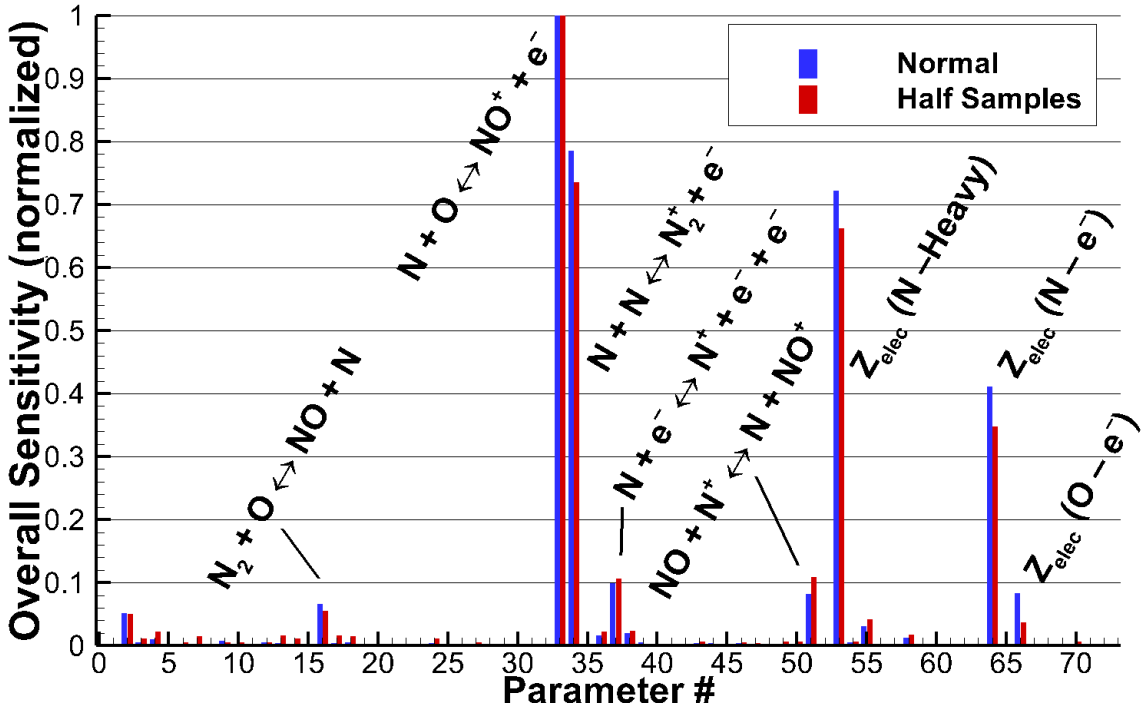

Figure 9.22 Normalized r^2 overall, variance weighted sensitivities for QoI_{IR} calculated from all and half of the samples.

CHAPTER 10

Conclusions

10.1 SUMMARY

In this dissertation, global Monte Carlo sensitivity analyses of DSMC input parameters were completed for ionizing hypersonic shock simulations. The scenarios modeled by the Computation of Hypersonic Ionizing Particles in Shocks (CHIPS) DSMC code reproduced experimental data obtained from the NASA Ames Electric Arc Shock Tube (EAST) for Earth and Saturn entry [1][2]. From comparisons with the experimental measurements and the sensitivity analyses, several parameter and modeling improvements were recommended. In addition, the sensitivity analysis results identified input parameters that could benefit from future experimental or theoretical determinations.

Before the preliminary sensitivity analyses could be completed, the original code inherited from Strand required various updates in order to model an ionizing hypersonic flow [6]. Initial improvements to the CHIPS code were completed for modeling charged particle physics including collisions, chemical reactions, and electronic excitation. Since the movement of free electrons requires special attention due to their low mass and high velocity, quasi-neutrality was assumed. This allowed for free electrons to be modeled by moving them with a paired ion. Upon the addition of charged particles and electronic excitation, calculations of the free electron and electronic temperatures were included in CHIPS. Substantial effort was also spent on improving the efficiency of the CHIPS code by applying a reduction scheme for the maximum collision cross-section and pre-calculating variables used to determine transitions in the electronic excitation model.

Once the CHIPS code was updated to model the expected ionizing hypersonic physics, nominal simulations were completed for a chosen Earth entry scenario. The EAST Campaign 47, Shot 37 experiment was selected as the nominal simulation which produced a 10.26 km/s shock with a 0.2 Torr freestream pressure in a synthetic air mixture [32]. CHIPS simulations were completed for 11-species air with and without the electronic excitation model. The results obtained from these simulations showed that the degree of ionization is low and Debye length is small enough that the assumption of quasi-neutrality is acceptable. The chosen simulations were also found to be well enough resolved to produce consistent results, but also efficient enough to avoid being prohibitively expensive for a sensitivity analysis. In comparing the two nominal cases, the number density of charged particles increased by an order of magnitude with the inclusion of electronic excitation. This demonstrates the importance of considering electronic excitation in a high temperature simulation since electronic excitation provides an additional internal mode for particles to store energy.

After establishing nominal simulations, two preliminary global Monte Carlo sensitivity analyses were performed, one with electronic excitation and one without. The Arrhenius pre-exponential constant for 53 reaction rates was varied over two orders of magnitude and selected from a uniform prior before each sensitivity analysis simulation. Several quantities of interest, QoIs, were analyzed to study the effects of the reaction rates on temperature and density outputs. In both sensitivity studies, several QoIs were correlated with the $N_2 + N \rightleftharpoons N + N + N$ dissociation reaction as this reaction was found to significantly affect the development of the shock. Since this reaction is endothermic, it absorbs energy from the flow within the shock which determines the downstream physics and conditions that occur. In addition, the associative ionization reactions, $N + O \rightleftharpoons NO^+ + e^-$ and $N + N \rightleftharpoons N_2^+ + e^-$, were also highly ranked in overall sensitivity. These two

reactions begin the ionization process and the former reaction produces the NO^+ that is involved in the $N + NO^+ \rightleftharpoons N^+ + NO$ charge exchange reaction. It was discovered that several QoIs had the highest sensitivity to this charge exchange reaction. This reaction has a considerable effect on the downstream region by preventing the molecular ions produced through associative ionization from recapturing electrons. Finally, the preliminary sensitivity analyses demonstrated that the selection of the domain size or QoI can change the sensitivity analysis results. With this understanding, the sensitivity domain must be carefully considered so that the results are meaningful to the experiment or case of interest.

When comparing the two preliminary sensitivity analyses, the most obvious distinction was that the $N + e^- \rightleftharpoons N^+ + e^- + e^-$ electron impact ionization reaction became the highest ranked reaction when the electronic excitation model was added. A possible explanation is that electronic excitation allows for particles to climb the energy ladder, making it easier for them to ionize, but several modeling issues seem to have affected the results. First, the electron impact ionization reaction, and a few other reactions, were missing backward rates meaning that the reaction was always in nonequilibrium. In addition, the TCE model requires an Arrhenius form that leads to errors in reproducing the equilibrium constant. Finally, energy from the electronic mode was allowed to contribute to the TCE reaction probability calculation and led to overprediction of the reaction rate.

Along with the preliminary sensitivity studies, Saturn entry simulations were performed with the CHIPS code. These CHIPS simulations represented a first attempt at reproducing hypersonic shock tube experiments for a H_2-He mixture with DSMC. Before simulations could be performed, input parameters for the VHS, Larsen-Borgnakke, Arrhenius, and electronic excitation models were fit or compiled. In a 1-dimensional

shock wave study with the CHIPS code, the inclusion of an electronic excitation model was again shown to have drastic effects on the charged particle number densities by increasing the atomic hydrogen ion and free electron number densities by an order of magnitude. In turn, the inclusion of an electronic excitation model improved the comparison of the CHIPS results to the experimental data.

Two EAST hypersonic shock tube experiments for Saturn entry were simulated with the CHIPS code [2]. To compare the simulations directly to the experimental measurements of the radiance, the CHIPS results were post-processed by passing the number densities and temperatures through the NEQAIR line-by-line radiation code [5]. In this study, the radiative quantities were calculated from NEQAIR assuming that the electronic temperature was equal to the free electron temperature. As a result, the simulated radiance was typically much larger than the experimental value, but the profiles were qualitatively similar to the experimental results. The simulations confirmed the experimental observation that atomic hydrogen diffuses upstream of the shock, although emission of the Lyman-α band in the upstream region was not seen. This could be explained by the representation of the electronic temperature as purely the translational temperature of the free electrons when passed to NEQAIR. Since free electrons are not present upstream, the electronic temperature is undefined and NEQAIR could not yield spectra. In analyzing the translational temperature of the atomic hydrogen upstream of the shock, it is obvious that these high temperature particles should be emitting in this region. Another potential source of error stems from calculating the radiative results solely from temperatures and number densities. This step could be omitted by passing the electronically excited states directly to NEQAIR which would retain the nonequilibrium distribution simulated by CHIPS. Discrepancies were also seen when comparing the number density of free electrons through the shock to the

experiments. The relative magnitudes of the free electron number density were similar, but the trends in the simulation did not match the experiment. This error is likely due to incorrect backward reaction rates calculated from the TCE model. Because of the limitations of the TCE model when simulating a backward reaction rate, large discrepancies in the electron capture reaction rates were necessary when curve fitting the backward reaction rates.

The conclusions from both the sensitivity analyses and the Saturn entry case pointed to problems with the TCE model. Upon studying the TCE model further, various underlying assumptions were identified that should be considered when using this model. The most important assumption for this research is that the energy modes contributing to the reaction probability calculation must be continuous. This means that the previous simulations were reproducing the incorrect reaction rate by allowing the discrete electronic energy mode to contribute in the TCE model. It was found that this led to an overprediction of several reaction rates in these simulations. In addition, limitations to the Arrhenius parameters used in the TCE model were presented which severely restrict the reaction rates that can be used with the TCE model. These conclusions indicated that the TCE model is inadequate for simulating high temperature flows accurately. For this reason, it is suggested that an alternative approach for modeling high temperature flows with electronic excitation and ionization should be developed in the future.

The complications encountered from the TCE model are exaggerated even further when attempting to model backward reaction rates. Since the rates are forced to be in Arrhenius form, substantial error in reproducing the equilibrium constant can result. As a solution, Boyd developed a model to directly calculate the backward reaction rate from partition functions [85]. In theory, this method is the most accurate method when high order partition functions are used, but in practice high order partition functions are

expensive to calculate in a DSMC simulation. A solution to the computational cost would be to use low order partition functions to calculate the equilibrium constant but this would result in errors. To address this, a new backward reaction model was proposed where the backward rate is calculated directly from the forward Arrhenius rate and an equilibrium constant curve fit. This method was found to reproduce the backward reaction rate accurately and efficiently for the entire valid range of the equilibrium constant. In addition, a method for extrapolating the equilibrium constant outside of this valid range was presented.

In addition to creating a backward reaction model, various models in the CHIPS code were updated based on the observations from the preliminary sensitivity analyses and comparisons with the Saturn entry condition experimental data. Improved VHS parameters from Ref. [18] and Arrhenius chemical reaction rates from Ref. [91] compliant with the TCE model were included in the CHIPS code. The electronic temperature computation was improved by calculating the temperature in each cell through a linear least squares fit of computed populations in excited states of each species. It was also discovered that the electronic excitation model was missing an appropriate relaxation collision number. Furthermore, to address errors in the radiative results, the approach used to post-process CHIPS results with NEQAIR was reassessed. Instead of calculating the radiation solely from the simulated temperatures and number densities, the electronically excited states simulated in CHIPS were passed directly to NEQAIR. The grouped excited states used in the CHIPS code models must be ungrouped before being sent to NEQAIR. To perform the ungrouping, a polynomial least squares curve fit was performed on the logarithms of species populations, i.e. a polynomial was fit to the populations represented on a Boltzmann plot. Each group was then ungrouped based on the local slope of the polynomial curve fit.

Once the CHIPS code was updated, a final nominal simulation was completed for a lunar return hypersonic shock scenario and the results were compared to multiple benchmark experiments performed in the EAST facility [1]. After post-processing the CHIPS simulation with the NEQAIR code, the results were directly compared to the experimental radiance data for the VUV, UV/Vis, Vis/NIR, and IR spectral ranges. When analyzing the results with specifically defined electronic collision numbers and the case where the electronic collision number is assumed to be one, it became apparent that species specific parameters are required to correctly model nonequilibrium electronic excitation using Liechty's model [24]. When the electronic collision number was specific to each collision pair, the radiative results showed significant improvement. The simulated radiance returned the correct order of magnitude and displayed trends similar to the experimental data in most cases. However, some discrepancies were also identified. In the CHIPS code, the misrepresentation of the forward reaction rate by the TCE model may have resulted in disagreements with the experiments on the relaxation time to radiative equilibrium. This is also observed when comparing the bound-free radiance in the UV/Vis range. In addition, the analytic equilibrium calculated from the initial conditions showed that the experiments are not producing the expected radiance at equilibrium. This could be due to several experimental uncertainties and may indicate that the simulated shock velocity differs from the experimental value at the measurement location. Although contrasting the simulation and experiments identifies areas where improvement is needed, these results are encouraging considering that the electronic excitation collision numbers used were not directly developed from experimental or theoretical data.

Assumptions like the ones required in the nominal simulation to determine the electronic collision numbers validate the need for sensitivity analyses where the

important input parameters can be identified. A final global Monte Carlo sensitivity analysis was performed that investigated six different QoIs: the translational temperature, the free electron number density, and the four spectral ranges measured in the EAST experiments. In this sensitivity analysis, 2,250 simulations were completed where random selections from uniform prior distributions were assigned to the reaction rates and electronic collision numbers used in the CHIPS code. While the preliminary sensitivity analyses demonstrated similar parameter rankings for the QoIs studied, the results of this last sensitivity analysis are more diverse for the QoIs investigated. For this reason, a final table was not included at the culmination of the sensitivity study. Instead, it is recommended that the figures for the individual QoI be studied to directly determine its relationship with the input parameters.

10.2 Recommended Investigations

In lieu of a final table of overall sensitivity rankings, the following list identifies several input parameters that require further analysis based on the sensitivity study and the opinion of the author. Included with this list is a short description of the reasoning behind the importance assigned to the input parameter and possible improvements. This list is not exhaustive and is primarily determined from the QoIs and models studied here. The relative importance of these input parameters is tentative, and a more in-depth study is required in future work to confirm the conclusions in this dissertation.

- $N + e^- \rightleftharpoons N^+ + e^- + e^-$ and $O + e^- \rightleftharpoons O^+ + e^- + e^-$

Although the QoIs studied were not particularly sensitive to either of these electron impact ionization reactions, many of the current difficulties identified in the CHIPS code affect these reactions. Because most published rates are far outside of the

Arrhenius parameters accepted by the TCE model, they cannot be used. In this dissertation, new reaction rates were fit, but these rates demonstrate errors when compared to the published rates. More importantly, these reactions were found to be important in the preliminary sensitivity analysis where electronic energy was allowed to contribute to the reaction probability. It is likely that the absence of electronic energy contributions to the TCE model led to a significant underprediction of the forward reaction rate. Also, the importance of electron impact ionization reactions for higher velocity entry scenarios is obvious. As more electrons are present in the simulation, an electron cascade occurs due to impact ionization. To improve modeling of this reaction in DSMC, a better Arrhenius fit could be performed within the TCE model limits, but in the opinion of the author, solving the TCE model problems are a higher priority. As with all of the following reaction rates, Molecular Dynamics/Quasi-Classical Trajectory (MD/QCT) reaction cross-section data would solve many of the difficulties mentioned and would allow for removal of the TCE model. While it is unlikely that MD/QCT data will be available soon for all of the reactions modeled in this research, the most sensitive reactions can be prioritized, and the rest can continue to use the TCE model. Assuming adequate potential energy surfaces are available, accurate reaction rates as a function of collision energy would improve the accuracy of the simulations.

- $NO + N^+ \rightleftharpoons N + NO^+$

The importance of this charge exchange chemical reaction was the biggest surprise of this research. Several temperature and number density QoIs were found to be significantly correlated to this reaction. It is hypothesized that this reaction stabilizes free electrons and is important to determining the post-shock chemical relaxation rate. To complicate matters further, the reaction rate is not well known. The original source of the

nominal rate does not provide insight into how this rate was obtained and no other references have been found [19]. The rate used in the final sensitivity analysis was recently estimated from cross-section data, but a more thorough study may be required [91].

- $N_2 + N \rightleftharpoons N + N + N$

The dissociation of nitrogen by an atomic nitrogen is clearly a significant reaction as it is responsible for energy absorption within the nonequilibrium region. As this reaction is important to the formation of the shock, its effects are felt far downstream since it determines the physical processes that follow. In addition, the concentration of N_2 in the freestream is 79% for synthetic air making it a common reaction. Unlike many of the parameters identified in the sensitivity analysis, this reaction and other N_2 dissociation reactions have been the topic of several studies pertaining to hypersonic simulations and is relatively well known [101][102][103][104].

- $N + O \rightleftharpoons NO^+ + e^-$ and $N + N \rightleftharpoons N_2^+ + e^-$

At least one of the associative ionization reactions was found to be meaningful for every QoI studied in the final sensitivity analysis. This outcome is the result of a couple different processes. First, these reactions are especially important to the ionization process as they create the initial electrons in the flow. The backward forms of the associative ionization reactions are also responsible for electron capture in the post-shock region. Like the N_2 dissociation reactions, associative ionization reactions are common within the shock and remove energy from the flow whenever an ionization reaction occurs. Finally, the radiative measurements were highly correlated to these reactions. Not only do the previously mentioned causes contribute, the creation or destruction of the

emitting species has an effect on their concentration. While reaction rates that are compatible with TCE were used in the CHIPS code, the most accurate rates are unable to be used with the TCE model. It would be beneficial to investigate these rates further for ionizing hypersonic flows.

- $Z_{elec}(N - e^-)$, $Z_{elec}(N - Heavy)$, $Z_{elec}(O - e^-)$, and $Z_{elec}(N_2^+ - e^-)$

From the final sensitivity analysis, the radiative QoIs studied were found to be sensitive to four electronic collision numbers. Besides $Z_{elec}(N - Heavy)$, the translational temperature and free electron number density QoIs analyzed were relatively independent of the electronic collision number. Since atomic nitrogen is prevalent in this hypersonic shock scenario, its excitation plays a role in storing energy in an internal electronic mode. When considering a radiative QoI, the important electronic collision numbers were always found to be those associated with the radiating species in that spectral range. With that in mind, it would seem that the appropriate course of action would be to determine accurate electronic collision numbers for the important species radiating in the spectral range of interest. These collision number could be calibrated with recent cross-section data from Huo or Park for example [94][105][106].

10.2 Future Work

To follow up on the current research, several approaches can be taken. One possibility is to pursue investigations of the input parameters discussed in the previous section. This can either be completed by fitting the parameters directly to published data or by calibrating the CHIPS code to experimental results. The EAST data used in the final nominal simulation provides an ideal experimental database to calibrate the chosen

CHIPS parameters. Using the Quantification of Uncertainty for Estimation, Simulation, and Optimization (QUESO) code, a Markov Chain Monte Carlo (MCMC) solution to the statistical inverse problem can be obtained [107]. Following a typical Metropolis-Hastings MCMC algorithm, a chain of simulations can be performed where the likelihood is calculated from the results of each simulation. A new chain position is accepted if the likelihood of the current simulation is greater than the previous simulation. The QUESO code improves on this parameter space exploration through the application of a delayed-rejection adaptive Metropolis algorithm where the covariance matrix is evolved to eliminate the selection of unlikely simulation parameters and, therefore, reduce the required number of chain positions until convergence [108]. In this way, the parameter space is explored and posterior probability density functions (PDFs) are obtained for each input parameter based on the density of chain points. From these PDFs, conclusions can be drawn about the uncertainty in each input parameter and the confidence in its nominal value. Since the MCMC calibration is expensive, the calibration would benefit from using the sensitivity analysis results to reduce the parameter space. By assuming that the less sensitive parameters are irrelevant, a more meaningful exploration of the parameter space can be completed, and the parameters being explored will have a better fit with the experimental data. This approach has previously been applied to calibrate a 1-dimensional shock to synthetic data [6].

Before the calibration can be performed, the uncertainties associated with the model parameters, simulation inputs, and observational data must be determined and assigned reasonable PDFs. The models that are contained in CHIPS include many input parameters that come with a varying degree of uncertainty. When performing an uncertainty quantification study, the input parameters of interest must be assigned prior distributions based on their confidence and knowledge of the physical limitations for each

parameter. Since DSMC is inherently a probabilistic method where macroscopic values are determined by averaging the particle properties in a cell, sampling errors will influence the results and must be accounted for. Finally, there are various uncertainties in the experimental data that should be considered. For example, a hypersonic shock in a shock tube moves with such high velocities that calculating the shock speed can be difficult. Pressure transducers are used to determine when the shock passes and to calculate the shock speed as it travels in the tube. Since these transducers have to be very sensitive to obtain an accurate measure of the time when the shock passes, there is a moderate degree of uncertainty in the shock speed measurement. Considering that radiation is very sensitive to the shock speed, this uncertainty must be accounted for in the calibration.

Another option for future work would be to update the CHIPS code with the most recent advancements in DSMC. In chapter 8, improved VHS parameters were obtained from Swaminathan-Gopalan and Stephani, but the implementation in the CHIPS code was incomplete [18]. The neutral-electron piecewise curve fits were only partially applied where the full function should have been added. The elastic collision model could be taken a step further with the Variable Soft Sphere (VSS) model which more accurately reproduces both diffusion and viscosity [109]. Reference [18] includes 11-species air parameters for the VSS model and includes parameters to fit the Coulombic charged-charged interactions. The modeling of charged particles would also improve with the introduction of ambipolar diffusion. Since the presence of free electrons is critical to various radiative processes, modeling ambipolar diffusion may influence the radiative results [11]. Including ambipolar diffusion would cause the free electrons and ions to diffuse further upstream. In the Saturn case, ambipolar diffusion could potentially allow the emission from the hot atomic hydrogen to be seen upstream of the shock. On the

other hand, it would lead to earlier ionization, making the discrepancy between the simulated and experimental ionization locations even greater. In addition, the simulated radiation could benefit from a more accurate electronic state ungrouping method. While the current polynomial least squares method is adequate, it could be improved by weighting the fit based on the number of simulated particles in each level.

Likely, the greatest advancements towards accurately modeling radiation would be the development of an improved electronic excitation model, the modeling of spontaneous emission within CHIPS, and the introduction of a chemistry model that can accurately handle electronic excitation. While the electronic collision numbers chosen in Chapter 8 performed relatively well in reproducing the experimental radiance, the accuracy of the model could be improved. Currently, a constant collision number is used for each species. The electronic collision number model could be improved by creating a temperature dependent and/or state dependent model based on experimental or theoretical results. Related to this, a state specific electronic excitation model could be applied to the CHIPS code. This method would be able to correctly reproduce allowed and forbidden transitions. Since the radiance in each spectral range is typically produced from specific transitions, modeling excitation rates for individual levels could improve the simulated accuracy. However, modeling individual transitions separately may be impossible if the number of particles required to minimize statistical fluctuations is unrealistic. In regard to specific excitations, particles in an excited state have some decay time before the excited state transitions to a lower level, emitting a photon. If the decay time is shorter than the transition rate of the excited state through particle collisions, simulating spontaneous emission may be necessary to correctly model the population of that excited state. In turn, this could influence the radiance predicted by NEQAIR for certain spectral ranges. Spontaneous emission may also reduce the energy contained in the system since the

emitted photons typically escape. Future work could investigate the impact and implementation of a spontaneous emission model.

As discussed throughout this conclusion, the limitations of the TCE model restrict the accuracy of the simulated hypersonic shock. In the TCE model, energy in the electronic mode cannot contribute to the total collision energy, meaning that this energy has no effect on the reaction rate and energy contained in this mode is "invisible" to chemical reactions. In reality, the excited state of the colliding particle should be the most important factor determining the ionization probability. The errors expected for ionization reactions simulated by the TCE model are increased further due to the incompatibility of most ionization reaction rates with the Arrhenius parameter limitations of the TCE model. Since there is no viable alternative model currently available, future work could focus on development of a new chemical reaction model that addresses simulations including electronic excitation and ionization reactions. If significant improvements are made to the physics represented in the CHIPS code, performing another iteration of the sensitivity study would be relatively simple to execute.

Even before these improvements to the CHIPS code are made, another simulation of the Saturn entry case could be performed. Since the CHIPS code has progressed significantly in the time since the previous Saturn simulation, it would be interesting to investigate how the changes affect the Saturn radiative results. Specific to the Saturn simulation, additional future work could be completed to update the 7-species H_2-He parameters. For example, improved VHS/VSS parameters could be obtained, the proposed backward reaction rate model could be applied, and a temperature dependent model for rotational relaxation of H_2 could be developed for high temperatures. Models in the NEQAIR code could also be addressed in the future. The inclusion of quasi-steady state rates for H in NEQAIR could reduce the difference in radiative magnitude between

the simulation and experiment by more accurately representing the nonequilibrium. Alternatively, the excited state distributions could be passed directly to NEQAIR following the method described in Chapter 8 which may result in substantial improvement of the radiative results. Once the most critical improvements have been completed, a global sensitivity analysis can be performed for the improved H_2-He parameters used in the DSMC simulation. This will be a significant step for identifying the most important input parameters in the system and for future research where the highest ranked parameters could be selected and calibrated to the EAST data with the MCMC method.

APPENDIX A

Supplementary Sensitivity Analysis Results

A.1 Overview

The results of the final sensitivity analysis for the $QoIs$ not discussed in Chapter 9 are presented in this appendix as a series of figures. Table A.1 repeats the input parameters listed in Chapters 8 and 9 which correspond to the parameter numbers in the following figures. Although the results are shown here, they have not been analyzed or described. Care must be taken when interpreting these results as different levels of convergence are observed due to noise present in the $QoIs$ measured. Note that the overall temperature for each species, T, plotted in Sections A.2.48-54 is calculated from the translational, rotational, and vibrational temperatures weighted by the degrees of freedom. In this calculation, the electronic temperature was ignored to avoid assuming an electronic degrees of freedom relationship.

A.2 SENSITIVITY ANALYSIS FIGURES

Table A.1 Arrhenius rate reactions and electronic collision number input parameters corresponding to the sensitivity analysis results.

1	$N_2 + N_2 \rightleftharpoons N + N + N_2$	27	$O_2 + NO^+ \rightleftharpoons O + O + NO^+$	52	$Z_{elec}(N_2 - Heavy)$
2	$N_2 + N \rightleftharpoons N + N + N$	28	$NO + N_2^+ \rightleftharpoons N + O + N_2^+$	53	$Z_{elec}(N - Heavy)$
3	$N_2 + O_2 \rightleftharpoons N + N + O_2$	29	$NO + N^+ \rightleftharpoons N + O + N^+$	54	$Z_{elec}(O_2 - Heavy)$
4	$N_2 + O \rightleftharpoons N + N + O$	30	$NO + O_2^+ \rightleftharpoons N + O + O_2^+$	55	$Z_{elec}(O - Heavy)$
5	$N_2 + NO \rightleftharpoons N + N + NO$	31	$NO + O^+ \rightleftharpoons N + O + O^+$	56	$Z_{elec}(NO - Heavy)$
6	$O_2 + N_2 \rightleftharpoons O + O + N_2$	32	$NO + NO^+ \rightleftharpoons N + O + NO^+$	57	$Z_{elec}(N_2^+ - Heavy)$
7	$O_2 + N \rightleftharpoons O + O + N$	33	$N + O \rightleftharpoons NO^+ + e^-$	58	$Z_{elec}(N^+ - Heavy)$
8	$O_2 + O_2 \rightleftharpoons O + O + O_2$	34	$N + N \rightleftharpoons N_2^+ + e^-$	59	$Z_{elec}(O_2^+ - Heavy)$
9	$O_2 + O \rightleftharpoons O + O + O$	35	$O + O \rightleftharpoons O_2^+ + e^-$	60	$Z_{elec}(O^+ - Heavy)$
10	$O_2 + NO \rightleftharpoons O + O + NO$	36	$N_2 + e^- \rightleftharpoons N + N + e^-$	61	$Z_{elec}(NO^+ - Heavy)$
11	$NO + N_2 \rightleftharpoons N + O + N_2$	37	$NO + e^- \rightleftharpoons N + O + e^-$	62	$Z_{elec}(e^- - Heavy)$
12	$NO + N \rightleftharpoons N + N + O$	38	$N + e^- \rightleftharpoons N^+ + e^- + e^-$	63	$Z_{elec}(N_2 - e^-)$
13	$NO + O_2 \rightleftharpoons N + O + O_2$	39	$O + e^- \rightleftharpoons O^+ + e^- + e^-$	64	$Z_{elec}(N^+ - e^-)$
14	$NO + O \rightleftharpoons N + O + O$	40	$N_2 + N^+ \rightleftharpoons N + N_2^+$	65	$Z_{elec}(O_2 - e^-)$
15	$NO + NO \rightleftharpoons N + O + NO$	41	$N_2 + O^+ \rightleftharpoons O + N_2^+$	66	$Z_{elec}(O - e^-)$
16	$N_2 + O \rightleftharpoons NO + N$	42	$O + O_2^+ \rightleftharpoons O_2 + O^+$	67	$Z_{elec}(NO - e^-)$
17	$O_2 + N \rightleftharpoons NO + O$	43	$NO + O^+ \rightleftharpoons O_2 + N^+$	68	$Z_{elec}(N_2^+ - e^-)$
18	$N_2 + N_2^+ \rightleftharpoons N + N + N_2^+$	44	$O_2 + NO^+ \rightleftharpoons NO + O_2^+$	69	$Z_{elec}(N^+ - e^-)$
19	$N_2 + N^+ \rightleftharpoons N + N + N^+$	45	$N + NO^+ \rightleftharpoons O + N_2^+$	70	$Z_{elec}(O_2^+ - e^-)$
20	$N_2 + O_2^+ \rightleftharpoons N + N + O_2^+$	46	$O + NO^+ \rightleftharpoons O_2 + N^+$	71	$Z_{elec}(O^+ - e^-)$
21	$N_2 + O^+ \rightleftharpoons N + N + O^+$	47	$N + O_2^+ \rightleftharpoons O_2 + N^+$	72	$Z_{elec}(NO^+ - e^-)$
22	$N_2 + NO^+ \rightleftharpoons N + N + NO^+$	48	$N_2 + O_2^+ \rightleftharpoons O_2 + N_2^+$		
23	$O_2 + N_2^+ \rightleftharpoons O + O + N_2^+$	49	$N + NO^+ \rightleftharpoons N_2 + O^+$		
24	$O_2 + N^+ \rightleftharpoons O + O + N^+$	50	$O + NO^+ \rightleftharpoons N + O_2^+$		
25	$O_2 + O_2^+ \rightleftharpoons O + O + O_2^+$	51	$NO + N^+ \rightleftharpoons N + NO^+$		
26	$O_2 + O^+ \rightleftharpoons O + O + O^+$				

A.2.1 Quantity of Interest: Mixture Number Density

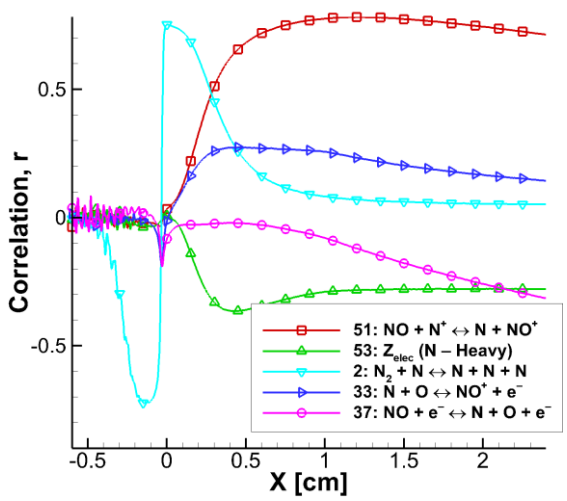

Figure A.1 Pearson correlation coefficient of the five most sensitive reaction rates when the mixture number density is the QoI ($QoI_{n_{mixture}}$).

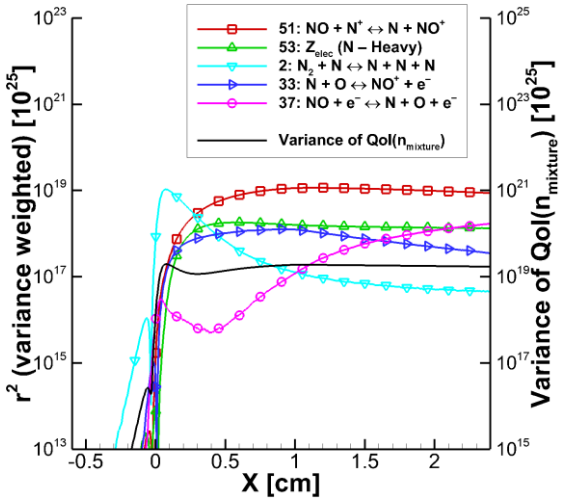

Figure A.2 Variance weighted r^2 sensitivities of the five most sensitive reaction rates for $QoI_{n_{mixture}}$, and the variance at each x −location.

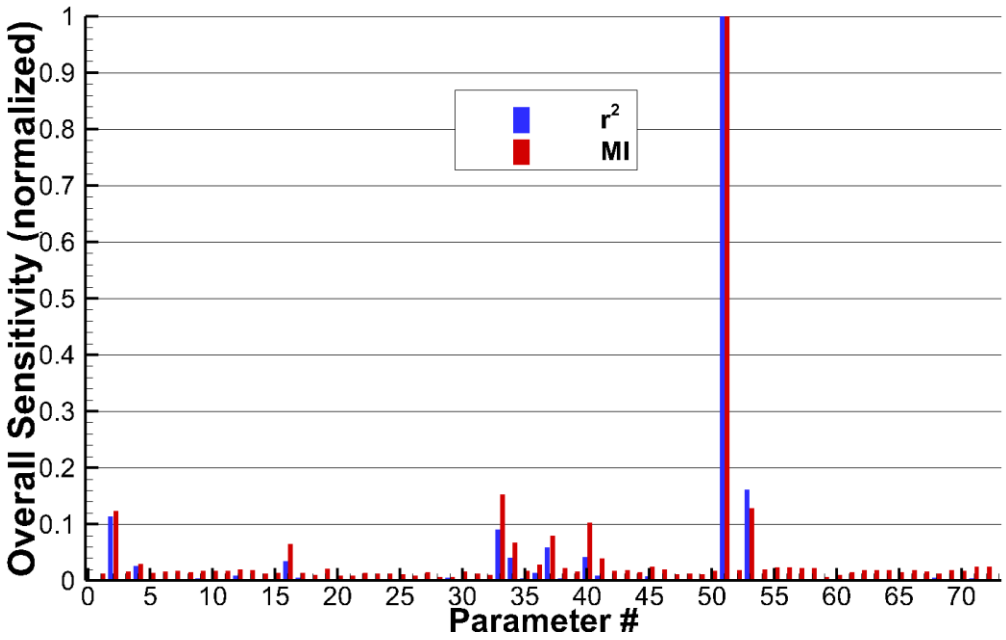

Figure A.3 Normalized r^2 and MI overall, variance weighted sensitivities for $QoI_{n_{mixture}}$.

A.2.2 Quantity of Interest: Molecular Nitrogen Number Density

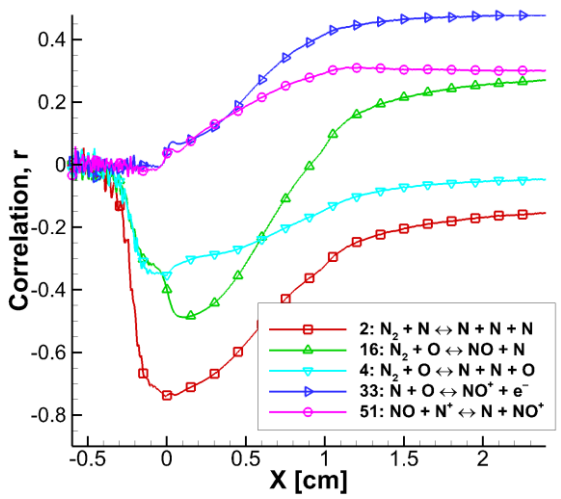

Figure A.4 Pearson correlation coefficient of the five most sensitive reaction rates when the molecular nitrogen number density is the QoI ($QoI_{n_{N_2}}$).

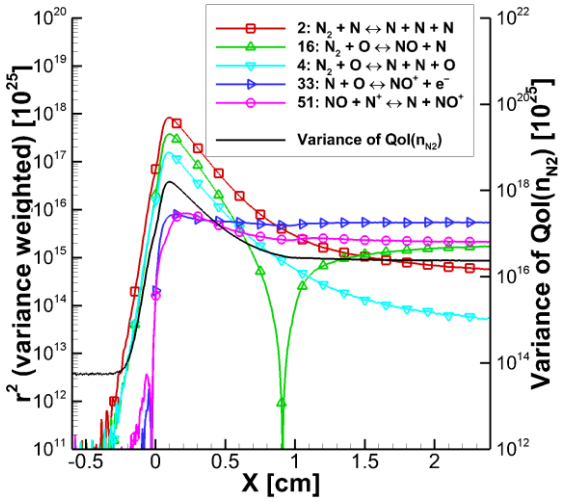

Figure A.5 Variance weighted r^2 sensitivities of the five most sensitive reaction rates for $QoI_{n_{N_2}}$, and the variance at each x −location.

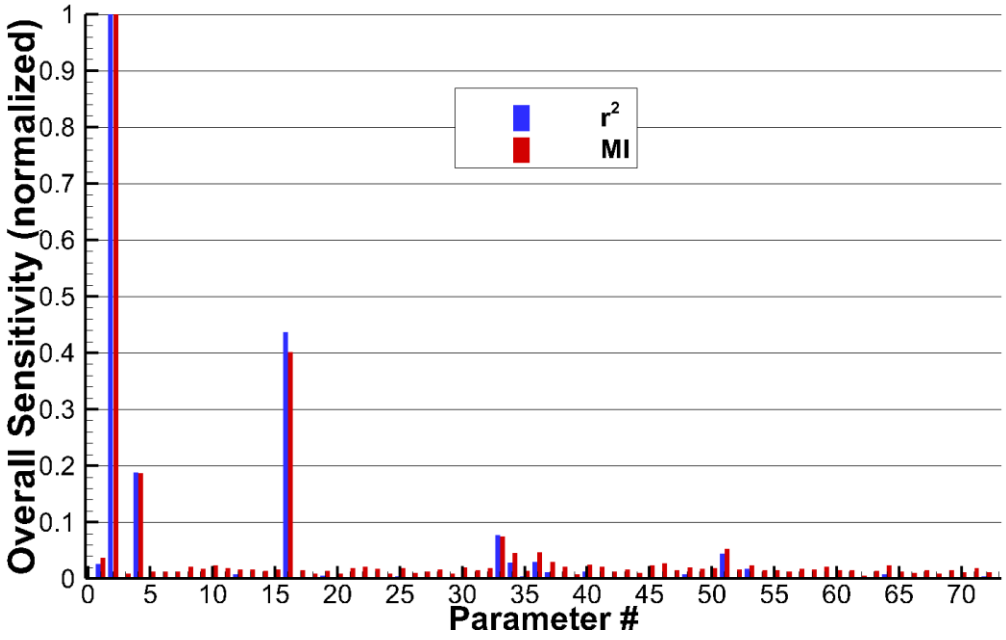

Figure A.6 Normalized r^2 and MI overall, variance weighted sensitivities for $QoI_{n_{N_2}}$.

A.2.3 Quantity of Interest: Atomic Nitrogen Number Density

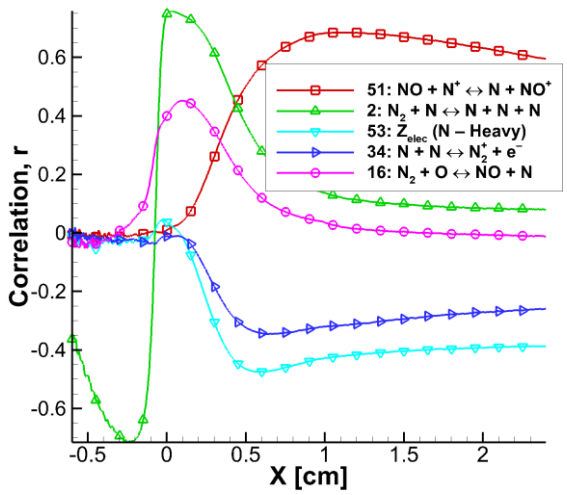

Figure A.7 Pearson correlation coefficient of the five most sensitive reaction rates when the atomic nitrogen number density is the QoI (QoI_{n_N}).

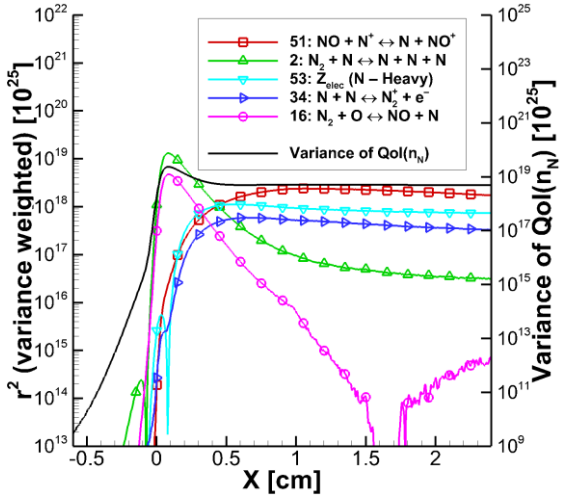

Figure A.8 Variance weighted r^2 sensitivities of the five most sensitive reaction rates for QoI_{n_N}, and the variance at each x −location.

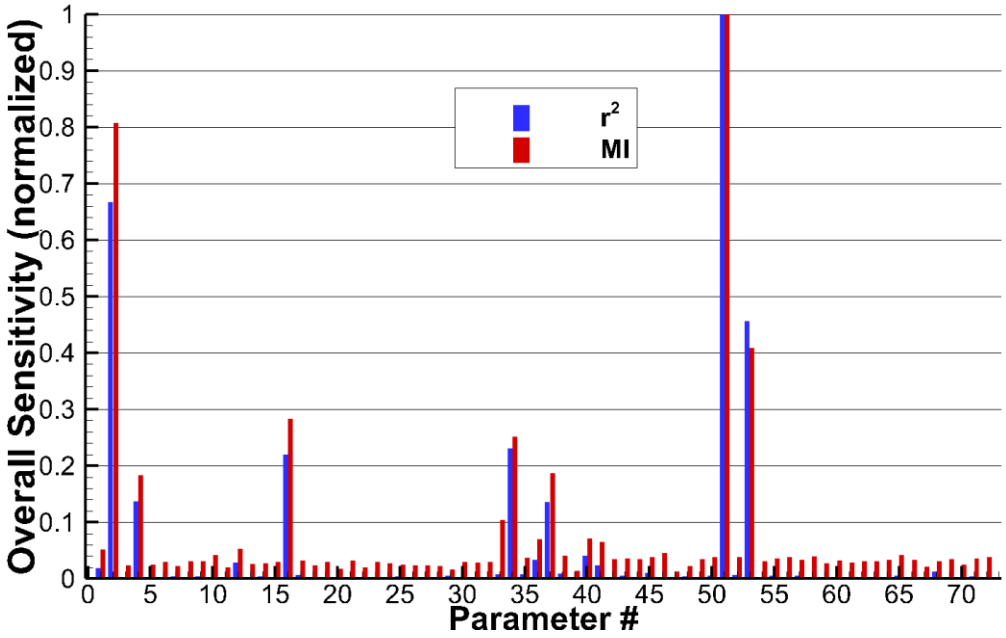

Figure A.9 Normalized r^2 and MI overall, variance weighted sensitivities for QoI_{n_N}.

A.2.4 Quantity of Interest: Molecular Oxygen Number Density

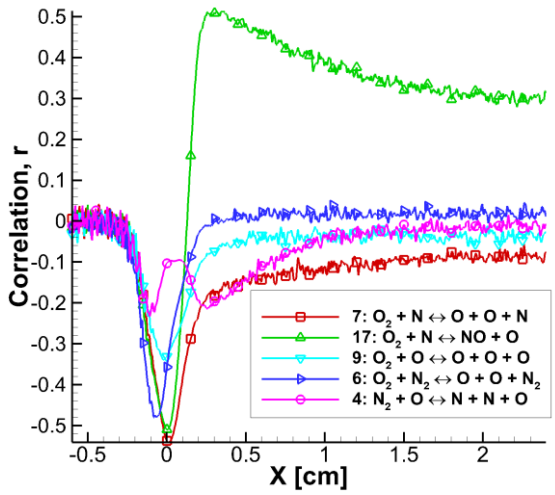

Figure A.10 Pearson correlation coefficient of the five most sensitive reaction rates when the molecular oxygen number density is the QoI ($QoI_{n_{O_2}}$).

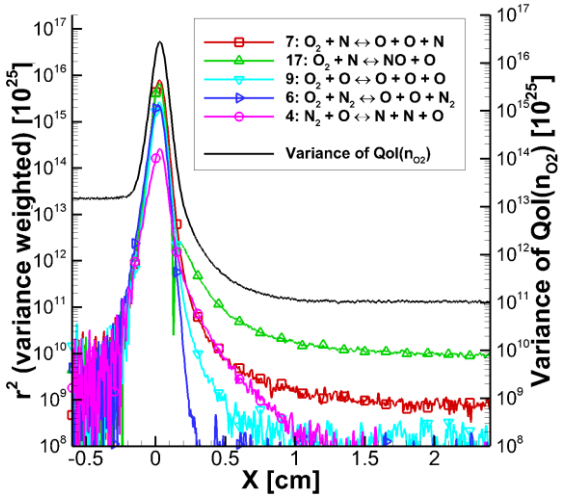

Figure A.11 Variance weighted r^2 sensitivities of the five most sensitive reaction rates for $QoI_{n_{O_2}}$, and the variance at each x −location.

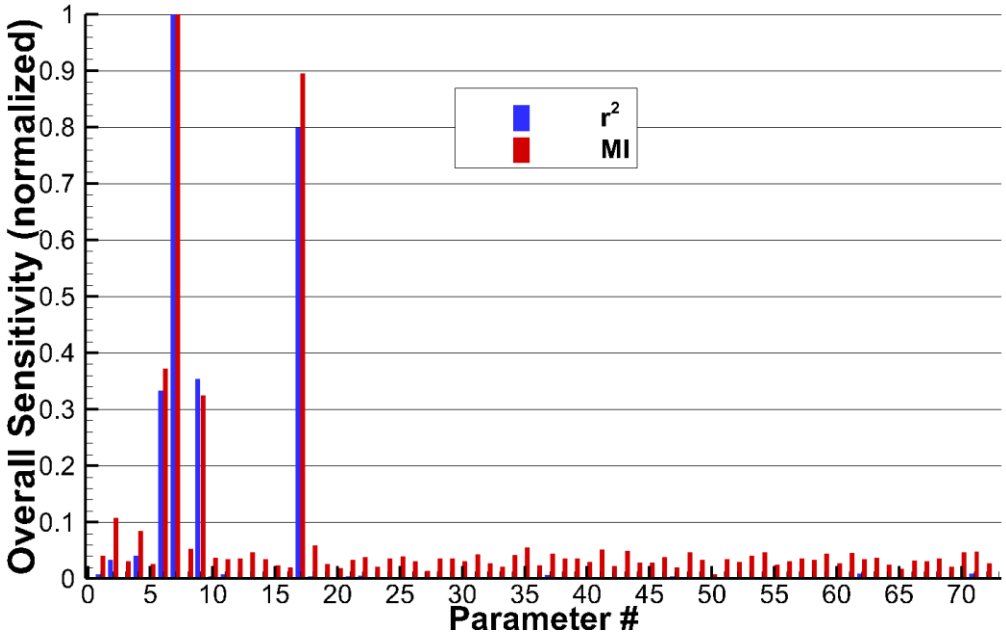

Figure A.12 Normalized r^2 and MI overall, variance weighted sensitivities for $QoI_{n_{O_2}}$.

A.2.5 Quantity of Interest: Atomic Oxygen Number Density

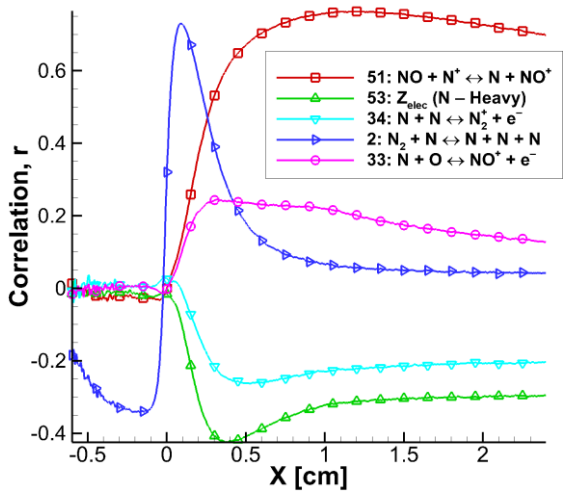

Figure A.13 Pearson correlation coefficient of the five most sensitive reaction rates when the atomic oxygen number density is the QoI (QoI_{n_O}).

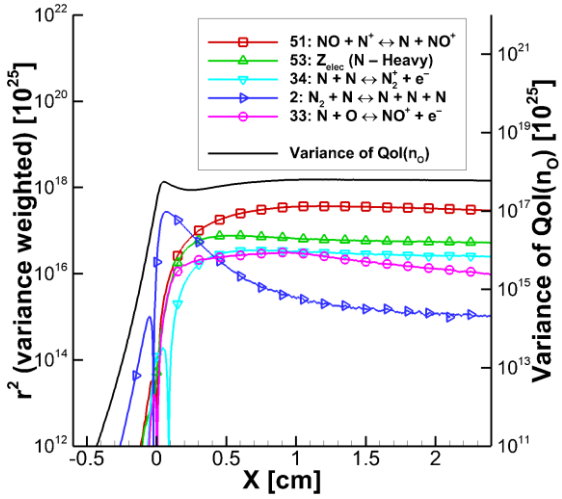

Figure A.14 Variance weighted r^2 sensitivities of the five most sensitive reaction rates for QoI_{n_O}, and the variance at each x −location.

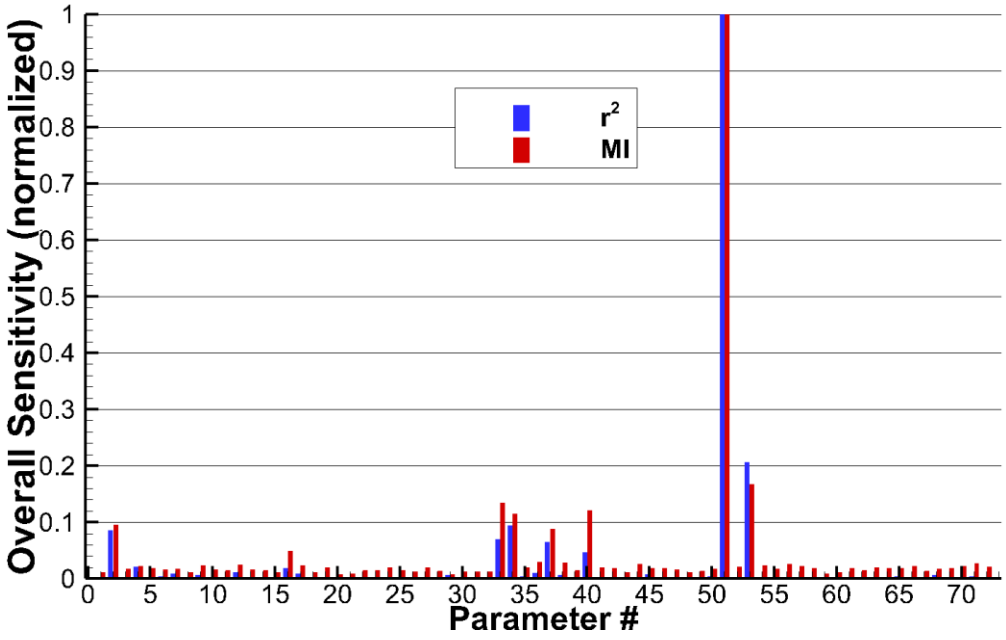

Figure A.15 Normalized r^2 and MI overall, variance weighted sensitivities for QoI_{n_O}.

A.2.6 Quantity of Interest: Nitric Oxide Number Density

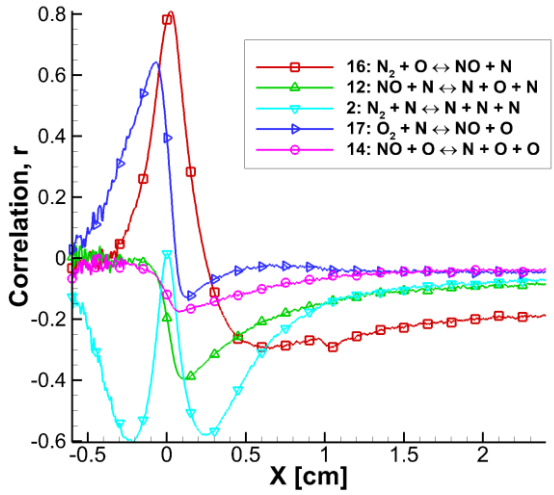

Figure A.16 Pearson correlation coefficient of the five most sensitive reaction rates when the nitric oxide number density is the QoI ($QoI_{n_{NO}}$).

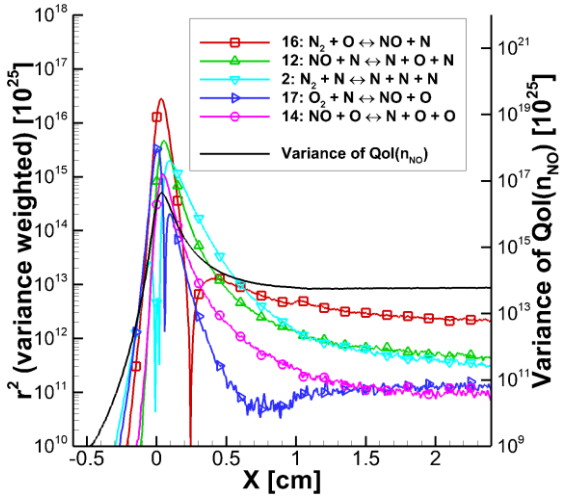

Figure A.17 Variance weighted r^2 sensitivities of the five most sensitive reaction rates for $QoI_{n_{NO}}$, and the variance at each x −location.

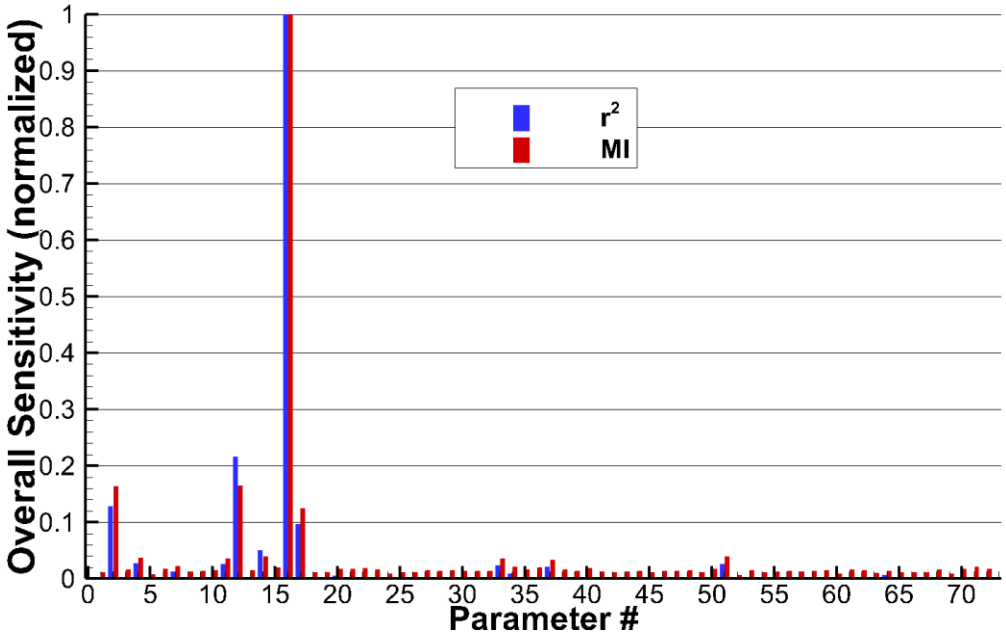

Figure A.18 Normalized r^2 and MI overall, variance weighted sensitivities for $QoI_{n_{NO}}$.

A.2.7 Quantity of Interest: Molecular Nitrogen Ion Number Density

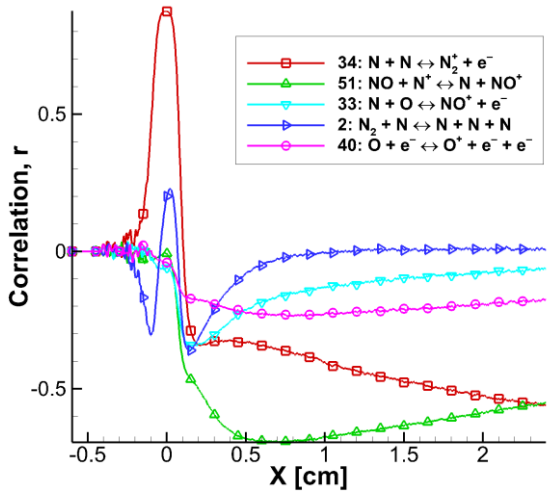

Figure A.19 Pearson correlation coefficient of the five most sensitive reaction rates when the molecular nitrogen ion number density is the QoI ($QoI_{n_{N_2^+}}$).

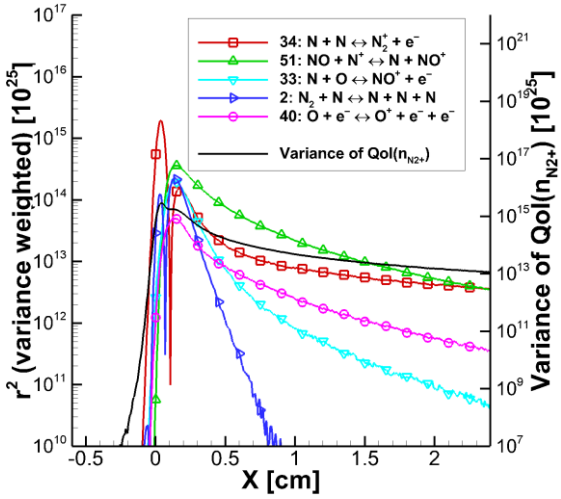

Figure A.20 Variance weighted r^2 sensitivities of the five most sensitive reaction rates for $QoI_{n_{N_2^+}}$, and the variance at each x −location.

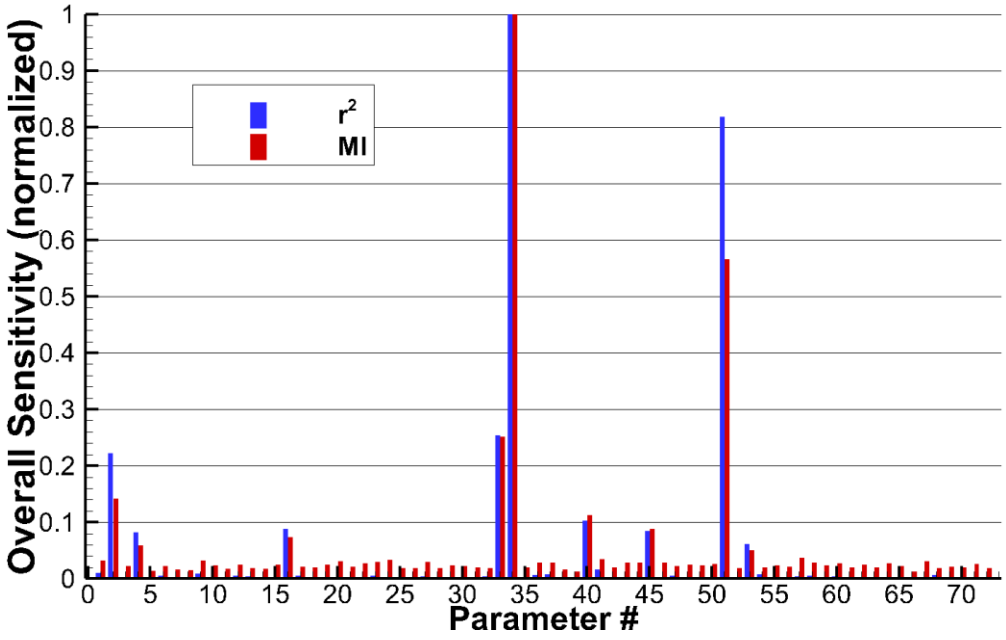

Figure A.21 Normalized r^2 and MI overall, variance weighted sensitivities for $QoI_{n_{N_2^+}}$.

A.2.8 Quantity of Interest: Atomic Nitrogen Ion Number Density

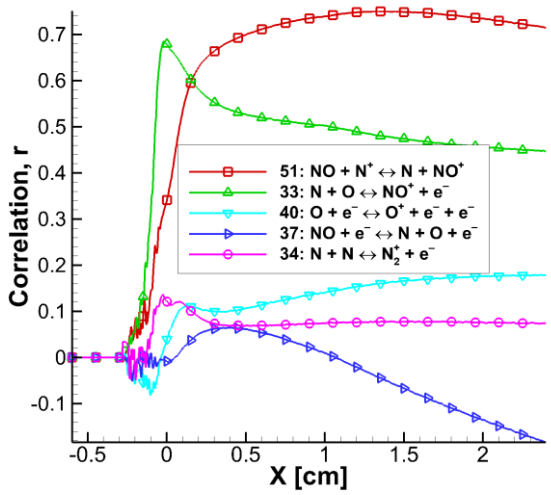

Figure A.22 Pearson correlation coefficient of the five most sensitive reaction rates when the atomic nitrogen ion number density is the QoI ($QoI_{n_{N^+}}$).

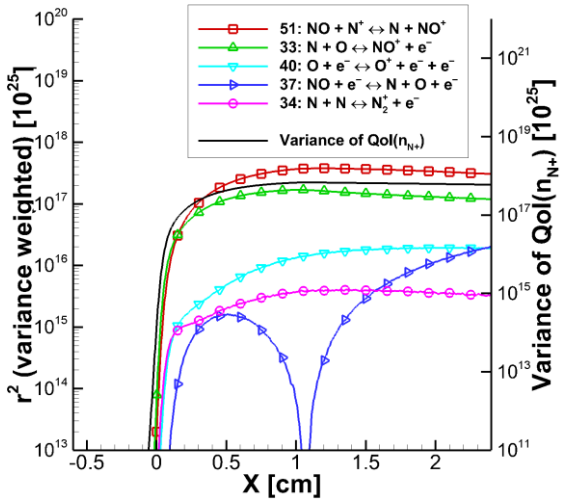

Figure A.23 Variance weighted r^2 sensitivities of the five most sensitive reaction rates for $QoI_{n_{N^+}}$, and the variance at each x −location.

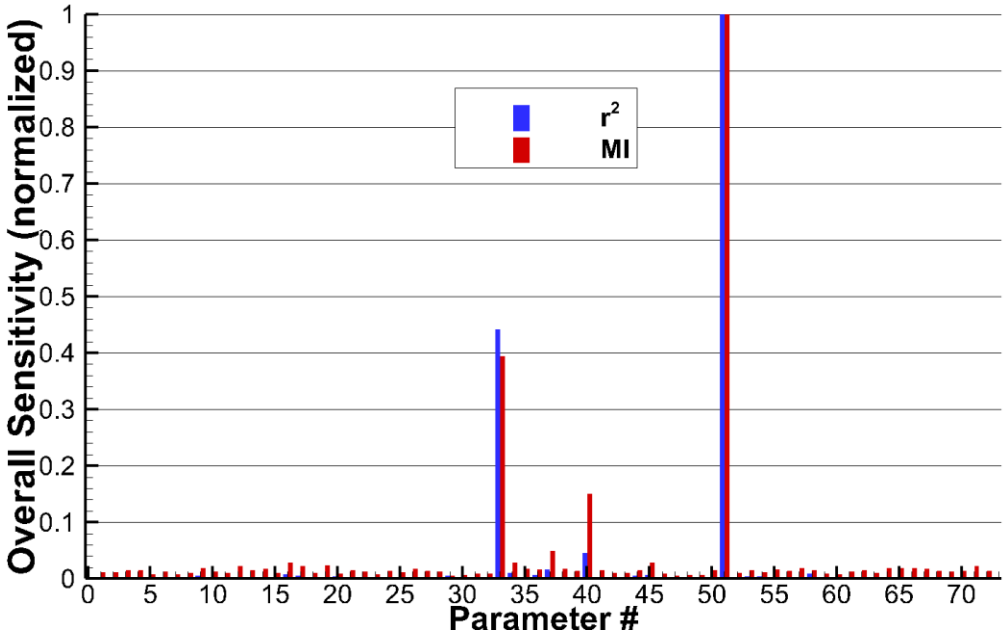

Figure A.24 Normalized r^2 and MI overall, variance weighted sensitivities for $QoI_{n_{N^+}}$.

A.2.9 Quantity of Interest: Molecular Oxygen Ion Number Density

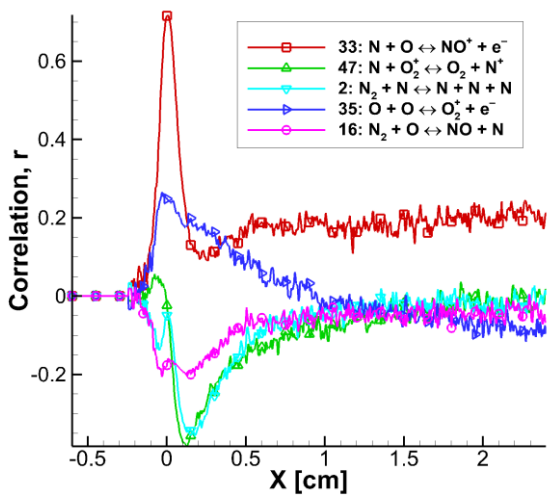

Figure A.25 Pearson correlation coefficient of the five most sensitive reaction rates when the molecular oxygen ion number density is the QoI ($QoI_{n_{o_2^+}}$).

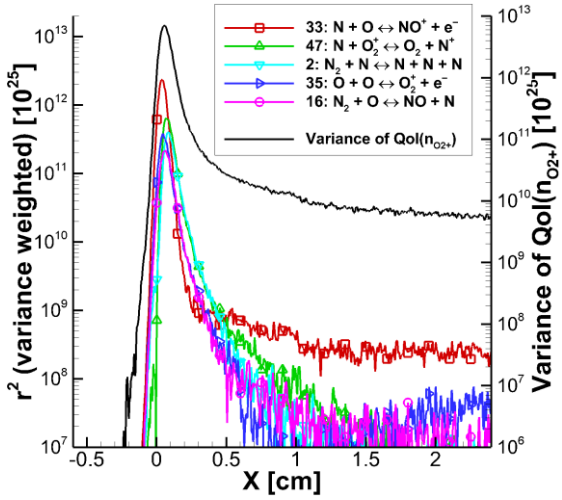

Figure A.26 Variance weighted r^2 sensitivities of the five most sensitive reaction rates for $QoI_{n_{o_2^+}}$, and the variance at each x −location.

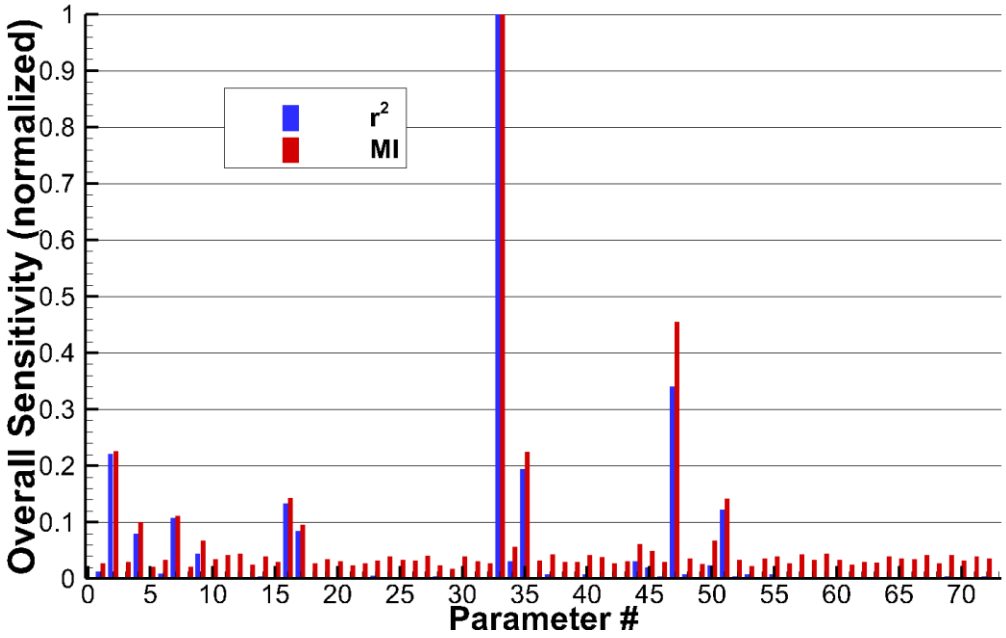

Figure A.27 Normalized r^2 and MI overall, variance weighted sensitivities for $QoI_{n_{o_2^+}}$.

A.2.10 Quantity of Interest: Atomic Oxygen Ion Number Density

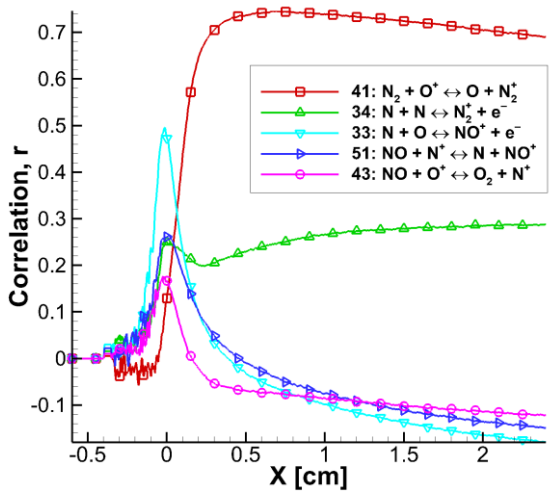

Figure A.28 Pearson correlation coefficient of the five most sensitive reaction rates when the atomic oxygen ion number density is the QoI ($QoI_{n_{O^+}}$).

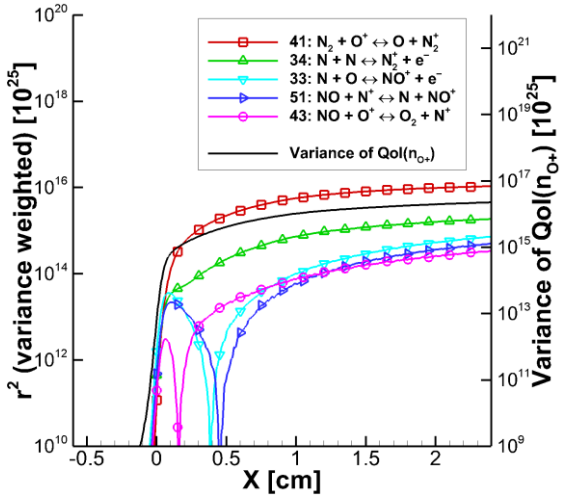

Figure A.29 Variance weighted r^2 sensitivities of the five most sensitive reaction rates for $QoI_{n_{O^+}}$, and the variance at each x −location.

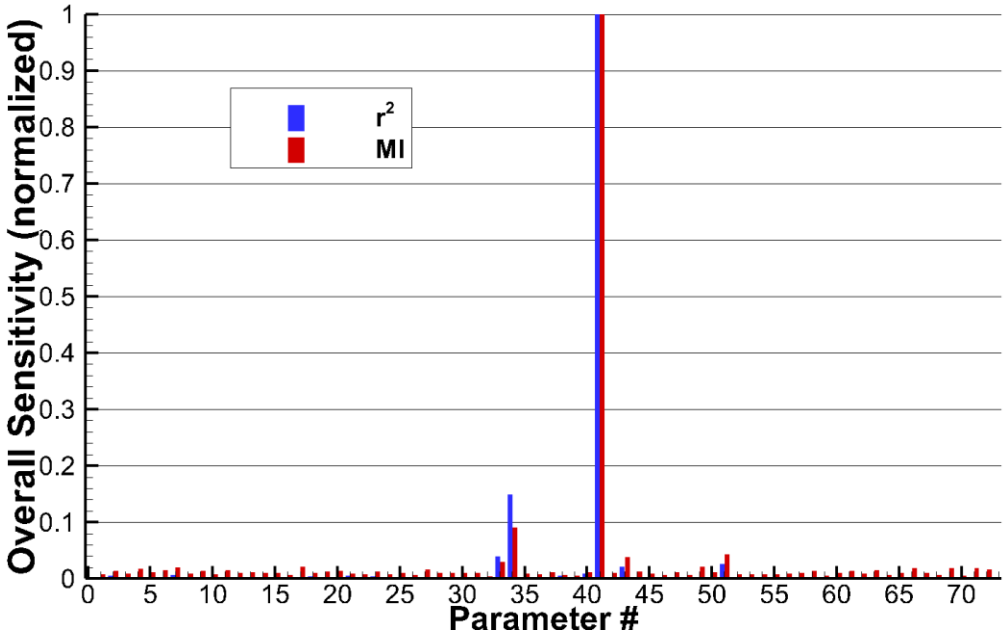

Figure A.30 Normalized r^2 and MI overall, variance weighted sensitivities for $QoI_{n_{O^+}}$.

A.2.11 Quantity of Interest: Nitric Oxide Ion Number Density

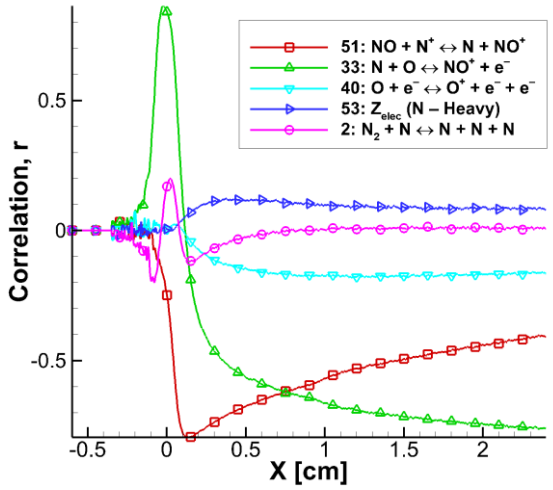

Figure A.31 Pearson correlation coefficient of the five most sensitive reaction rates when the nitric oxide ion number density is the QoI ($QoI_{n_{NO^+}}$).

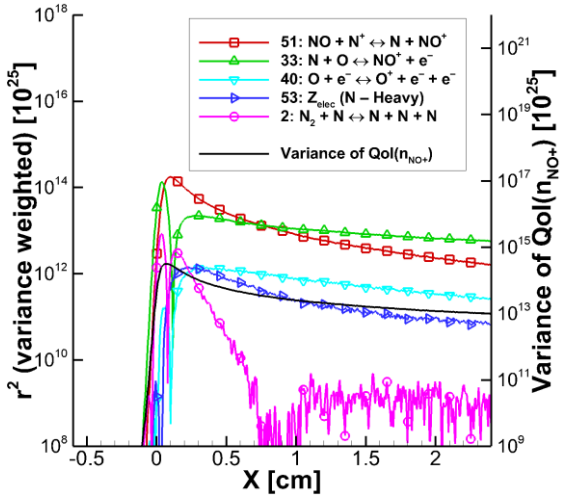

Figure A.32 Variance weighted r^2 sensitivities of the five most sensitive reaction rates for $QoI_{n_{NO^+}}$, and the variance at each x −location.

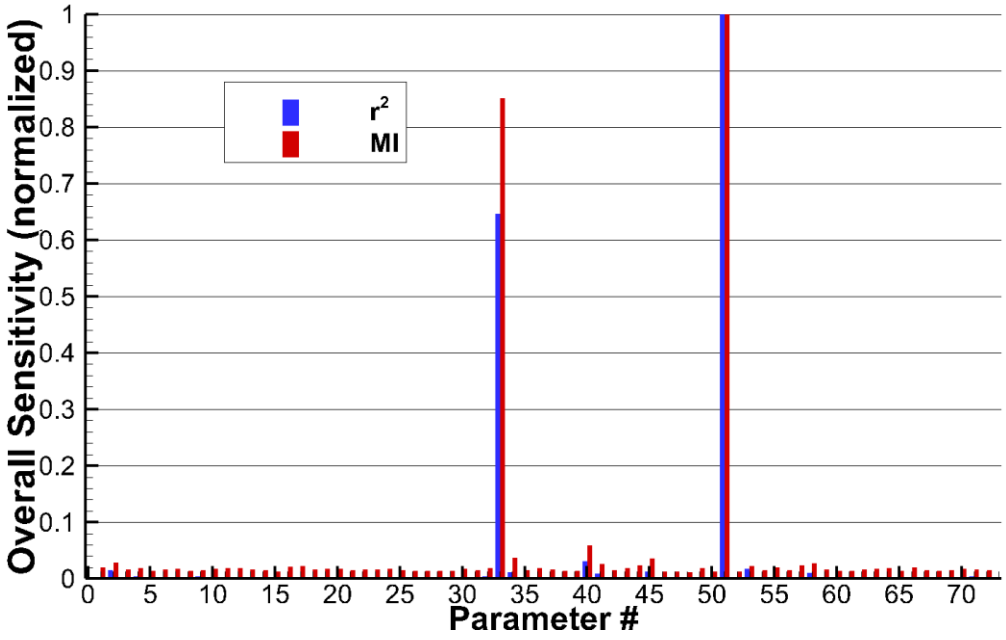

Figure A.33 Normalized r^2 and MI overall, variance weighted sensitivities for $QoI_{n_{NO^+}}$.

A.2.12 Quantity of Interest: Molecular Nitrogen Translational Temperature

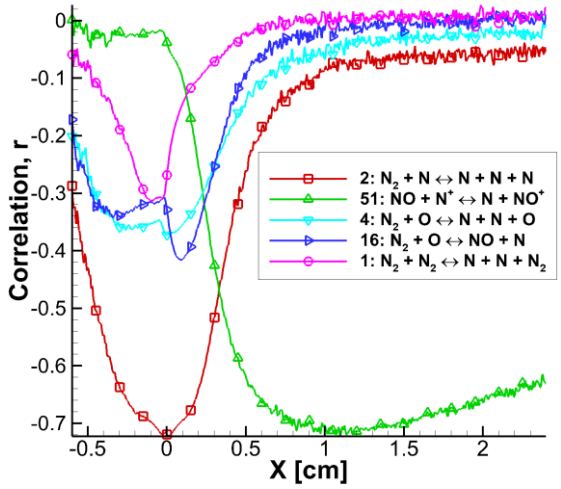

Figure A.34 Pearson correlation coefficient of the five most sensitive reaction rates when the molecular nitrogen translational temperature is the QoI ($QoI_{T_{tr_{N_2}}}$).

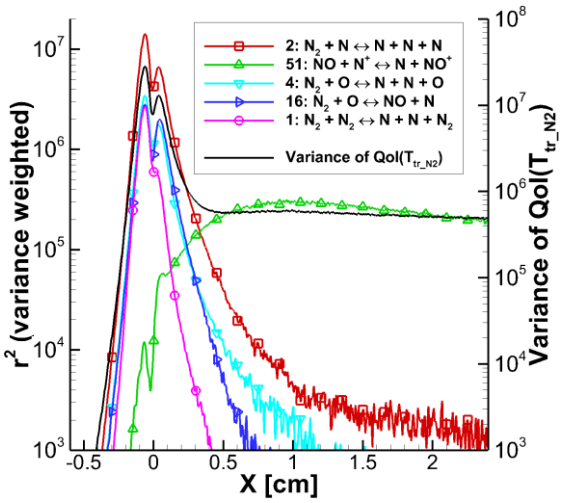

Figure A.35 Variance weighted r^2 sensitivities of the five most sensitive reaction rates for $QoI_{T_{tr_{N_2}}}$, and the variance at each $x-$location.

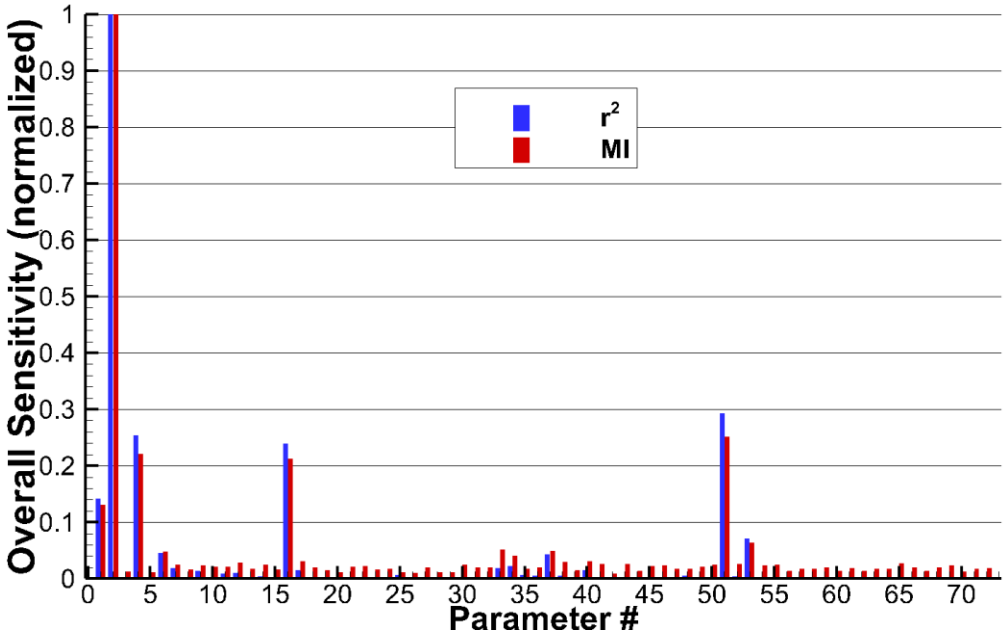

Figure A.36 Normalized r^2 and MI overall, variance weighted sensitivities for $QoI_{T_{tr_{N_2}}}$.

A.2.13 Quantity of Interest: Atomic Nitrogen Translational Temperature

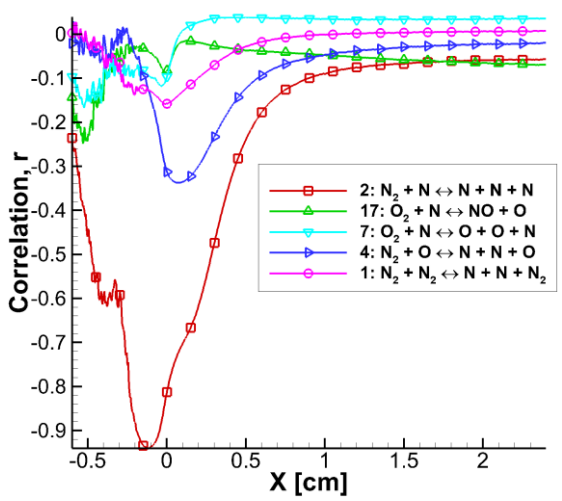

Figure A.37 Pearson correlation coefficient of the five most sensitive reaction rates when the atomic nitrogen translational temperature is the QoI ($QoI_{T_{tr_N}}$).

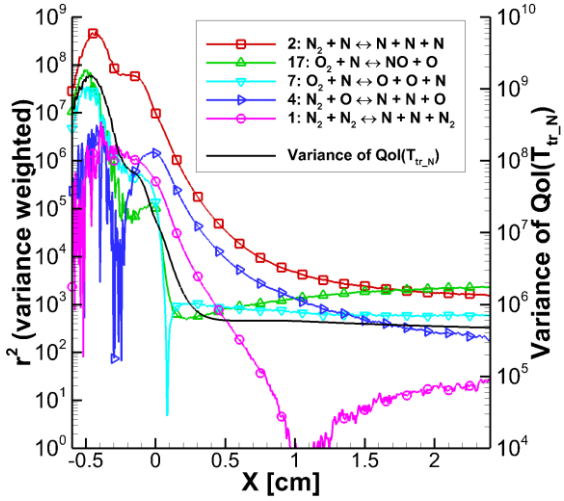

Figure A.38 Variance weighted r^2 sensitivities of the five most sensitive reaction rates for $QoI_{T_{tr_N}}$, and the variance at each x −location.

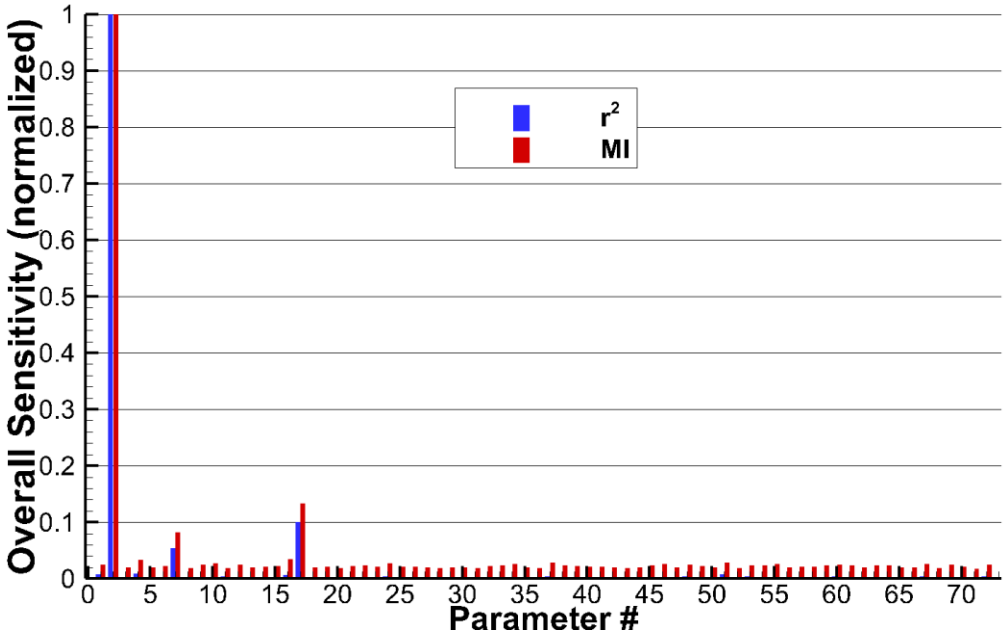

Figure A.39 Normalized r^2 and MI overall, variance weighted sensitivities for $QoI_{T_{tr_N}}$.

A.2.14 Quantity of Interest: Molecular Oxygen Translational Temperature

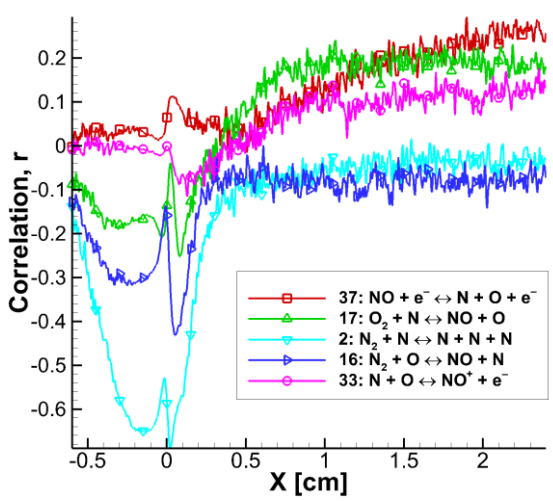

Figure A.40 Pearson correlation coefficient of the five most sensitive reaction rates when the molecular oxygen translational temperature is the QoI ($QoI_{T_{tr_{O_2}}}$).

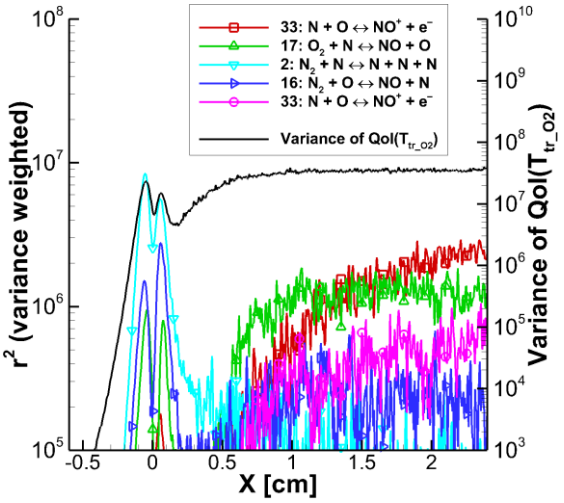

Figure A.41 Variance weighted r^2 sensitivities of the five most sensitive reaction rates for $QoI_{T_{tr_{O_2}}}$, and the variance at each $x-$location.

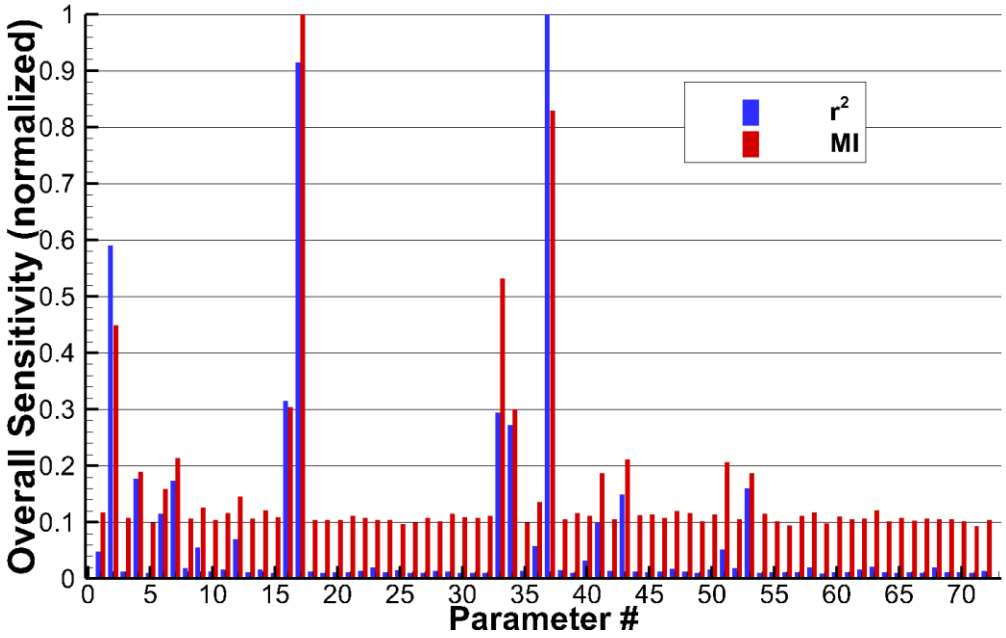

Figure A.42 Normalized r^2 and MI overall, variance weighted sensitivities for $QoI_{T_{tr_{O_2}}}$.

A.2.15 Quantity of Interest: Atomic Oxygen Translational Temperature

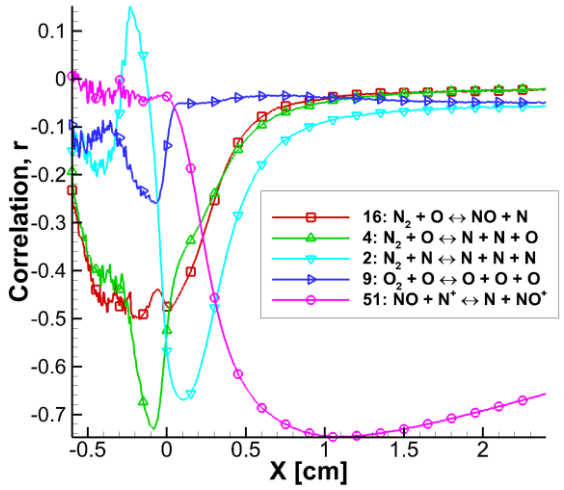

Figure A.43 Pearson correlation coefficient of the five most sensitive reaction rates when the atomic oxygen translational temperature is the QoI ($QoI_{T_{tr_O}}$).

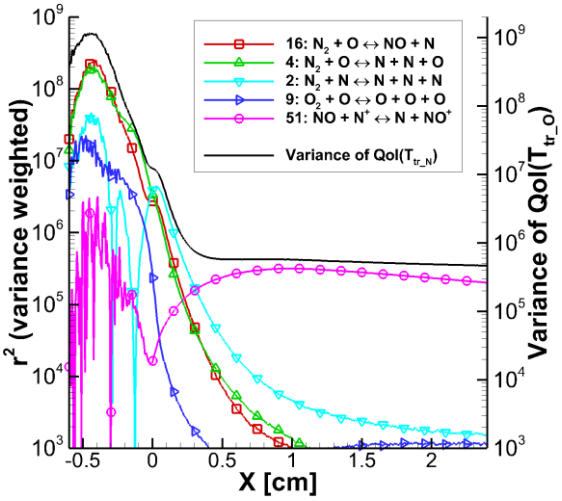

Figure A.44 Variance weighted r^2 sensitivities of the five most sensitive reaction rates for $QoI_{T_{tr_O}}$, and the variance at each x −location.

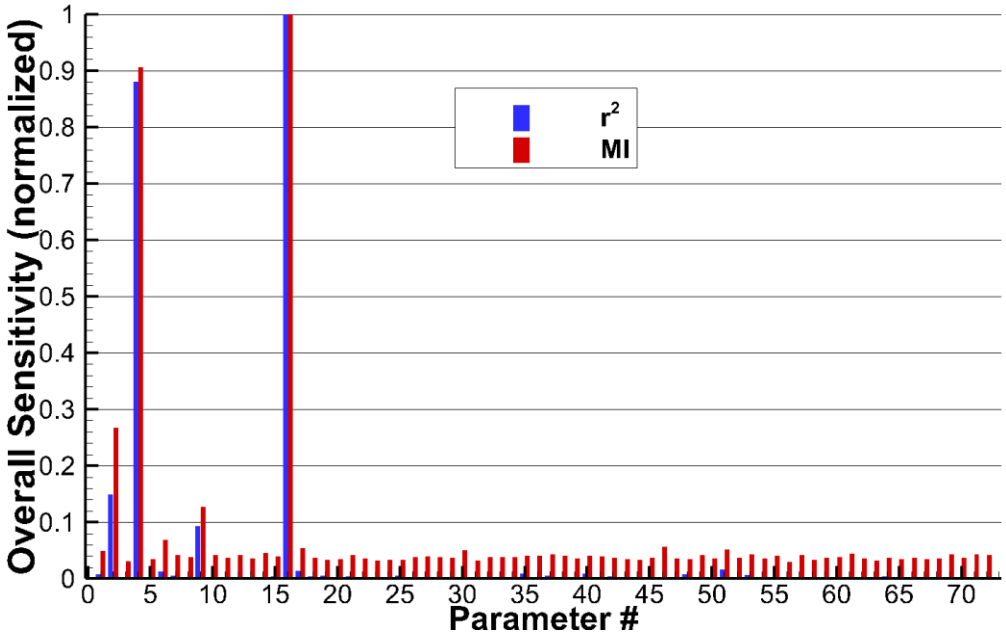

Figure A.45 Normalized r^2 and MI overall, variance weighted sensitivities for $QoI_{T_{tr_O}}$.

A.2.16 Quantity of Interest: Nitric Oxide Translational Temperature

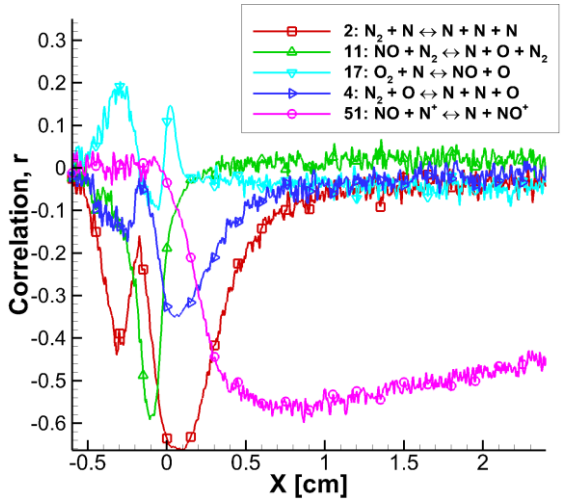

Figure A.46 Pearson correlation coefficient of the five most sensitive reaction rates when the nitric oxide translational temperature is the QoI ($QoI_{T_{tr_{NO}}}$).

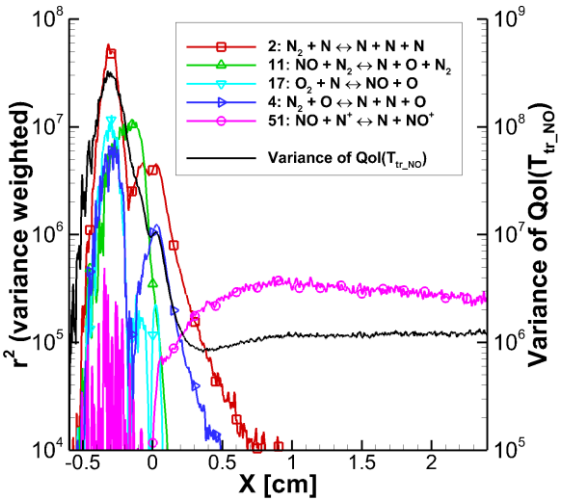

Figure A.47 Variance weighted r^2 sensitivities of the five most sensitive reaction rates for $QoI_{T_{tr_{NO}}}$, and the variance at each $x-$location.

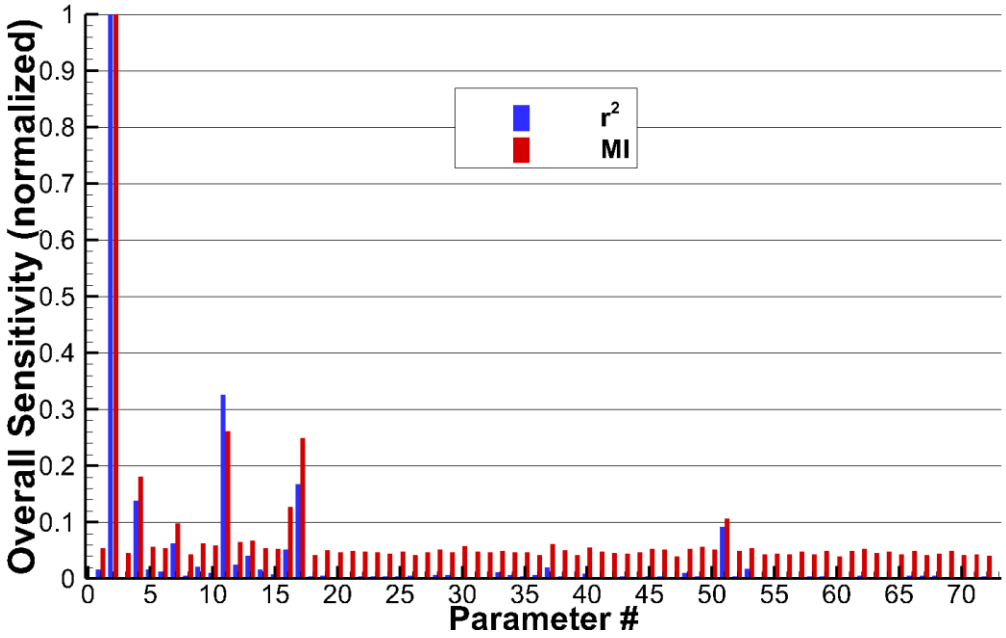

Figure A.48 Normalized r^2 and MI overall, variance weighted sensitivities for $QoI_{T_{tr_{NO}}}$.

A.2.17 Quantity of Interest: Molecular Nitrogen Ion Translational Temperature

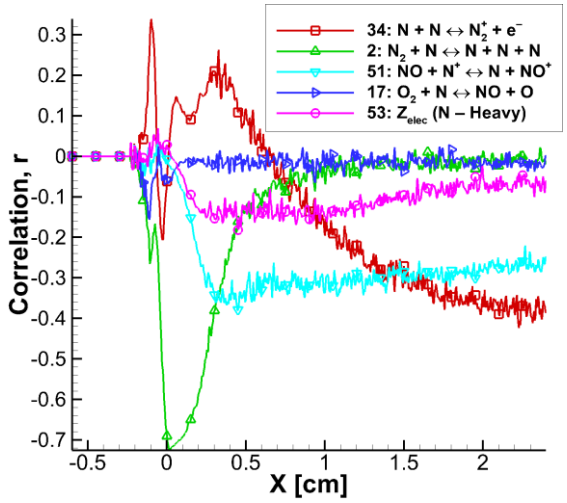

Figure A.49 Pearson correlation coefficient of the five most sensitive reaction rates when the molecular nitrogen ion translational temperature is the QoI ($QoI_{T_{tr_{N2+}}}$).

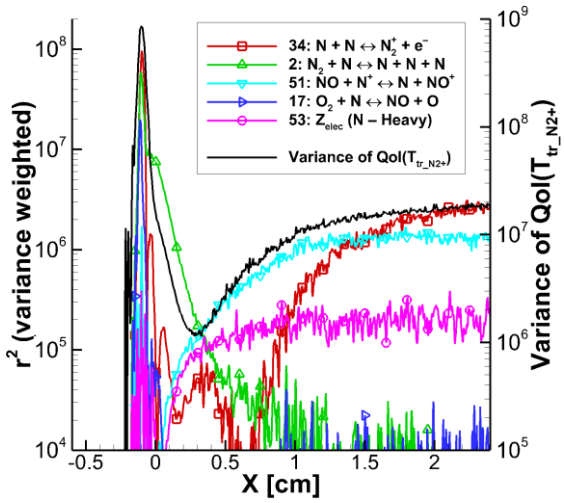

Figure A.50 Variance weighted r^2 sensitivities of the five most sensitive reaction rates for $QoI_{T_{tr_{N2+}}}$, and the variance at each x −location.

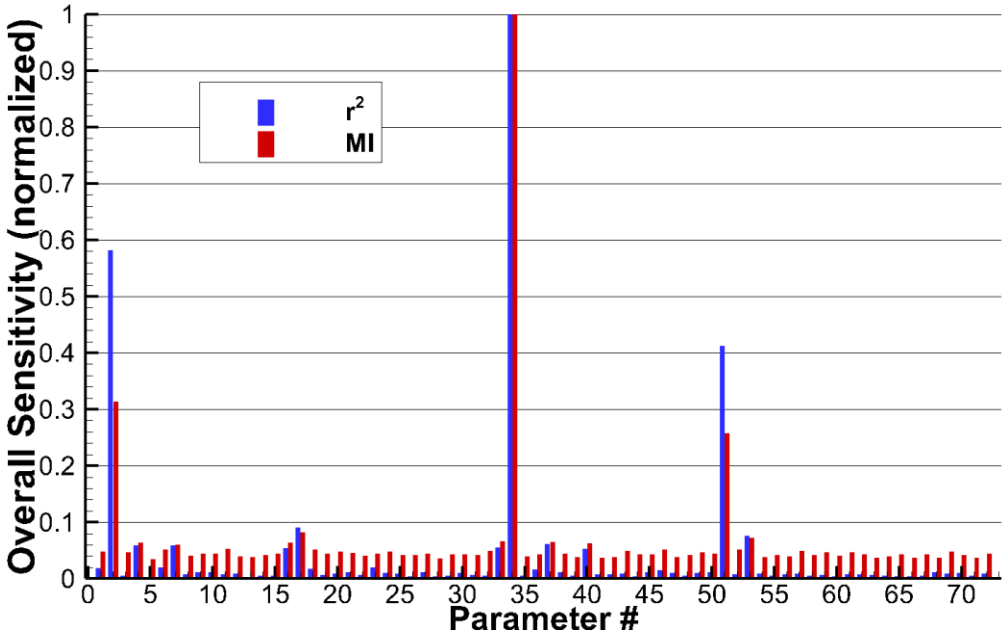

Figure A.51 Normalized r^2 and MI overall, variance weighted sensitivities for $QoI_{T_{tr_{N2+}}}$.

A.2.18 Quantity of Interest: Atomic Nitrogen Ion Translational Temperature

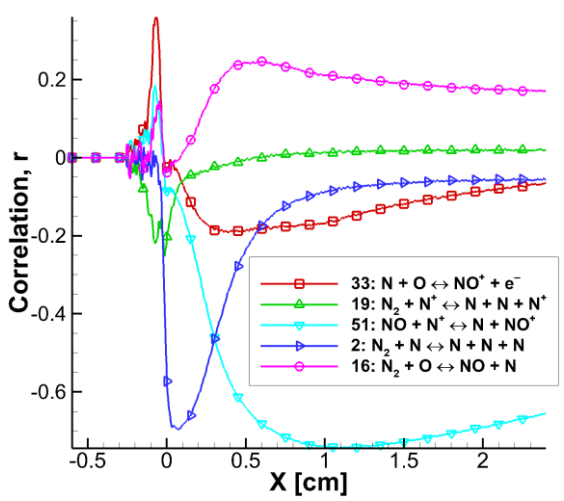

Figure A.52 Pearson correlation coefficient of the five most sensitive reaction rates when the atomic nitrogen ion translational temperature is the QoI ($QoI_{T_{tr_{N^+}}}$).

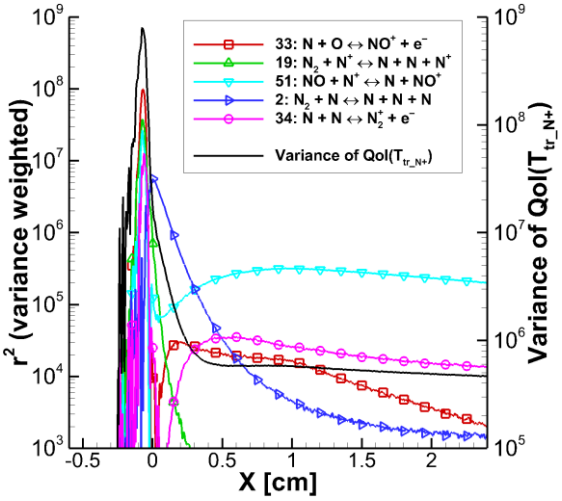

Figure A.53 Variance weighted r^2 sensitivities of the five most sensitive reaction rates for $QoI_{T_{tr_{N^+}}}$, and the variance at each x −location.

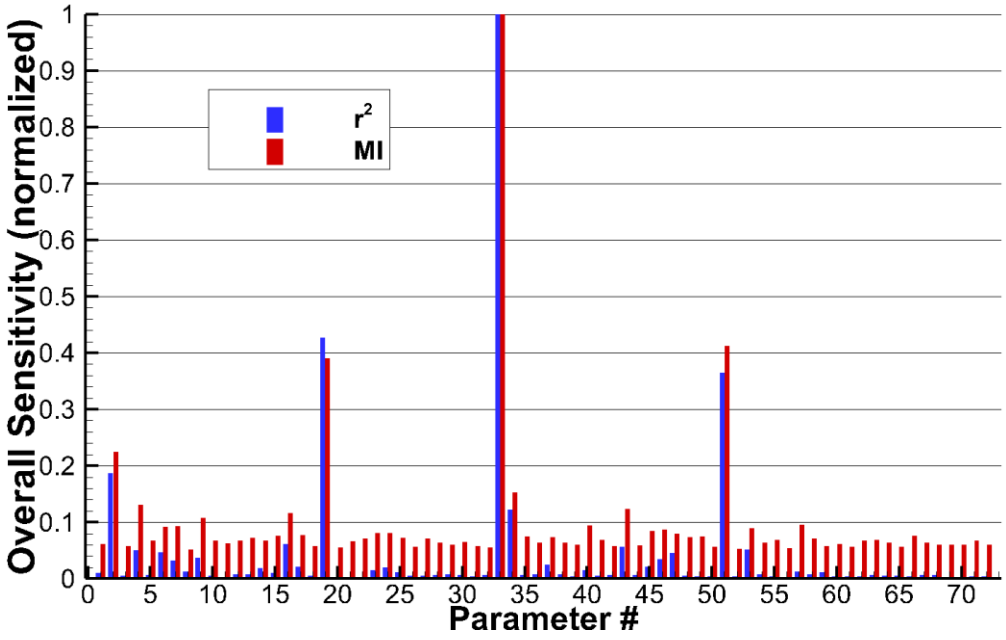

Figure A.54 Normalized r^2 and MI overall, variance weighted sensitivities for $QoI_{T_{tr_{N^+}}}$.

A.2.19 Quantity of Interest: Molecular Oxygen Ion Translational Temperature

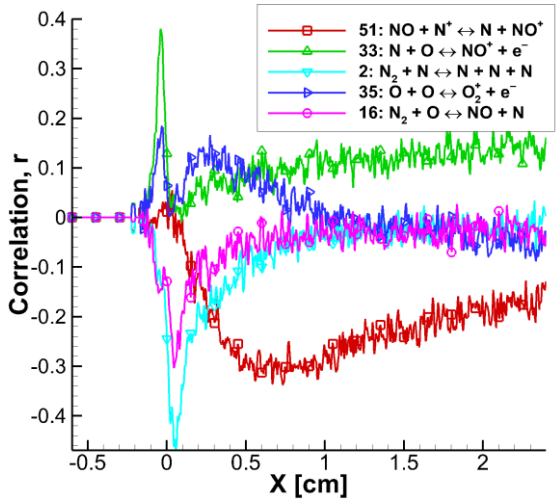

Figure A.55 Pearson correlation coefficient of the five most sensitive reaction rates when the molecular oxygen ion translational temperature is the QoI ($QoI_{T_{tr_{O2+}}}$).

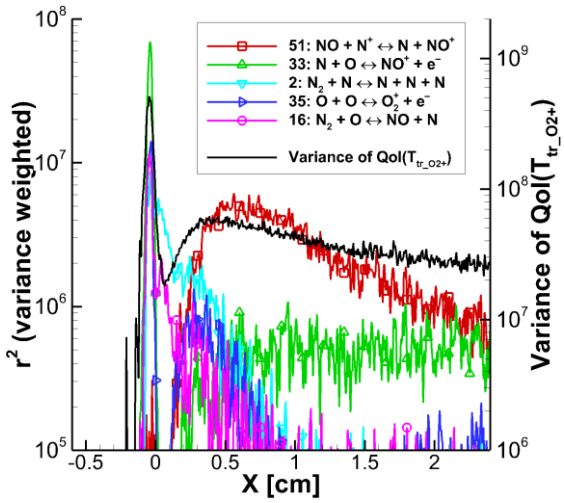

Figure A.56 Variance weighted r^2 sensitivities of the five most sensitive reaction rates for $QoI_{T_{tr_{O2+}}}$, and the variance at each x −location.

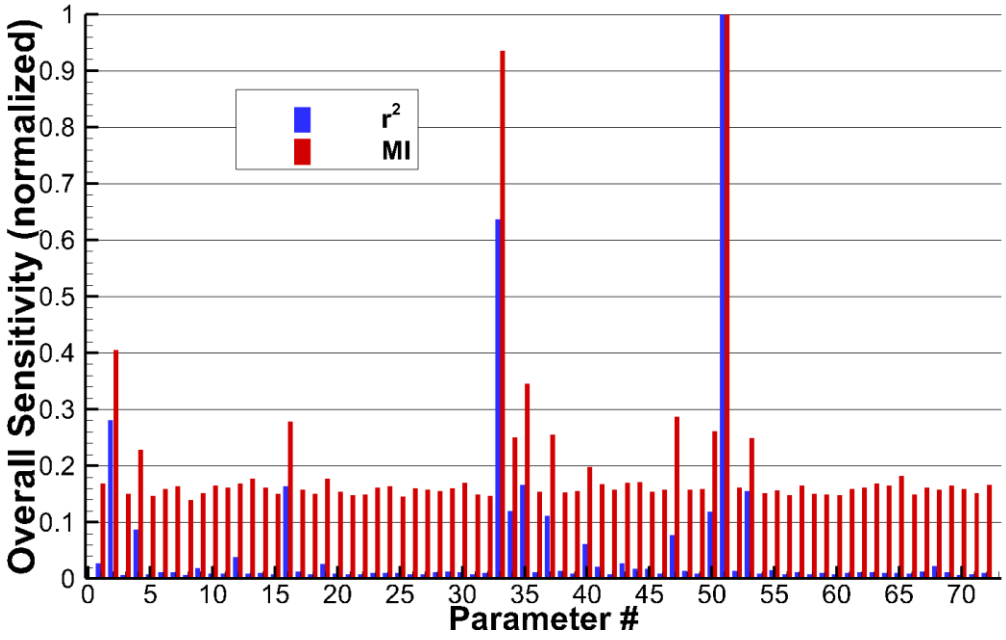

Figure A.57 Normalized r^2 and MI overall, variance weighted sensitivities for $QoI_{T_{tr_{O2+}}}$.

A.2.20 Quantity of Interest: Atomic Oxygen Ion Translational Temperature

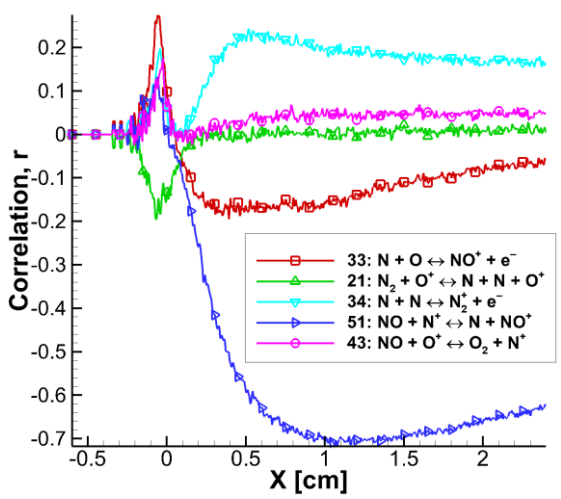

Figure A.58 Pearson correlation coefficient of the five most sensitive reaction rates when the atomic oxygen ion translational temperature is the QoI ($QoI_{T_{tr_{O^+}}}$).

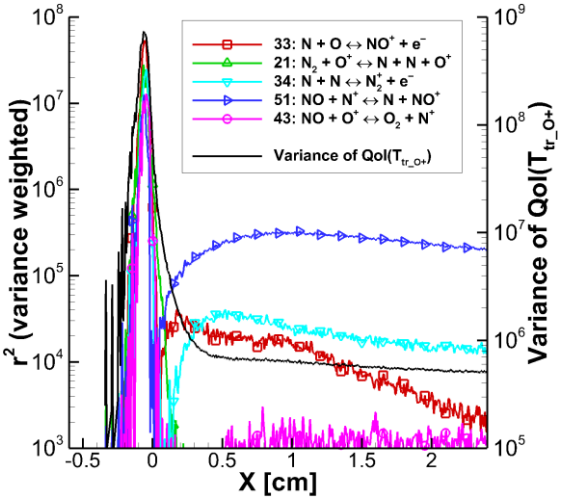

Figure A.59 Variance weighted r^2 sensitivities of the five most sensitive reaction rates for $QoI_{T_{tr_{O^+}}}$, and the variance at each x −location.

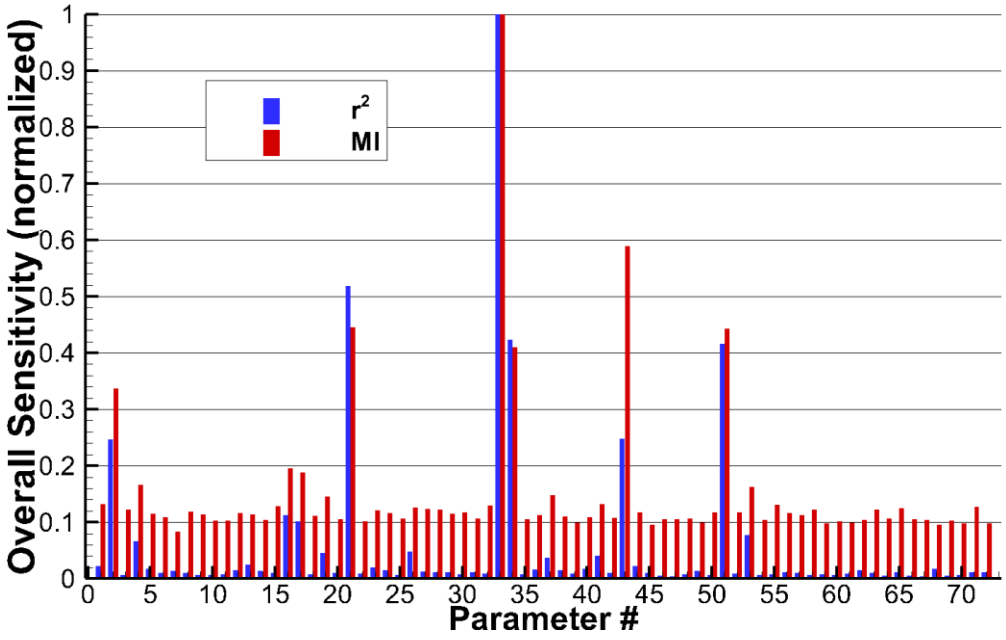

Figure A.60 Normalized r^2 and MI overall, variance weighted sensitivities for $QoI_{T_{tr_{O^+}}}$.

A.2.21 Quantity of Interest: Nitric Oxide Ion Translational Temperature

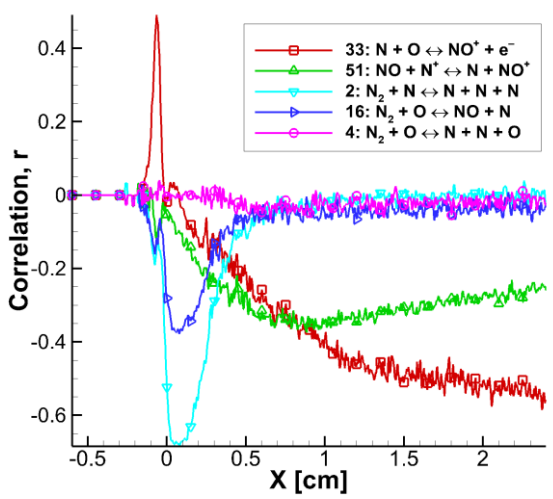

Figure A.61 Pearson correlation coefficient of the five most sensitive reaction rates when the nitric oxide ion translational temperature is the QoI ($QoI_{T_{tr_{NO^+}}}$).

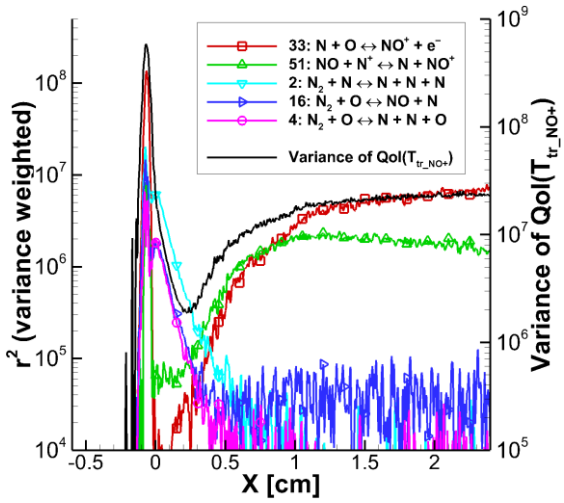

Figure A.62 Variance weighted r^2 sensitivities of the five most sensitive reaction rates for $QoI_{T_{tr_{NO^+}}}$, and the variance at each $x-$location.

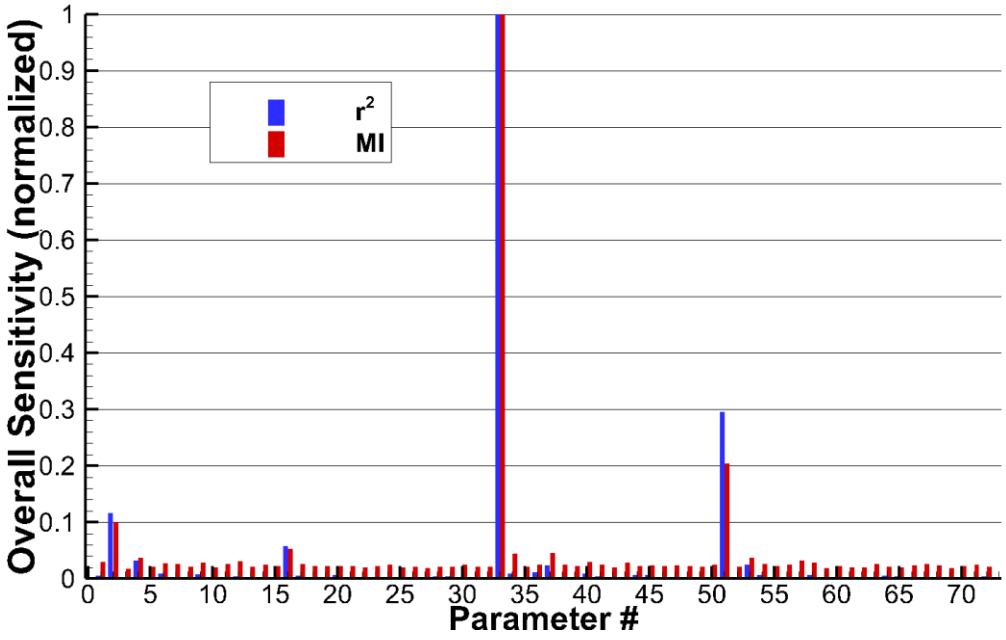

Figure A.63 Normalized r^2 and MI overall, variance weighted sensitivities for $QoI_{T_{tr_{NO^+}}}$.

A.2.22 Quantity of Interest: Free Electron Temperature

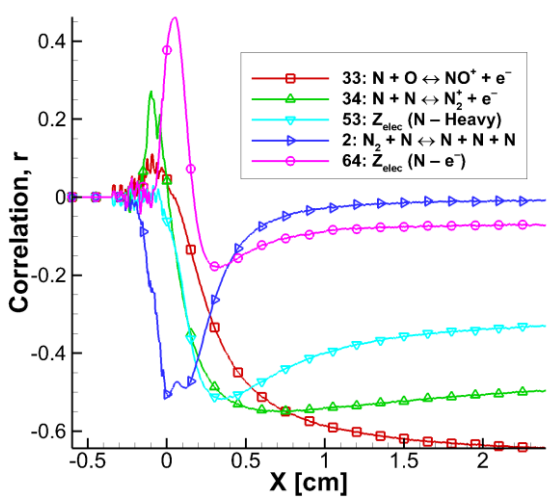

Figure A.64 Pearson correlation coefficient of the five most sensitive reaction rates when the free electron temperature is the QoI ($QoI_{T_{e^-}}$).

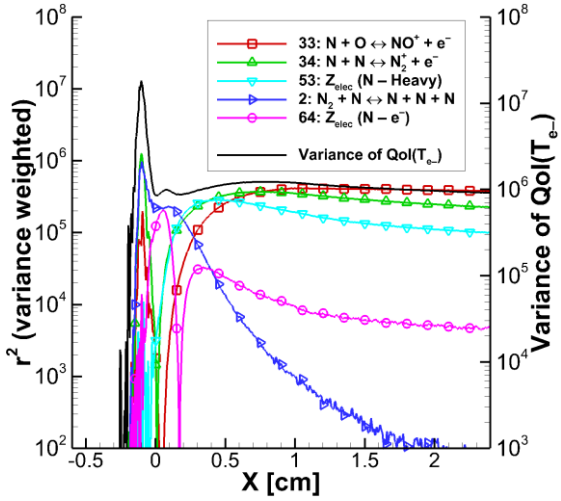

Figure A.65 Variance weighted r^2 sensitivities of the five most sensitive reaction rates for $QoI_{T_{e^-}}$, and the variance at each x −location.

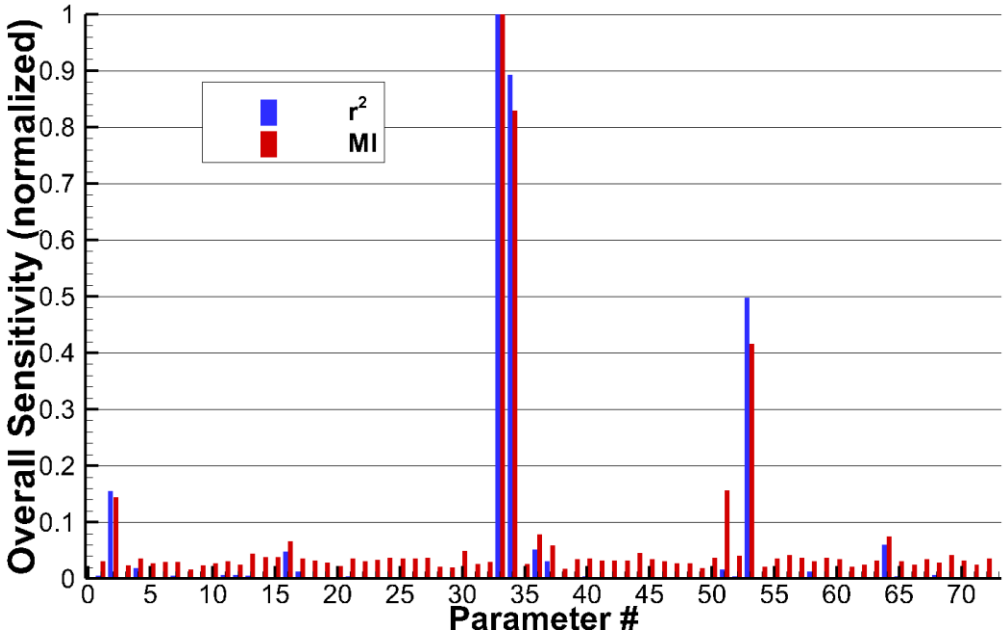

Figure A.66 Normalized r^2 and MI overall, variance weighted sensitivities for $QoI_{T_{e^-}}$.

A.2.23 Quantity of Interest: Mixture Rotational Temperature

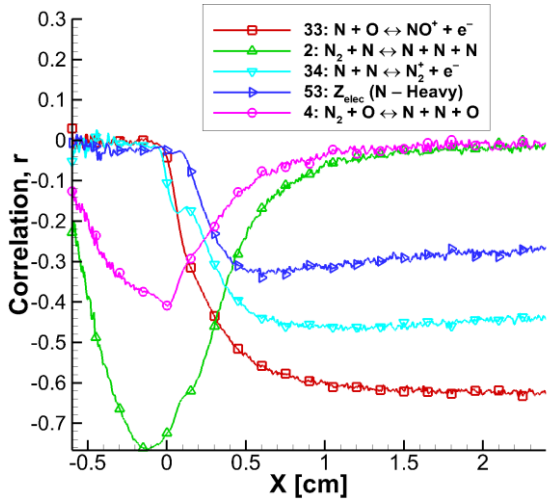

Figure A.67 Pearson correlation coefficient of the five most sensitive reaction rates when the mixture rotational temperature is the QoI ($QoI_{T_{rot}}$).

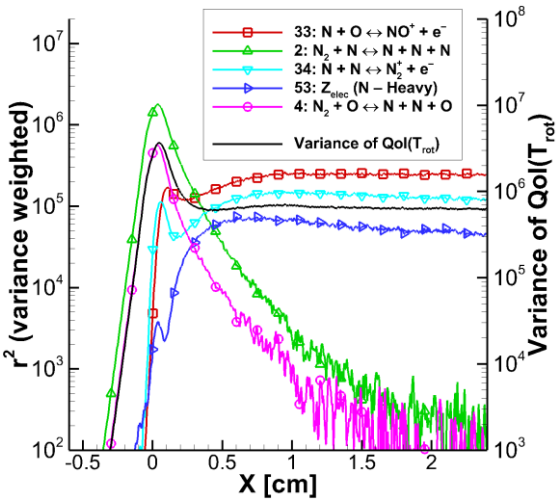

Figure A.68 Variance weighted r^2 sensitivities of the five most sensitive reaction rates for $QoI_{T_{rot}}$, and the variance at each x −location.

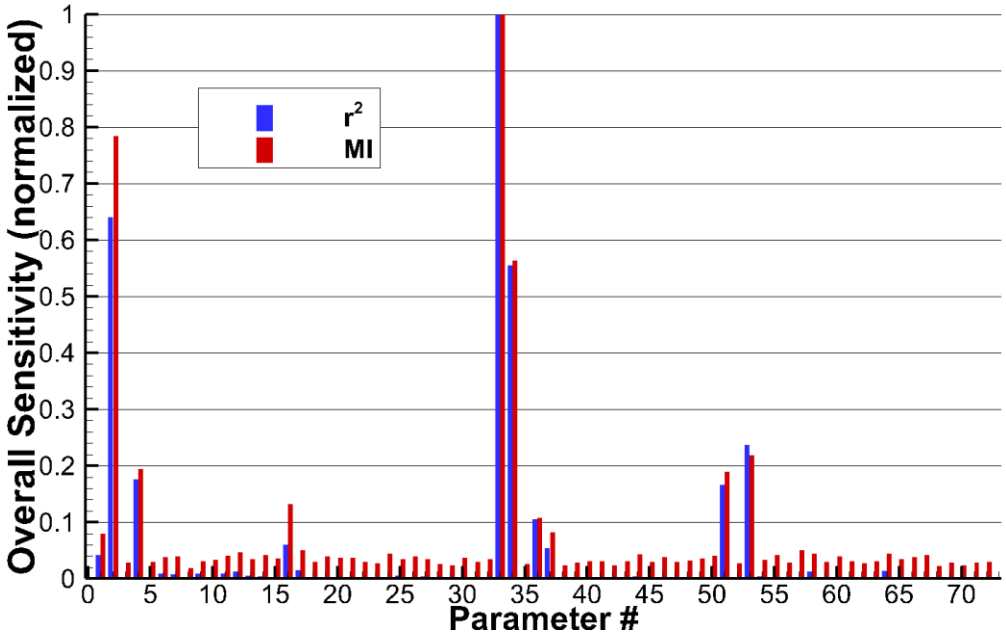

Figure A.69 Normalized r^2 and MI overall, variance weighted sensitivities for $QoI_{T_{rot}}$.

A.2.24 Quantity of Interest: Molecular Nitrogen Rotational Temperature

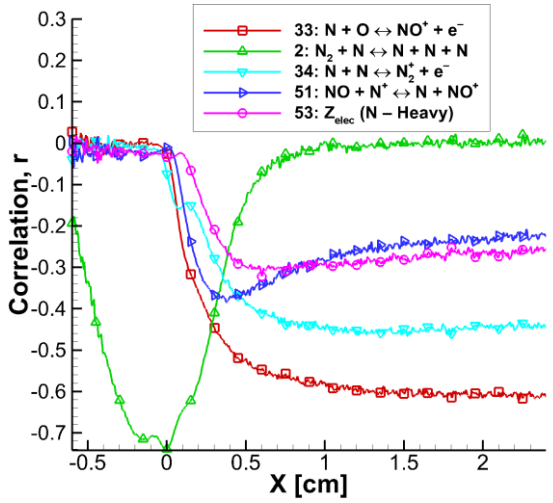

Figure A.70 Pearson correlation coefficient of the five most sensitive reaction rates when the molecular nitrogen rotational temperature is the QoI ($QoI_{T_{rot_{N2}}}$).

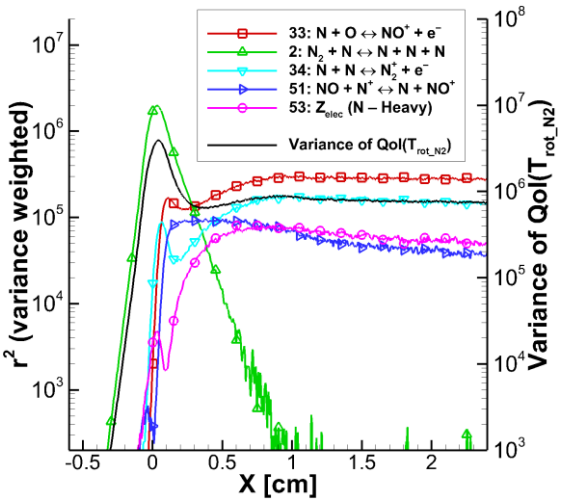

Figure A.71 Variance weighted r^2 sensitivities of the five most sensitive reaction rates for $QoI_{T_{rot_{N2}}}$, and the variance at each x −location.

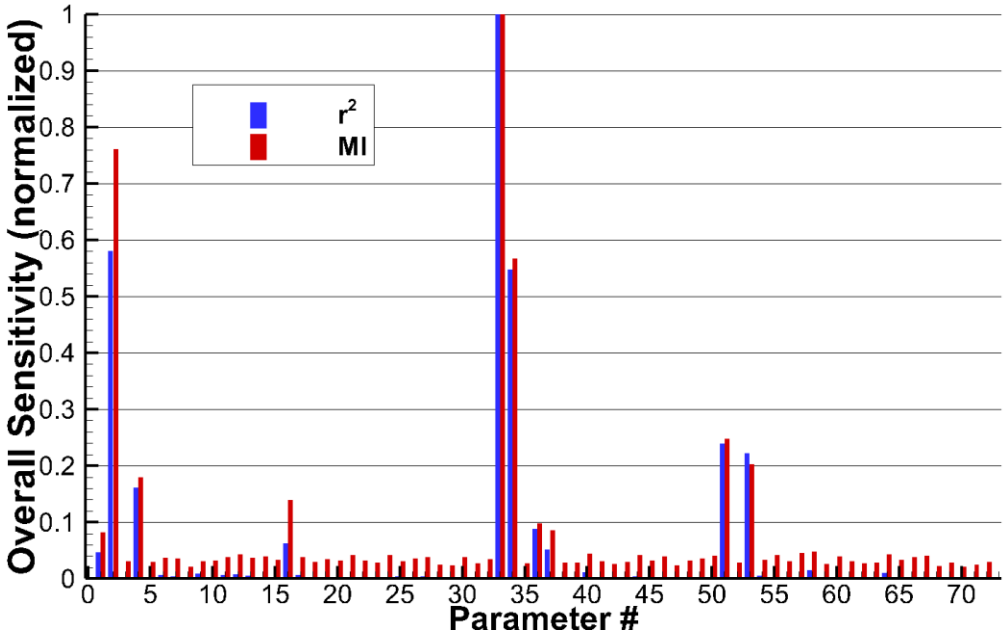

Figure A.72 Normalized r^2 and MI overall, variance weighted sensitivities for $QoI_{T_{rot_{N2}}}$.

A.2.25 Quantity of Interest: Molecular Oxygen Rotational Temperature

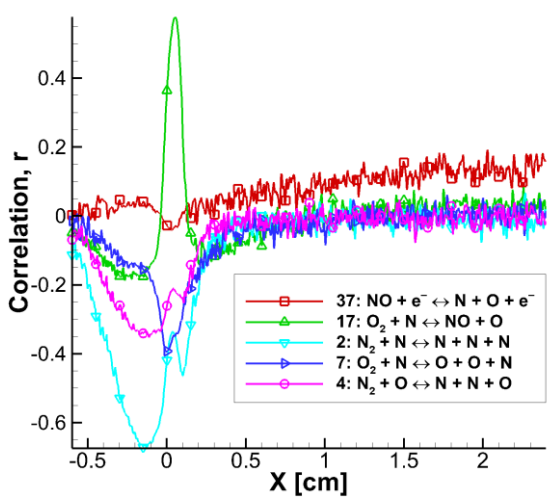

Figure A.73 Pearson correlation coefficient of the five most sensitive reaction rates when the molecular oxygen rotational temperature is the QoI ($QoI_{T_{rot_{O2}}}$).

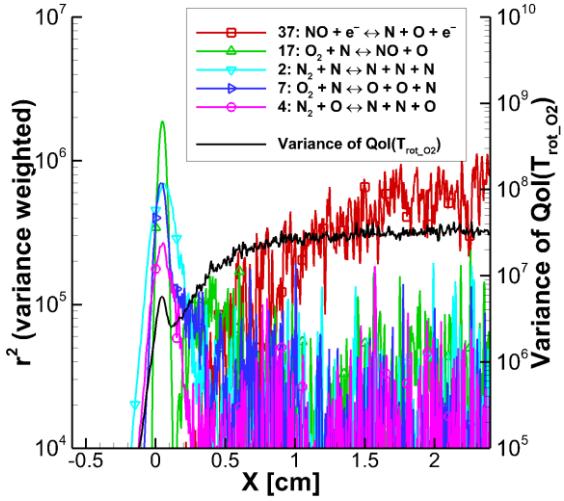

Figure A.74 Variance weighted r^2 sensitivities of the five most sensitive reaction rates for $QoI_{T_{rot_{O2}}}$, and the variance at each x −location.

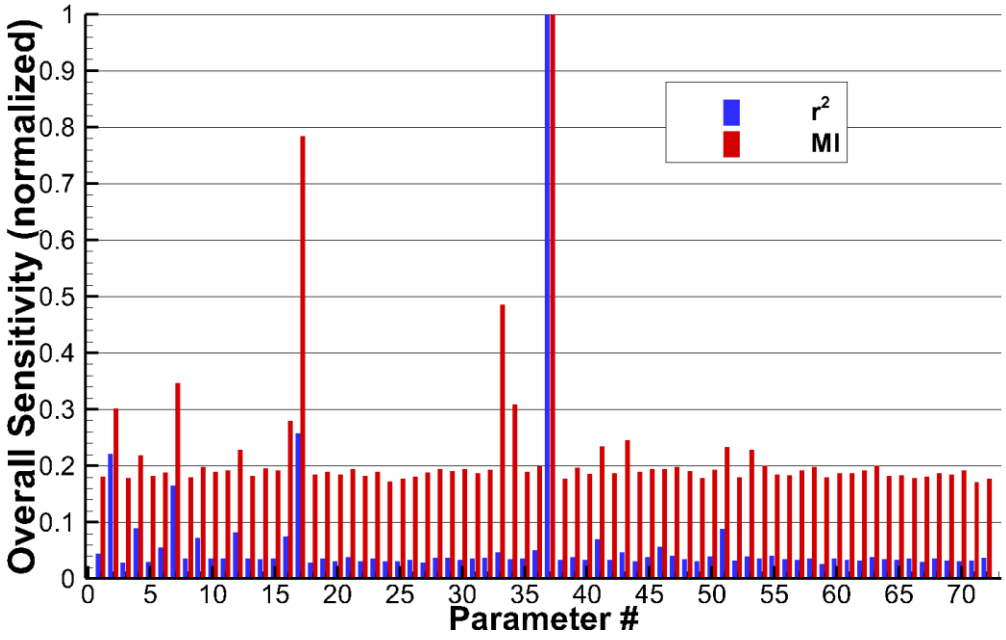

Figure A.75 Normalized r^2 and MI overall, variance weighted sensitivities for $QoI_{T_{rot_{O2}}}$.

A.2.26 Quantity of Interest: Nitric Oxide Rotational Temperature

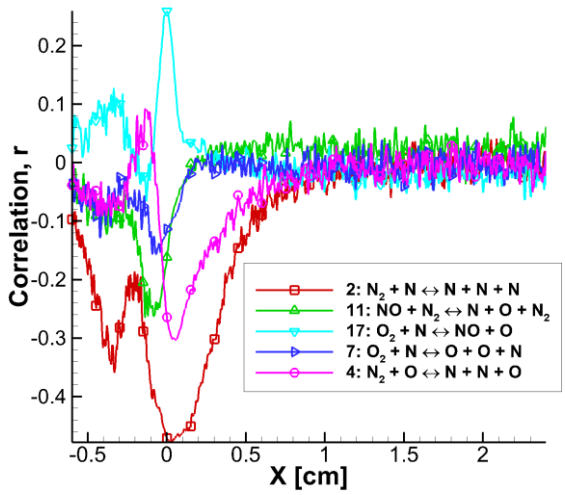

Figure A.76 Pearson correlation coefficient of the five most sensitive reaction rates when the nitric oxide rotational temperature is the QoI ($QoI_{T_{rot_{NO}}}$).

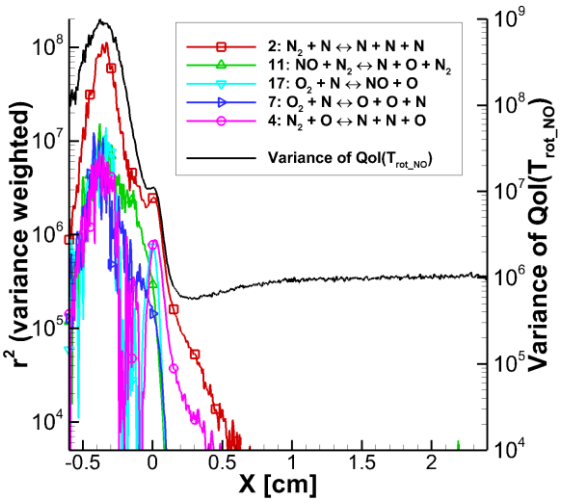

Figure A.77 Variance weighted r^2 sensitivities of the five most sensitive reaction rates for $QoI_{T_{rot_{NO}}}$, and the variance at each x −location.

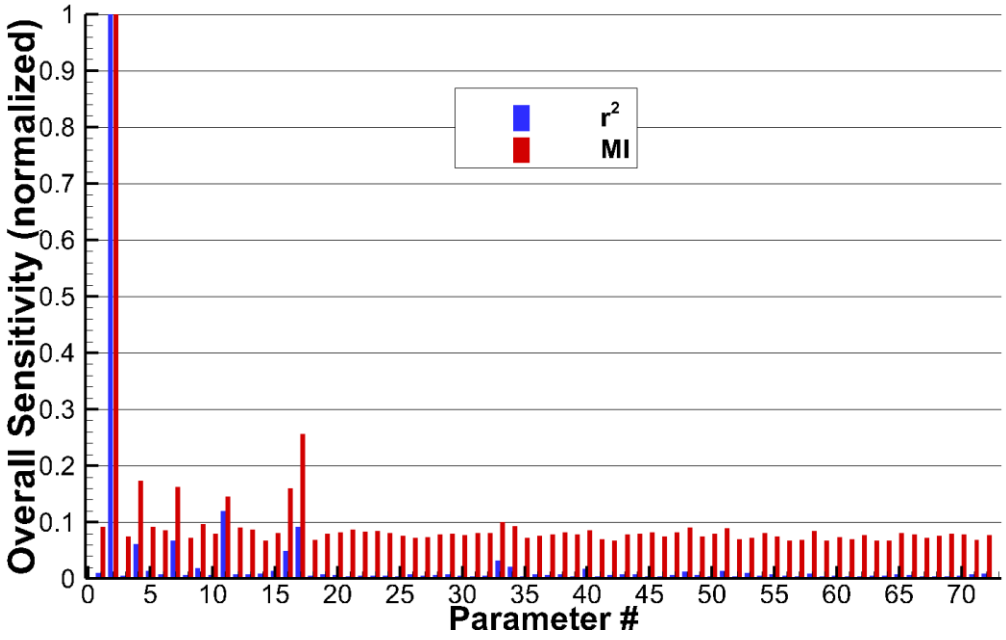

Figure A.78 Normalized r^2 and MI overall, variance weighted sensitivities for $QoI_{T_{rot_{NO}}}$.

A.2.27 Quantity of Interest: Molecular Nitrogen Ion Rotational Temperature

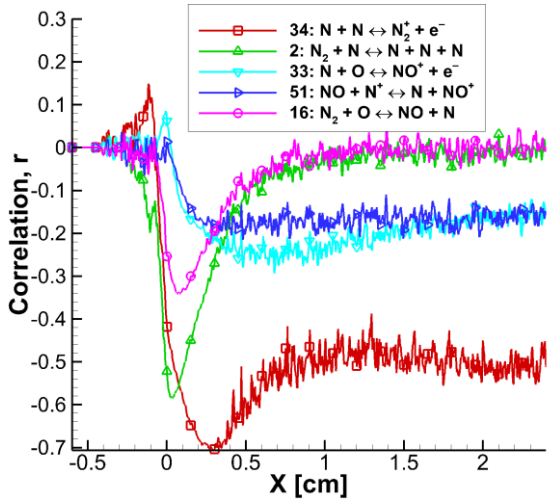

Figure A.79 Pearson correlation coefficient of the five most sensitive reaction rates when the molecular nitrogen ion rotational temperature is the QoI ($QoI_{T_{rot_{N2+}}}$).

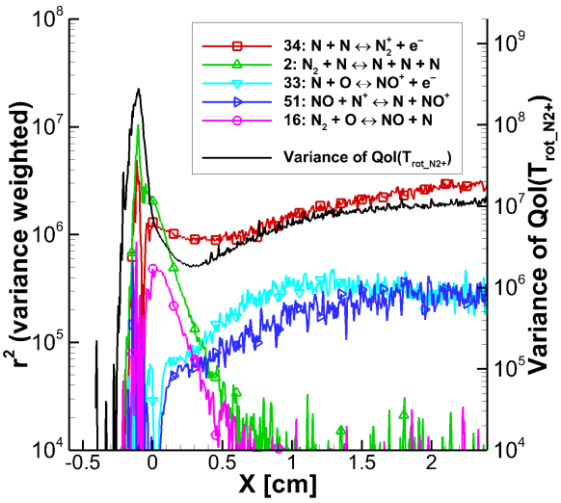

Figure A.80 Variance weighted r^2 sensitivities of the five most sensitive reaction rates for $QoI_{T_{rot_{N2+}}}$, and the variance at each x −location.

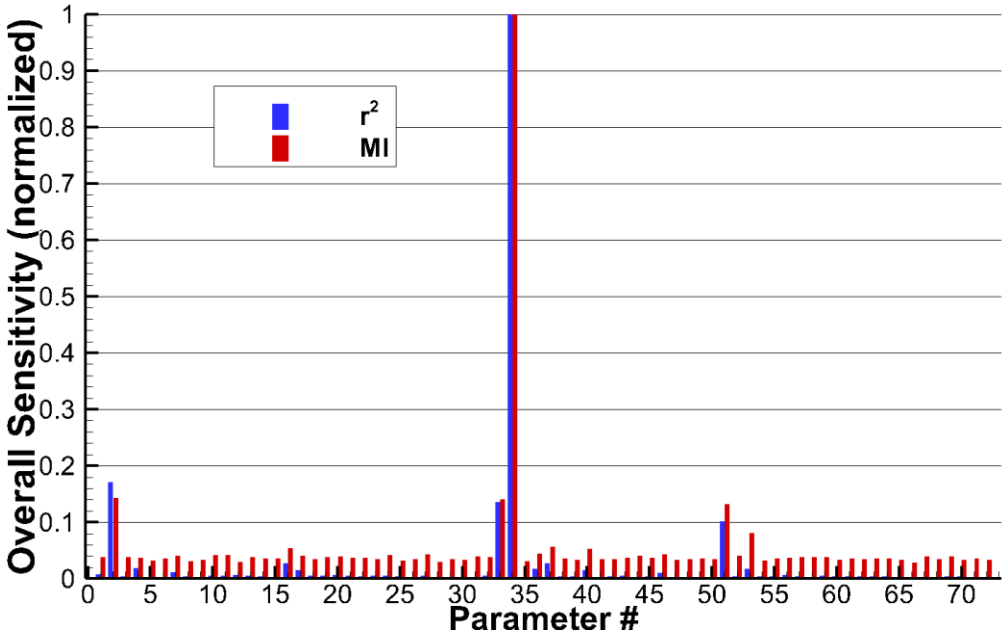

Figure A.81 Normalized r^2 and MI overall, variance weighted sensitivities for $QoI_{T_{rot_{N2+}}}$.

A.2.28 Quantity of Interest: Molecular Oxygen Ion Rotational Temperature

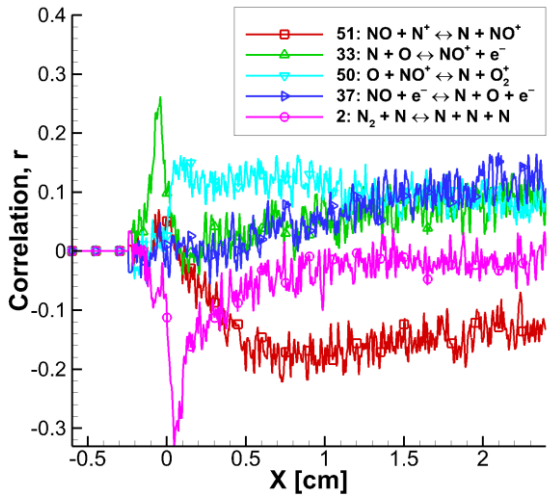

Figure A.82 Pearson correlation coefficient of the five most sensitive reaction rates when the molecular oxygen ion rotational temperature is the QoI ($QoI_{T_{rot_{O2+}}}$).

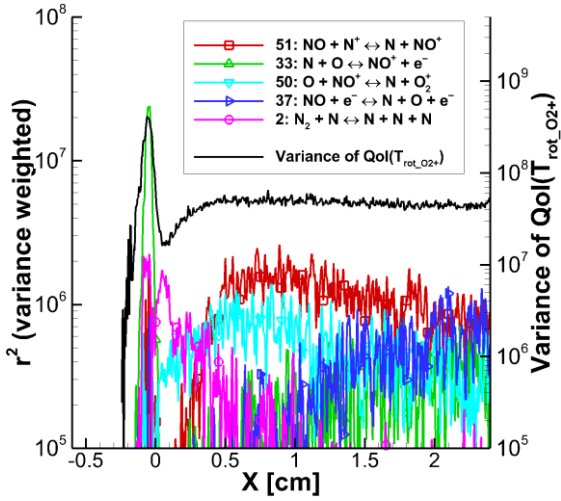

Figure A.83 Variance weighted r^2 sensitivities of the five most sensitive reaction rates for $QoI_{T_{rot_{O2+}}}$, and the variance at each x −location.

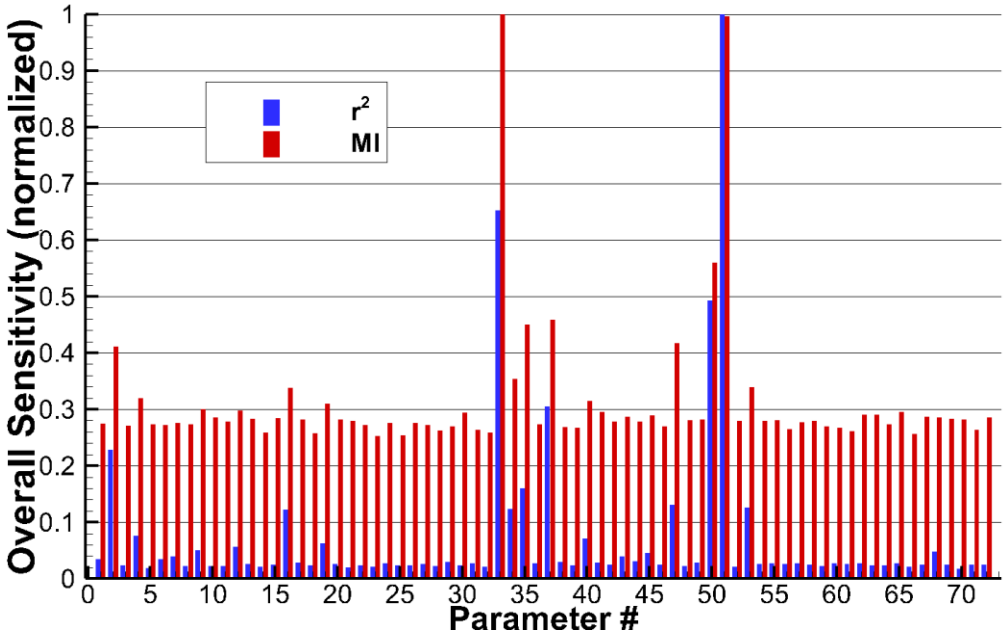

Figure A.84 Normalized r^2 and MI overall, variance weighted sensitivities for $QoI_{T_{rot_{O2+}}}$.

A.2.29 Quantity of Interest: Nitric Oxide Ion Rotational Temperature

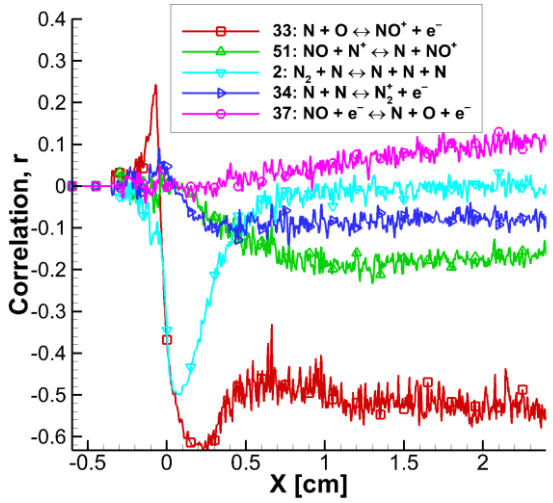

Figure A.85 Pearson correlation coefficient of the five most sensitive reaction rates when the nitric oxide ion rotational temperature is the QoI ($QoI_{T_{rot_{NO^+}}}$).

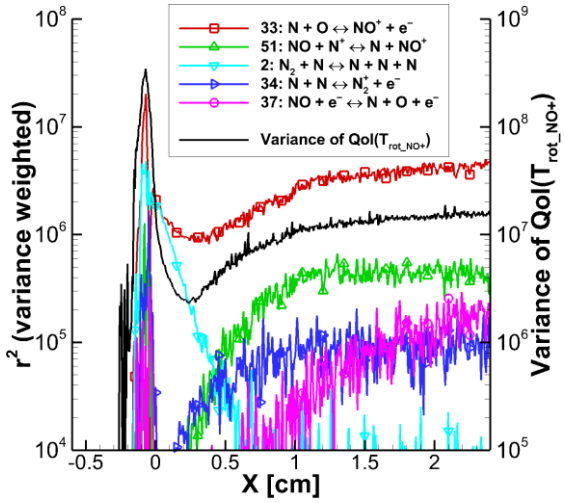

Figure A.86 Variance weighted r^2 sensitivities of the five most sensitive reaction rates for $QoI_{T_{rot_{NO^+}}}$, and the variance at each x −location.

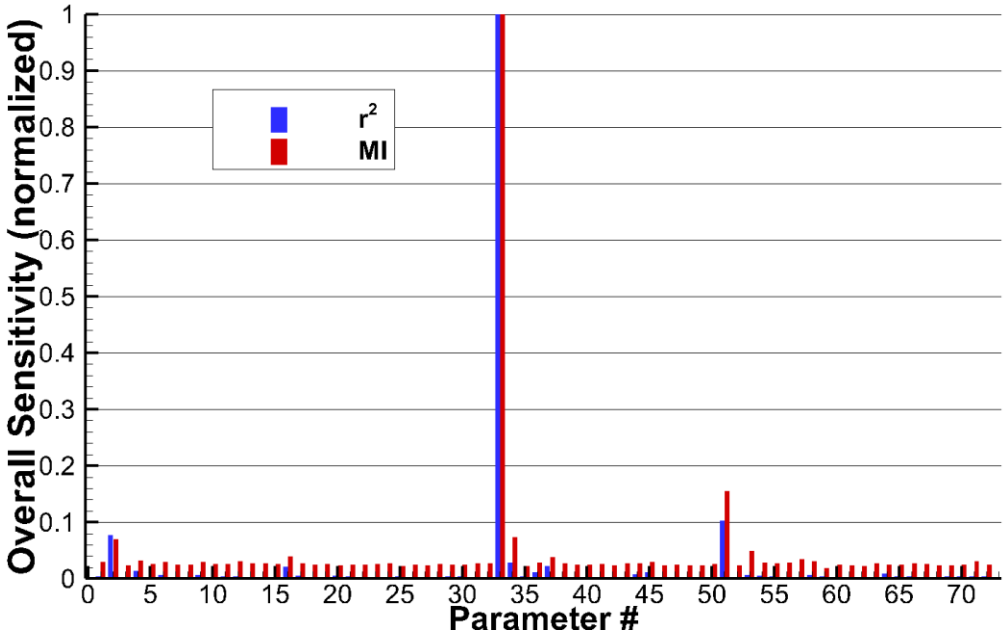

Figure A.87 Normalized r^2 and MI overall, variance weighted sensitivities for $QoI_{T_{rot_{NO^+}}}$.

A.2.30 Quantity of Interest: Mixture Vibrational Temperature

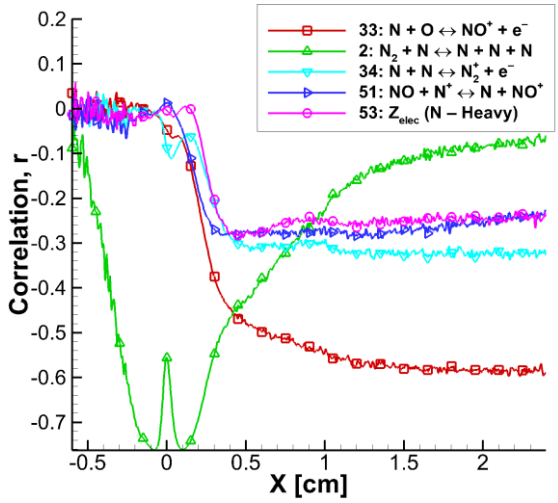

Figure A.88 Pearson correlation coefficient of the five most sensitive reaction rates when the mixture vibrational temperature is the QoI ($QoI_{T_{vib}}$).

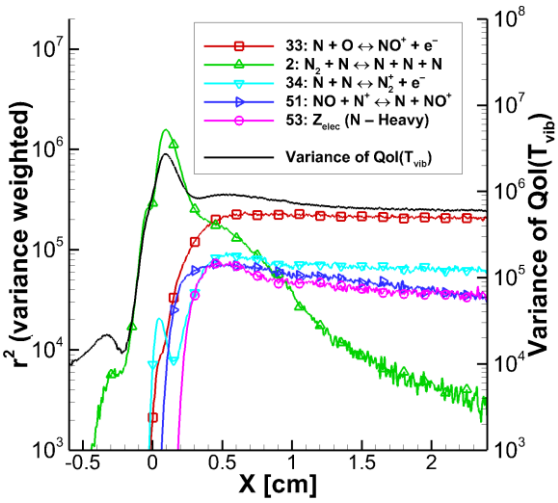

Figure A.89 Variance weighted r^2 sensitivities of the five most sensitive reaction rates for $QoI_{T_{vib}}$, and the variance at each x −location.

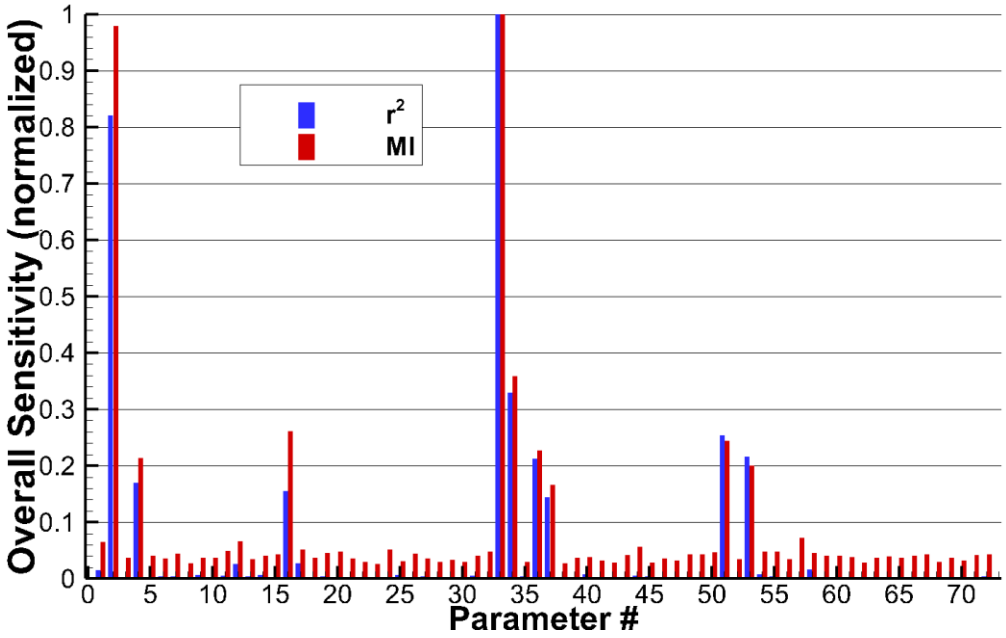

Figure A.90 Normalized r^2 and MI overall, variance weighted sensitivities for $QoI_{T_{vib}}$.

A.2.31 Quantity of Interest: Molecular Nitrogen Vibrational Temperature

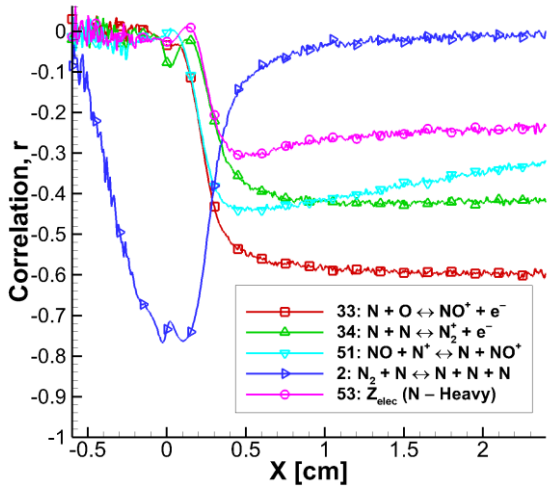

Figure A.91 Pearson correlation coefficient of the five most sensitive reaction rates when the molecular nitrogen vibrational temperature is the QoI ($QoI_{T_{vib_{N2}}}$).

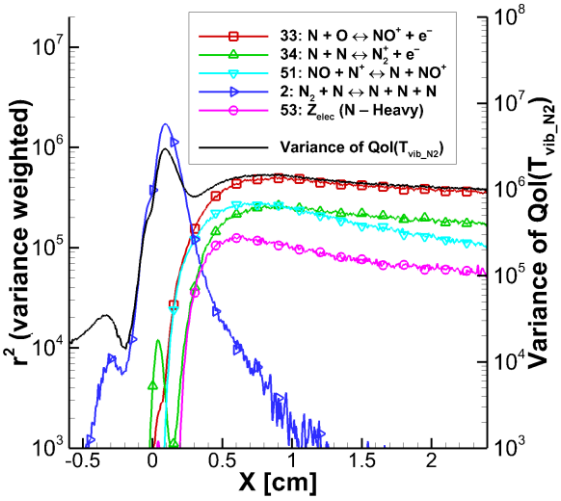

Figure A.92 Variance weighted r^2 sensitivities of the five most sensitive reaction rates for $QoI_{T_{vib_{N2}}}$, and the variance at each x −location.

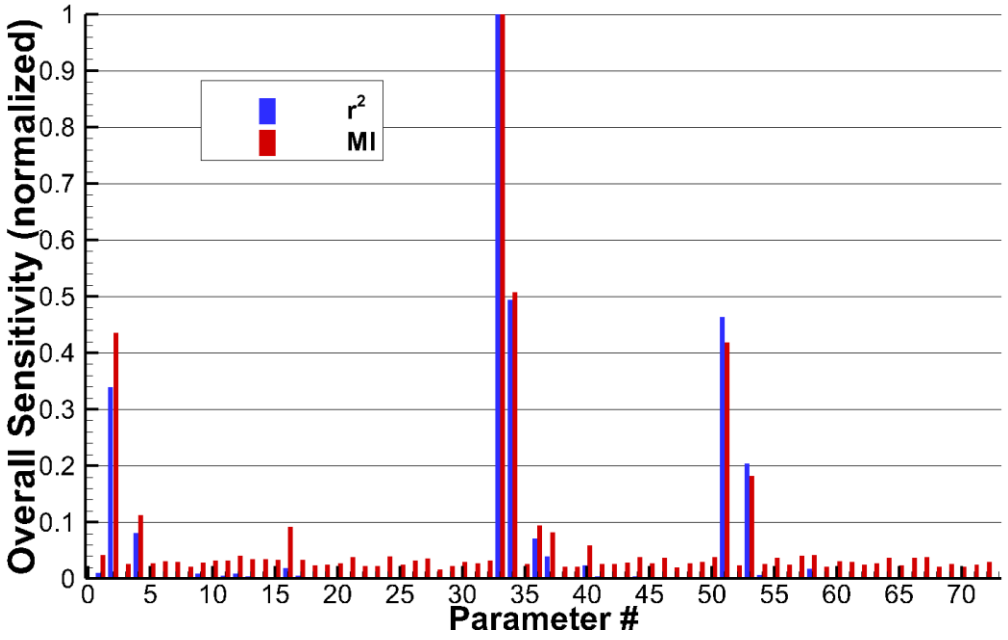

Figure A.93 Normalized r^2 and MI overall, variance weighted sensitivities for $QoI_{T_{vib_{N2}}}$.

A.2.32 Quantity of Interest: Molecular Oxygen Vibrational Temperature

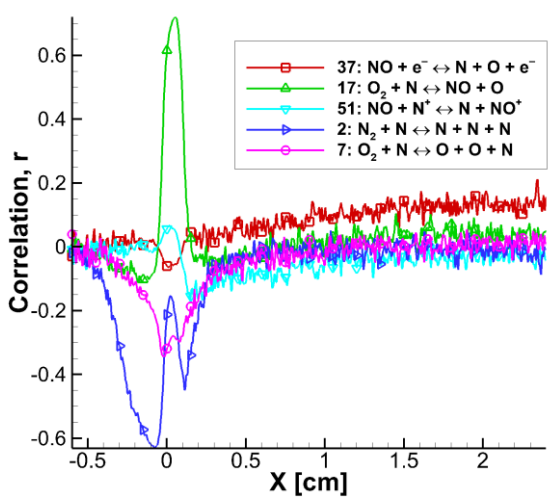

Figure A.94 Pearson correlation coefficient of the five most sensitive reaction rates when the molecular oxygen vibrational temperature is the QoI ($QoI_{T_{vib_{O2}}}$).

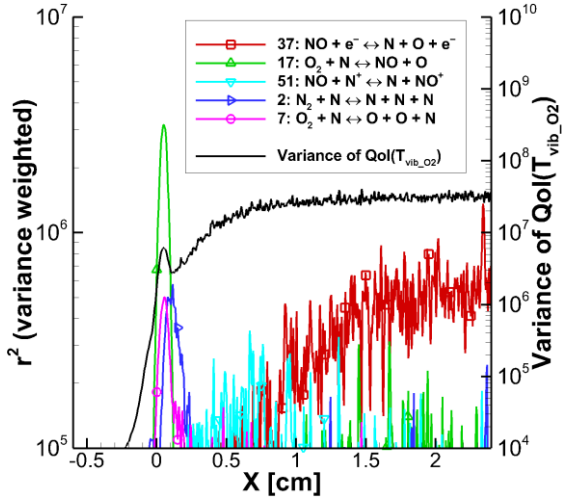

Figure A.95 Variance weighted r^2 sensitivities of the five most sensitive reaction rates for $QoI_{T_{vib_{O2}}}$, and the variance at each x −location.

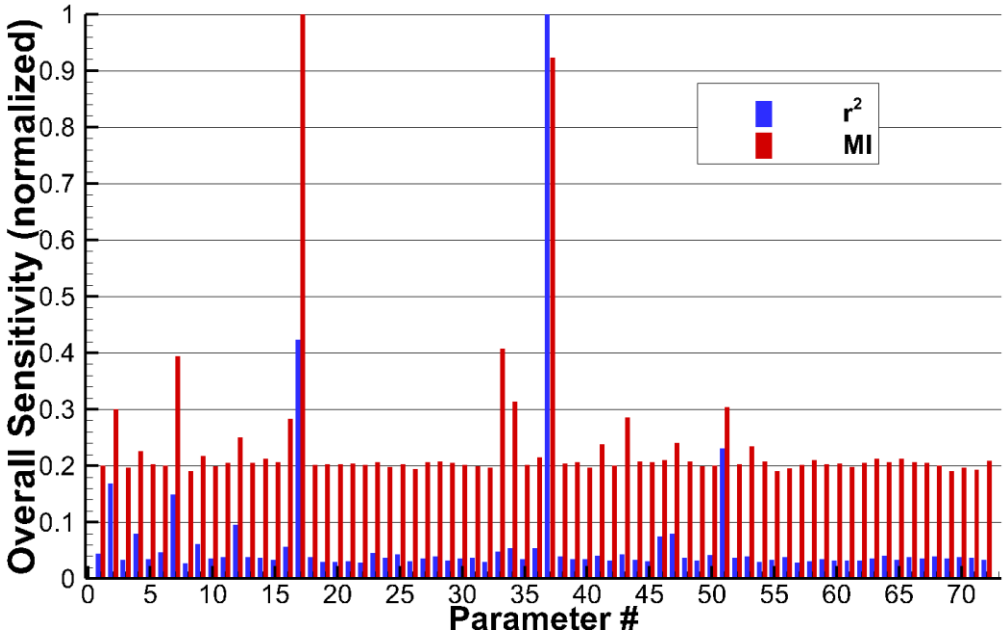

Figure A.96 Normalized r^2 and MI overall, variance weighted sensitivities for $QoI_{T_{vib_{O2}}}$.

A.2.33 Quantity of Interest: Nitric Oxide Vibrational Temperature

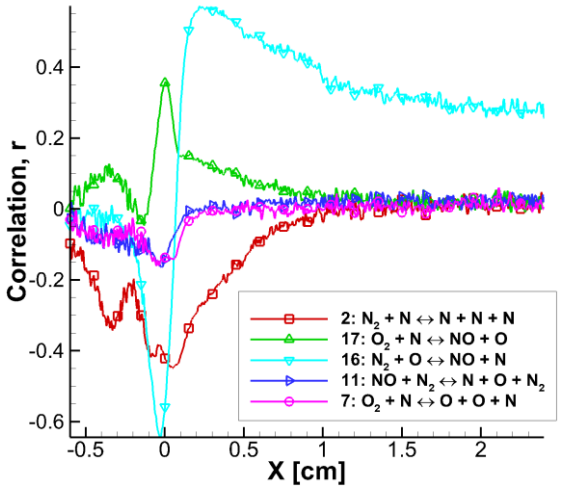

Figure A.97 Pearson correlation coefficient of the five most sensitive reaction rates when the nitric oxide vibrational temperature is the QoI ($QoI_{T_{vib_{NO}}}$).

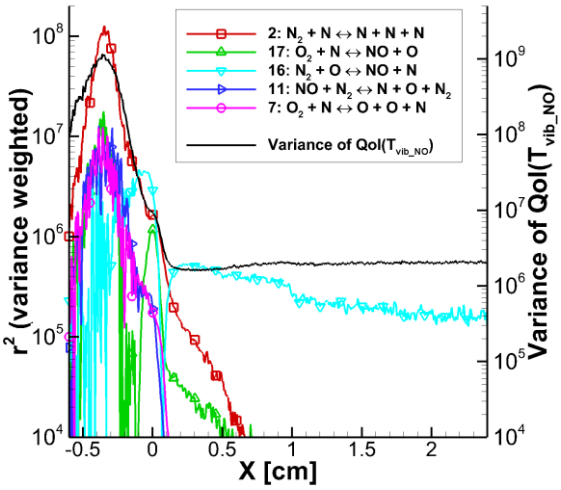

Figure A.98 Variance weighted r^2 sensitivities of the five most sensitive reaction rates for $QoI_{T_{vib_{NO}}}$, and the variance at each $x-$location.

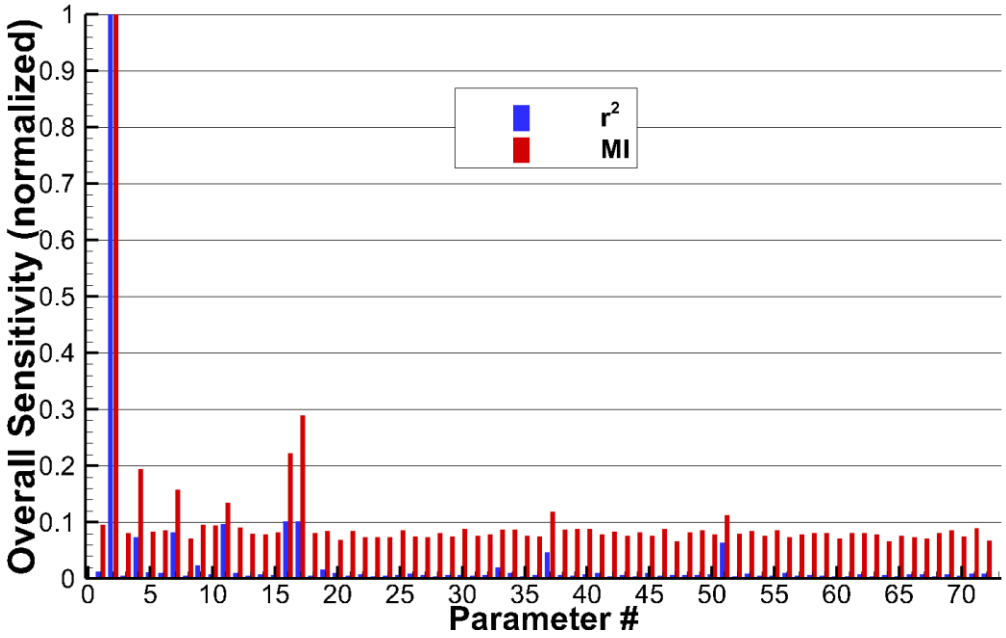

Figure A.99 Normalized r^2 and MI overall, variance weighted sensitivities for $QoI_{T_{vib_{NO}}}$.

A.2.34 Quantity of Interest: Molecular Nitrogen Ion Vibrational Temperature

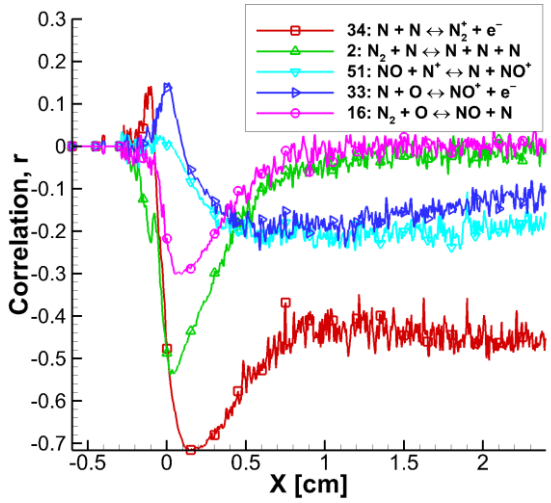

Figure A.100 Pearson correlation coefficient of the five most sensitive reaction rates when the molecular nitrogen ion vibrational temperature is the QoI ($QoI_{T_{vib_{N2+}}}$).

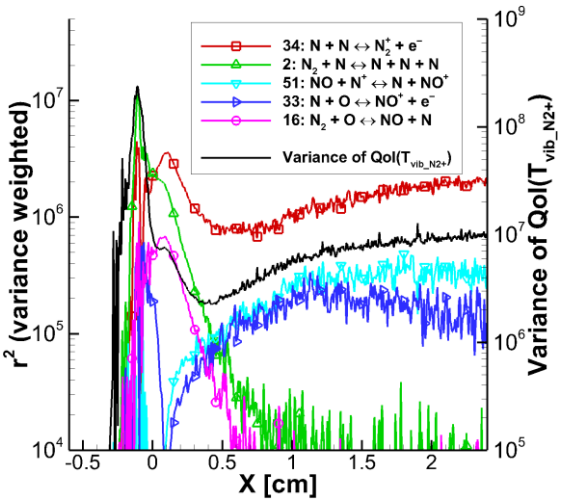

Figure A.101 Variance weighted r^2 sensitivities of the five most sensitive reaction rates for $QoI_{T_{vib_{N2+}}}$, and the variance at each x −location.

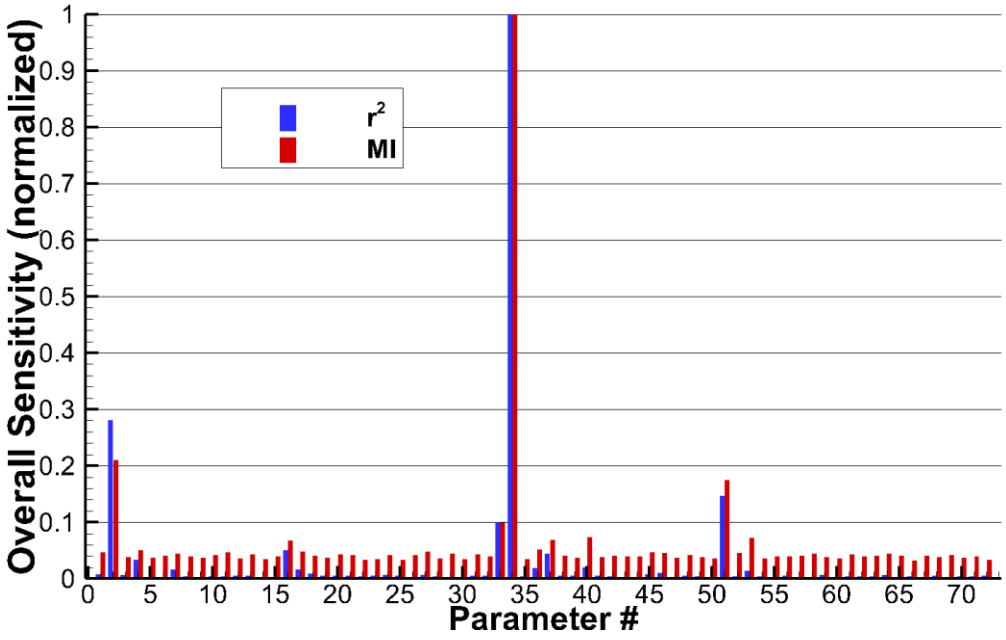

Figure A.102 Normalized r^2 and MI overall, variance weighted sensitivities for $QoI_{T_{vib_{N2+}}}$.

A.2.35 Quantity of Interest: Molecular Oxygen Ion Vibrational Temperature

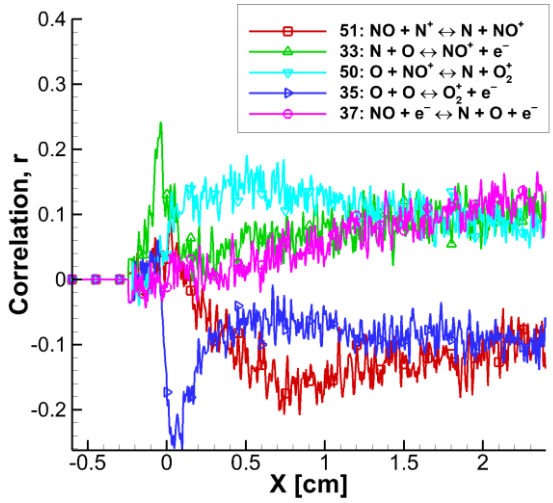

Figure A.103 Pearson correlation coefficient of the five most sensitive reaction rates when the molecular oxygen ion vibrational temperature is the QoI ($QoI_{T_{vib_{O2+}}}$).

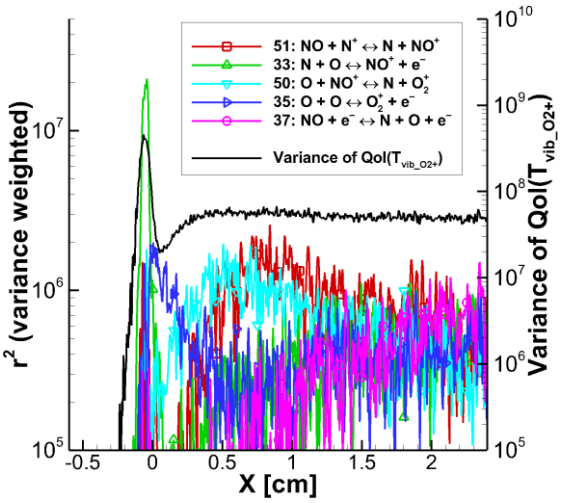

Figure A.104 Variance weighted r^2 sensitivities of the five most sensitive reaction rates for $QoI_{T_{vib_{O2+}}}$, and the variance at each x −location.

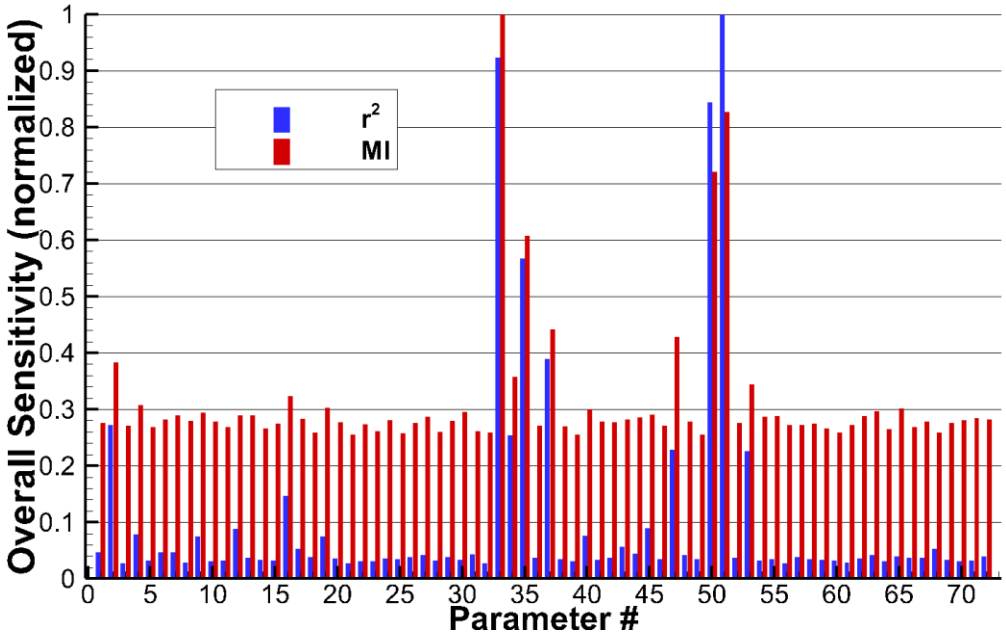

Figure A.105 Normalized r^2 and MI overall, variance weighted sensitivities for $QoI_{T_{vib_{O2+}}}$.

A.2.36 Quantity of Interest: Nitric Oxide Ion Vibrational Temperature

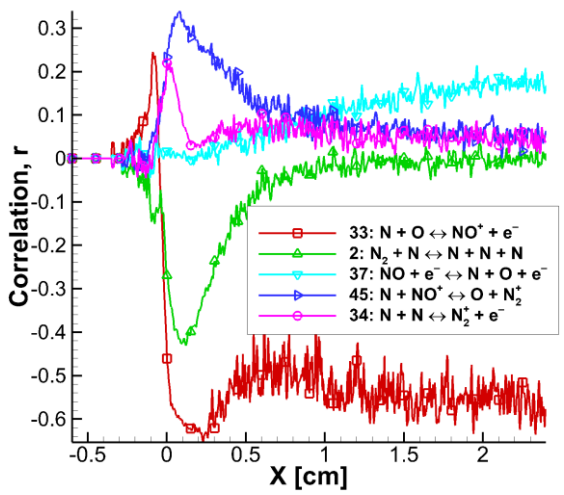

Figure A.106 Pearson correlation coefficient of the five most sensitive reaction rates when the nitric oxide ion vibrational temperature is the QoI ($QoI_{T_{vib_{NO^+}}}$).

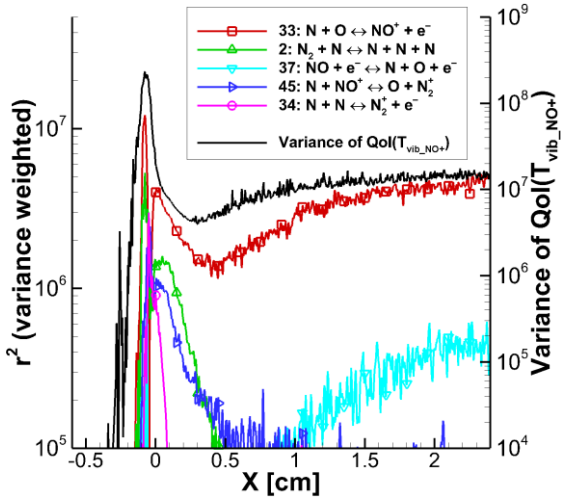

Figure A.107 Variance weighted r^2 sensitivities of the five most sensitive reaction rates for $QoI_{T_{vib_{NO^+}}}$, and the variance at each x −location.

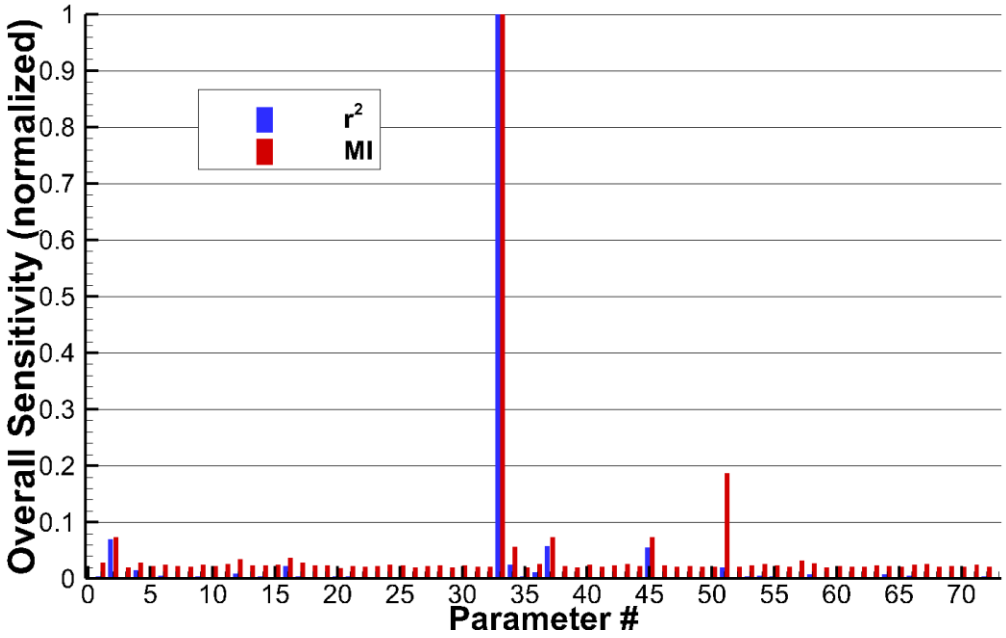

Figure A.108 Normalized r^2 and MI overall, variance weighted sensitivities for $QoI_{T_{vib_{NO^+}}}$.

A.2.37 Quantity of Interest: Mixture Electronic Temperature

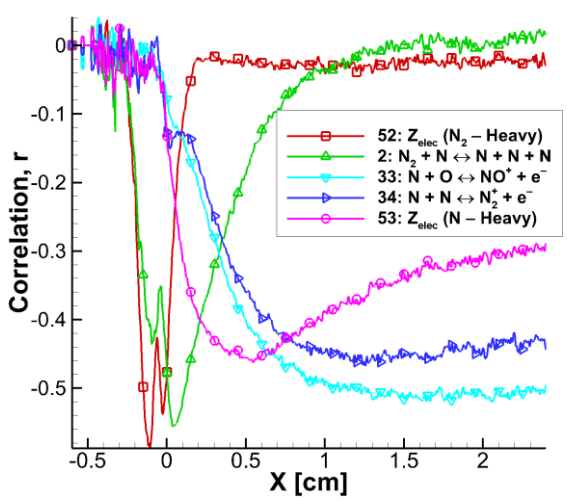

Figure A.109 Pearson correlation coefficient of the five most sensitive reaction rates when the mixture electronic temperature is the QoI ($QoI_{T_{elec}}$).

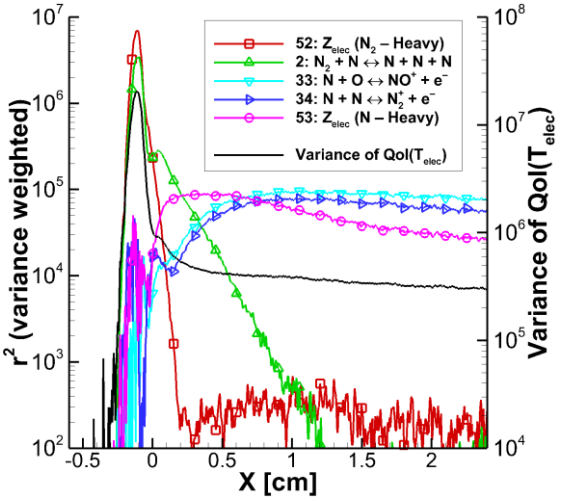

Figure A.110 Variance weighted r^2 sensitivities of the five most sensitive reaction rates for $QoI_{T_{elec}}$, and the variance at each x −location.

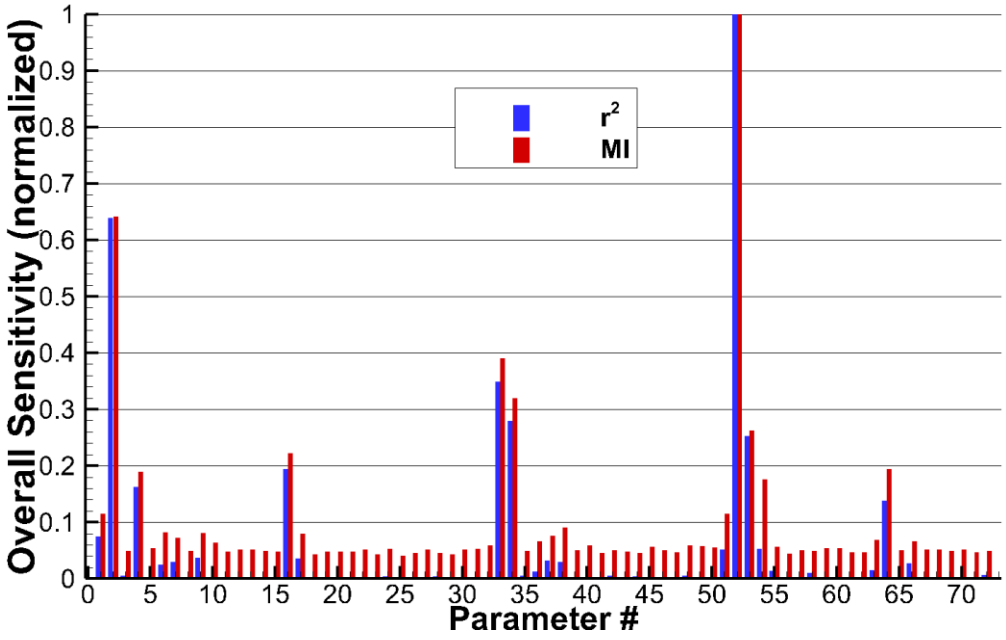

Figure A.111 Normalized r^2 and MI overall, variance weighted sensitivities for $QoI_{T_{elec}}$.

A.2.38 Quantity of Interest: Molecular Nitrogen Electronic Temperature

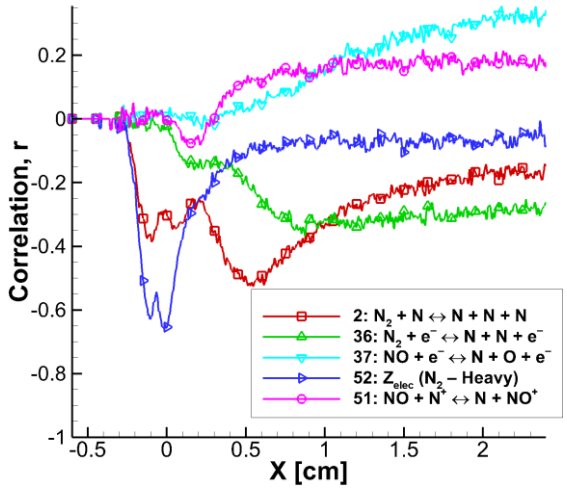

Figure A.112 Pearson correlation coefficient of the five most sensitive reaction rates when the molecular nitrogen electronic temperature is the QoI ($QoI_{T_{elec_{N2}}}$).

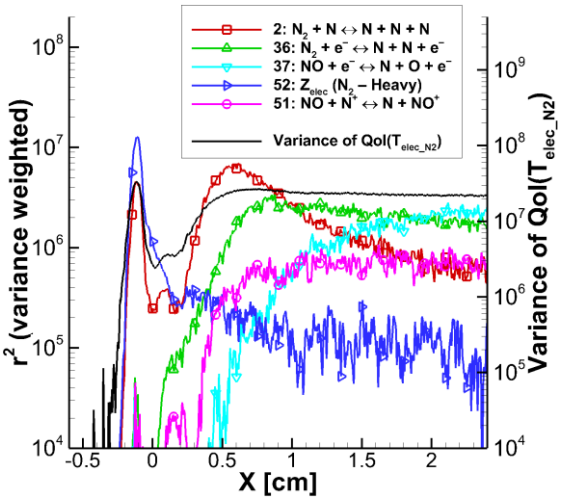

Figure A.113 Variance weighted r^2 sensitivities of the five most sensitive reaction rates for $QoI_{T_{elec_{N2}}}$, and the variance at each x −location.

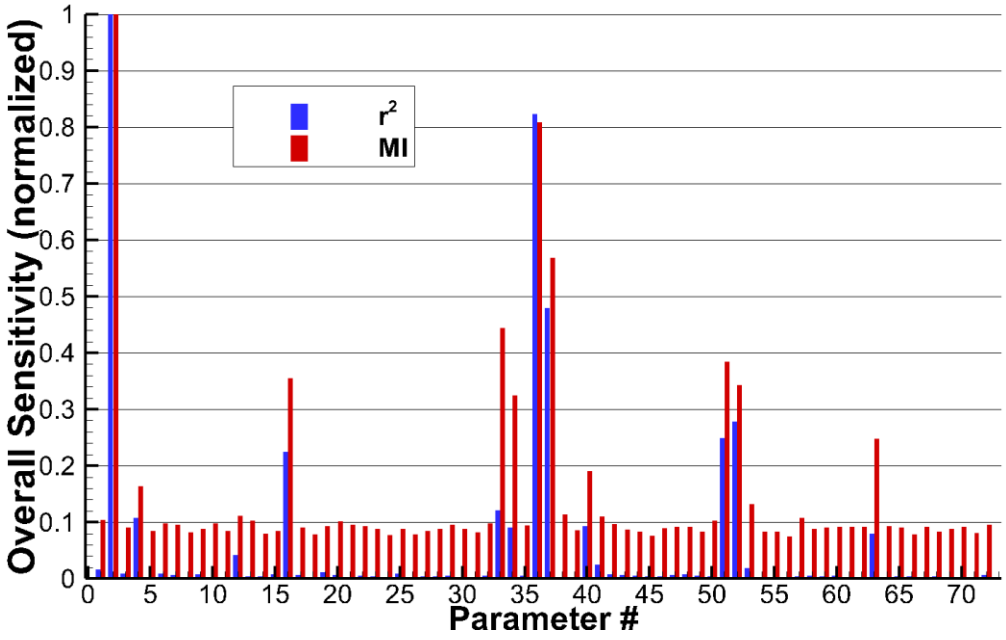

Figure A.114 Normalized r^2 and MI overall, variance weighted sensitivities for $QoI_{T_{elec_{N2}}}$.

A.2.39 Quantity of Interest: Atomic Nitrogen Electronic Temperature

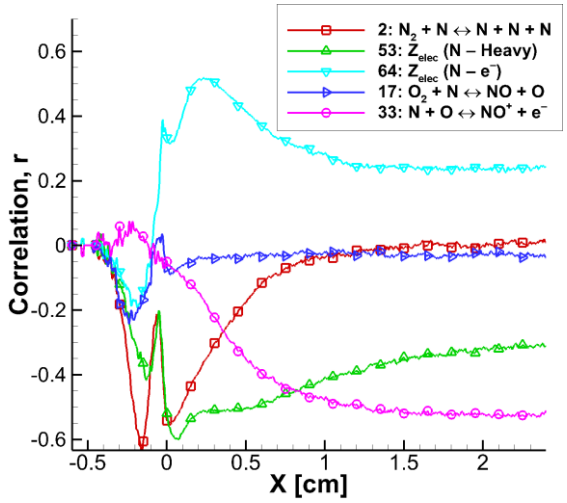

Figure A.115 Pearson correlation coefficient of the five most sensitive reaction rates when the atomic nitrogen electronic temperature is the QoI ($QoI_{T_{elec_N}}$).

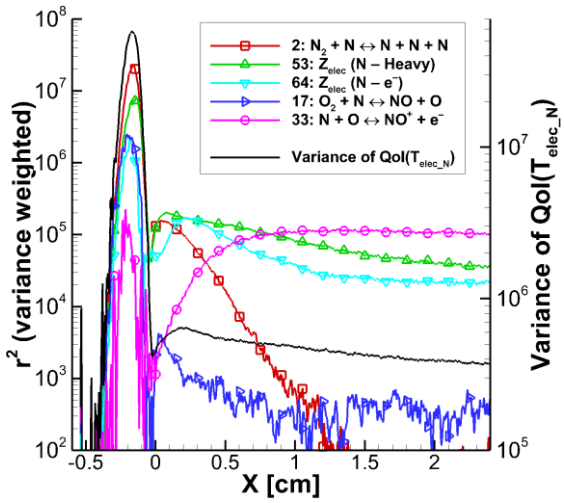

Figure A.116 Variance weighted r^2 sensitivities of the five most sensitive reaction rates for $QoI_{T_{elec_N}}$, and the variance at each x −location.

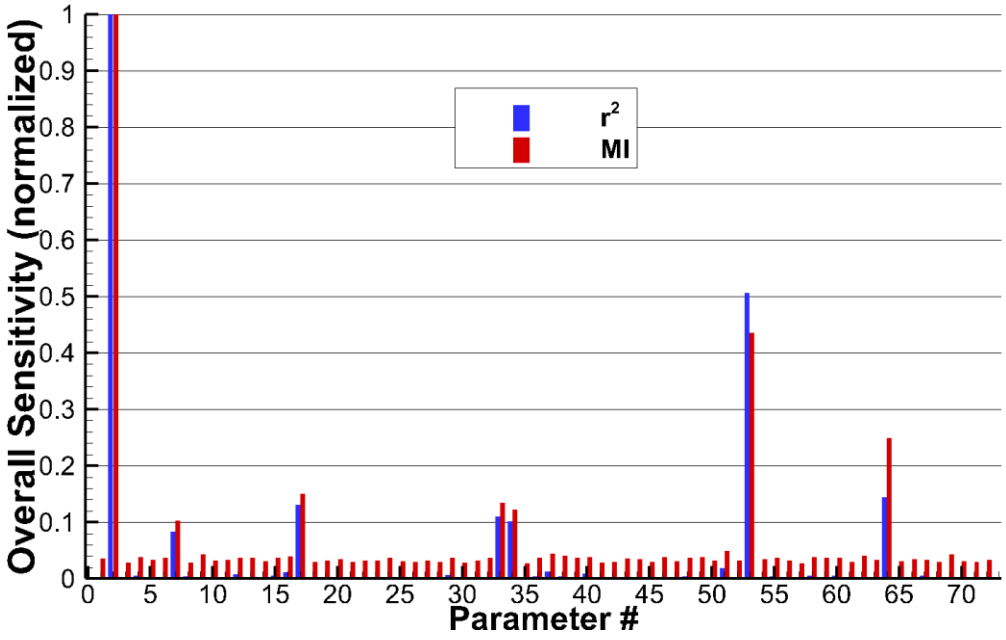

Figure A.117 Normalized r^2 and MI overall, variance weighted sensitivities for $QoI_{T_{elec_N}}$.

A.2.40 Quantity of Interest: Molecular Oxygen Electronic Temperature

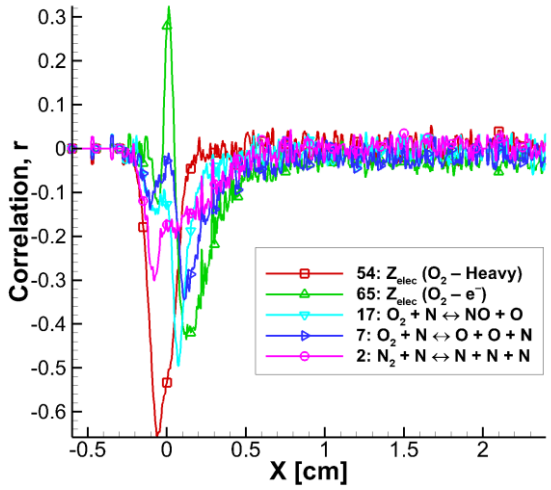

Figure A.118 Pearson correlation coefficient of the five most sensitive reaction rates when the molecular oxygen electronic temperature is the QoI ($QoI_{T_{elec_{O2}}}$).

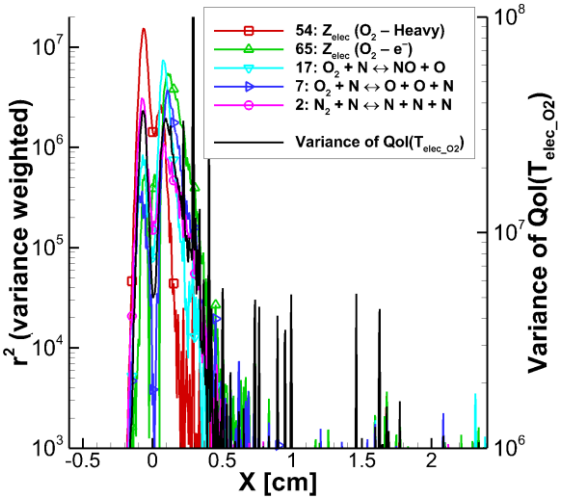

Figure A.119 Variance weighted r^2 sensitivities of the five most sensitive reaction rates for $QoI_{T_{elec_{O2}}}$, and the variance at each x −location.

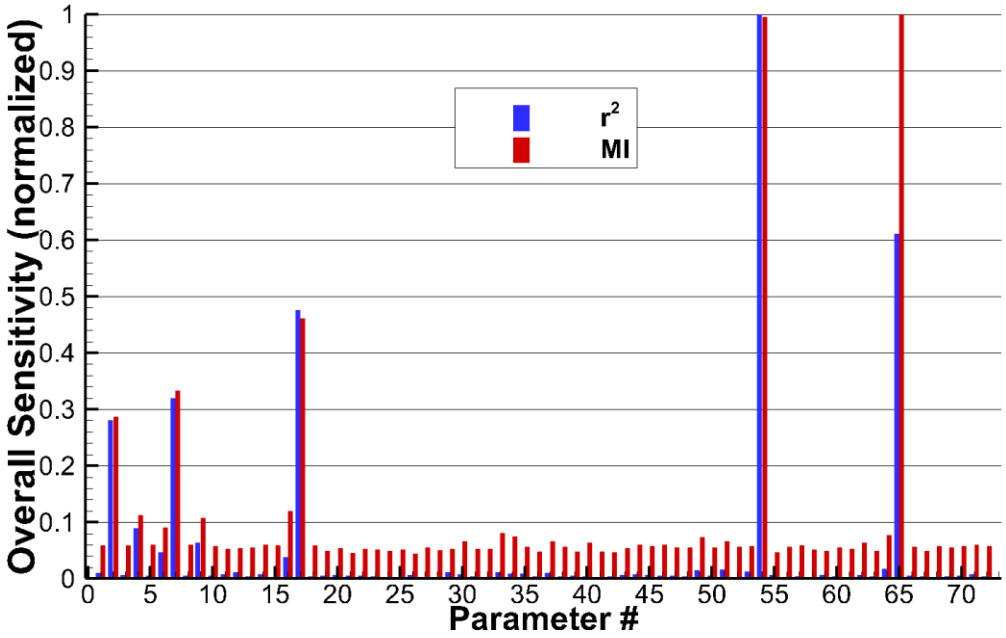

Figure A.120 Normalized r^2 and MI overall, variance weighted sensitivities for $QoI_{T_{elec_{O2}}}$.

A.2.41 Quantity of Interest: Atomic Oxygen Electronic Temperature

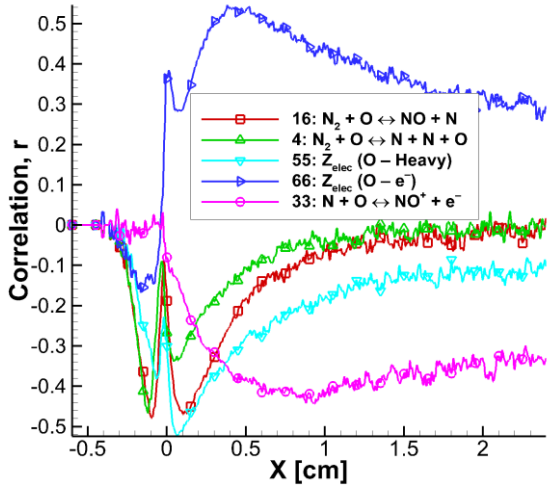

Figure A.121 Pearson correlation coefficient of the five most sensitive reaction rates when the atomic oxygen electronic temperature is the QoI ($QoI_{T_{elec_O}}$).

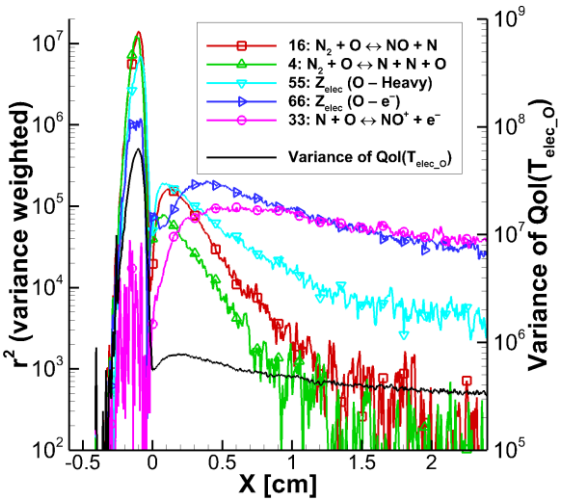

Figure A.122 Variance weighted r^2 sensitivities of the five most sensitive reaction rates for $QoI_{T_{elec_O}}$, and the variance at each x −location.

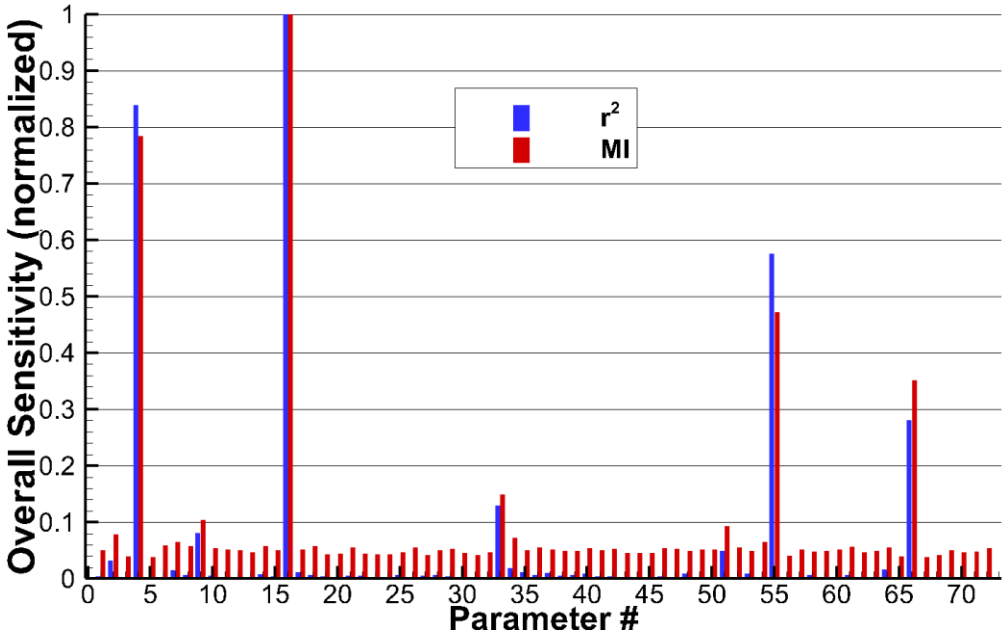

Figure A.123 Normalized r^2 and MI overall, variance weighted sensitivities for $QoI_{T_{elec_O}}$.

A.2.42 Quantity of Interest: Nitric Oxygen Electronic Temperature

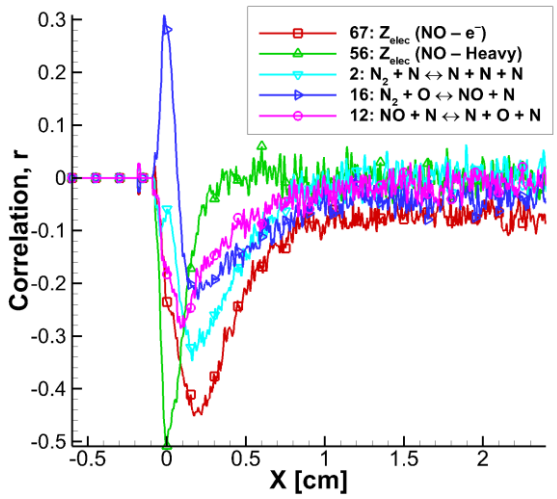

Figure A.124 Pearson correlation coefficient of the five most sensitive reaction rates when the nitric oxide electronic temperature is the QoI ($QoI_{T_{elec_{NO}}}$).

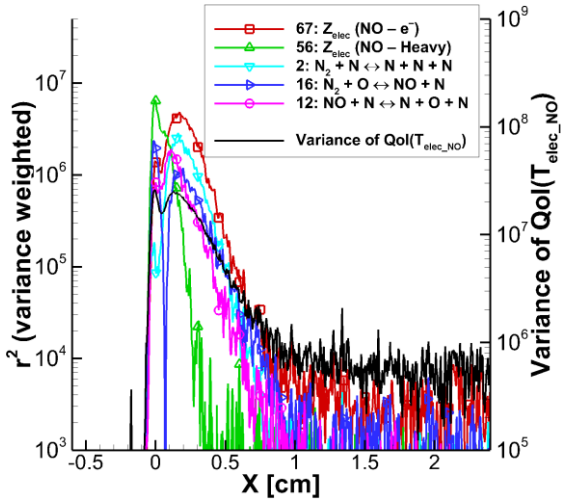

Figure A.125 Variance weighted r^2 sensitivities of the five most sensitive reaction rates for $QoI_{T_{elec_{NO}}}$, and the variance at each x −location.

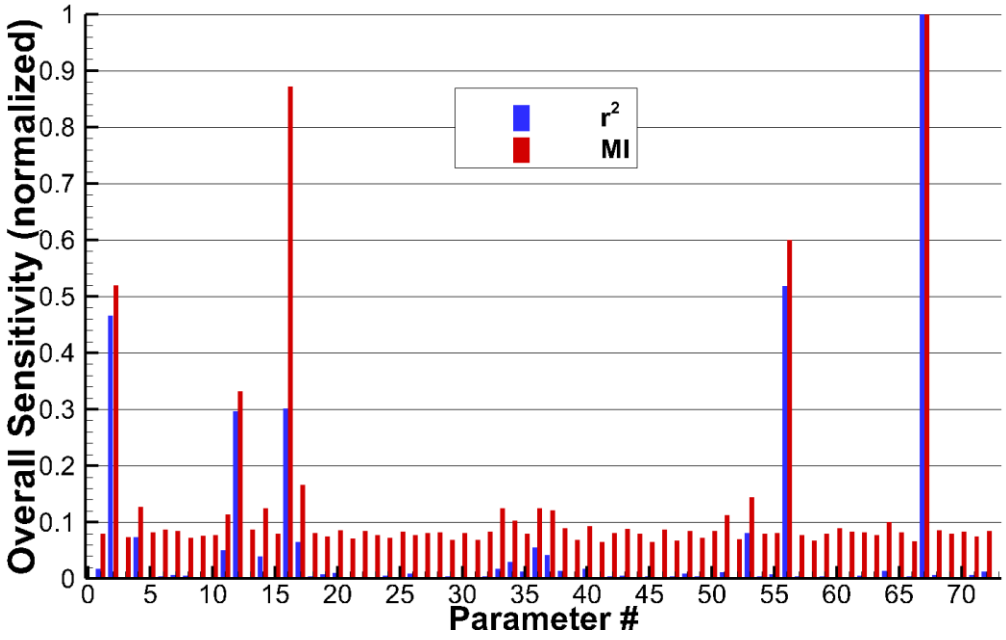

Figure A.126 Normalized r^2 and MI overall, variance weighted sensitivities for $QoI_{T_{elec_{NO}}}$.

A.2.43 Quantity of Interest: Molecular Nitrogen Ion Electronic Temperature

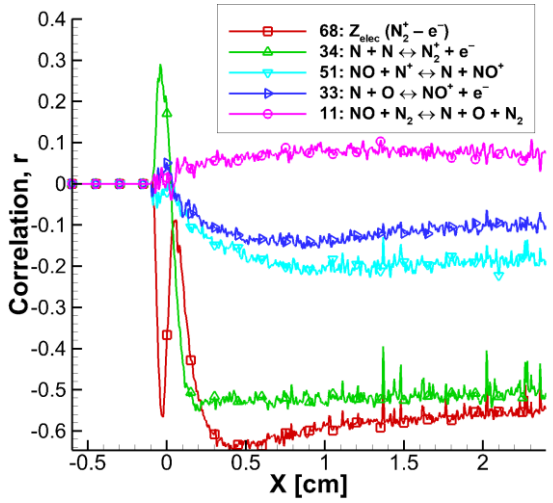

Figure A.127 Pearson correlation coefficient of the five most sensitive reaction rates when the molecular nitrogen ion electronic temperature is the QoI ($QoI_{T_{elec_{N2+}}}$).

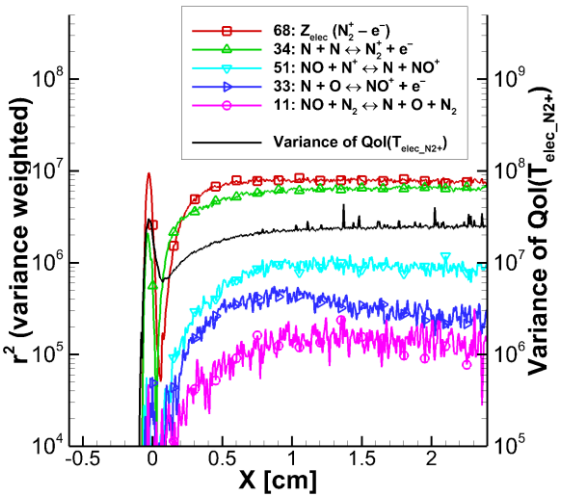

Figure A.128 Variance weighted r^2 sensitivities of the five most sensitive reaction rates for $QoI_{T_{elec_{N2+}}}$, and the variance at each x −location.

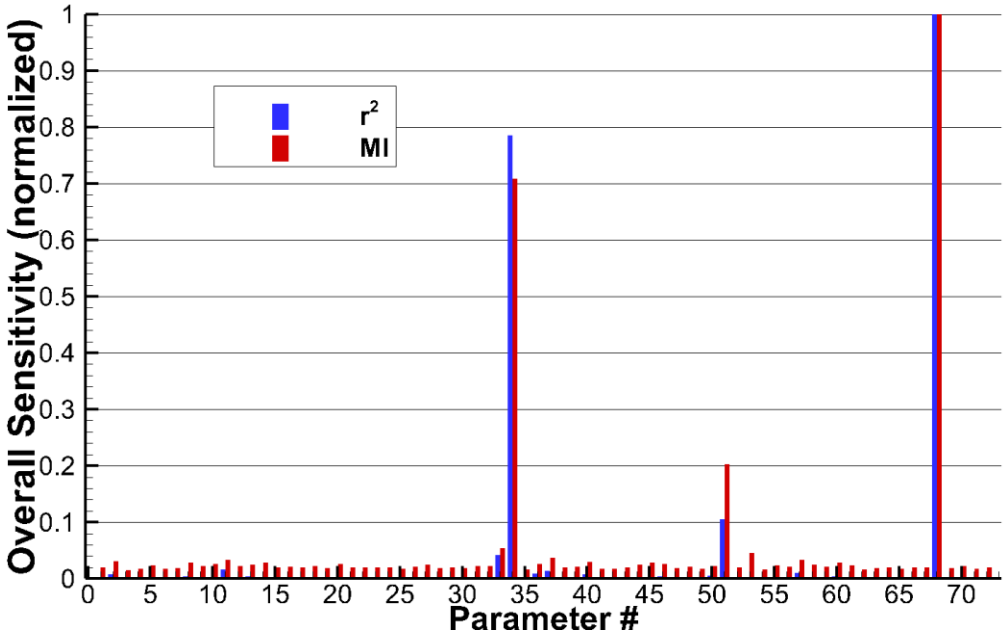

Figure A.129 Normalized r^2 and MI overall, variance weighted sensitivities for $QoI_{T_{elec_{N2+}}}$.

A.2.44 Quantity of Interest: Atomic Nitrogen Ion Electronic Temperature

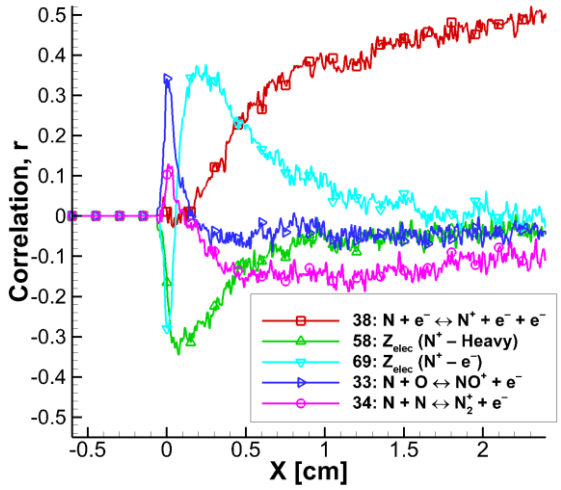

Figure A.130 Pearson correlation coefficient of the five most sensitive reaction rates when the atomic nitrogen ion electronic temperature is the QoI ($QoI_{T_{elec_{N^+}}}$).

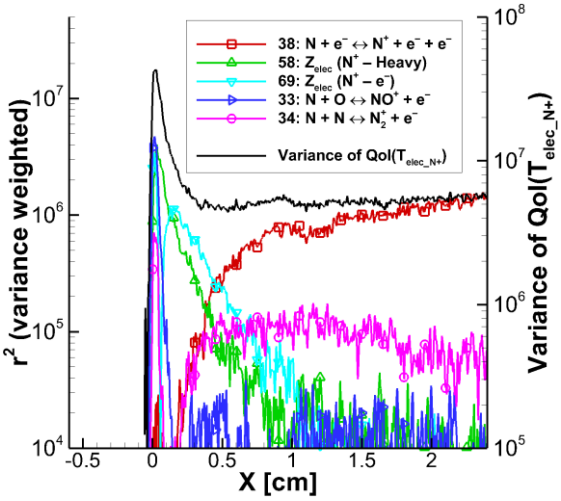

Figure A.131 Variance weighted r^2 sensitivities of the five most sensitive reaction rates for $QoI_{T_{elec_{N^+}}}$, and the variance at each x −location.

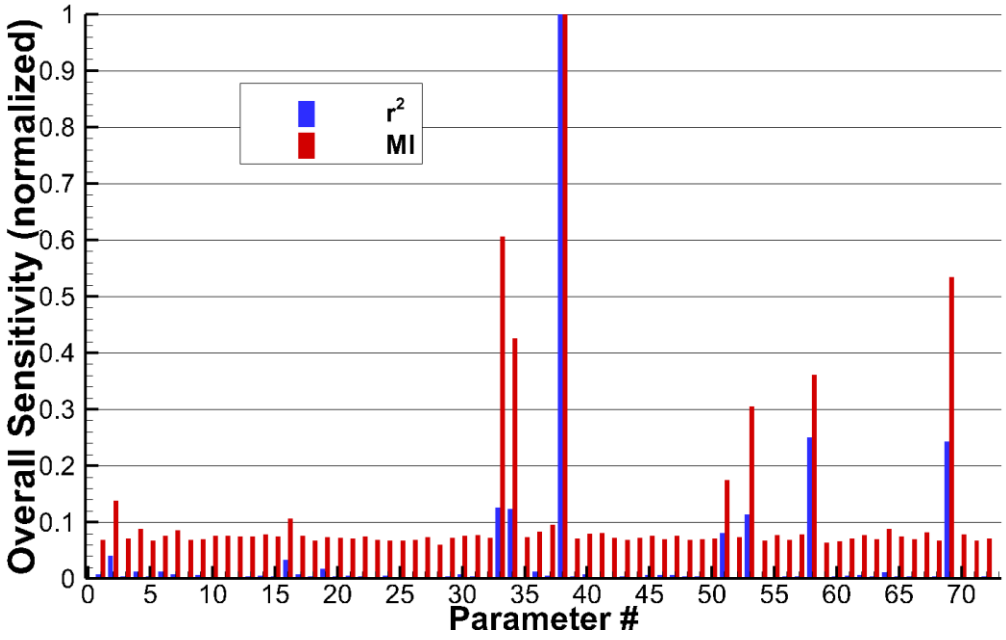

Figure A.132 Normalized r^2 and MI overall, variance weighted sensitivities for $QoI_{T_{elec_{N^+}}}$.

A.2.45 Quantity of Interest: Molecular Oxygen Ion Electronic Temperature

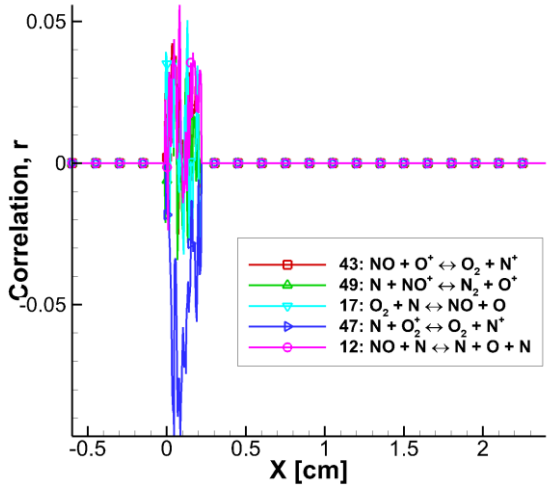

Figure A.133 Pearson correlation coefficient of the five most sensitive reaction rates when the molecular oxygen ion electronic temperature is the QoI ($QoI_{T_{elec_{O2+}}}$).

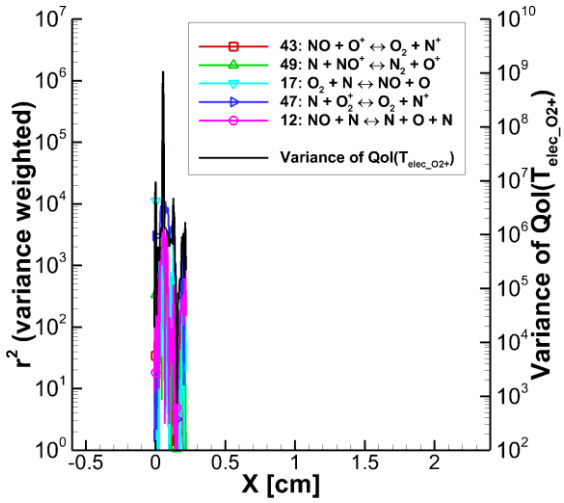

Figure A.134 Variance weighted r^2 sensitivities of the five most sensitive reaction rates for $QoI_{T_{elec_{O2+}}}$, and the variance at each x −location.

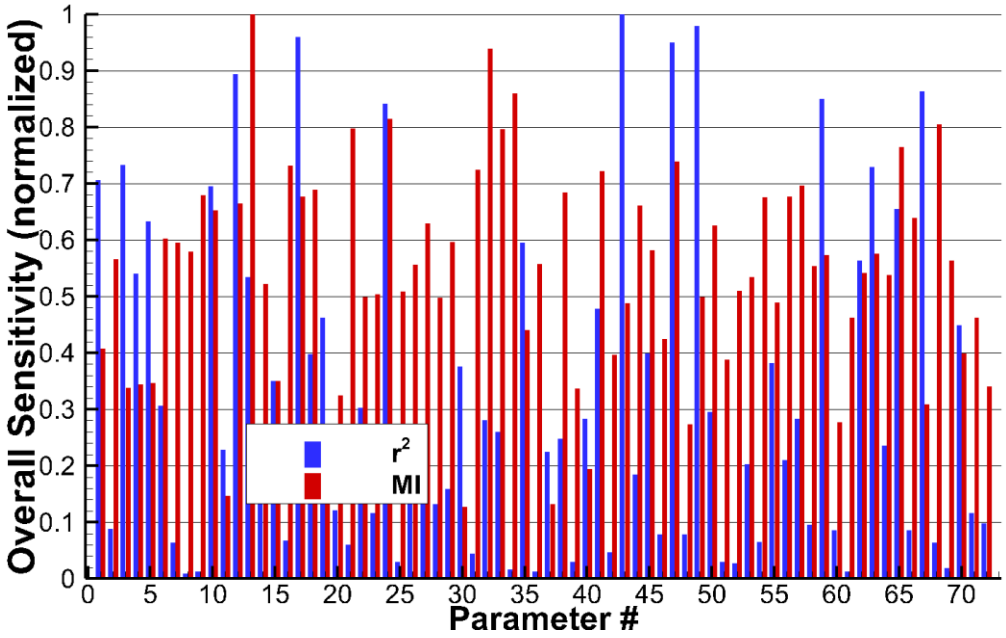

Figure A.135 Normalized r^2 and MI overall, variance weighted sensitivities for $QoI_{T_{elec_{O2+}}}$.

A.2.46 Quantity of Interest: Atomic Oxygen Ion Electronic Temperature

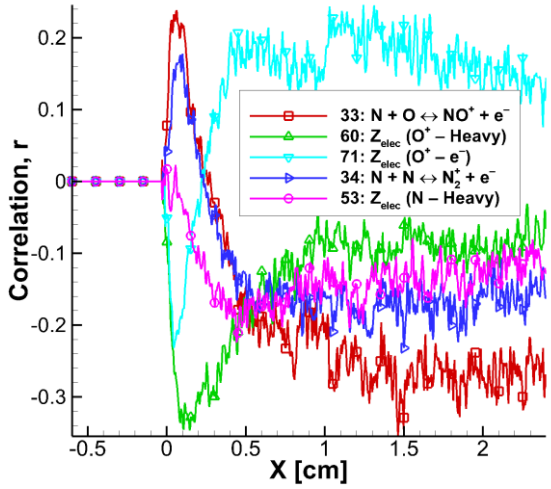

Figure A.136 Pearson correlation coefficient of the five most sensitive reaction rates when the atomic oxygen ion electronic temperature is the QoI ($QoI_{T_{elec_{O^+}}}$).

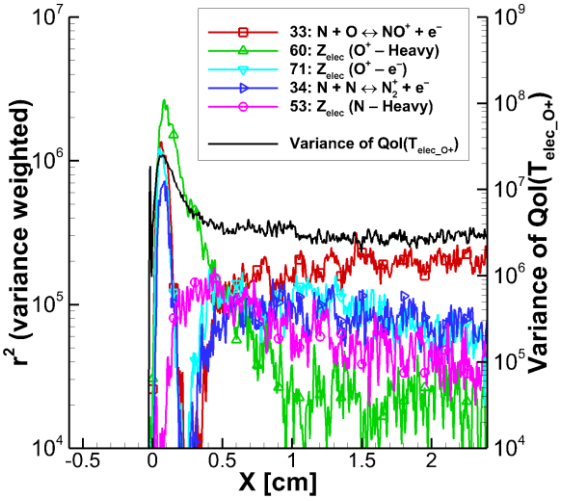

Figure A.137 Variance weighted r^2 sensitivities of the five most sensitive reaction rates for $QoI_{T_{elec_{O^+}}}$, and the variance at each x −location.

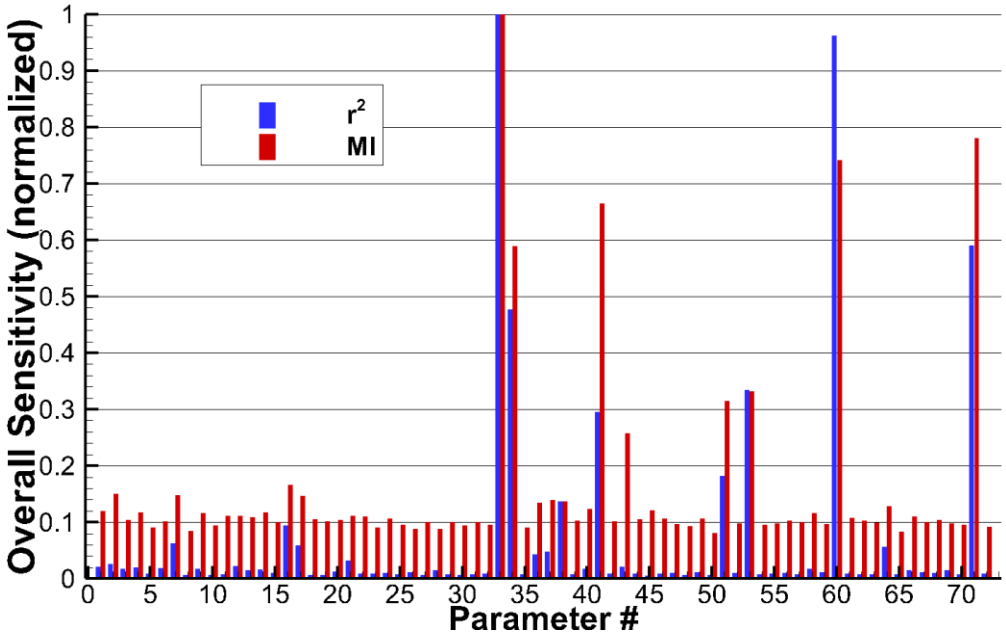

Figure A.138 Normalized r^2 and MI overall, variance weighted sensitivities for $QoI_{T_{elec_{O^+}}}$.

A.2.47 Quantity of Interest: Nitric Oxide Ion Electronic Temperature

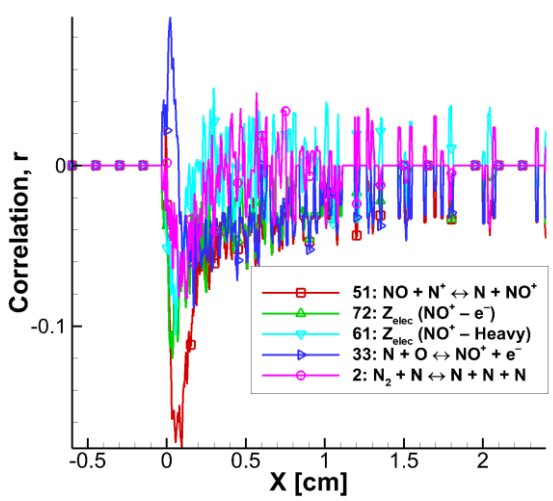

Figure A.139 Pearson correlation coefficient of the five most sensitive reaction rates when the nitric oxide ion electronic temperature is the QoI ($QoI_{T_{elec_{NO^+}}}$).

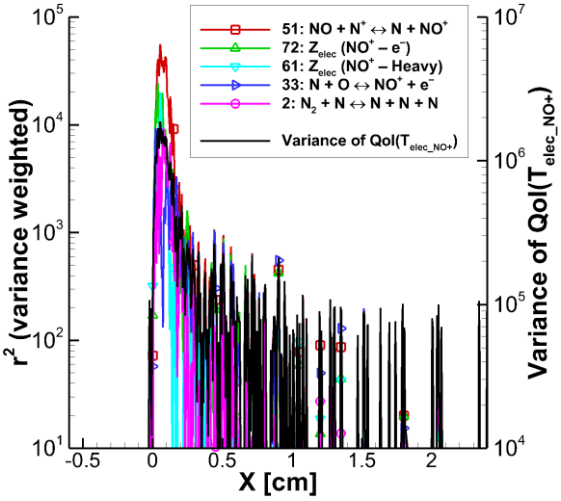

Figure A.140 Variance weighted r^2 sensitivities of the five most sensitive reaction rates for $QoI_{T_{elec_{NO^+}}}$, and the variance at each x −location.

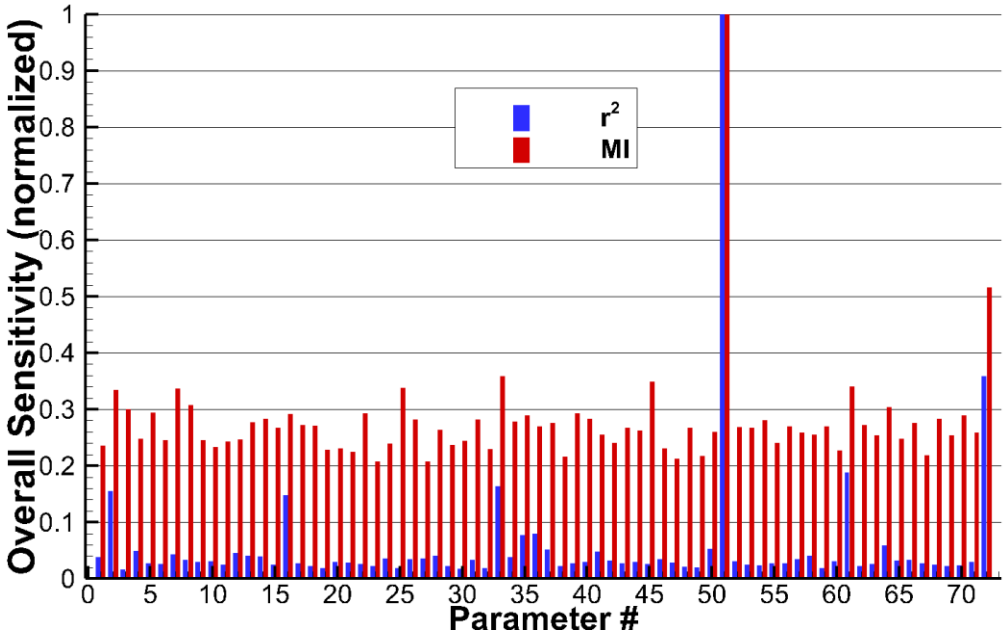

Figure A.141 Normalized r^2 and MI overall, variance weighted sensitivities for $QoI_{T_{elec_{NO^+}}}$.

A.2.48 Quantity of Interest: Mixture Overall Temperature

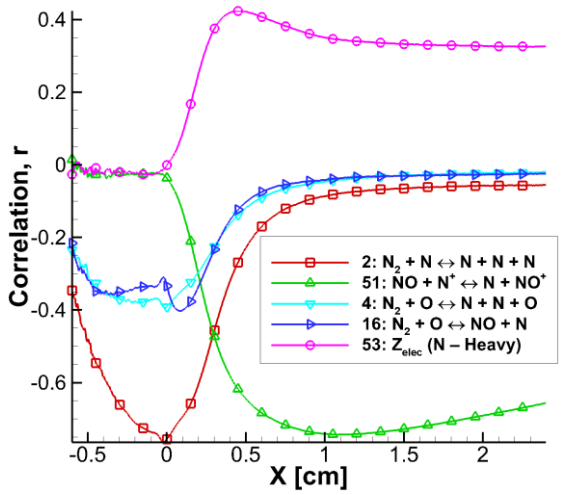

Figure A.142 Pearson correlation coefficient of the five most sensitive reaction rates when the mixture overall temperature is the QoI ($QoI_{T_{mixture}}$).

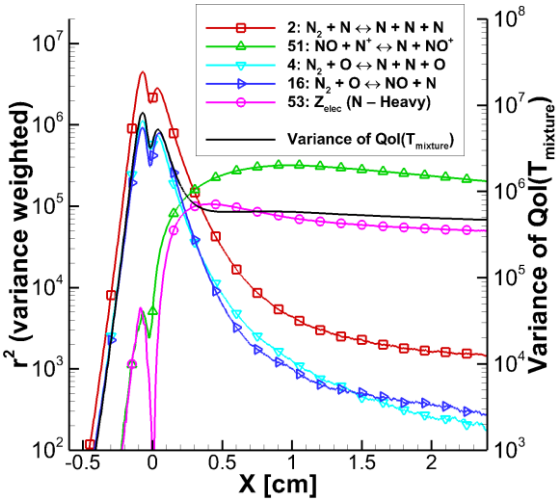

Figure A.143 Variance weighted r^2 sensitivities of the five most sensitive reaction rates for $QoI_{T_{mixture}}$, and the variance at each x −location.

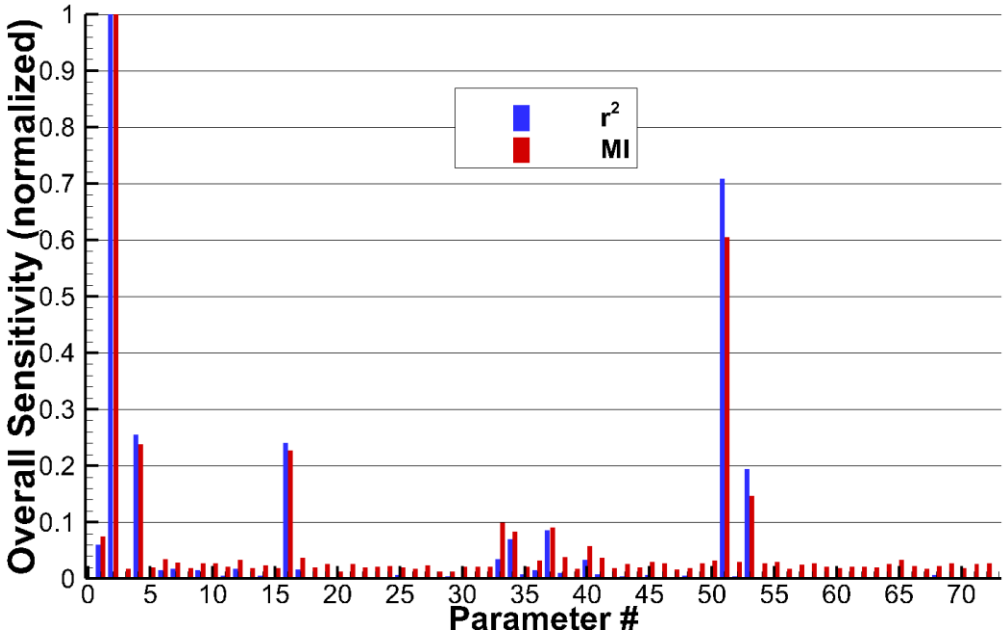

Figure A.144 Normalized r^2 and MI overall, variance weighted sensitivities for $QoI_{T_{mixture}}$.

A.2.49 Quantity of Interest: Molecular Nitrogen Overall Temperature

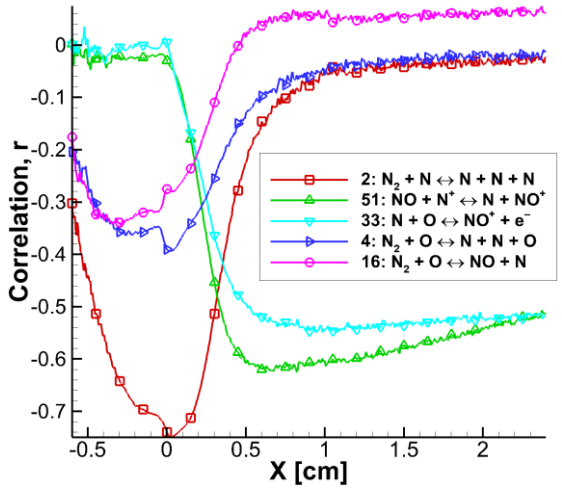

Figure A.145 Pearson correlation coefficient of the five most sensitive reaction rates when the molecular nitrogen overall temperature is the QoI ($QoI_{T_{N_2}}$).

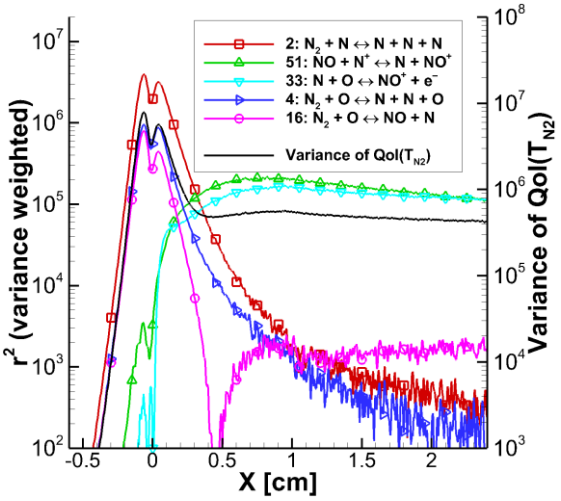

Figure A.146 Variance weighted r^2 sensitivities of the five most sensitive reaction rates for $QoI_{T_{N_2}}$, and the variance at each x −location.

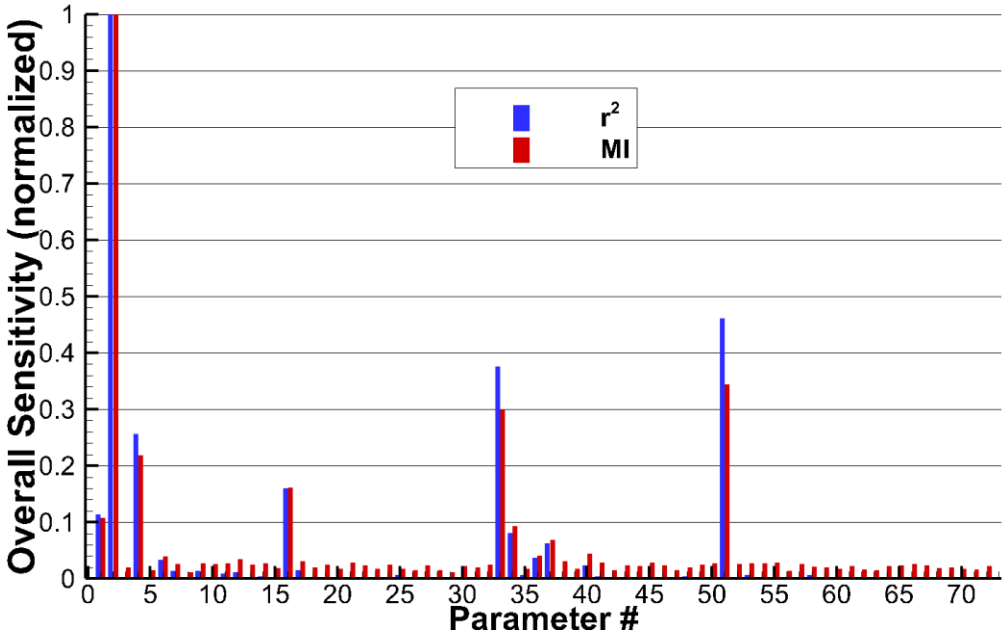

Figure A.147 Normalized r^2 and MI overall, variance weighted sensitivities for $QoI_{T_{N_2}}$.

A.2.50 Quantity of Interest: Molecular Oxygen Overall Temperature

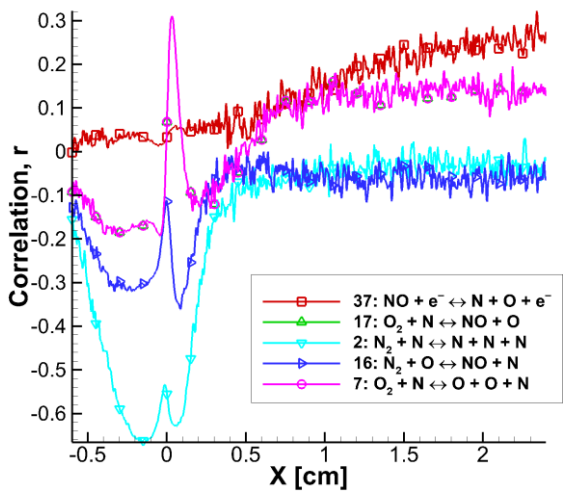

Figure A.148 Pearson correlation coefficient of the five most sensitive reaction rates when the molecular oxygen overall temperature is the QoI ($QoI_{T_{O_2}}$).

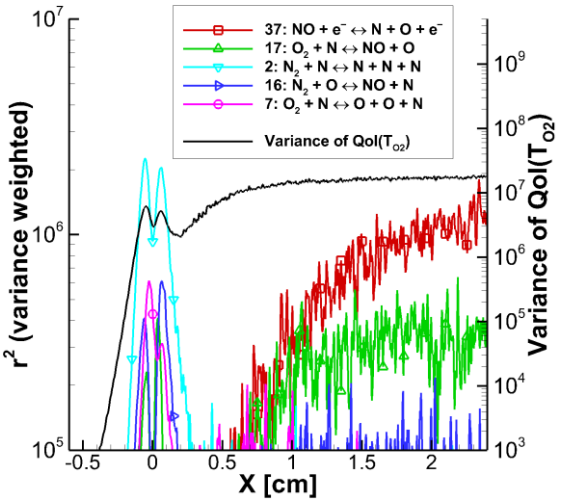

Figure A.149 Variance weighted r^2 sensitivities of the five most sensitive reaction rates for $QoI_{T_{O_2}}$, and the variance at each x −location.

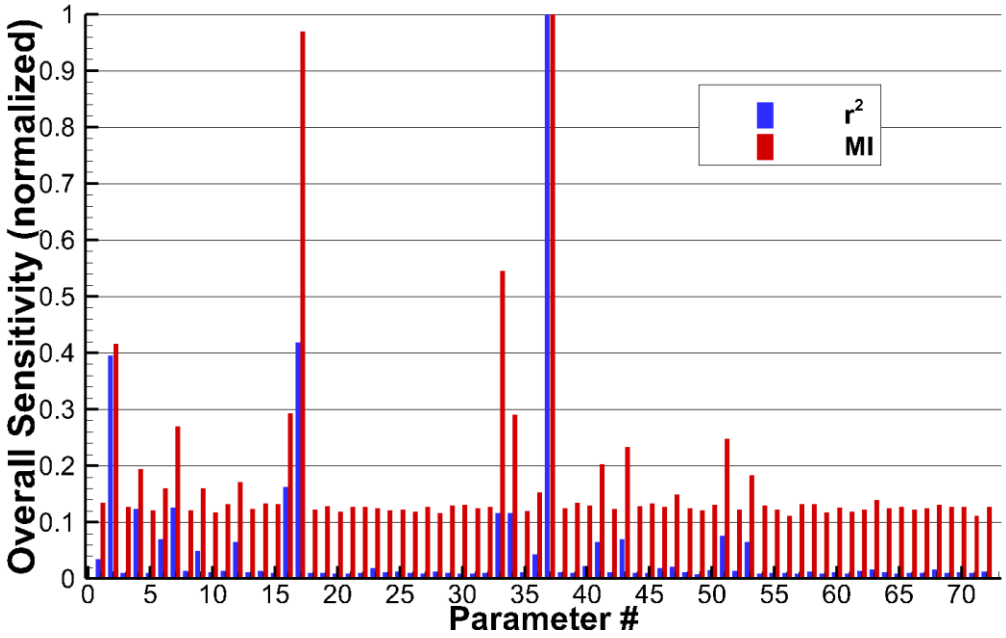

Figure A.150 Normalized r^2 and MI overall, variance weighted sensitivities for $QoI_{T_{O_2}}$.

A.2.51 Quantity of Interest: Nitric Oxide Overall Temperature

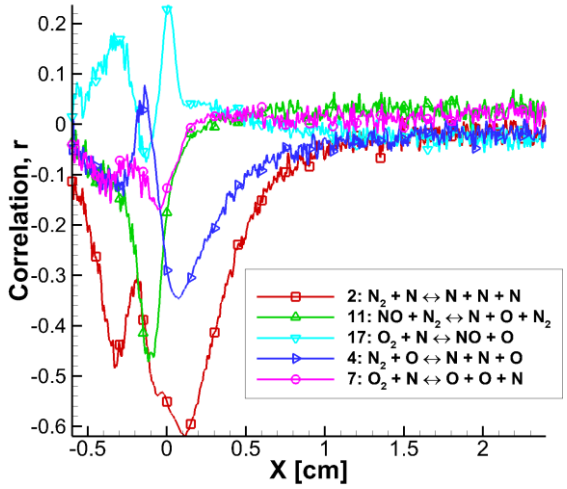

Figure A.151 Pearson correlation coefficient of the five most sensitive reaction rates when the nitric oxide overall temperature is the QoI ($QoI_{T_{NO}}$).

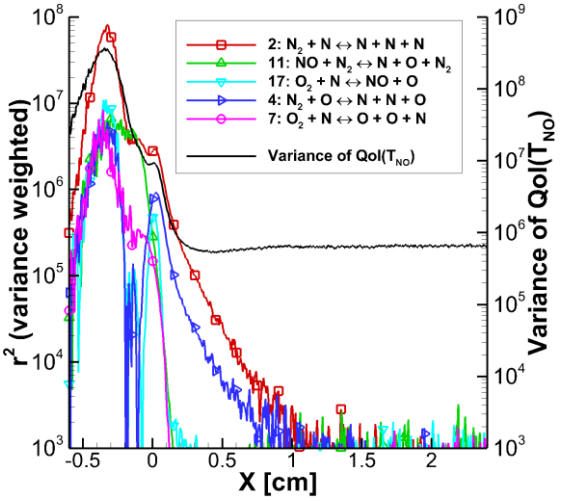

Figure A.152 Variance weighted r^2 sensitivities of the five most sensitive reaction rates for $QoI_{T_{NO}}$, and the variance at each x −location.

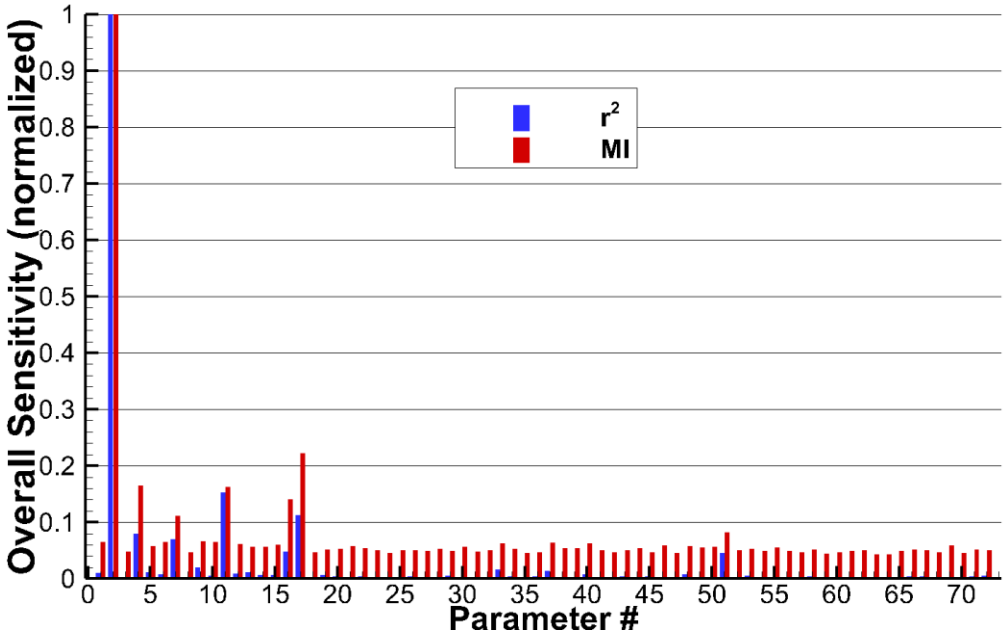

Figure A.153 Normalized r^2 and MI overall, variance weighted sensitivities for $QoI_{T_{NO}}$.

A.2.52 Quantity of Interest: Molecular Nitrogen Ion Overall Temperature

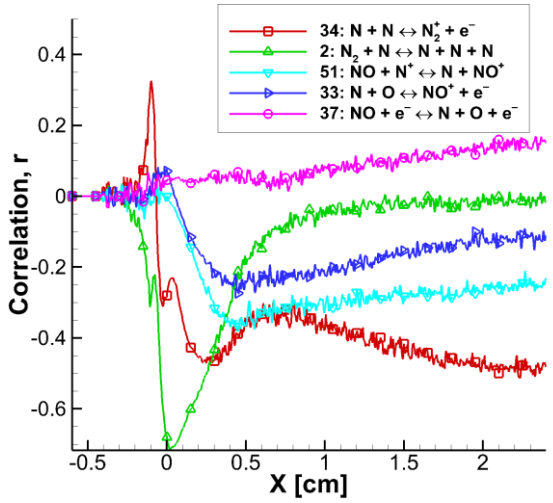

Figure A.154 Pearson correlation coefficient of the five most sensitive reaction rates when the molecular nitrogen ion overall temperature is the QoI ($QoI_{T_{N_2^+}}$).

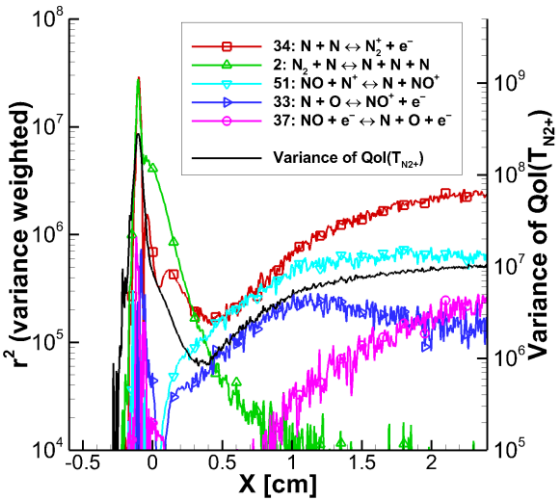

Figure A.155 Variance weighted r^2 sensitivities of the five most sensitive reaction rates for $QoI_{T_{N_2^+}}$, and the variance at each x −location.

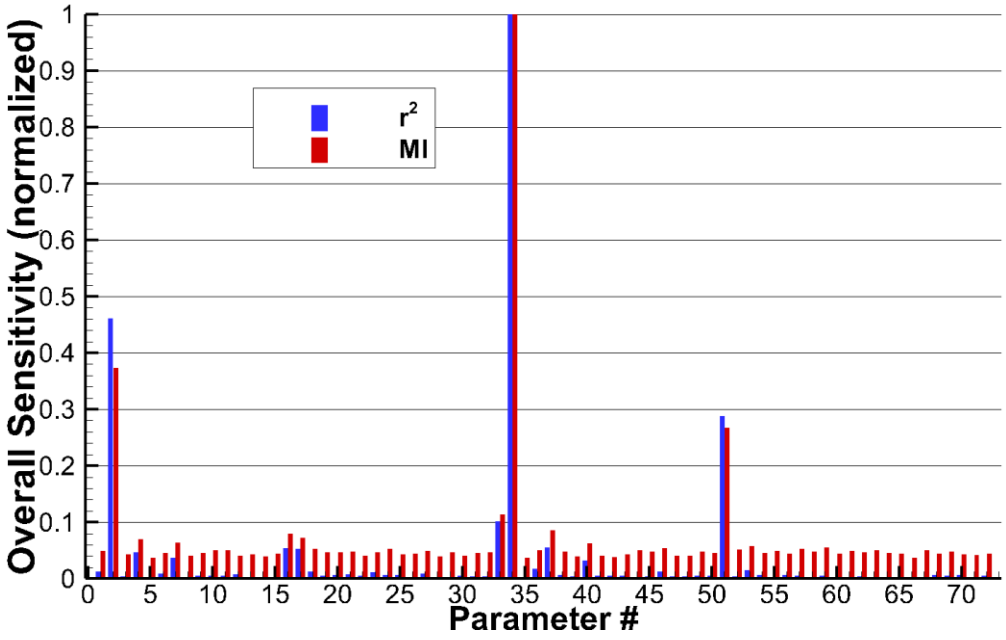

Figure A.156 Normalized r^2 and MI overall, variance weighted sensitivities for $QoI_{T_{N_2^+}}$.

A.2.53 Quantity of Interest: Molecular Oxygen Ion Overall Temperature

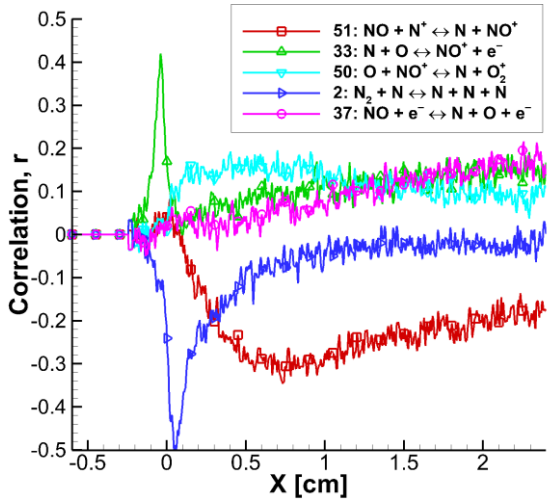

Figure A.157 Pearson correlation coefficient of the five most sensitive reaction rates when the molecular oxygen ion overall temperature is the QoI ($QoI_{T_{O_2^+}}$).

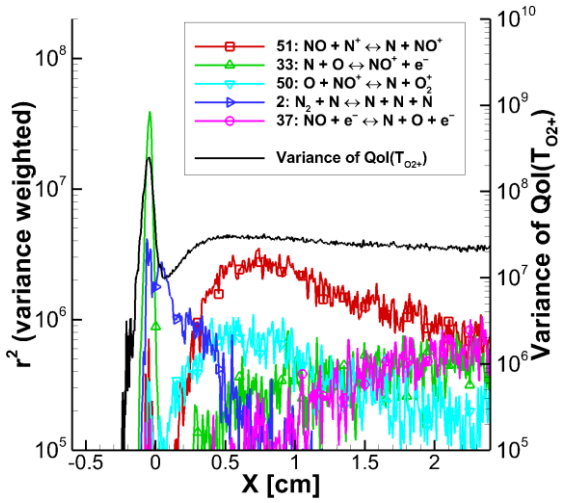

Figure A.158 Variance weighted r^2 sensitivities of the five most sensitive reaction rates for $QoI_{T_{O_2^+}}$, and the variance at each x −location.

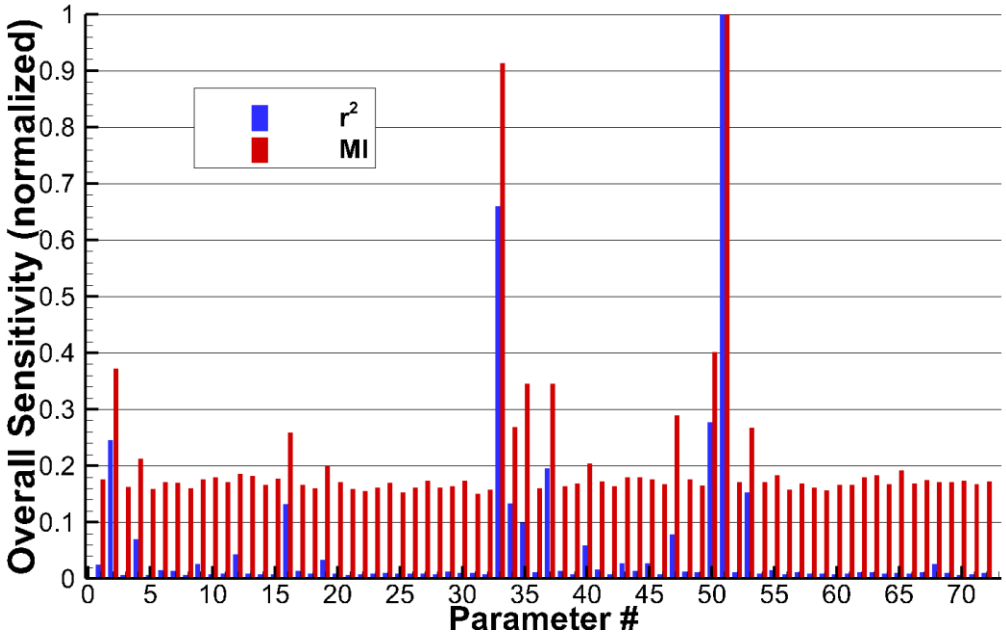

Figure A.159 Normalized r^2 and MI overall, variance weighted sensitivities for $QoI_{T_{O_2^+}}$.

A.2.54 Quantity of Interest: Nitric Oxide Ion Overall Temperature

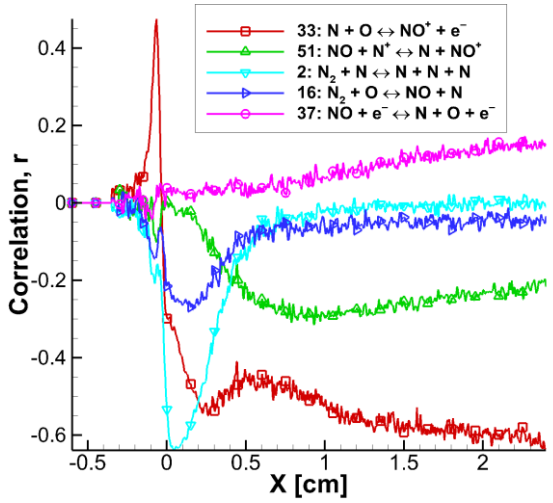

Figure A.160 Pearson correlation coefficient of the five most sensitive reaction rates when the nitric oxide ion overall temperature is the QoI ($QoI_{T_{NO^+}}$).

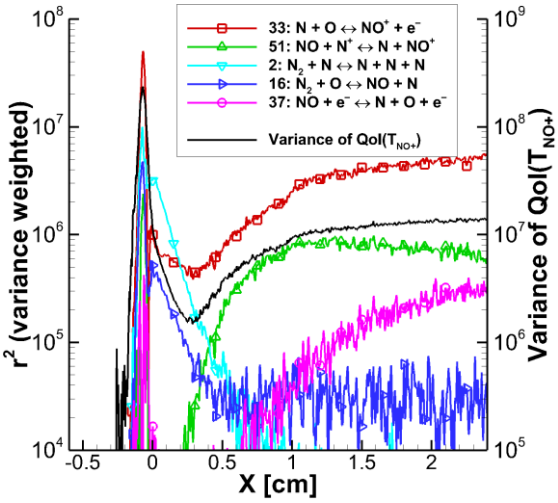

Figure A.161 Variance weighted r^2 sensitivities of the five most sensitive reaction rates for $QoI_{T_{NO^+}}$, and the variance at each x −location.

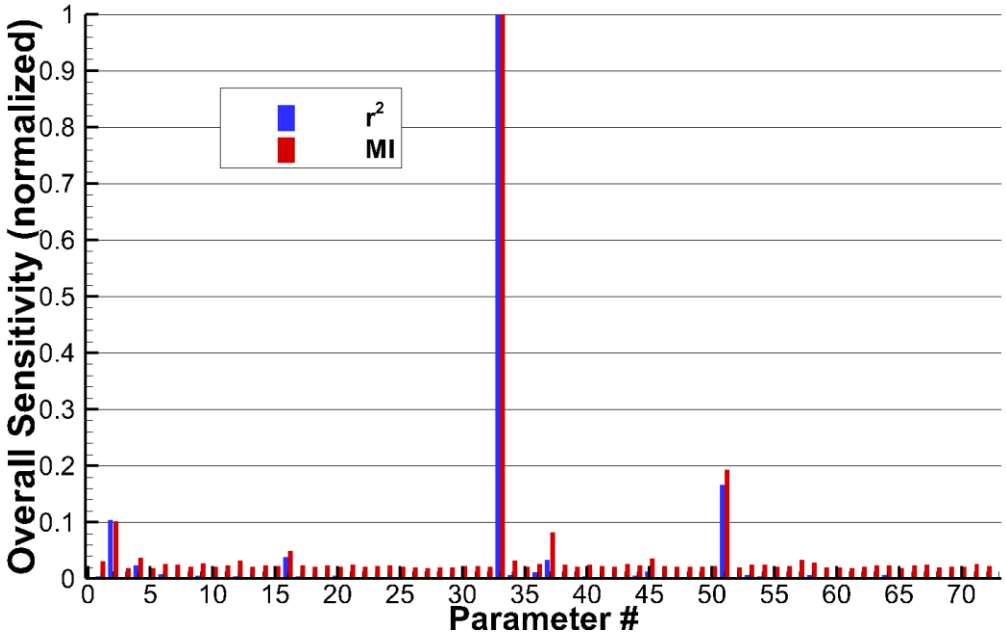

Figure A.162 Normalized r^2 and MI overall, variance weighted sensitivities for $QoI_{T_{NO^+}}$.

A.2.54 Quantity of Interest: Shock Speed

The shock speed QoI ($QoI_{U_{shock}}$) is a scalar quantity, meaning that Figure A.163 is determined from a single value without variance weighting. In the CHIPS code, the freestream velocity is set beforehand, but the shock speed is a result of the initial conditions and the physics determined by the input parameters. Since a sensitivity analysis explores these input parameters, the shock speed can fluctuate between simulations. During the sensitivity analysis, the shock fluctuated approximately ± 90 m/s which corresponds to a simulated shock velocity error of $\pm 0.87\%$ for the 10.28 km/s shock simulated in this sensitivity analysis.

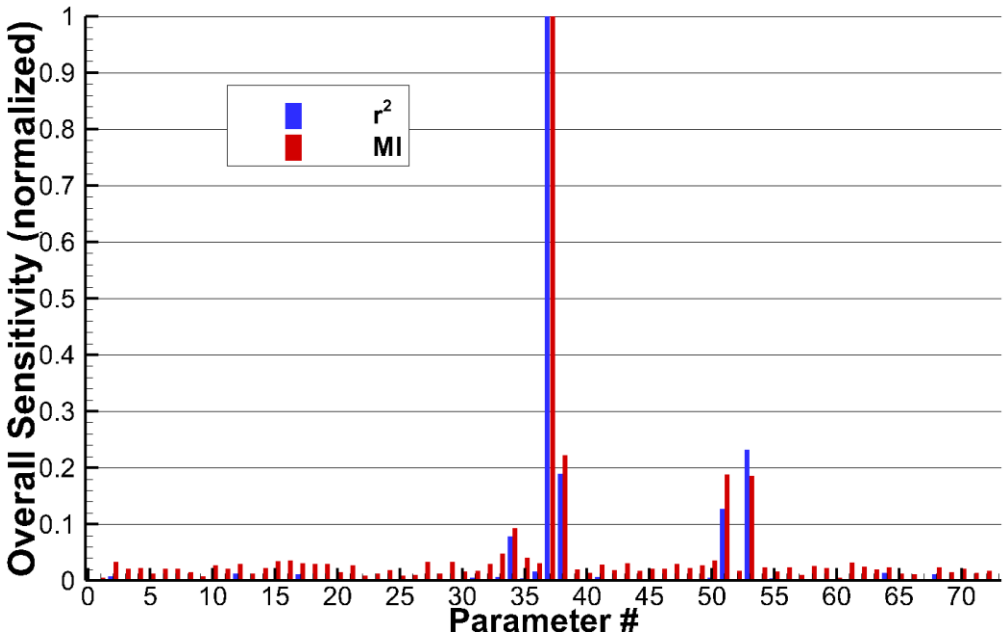

Figure A.163 Normalized r^2 and MI overall sensitivities for $QoI_{U_{shock}}$.

References

[1] Brandis, A. M., and Cruden, B. A., "Benchmark Shock Tube Experiments of Radiative Heating Relevant to Earth Re-entry," *55th AIAA Aerospace Sciences Meeting*, AIAA SciTech Forum, AIAA Paper No. 2017-1145, 2017.

[2] Cruden, B. A., and Bogdanoff, D. W., "Shock Radiation Tests for Saturn and Uranus Entry Probes," *Journal of Spacecraft and Rockets*, Vol. 54, No. 6, 2017, pp. 1246-1257.

[3] Bird, G. A., *Molecular Gas Dynamics and the Direct Simulation of Gas Flows*, Clarendon Press, Oxford, England, U.K., 1994.

[4] Higdon, K. J., Goldstein, D. B., and Varghese, P. L., "Sensitivity Analysis of Direct Simulation Monte Carlo Parameters for Ionizing Hypersonic Flows," *Journal of Thermophysics and Heat Transfer*, Vol. 32, No. 1, 2018, pp. 90-102.

[5] Whiting, E., Yen, L., Arnold, J., and Paterson, J., "NEQAIR96, Nonequilibrium and Equilibrium Radiative Transport and Spectra Program: User's Manual," NASA Ames Research Center TR RP-1389, 1996.

[6] Strand, J.S., "Statistical Methods for the Analysis of DSMC Simulations of Hypersonic Shocks," Ph.D. Dissertation, Dept. of Aerospace Engineering, The University of Texas at Austin, Austin, TX, 2012.

[7] Goldstein, D. B., Sturtevant, B., and Broadwell, J. E., "Investigations of the Motion of Discrete-Velocity Gases," *Rarefied Gas Dynamics, Progress in Astronautics and Aeronautics*, Vol. 118, 1989, pp. 100-117.

[8] Goldstein, D. B., and Sturtevant, B., "Discrete Velocity Gasdynamics Simulations in a Parallel Processing Environment," *24th AIAA Thermophysics Conference*, AIAA Paper No. 89-1668, Buffalo, NY, 1989.

[9] Roveda, R., Goldstein, D. B., and Varghese, P. L., "Hybrid Euler/Particle Approach for Continuum/Rarefied Flows," *Journal of Spacecraft and Rockets*, Vol. 35, No. 3, 1998, pp. 258-265.

[10] Zhu, T., Zheng, L., and Levin, D. A., "Modeling of NO Radiation from Unsteady and Steady Shocks Using DSMC," *44th AIAA Thermophysics Conference*, AIAA Paper No. 2013-2786, San Diego, CA, 2013.

[11] Bird, G. A., "Direct Simulation of Typical AOTV Entry Flows," *AIAA and ASME Fourth Joint Thermophysics and Heat Transfer Conference*, AIAA Paper No. 86-1310, Boston, MA, 1986.

[12] Tonks, L. and Langmuir, I., "General theory of a plasma arc," *Physical Review*, Vol. 34, No. 1, 1929, pp. 876-922.

[13] Boyd, I. D., "Monte Carlo simulation of nonequilibrium flow in a low-power hydrogen arcjet," *Physics of Fluids*, Vol. 9, No. 10, 1997, pp. 4575-4584.

[14] Farbar, E. D., and Boyd, I. D., "Modeling of the Plasma Generated in a Rarefied Hypersonic Shock Layer," *Physics of Fluids*, Vol. 22, No. 10, 2010.

[15] Bird, G. A., "Monte Carlo Simulation in an Engineering Context," *Rarefied Gas Dynamics*, edited by S. S. Fisher, Part 1, AIAA, New York, 1981, pp. 239-255.

[16] Ozawa, T., Zhong, J., and Levin, D. A., "Development of Kinetic-Based Energy Exchange Models for Noncontinuum, Ionized Hypersonic Flows," *Physics of Fluids*, Vol. 20, No. 4, 2008, Paper 046102.

[17] Gallis, M. A., Prasad, R., and Harvey, J. K., "The effect of plasmas on the aerodynamic performance of vehicles," AIAA Paper 1998-2666, presented at the 29th AIAA Plasmadynamics and Lasers Conference, Albuquerque, NM, 1998.

[18] Swaminathan-Gopalan, K. and Stephani, K. A., "Recommended direct simulation Monte Carlo collision model parameters for modeling ionized air transport processes," *Physics of Fluids*, Vol. 28, No. 2, 2016.

[19] Bird, G. A., "Nonequilibrium Radiation During Re-Entry at 10 km/s," *AIAA 22nd Thermophysics Conference*, AIAA Paper No. 1987-1543, Honolulu, HI, 1987, pp. 12.

[20] Carlson, A. B., and Hassan, H. A., "Radiation Modeling with Direct Simulation Monte Carlo," *Journal of Thermophysics and Heat Transfer*, Vol. 6, No. 4, 1992, pp. 631-636.

[21] Burt, J. M., and Josyula, E., "DSMC modeling of nonequilibrium electronic excitation and emission for hypersonic sensor applications," *45th AIAA Thermophysics Conference*, AIAA Paper No. 2015-2511, Dallas, TX, 2015.

[22] Gallis, M. A., and Harvey, J. K., "Atomic species radiation from air shock layers modelled with DSMC," AIAA Paper No. 94-2108, 1994.

[23] Ozawa, T., Li, Z., Sohn, I., Levin, D. A., and Modest, M. F., "Modeling of electronic excitation and radiation for hypersonic reentry flows in DSMC," *48th AIAA Aerospace Sciences Meeting*, AIAA Paper No. 2010-987, Orlando, FL, 2010.

[24] Liechty, D. S., and Lewis, M. J., "Extension of the Quantum-kinetic Model to Lunar and Mars Return Physics," *Physics of Fluids*, Vol. 26, No. 2, 2014, Paper 027106.

[25] Borgnakke, C. and Larsen, P. S., "Statistical Collision Model for Monte Carlo Simulation of Polyatomic Gas Mixture," *Journal of Computational Physics*, Vol. 18, No. 4, 1975, pp. 402-420.

[26] Boyd, I. D., and Phillips, W. D., "Prediction of Ultraviolet Radiation in Nonequilibrium Hypersonic Bow-Shock Waves," *Journal of Thermophysics and Heat Transfer*, Vol. 12, No. 1, 1998. pp. 38-44.

[27] Sohn, I., Li, Z., and Levin, D. A., "Effect of Nonlocal Vacuum Ultraviolet Radiation on Hypersonic Nonequilibrium Flow," *Journal of Thermophysics and Heat Transfer*, Vol. 26, No. 3, 2012, pp. 393-406

[28] Ozawa, T., Levin, D. A., Wang, A., and Modest, M., "Development of Coupled Particle Hypersonic Flowfield-Photon Monte Carlo Radiation Methods," *Journal of Thermophysics and Heat Transfer*, Vol. 24, No. 3, 2010, pp. 612-622.

[29] Burt, J. M, and Josyula, E., "Global Sensitivity Analysis and Uncertainty Quantification for a Hypersonic Shock Interaction Flow," *Journal of Thermophysics and Heat Transfer*, Vol. 29, No. 3, 2015, pp. 439-449.

[30] Strand, J. S., and Goldstein, D. B., "Application of Bayesian Statistical Methods for the Analysis of DSMC Simulations of Hypersonic Shocks," *41st AIAA Fluid Dynamics Conference and Exhibit*, AIAA Paper 2011-3705, 2011.

[31] Strand, J.S., and Goldstein, D. B., "Global Sensitivity Analysis for DSMC Simulations of Hypersonic Shocks," *Journal of Computational Physics*, Vol. 246, 2013.

[32] Grinstead, J., Wilder, M., Olejniczak, J., Bogdanoff, D., Allen, G., and Danf, K., "Shock-heated Air Radiation Measurements at Lunar Return Conditions," *46th AIAA Aerospace Sciences Meeting*, AIAA Paper 2008-1244, 2008.

[33] Cruden, B. A., "Absolute Radiation Measurements in Earth and Mars Entry Conditions," NASA Technical Report ARC-E-DAA-TN13965, 2014.

[34] Miki, K., Panesi, M., Prudencio, E. E., and Prudhomme, S., "Estimation of the Nitrogen Ionization Reaction Rate Using Electric Arc Shock Tube Data and Bayesian Model Analysis," *Physics of Plasmas*, Vol. 19, No. 2, 2012, Paper 023507.

[35] Bird, G. A., *The DSMC Method*, Author, 2013.

[36] Boyd, I. D., and Schwartzentruber, T. E., *Nonequilibrium Gas Dynamics and Molecular Simulation*, Cambridge University Press, New York, NY, 2017.

[37] Parker, J. G., "Rotational and Vibrational Relaxation in Diatomic Gases," *Physics of Fluids*, Vol. 2, No. 4, 1959, pp. 449-462.

[38] Millikan, R. C., and White, D. R., "Systematics of Vibrational Relaxation," *Journal of Chemical Physics*, Vol. 39, No. 12, 1963, pp. 3209-3213.

[39] G. J. LeBeau, "A parallel implementation of the direct simulation Monte Carlo method," *Journal of Computational Methods in Applied Mechanics and Engineering*, Vol. 175, No. 3-4, 1999, pp. 319-337.

[40] Gallis, M. A., Torczynski, J. R., Plimpton, S. J., Rader, D. J., and Koehler, T., "Direct Simulation Monte Carlo: The Quest for Speed," *29th International*

Symposium on Rarefied Gas Dynamics, Xi'an, China, AIP Conf. Proc. 1628, 2014.

[41] Nanbu, K., "Probability Theory of Electron-Molecule, Ion-Molecule, Molecule-Molecule, and Coulomb Collisions for Particle Modeling of Materials Processing Plasmas and Gases," *IEEE Transactions of Plasma Science*, Vol. 28, No. 3, 2000, pp. 971-990.

[42] Zhang, C., and Schwartzentruber, T. E., "Inelastic Collision Selection Procedures for Direct Simulation Monte Carlo Calculations of Gas Mixtures," *Physics of Fluids*, Vol. 25, No. 10, 2013, Paper 106105.

[43] Haas, B. L., Hash, D. B., Bird, G. A., Lumpkin, F. E., and Hassan, H. A., "Rates of Thermal Relaxation in Direct Simulation Monte Carlo Methods," *Physics of Fluids*, Vol. 6, No. 6, 1994, pp. 2191-2201.

[44] Park, C., "Review of Chemical-Kinetic Problems of Future NASA Missions, I: Earth Entries," *Journal of Thermophysics and Heat Transfer*, Vol. 7, No. 3, 1993, pp. 385-398.

[45] Carlson, A. B., and Hassan, H. A., "Direct Simulation of Reentry Flows with Ionization," *Journal of Thermophysics and Heat Transfer*, Vol. 6, No. 3, 1992, pp. 400-404.

[46] Lee, J. H., "Electron-impact Vibrational Relaxation in High-Temperature Nitrogen," *Journal of Thermophysics and Heat Transfer*, Vol. 7, No. 3, 1993, pp. 399-405.

[47] Park, C., *Nonequilibrium Hypersonic Aerothermodynamics*, Wiley, New York, 1990.

[48] "NIST Atomic Spectra Database Levels Form [online database]," National Inst. Of Standards and Technology, http://physics.nist.gov/PhysRefData/ASD/levels_form.html [retrieved July 2015].

[49] Liechty, D. S., "Extension of a Kinetic Approach to Chemical Reactions to Electronic Energy Levels and Reactions Involving Charged Species with Application to DSMC Simulations," *NASA Technical Publication*, NASA TP-2014-218254, 2014.

[50] Radzig, A. A., and Smirnov, B. M., *Reference Data on Atoms, Molecules, and Ions*, Springer-Verlag, Moscow, 1980.

[51] Higdon, K. J., Goldstein, D. B., and Varghese, P. L., "Sensitivity Analysis of DSMC Parameters for an 11-Species Air Hypersonic Flow," *30th International Symposium on Rarefied Gas Dynamics*, AIP Conf. Proc. 1786, Victoria, B. C., July 2016.

[52] Shannon, C. E., "A Mathematical Theory of Communication," *The Bell System Technical Journal*, Vol. 27, 1948, pp. 379-423, 623-656.

[53] Steuer, R., Kurths, J., Daub, C. O., Weise, J., and Selbig, J., "The Mutual Information: Detecting and Evaluating Dependencies Between Variables," *Bioinformatics*, Vol. 18, No. 2, 2002, pp. S231–S240.

[54] Johnston, C. O., "Nonequilibrium Shock-layer Radiative Heating for Earth and Titan Entry," Ph.D. Dissertation, Virginia Polytechnic Institute and State University, Blacksburg, Virginia, 2006.

[55] Cruden, B. A., Martinez, R., Grinstead, J. H., and Olejniczak, J., "Simulation Vacuum Ultraviolet Through Near IR Absolute Radiation Measurement with Spatiotemporal Resolution in an Electric Arc Shock Tube," *41st AIAA Thermophysics Conference*, AIAA Paper No. 09-4240, San Antonio, TX, 2009.

[56] Higdon, K. J., Cruden, B. A., Brandis, A. M., Liechty, D. S., Goldstein, D. B., and Varghese, P. L., "Direct Simulation Monte Carlo Shock Simulation of Saturn Entry Probe Conditions," *Journal of Thermophysics and Heat Transfer*, Vol. 32, No. 3, 2018, pp. 680-690.

[57] National Research Council, *Vision and Voyages for Planetary Science in the Decade 2013-2022*, National Academies Press, Washington, D.C., 2012, pp. 206-208.

[58] Palmer, G., Prabhu, D., and Cruden, B. A., "Aeroheating Uncertainties in Uranus and Saturn Entries by the Monte Carlo Method," *Journal of Spacecraft and Rockets*, Vol. 51, No. 3, 2014, pp. 801-814.

[59] Haas, B. L., and Milos, F. S., "Simulated Rarefied Entry of the Galileo Probe into the Jovian Atmosphere," *Journal of Spacecraft and Rockets*, Vol. 32, No. 3, 1995, pp. 398-403.

[60] Moss, J. N., LeBeau, G. J., Blanchard, R. C., and Price, J. M., "Rarefaction Effects on Galileo Probe Aerodynamics," *NASA Technical Report*, NASA TM-111620, 1996.

[61] Myo, K. S., Zhou, W., Lee, K. L., Yu, S., and Hua, W., "Direct Monte Carlo simulation of nanoscale mixed gas bearings," *Advances in Mechanical Engineering*, Vol. 7, No. 6, 2015.

[62] Boyd, I. D., Jafry, Y. R., and Beukel, J. V., "Particle Simulations of Helium Microthruster Flows," *Journal of Spacecraft and Rockets*, Vol. 31, No. 2, 1994, pp. 271-277.

[63] Boyd, I. D., Beattie, D. R., and Cappelli, M. A., "Numerical and experimental investigations of low-density supersonic jets of hydrogen," *Journal of Fluid Mechanics*, Vol. 280, Dec. 1994, pp. 41-67.

[64] Wysong, I. J., Pobst, J. A., and Boyd, I. D., "Comparisons of hydrogen atom measurements in an arcjet plume with DSMC predictions," *32nd Joint Propulsion*

Conference and Exhibit, AIAA Paper No. 1996-3185, Lake Buena Vista, FL, 1996.

[65] Boyd, I. D., "Extensive Validation of a Monte Carlo Model for Hydrogen Arcjet Flowfields," *Journal of Propulsion and Power*, Vol. 13, No. 6, 1997, pp. 775-782.

[66] Bondar, Ye. A., Trotsyuk, A. V., and Ivanov, M. S., "DSMC Modeling of the Detonation Wave Structure in Narrow Channels," *47th AIAA Aerospace Sciences Meeting*, AIAA Paper No. 2009-1568, Orlando, FL, 2009.

[67] Bondar, Ye. A., and Ivanov, M. S., "DSMC Study of an H2/O2 Detonation Wave Structure," *10th AIAA/ASME Joint Thermophysics and Heat Transfer Conference*, AIAA Paper No. 2010-4504, Chicago, IL, 2010.

[68] Bondar, Ye. A., Maruta, K., and Ivanov, M. S., "Hydrogen-Oxygen Detonation Study by the DSMC Method," *27th International Symposium on Rarefied Gas Dynamics*, *AIP Conference Proceedings,* Vol. 1333, Pacific Grove, CA, 2011, pp. 1209-1214.

[69] Sebastiao, I. B., and Alexeenko, A., "Consistent post-reaction vibrational energy redistribution in DSMC simulations using TCE model," *Physics of Fluids*, Vol. 28, No. 10, 2016, Paper 107103.

[70] Takama, Y., and Suzuki, K., "Study on rotational relaxation in a steady hydrogen plasma jet using emission spectroscopy", *Journal of Thermophysics and Heat Transfer*, Vol. 24, No. 3, 2010, pp. 598-602.

[71] Willauer, D. L., and Varghese, P. L., "Direct Simulation of Rotational Relaxation Using State-to-State Cross Sections," *Journal of Thermophysics and Heat Transfer*, Vol. 7, No. 1, 1993, pp. 49-54.

[72] Liebowitz, L. P., and Kuo, T. J., "Ionizational Nonequilibrium Heating During Outer Planetary Entries," *AIAA Journal*, Vol. 14, No. 9, 1976, pp. 1324-1329.

[73] Gordon, S. and McBride, B. J., "Computer Program for Calculation of Complex Chemical Equilibrium Compositions and Applications," *NASA Technical Report*, RP 1311, 1994.

[74] Park, C., "Nonequilibrium ionization and radiation in hydrogen-helium mixtures", *Journal of Thermophysics and Heat Transfer*, Vol. 26, No. 2, 2012, pp. 231-243.

[75] Vincenti, W. G., and Kruger, C. H., *Introduction to Physical Gas Dynamics*, Wiley, NY, 1965, pp. 108-145, 219-228.

[76] Parsons, N. S., and Levin, D. A., "DSMC implementation of MD/QCT generated energy distributions for SO2 + O collisions," *44th AIAA Thermophysics Conference*, San Diego, CA, Paper No. AIAA 2013-2785, 2013.

[77] Hinshelwood, C. N., *Kinetics of Chemical Change*, Clarendon Press, Oxford, 1940, pp. 36-39.

[78] Strand, J. S., and Goldstein, D. B., "Sensitivity Analysis for DSMC Simulations of High-Temperature Air Chemistry," *49th AIAA Aerospace Sciences Meeting*, Paper No. AIAA 2011-535, Orlando, FL, 2011.

[79] Choquet, I., "Thermal nonequilibrium modeling using the direct simulation Monte Carlo method: Application to rotational energy," *Physics of Fluids*, Vol. 6, No. 12, 1994, pp. 4042-4053.

[80] Wysong, I. J., and Wadsworth, D. C., "Assessment of direct simulation Monte Carlo phenomenological rotational relaxation models," *Physics of Fluids*, Vol. 10, No. 11, 1998, pp. 2983-2994.

[81] Zhang, C., Valentini, P., and Schwartzentruber, T. E., "Nonequilibrium-Direction-Dependent Rotational Energy Model for Use in Continuum and Stochastic Molecular Simulation," *AIAA Journal*, Vol. 52, No. 3, 2014, pp. 604-617.

[82] Fowler, R., and Guggenheim, E. A., *Statistical Thermodynamics*, Cambridge University Press, Cambridge, 1956, pp. 497-499.

[83] Gimelshein, S. F., Gimelshein, N. E., Levin, D. A., Ivanov, M. S., and Wysong, I. J., "On the use of chemical reaction rates with discrete internal energies in the direct simulation Monte Carlo method," *Physics of Fluids*, Vol. 16, No. 7, 2004.

[84] Haas, B. L., and Boyd, I. D., "Models for direct Monte Carlo simulation of coupled vibration-dissociation," *Physics of Fluids*, Vol. 5, No. 2, 1993, pp.478-489.

[85] Boyd, I. D., "Modeling Backward Chemical Rate Processes in the Direct Simulation Monte Carlo Method," *Physics of Fluids*, Vol. 19, No. 12, 2007, Paper 126103.

[86] Gupta, R. N., Yos, J. M., Thompson, R. A., and Lee, K.P., "A Review of Reaction Rates and Thermodynamic and Transport Properties for an 11-Species Air Model for Chemical and Thermal Nonequilibrium Calculations to 30000 K," *NASA Technical Report*, NASA-RP-1232, 1990.

[87] Gordon, S., and McBride, B. J., "Thermodynamic Data to 20,000 K for Monatomic Gases," *NASA Technical Report*, NASA-TP-1999-208523, 1999.

[88] Boyd, I. D., and Gokcen, T., "Computation of Axisymmetric and Ionized Hypersonic Flows Using Particle and Continuum Methods," *AIAA Journal*, Vol. 32, No. 9, 1994, pp. 1828-1835.

[89] Barnhardt, M. D., "Modeling and Simulation of High-Speed Wake Flows," Ph.D. Dissertation, Dept. of Aerospace Engineering and Mechanics, University of Minnesota, Minneapolis, MN, 2009.

[90] "Chemical Equilibrium with Applications [online code download]," NASA Glenn Research Center, https://www.grc.nasa.gov/www/CEAWeb/ [retrieved June 2017].

[91] Cruden, B. A., and Brandis, A. M., "Measurement and Prediction of Radiative Non-equilibrium for Air Shocks Between 7-9 km/s," *47th Thermophysics Conference*, Denver, Colorado, June 2017.

[92] Park, C. and Menees, G. P., "Odd nitrogen production by meteoroids," *Journal of Geophysical Research: Oceans*, Vol. 83, No. C8, 1978, pp. 4029-4035.

[93] Wilson, J., "Ionization rate of air behind high-speed shock waves," *Physics of Fluids*, Vol. 9, No. 10, 1966, pp. 1913-1921.

[94] Huo, W. M., Liu, Y., Panesi, M., Munafo, A., Wray, A., and Carbon, D. F., "Electron-Impact Excitation Cross Sections for Modeling Non-Equilibrium Gas," *53rd AIAA Aerospace Sciences Meeting*, Kissimmee, FL, 2015.

[95] Johnston, C. O. and Panesi, M., "Impact of State-Specific Flowfield Modeling on Atomic Nitrogen Radiation," *Physical Review of Fluids*, Vol. 3, 2018, pp. 013402-1 – 013402-24.

[96] Panesi, M. and Lani, A., "Collisional radiative coarse-grain model for ionization in air," *Physics of Fluids*, Vol. 25, 2013, pp. 057101-1 – 057101-27.

[97] Panesi, M., Magin, T., Bourdon, A., Bultel, A., and Chazot, O., "Fire II Flight Experiment Analysis by Means of a Collisional-Radiative Model," *Journal of Thermophysics and Heat Transfer*, Vol. 23, No. 2, 2009, pp. 236-248.

[98] McBride, B. J., and Gordon, S., "Chemical Equilibrium with Applications Code," https://www.grc.nasa.gov/www/CEAWeb/ [retrieved June 2017].

[99] Brandis, A. M., Johnston, C. O., and Cruden, B. A., "Investigation of Non-equilibrium Radiation for Earth Entry," *46th AIAA Thermophysics Conference*, AIAA Aviation, Washington, D.C., 2016.

[100] Brandis, A. M., Johnston, C. O., Cruden, B. A., Prabhu, D., and Bose, D., "Uncertainty Analysis and Validation of Radiation Measurements for Earth Reentry," *Journal of Thermophysics and Heat Transfer*, Vol. 29, No. 2, 2015, pp. 209-221.

[101] Voelkel, S., and Varghese, P. L., "Multitemperature Dissociation Rate of $N_2 + N_2 \rightarrow N_2 + N + N$ Calculated Using Selective Sampling Quasi-Classical Trajectory Analysis," *Journal of Thermophysics and Heat Transfer*, Vol. 31, No. 4, 2017, pp. 965-975.

[102] Mankodi, T. K., Bhandarkar, U. V., and Puranik, B. P., "An ab initio chemical reaction model for the direct simulation Monte Carlo study of non-equilibrium nitrogen flows," *The Journal of Chemical Physics*, Vol. 147, 2017, pp. 08305-1 – 084305-10.

[103] Mankodi, T. K., Bhandarkar, U. V., and Bhalchandra, P. P., "Dissociation cross sections for $N_2 + N \rightarrow 3N$ and $O_2 + O \rightarrow 3O$ using the QCT method," *The Journal of Chemical Physics*, Vol. 146, 2017, pp. 204307-1 – 204307-11.

[104] Wysong, I., Gimelshein, S., Gimelshein, N., McKeon, W., and Esposito, F., "Reaction cross sections for two direct simulation Monte Carlo models: Accuracy and sensitivity analysis," *Physics of Fluids*, Vol. 24, 2012, pp. 042002-1 – 042002-15.

[105] Park, C., "Rate Parameters for Electronic Excitation of Diatomic Molecules 1. Electron-Impact Processes," *46th AIAA Aerospace Sciences Meeting and Exhibit*, AIAA 2008-1206, 2008.

[106] Park, C., "Rate Parameters for Electronic Excitation of Diatomic Molecules II. Heavy Particle-Impact Processes," *46th AIAA Aerospace Sciences Meeting and Exhibit*, AIAA 2008-1446, 2008.

[107] Prudencio, E. and Schulz, K. W., "The Parallel C++ Statistical Library 'QUESO': Quantification of Uncertainty for Estimation, Simulation, and Optimization," *Euro-Par 2011: Parallel Processing Workshops*, Vol. 7155, 2011.

[108] Haario, H., Laine, M., Mira, A., and Saksman, E., "DRAM: Efficient adaptive MCMC," *Statistics and Computing*, Vol. 16, 2006.

[109] Koura, K. and Matsumoto, H., "Variable soft sphere molecular model for inverse-power-law or Lennard-Jones potential," *Physics of Fluids*, Vol. 4, No. 5, 1992, pp. 1083-1085.